

**DEVELOPMENT OF FLUORESCENT
TRACERS FOR VELOCIMETRY
MEASUREMENTS IN
MULTICONSTITUENT / MULTIPHASE
FLOWS**



Mourad Chennaoui

Degree of Doctor of Philosophy

The University of Edinburgh

2008

ABSTRACT

This thesis describes the development of optimised fluorescent dye-doped tracer droplets for gas phase particle image velocimetry (PIV), to study mixing in multi-phase flows. The use of these tracer droplets in applications where flare can be an obstacle to obtaining velocity flow data is also demonstrated. In PIV, micron-sized tracer particles are normally required to accurately follow the flow while at the same time providing optimum fluorescence signal for proper image capture. Thus, there is a requirement to identify dyes with high quantum yield that can be dissolved in suitable nebulisable solvents at high concentrations and to investigate the effect of high concentration on fluorescence properties, such as fluorescence concentration quenching effects that could lead to a decrease of the fluorescence signal from tracer droplets.

The selection criteria of candidate dyes and the study of their fluorescence properties by steady-state spectrofluorometry are presented. Bis-MSB and DCM were identified to be the optimum blue and red emitting dyes and to offer high solubility in *o*-xylene and DMSO respectively. As quantitative intensity measurement in conventional cuvette-based measurements is limited to highly diluted solutions, a novel experimental approach employing stabilised emulsions to emulate the fluorescence properties of micron-sized tracer droplets has been developed. Dye-doped oil-in-water and water-oil emulsions, stabilised by nanoparticles, have been prepared and characterised and their fluorescence properties investigated using a custom-built spectrometric system. This technique allowed quantitative fluorescence intensity measurements of emulsion droplets containing dye concentrations up to the solubility limit ($\sim 10^{-2}\text{M}$) and showed that no concentration quenching of fluorescence occurs in highly dye-doped micron-sized tracer droplets.

The development of a single-colour-camera PIV system that can image micron-sized and spectrally distinct fluorescent tracers in a two-phase flow is reported. Each of the flows is seeded with either highly-doped droplets containing Bis-MSB or DCM dyes.

The system exploits the inherent co-registration offered by a 3-chip colour CCD camera with the images recorded in the 3 colour planes enabling flow constituent / phase to be determined as well as pulse order. The PIV system and seeding strategy are described and discussed. The PIV results show that the spectral discrimination process is robust and in a well-mixed gas-phase flow the average error between the flow velocities in the two constituents is less than 4%.

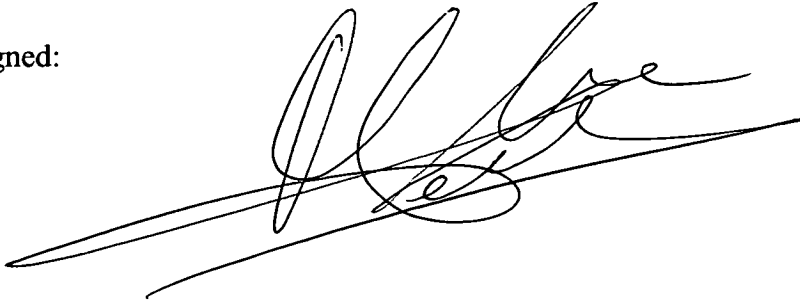
In some applications where flow velocity information in the vicinity of an object is critical, the illuminating light sheet impinging on the object surface produces flare that prevents PIV data from being obtained. In a novel approach, using 1 μm tracer particles of *o*-xylene doped with Bis-MSB and an appropriate optical filter, the illuminating light has been spectrally separated from the imaging signal and the elastically scattered flare removed.

The use of dye-doped microemulsions in a novel micro-PIV seeding methodology for full field velocity measurements in microfluidic devices is presented. This approach gives improved particle image contrast and reduced motion parallax uncertainty, when compared to conventional solid seed particles. Results of micro-PIV measurements in T- and Y- junction microfluidic chips are presented. Channel velocity profiles were found to agree with CFD simulations and slight deviations from the ideal behaviour are discussed.

DECLARATION

I declare that the work presented in this thesis is my own unless stated by reference.

Signed:

A handwritten signature in black ink, consisting of several loops and a long horizontal stroke at the end, positioned above a horizontal line.

Date:

06.02.2003

ACKNOWLEDGEMENTS

Firstly I wish to express my gratitude to my supervisor, Dr. Anita Jones for her continued encouragement and invaluable suggestions during this work. I would like to also thank her for always keeping me in focus and knowing whether I needed a word of encouragement or a kick in the butt. I could not have wished for a better mentor for my PhD.

I would also like to thank Prof. Towers for the opportunity to undertake this PhD and for his valuable advice, constructive feedback and comments. My further thanks go to his group with whom it was a privilege to work. I benefitted greatly from their inventiveness and my special thanks go to Diego, Matt and Ewan for providing crucial help with their PIV work, and to Natalia for writing the image processing code.

My sincere gratitude to Dr. David Mendels for giving me the chance to work on the Micro-PIV experiments, for offering his advice and for his help in solving the flow modelling.

I am indebted to all those who helped me and contributed directly or indirectly to my work, especially to my group for the advice and assistance, particularly to Trish and Rob. Massive thanks to Bradley's group for letting me use their equipment, and particularly to Juanjo, Lois and Rosario, with whom it was a great pleasure to work.

I could not forget to thank the store, mechanical workshop and teaching lab staff for their joy and willingness to help.

One of the most important people who have been with me through every moment of my PhD years is my cherished wife Orla. I would like to thank her for the many sacrifices she has made to support me in undertaking my doctoral studies. I want also to thank Austin and Mairead for their relentless support and encouragement, and my parents for their love and understanding.

My thanks go also to my friends, especially Jimbo, Laurent, Fran and John, and also to my brother and sister Farid and Soraya for their endless encouragement and the good times spent together.

scientia vincere tenebras

TABLE OF CONTENTS

CHAPTER 1: INTRODUCTION.....	1
1. Overview	1
2. The context.....	3
2.1. CO₂ Emission Regulations and Standards in the European Union.....	3
2.2. Gasoline Direct Injection.....	4
2.2.1- Comparison of conventional and GDI engines	4
2.2.2- Optimisation of the GDI engine to reduce CO ₂ emissions and fuel consumption	6
2.2.3- The importance of monitoring air/fuel mixture and spray characteristics in the GDI engine.....	7
3. Flow measurements.....	9
4. Particle Image Velocimetry	10
4.1. Development	10
4.2. Multiphase PIV	13
4.3. Use of Emulsions for Fluorescent Tracer Optimisation	17
4.4. Flare Removal in Gas Phase PIV.....	18
5. Micro-PIV using novel FLuorescent droplet emulsions	19
6. References	20
CHAPTER 2: BACKGROUND.....	25
1. Absorption and fluorescence.....	25
1.1. Light Absorption	25
1.1.1- Generalities.....	25
1.1.2- Transition probability and absorption coefficient	26
1.1.2.1- Selection rules for a transition.....	35
1.1.2.2- Absorption coefficient.....	36
1.1.3- Franck-Condon principle.....	28
1.2. Fluorescence	29
1.2.1- Fluorescence characteristics	29
1.2.2- Fluorescence quenching	33
1.2.3- Solvent effect.....	34
1.3. Steady-state Spectrofluorometry	36
1.3.1- The spectrofluorometer	36
1.3.2- Steady-state fluorescence	38
1.3.3- The inner-filter effect	38

2. Particle image velocimetry	40
2.1. Principle of Particle Image Velocimetry	40
2.2. Laser source and laser light sheet generation	41
2.3. PIV Laser	41
2.3.1- Laser light sheet generation.....	42
2.4. Tracer Particles	43
2.4.1- Tracers in a Flow	43
2.4.2- Light scattering from particles	44
2.4.3- Fluorescence from tracer droplets	45
2.4.4- Generation of tracers	47
2.5. Data and Image Processing	48
2.6. Image Recorder and Optical System.....	50
2.6.1- Cross-correlation PIV camera	50
2.6.2- Recording optics.....	51
2.6.2.1- Particle image size.....	66
2.6.2.2- Depth of field.....	67
3. Emulsions	54
3.1. Emulsion instability processes	54
3.2. The Stability of Pickering Emulsions	56
3.3. Emulsification Processes.....	58
3.3.1- Emulsification with Rotor-stator processors	58
3.3.2- Emulsification with Ultrasonic processors.....	59
4. References	60
CHAPTER 3: EXPERIMENTAL.....	63
1. Spectroscopy	63
1.1. Steady state Fluorescence measurements	63
1.2. UV-VIS Measurements.....	64
2. EMulsion Preparation, charActerisation and imaging.....	64
2.1. Emulsions preparation	64
2.2. Microscope imaging	64
2.3. Emulsion droplet size distribution.....	65
2.4. Flow Cytometry	66
3. Particle image velocimetry	66
3.1. Macro-PIV	66
3.1.1- Tracer droplets generation.....	66
3.1.2- Lasers	67
3.1.3- Imaging system	68
3.1.4- Recording medium	68
3.1.5- Data Processing.....	68
3.2. Micro-PIV	68

CHAPTER 4: IDENTIFICATION AND CHARACTERISATION OF AN OPTIMUM FLUOROPHORE FOR PRODUCTION OF DOPED TRACER DROPLET.....71

1. Introduction	71
1.1. Required Properties of the Fluorophore.....	73
2. materials.....	76
3. Experimental	77
3.1. Fluorescence and Absorption Measurements on Bulk Solutions	77
3.2. Emulsion Preparation.....	77
3.2.1- Preparation of oil-in-water emulsions	77
3.2.2- Preparation of water-in-oil emulsions	78
3.2.3- Characterisation of Emulsions	78
3.3. Fluorescence Measurements on Emulsions	79
4. Results and Discussion	81
4.1. Fluorescence of Bulk Solutions	81
4.1.1- Blue emitting dyes.....	81
4.1.2- Red emitting dyes.....	87
4.2. Optimisation and Characterisation of Emulsions.....	89
4.2.1- Oil in water (O/W) emulsions	89
4.2.1.1- Formulation 1.....	112
4.2.1.2- Formulation 2.....	121
4.2.2- Water in oil (W/O) emulsion.....	101
4.3. Fluorescence of Emulsions	104
4.3.1- Fluorescence of doped O/W emulsions.....	104
4.3.2- Fluorescence of doped W/O emulsions.....	106
5. Conclusions	109
6. References	110

CHAPTER 5: OPTIMISED FLUORESCENT TRACERS FOR MULTI-PHASE PIV.....114

1. Introduction	113
2. Fluorescent Tracer Selection and Imaging System.....	116
3. Experimental	118
3.1. Material.....	118
3.2. Experimental	118
3.2.1- Laser light sheet formation.....	118
3.2.2- Laser light sheets alignments	119
3.2.3- Seeding methodology and imaging	119
3.2.4- Tracers droplets sizing	120

4. Results and discussions	122
4.1. Light Sheet alignments and Beam Profile	122
4.2. Drop sizing	123
4.3. Cross-Talk Elimination	125
4.4. Image corrections	128
4.5. Flow Field Velocity Vectors	129
5. Conclusions	134
6. References	135

CHAPTER 6: OPTIMISED FLUORESCENT TRACERS FOR FLARE REMOVAL IN GAS PHASE PIV.....136

1. Introduction	136
2. EXPERIMENTAL	138
2.1. Materials	138
2.2. Seeding methodology	138
2.2.1- Tracers droplets sizing	138
2.3. Experimental setup	138
2.3.1- Laser sheets alignments.....	138
2.3.2- Flow field against a turbine blade surface model.....	139
2.3.3- Imaging system and data processing.....	139
2.3.4- 532 nm Illumination.....	140
2.3.5- 355 nm Illumination.....	140
3. Results and discussions	141
3.1. Drop Sizing	141
3.2. 532 nm Illumination PIV Results	142
3.3. 355 nm Illumination PIV Results	144
4. Conclusions	146
5. References	147

CHAPTER 7: IMPLEMENTATION OF EMULSION DROPLETS AS TRACERS FOR MICRO-PIV MEASUREMENT148

1. Introduction	148
2. Experimental	151
2.1. Material	151
2.2. W/O Emulsion Preparation	151
2.3. Micro-PIV System	151

3. Results and discussion.....	154
3.1. Emulsion Characterisation.....	154
3.2. Micro-PIV Results.....	156
3.2.1- Validation of water-in-oil emulsion as tracers	156
3.2.2- Velocity results.....	158
4. Conclusions	161
5. Reference.....	162
CHAPTER 8: CONCLUSIONS.....	163
APPENDIX I: QUANTITATIVE FLUORESCENCE MEASUREMENT FROM IMAGING AIRBORNE MICRON-SIZED FLUORESCENT DROPLETS.....	165
1. Introduction	165
2. Background.....	166
3. Experimental	166
4. Results and Discussions	168
5. References	175
APPENDIX II.....	176
Lectures and Conferences	176
Postgraduate Lectures and Courses	176
Conferences and Meetings.....	176
Publications.....	177
Reprint of Publications	178

CHAPTER 1:

INTRODUCTION

1. OVERVIEW

Today, car manufacturers are facing ever more, increasingly stringent, regulations and standards, on fuel consumption and emissions. To face up to the challenge, Gasoline Direct Injection (GDI) is one of the advances in engine design that the industry is developing to produce Ultra Low Emissions Vehicles (ULEV). To guarantee an optimum performance, a GDI engine relies on the control of the mixture formation in the combustion chamber.

In order to gain an in-depth understanding of the mixing process, the development of non-intrusive techniques is being pursued. One of the most promising techniques is based on the combination of optical sensor instrumentation and computational fluid dynamics.

The research described in this thesis, carried out in collaboration with Prof D.P. Towers of the Department of Mechanical Engineering of Leeds University, is concerned with the development of novel techniques to characterise multiconstituent/multiphase spray systems, and the related mixing phenomena in the engine, within the cylinder. The instrumentation to be elaborated is based upon the principle of Particle Image Velocimetry (PIV) and the overall goals of the project were:

1. to devise full-field optical instrumentation for simultaneous multiconstituent/phase velocity vector measurements with the aid of optically active seed particles with optimised fluorescent yield.

2. to develop and optimise sets of fluorescent tracers and solvents, giving peak fluorescence detectability by the PIV imaging system; to achieve flare removal in gas phase PIV.

2. THE CONTEXT

2.1. CO₂ Emission Regulations and Standards in the European Union

Under the Kyoto Protocol of the United Nations Convention on Climate Change, the European Union committed itself to reducing greenhouse gas (GHG) emissions by 8 % by 2008-2012 compared to the 1990 level. One of the major contributors to GHG emission is the sector of road transport, since CO₂ emissions in the EU-15 grew on average by 1.6% per year between 1990 and 1995 and by 2 % per year between 1995 and 2001. Overall, CO₂ emissions from road transport grew by 22 % between 1990 and 2001. In the latter year, road transport accounted for 24 % of the total manmade CO₂ emissions in the EU-15, and passenger car traffic was probably responsible for around 60 per cent of this.¹

As projected by the European Auto-Oil II Program* (AOPII), with the regulations that have already been decided, the problem of toxic emissions from road transport in Europe will be solved by 2020. The only sticking point is that CO₂ emissions will have to be tackled actively². Thus, the strategy adopted by the European Union in 1998 to reduce CO₂ releases from passenger cars, consists of a voluntary commitment by the automobile industry on fuel economy improvements (ACEA Agreement) by mainly technological developments and the subsequent market changes. The set targets on CO₂ emission for new passenger cars are of 140 g CO₂/km by 2008 and 120 g CO₂/km in 2012.³ These stringent regulations have forced the car manufacturers to rethink the engine internal combustion concept, which has prompted the development of new engine designs such as High Speed Direct Injection Diesel (HDI) engines, and Gasoline Direct Injection (GDI) engines.

* The Auto-Oil II Programme (AOPII) was launched in spring 1997 initially in order to fulfil the aims of the review clauses in the EU Commission's "Auto-Oil I" proposals. These referred to the need to come forward with an updated strategy to meet the requirements of the Community air quality standards and related objectives by 2010 at least cost.

2.2. Gasoline Direct Injection

From the early 1990's fuel economy and CO₂ emission reduction became one of the major challenges to be tackled by the automotive industry. Since then, much research effort has been deployed in the development of new engines, allying both the superior performance and cleaner exhaust gas of gasoline spark-ignition (SI) engines, and the higher fuel economy of compression-ignition (CI) diesel engines. The enhanced fuel economy achieved by a diesel CI engine when compared to a SI gasoline engine is mainly due to the use of higher compression ratio, combined with unthrottled operation⁴ (throttling: engine speed and torque level controlled by the amount of fuel injected). On the other hand, diesel engines exhibit higher noise and vibration as well as particulate and NO_x emission levels than a gasoline SI engine.⁵ Although the gasoline direct injection engine concept is not new in essence and dates back to the early 1950's, its emergence into mass production was impeded by technical limitations such as high hydrocarbon and soot emission and poor performance⁶. Today, advances in GDI engine design as well as electronic control of direct-injection injectors and pumps, make GDI engines a viable technology for the mass market.

The GDI engine's potential of achieving high power output and fuel economy consists in the precise control over the fuel injection timings and amount of fuel delivered in the combustion chamber. These two parameters are constantly varied in order to match the driving load conditions so that at low load, the engine operates in a extremely lean condition (stratified charge), whereas at high load, fuel injection modulation governs the engine power in similar fashion than diesel engine.

Far from presenting an in-depth exposition of the technical features of the GDI engine and its functioning mode, this thesis will present the most relevant aspects of this technology to emphasise the context of this research.

2.2.1. Comparison of conventional and GDI engines

The main difference between current "conventional" SI gasoline engines and GDI engines resides in the air/fuel mixture preparation approach. Current SI engines are

based on a fuel injection system known as Multi-Point Injection (MPI) - which replaced the carburation system of the 1970's- where the fuel is injected into each intake port of each individual cylinder before the intake valve opens (Figure 1.1).

On the other hand, a GDI engine is devised to operate in a similar way to a diesel engine; the gasoline is injected directly into the cylinder (Figure 1.2).

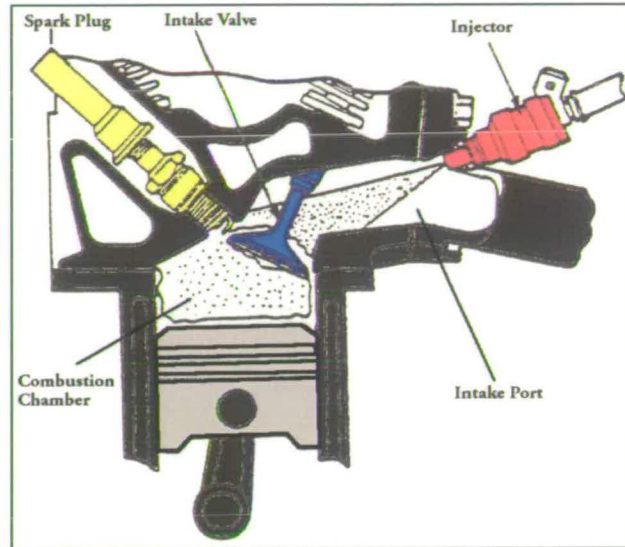


Figure 1.1: Mixture preparation in a typical MPI SI engine⁷.

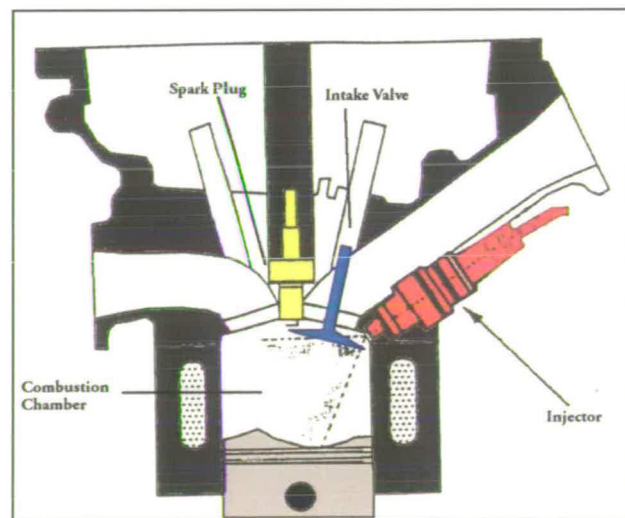


Figure 1.2: Mixture preparation in a typical GDI engine⁷.

2.2.2. Optimisation of the GDI engine to reduce CO₂ emissions and fuel consumption

Although the MPI SI gasoline engine has proven its reliability, in term of fuel economy it still suffers from two major limitations. At engine start (cranking) or cold starting, fuel metering can be inaccurate due to the formation of a puddle of liquid fuel in the intake valve. Consequently, the engine operates in rich mixture conditions, which in return increases the levels of unburned hydrocarbons and emission. Secondly, the engine load is controlled by throttling which is thermodynamically inefficient due to pumping losses i.e. the energy loss due to the work required to displace air into and out of the cylinders.

These limitations are avoided in the GDI engine, as the fuel is injected directly into the cylinder. This allows greater fine-tuning and more precise control over the amount of injected fuel as well as a better control of the injection timing to match the engine load conditions.

The key feature associated with the fuel economy of direct injection is the concept of stratified charge⁸. GDI's electronic controls allow the fuel to be injected in two different ways, depending on the engine's load, as illustrated in Figure 1.3. During high load demand (for example in-town driving), fuel is injected so that the air/fuel mixture is evenly distributed throughout the combustion chamber; this is homogeneous charge. Meanwhile, at low load demand (for example motorway driving), a smaller, and more concentrated air/fuel mixture cloud is formed around the spark plug; this is lean-burn or stratified-charge operation.

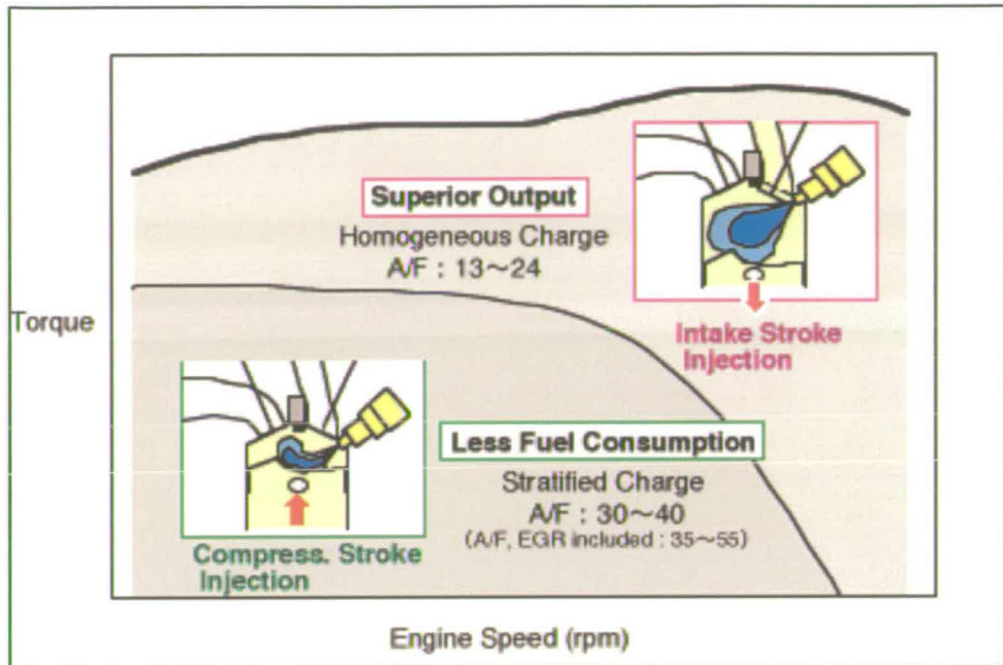


Figure 1.3: Variability of fuel delivery in the GDI engine (A/F: air/fuel ratio; EGR: Exhaust Gas Recirculation system, fresh air or inert gas returned to the combustion charge during stratified-charge operation)⁹.

2.2.3. The importance of monitoring air/fuel mixture and spray characteristics in the GDI engine

Amongst many determining factors for the delivery of optimum performance by a GDI engine, two important factors are of interest in the context of this thesis. The first concerns the impact of the in-cylinder/spray injector design on directing and stabilising the mixture plume around the spark plug during stratified operation, in order to produce satisfactory ignition. The second relates to the air/fuel mixture-preparation prior to combustion.

Injecting fuel directly into fuel chambers reduces the time for mixture preparation which can lead to cylinder wall wetting and other effects producing incomplete combustion with unacceptably high emissions of hydrocarbons or soot. Therefore, the monitoring and diagnosis of the impact of different designs of in-cylinder injector on mixture stratification as well as the influence of combustion chamber conditions (pressure, temperature, air flow field...) on spray evolution, droplet atomisation,

dispersion and evaporation, are of the highest importance for understanding and improving the quality of the combustion process.

Active research work has been done in this area, such as that of (to cite only a few) Aoki *et al.* where the combination of experimental and computational fluid dynamic calculations were used to evaluate air/fuel mixture distribution and movement in combustion chamber¹⁰, Lee *et al.* on the spray structure and the atomisation mechanism of the high-pressure swirl-type GDI injector using a phase Doppler anemometer (PDA) system¹¹ and Park *et al.* on the sizing spray droplets within the engine in-cylinder using a planar imaging technique based on laser-induced fluorescence (LIF) and the Mie scattering.¹² Yamakawa *et al.* investigated the air velocity distribution in and around a GDI gasoline spray using a combined LIF- PIV system¹³, whereas work on the effect of piston shape and intake flow on the fuel mixture was carried by Kang *et al.* using a laser induced exciplex fluorescence technique¹⁴.

Monitoring and diagnosis techniques for quantitative/qualitative flow measurements and characterisation are various, and often involve the use of a CCD camera as a means of image recording and/or analysis. These methods encompass a broad range of instrumentations, such as endoscopic setups for direct imaging, Laser Doppler Anemometry (LDA) or Phase Doppler Anemometry (PDA) for droplet sizing, fuel atomization and evaporation^{12,15,16}; or Laser Induced Fluorescence (LIF) and/or Particle Image Velocimetry (PIV) for spray structure visualisation, flow field velocity measurements and droplet sizing¹⁷⁻²¹.

3. FLOW MEASUREMENTS

Flows, and particularly turbulent flows, are present in a wide range of naturally occurring phenomena and technological applications. The complexity in mathematically treating the chaotic and stochastic characteristics of turbulent flows renders their measurement of great importance. Historically, quantitative and qualitative flow measurements evolved from the use of point velocity techniques, such as Hot-Wire Anemometry²²⁻²⁴ (HWA) in the 1920. HWA is based on the principle of heat transfer between the sensing surface of a probe and the properties of the fluid passing over it. Although this technique shows both high spatial and temporal resolution, it is intrusive and interferes with the flow. The invention of lasers in the 1960 allowed the use of the laser beam as a non-intrusive tool to probe the flow, which led to the development of Laser-Doppler Anemometry²⁵⁻²⁷ (LDA). In LDA, flow velocimetry measurements are inferred from the Doppler shift due to the velocity of micron-sized particles seeded in the flow. Essentially, when the incident laser beam is focused on a measurement section of the flow, the scattered light from the particles incurs a frequency shift which is linearly proportional to their velocity. The use of more than one laser beam combined with interferometric methods and optics allows two- or three-component velocimetry measurements to be made.

The LDA technique was successful in turbulent flow research because of its high temporal/spatial resolution, non-intrusiveness and directional response, but as with HWA, it is a point velocimetry technique, which means that only one section of the flow volume can be sampled at a time. Larger flow sections can be quantified by LDA through a scanning approach; however, this can be time consuming and limited to steady-state flows.

The advances in laser, camera and computer technology from the 1980 opened the way for the development of full field (or global) velocimetry measurement techniques, amongst which PIV emerged to be the most widely today for qualitative and quantitative flow characterisation.

4. PARTICLE IMAGE VELOCIMETRY

4.1. Development

The development of particle image velocimetry emerged from the initial applications of Laser Speckle Velocimetry²⁸⁻³⁰ (LSV) as a technique for full-field fluid velocity measurements. In LSV, a laser light sheet is used to illuminate the flow which has been seeded with a high density of tracer particle, the light scattered from which interferes to produce speckle patterns. Double exposure recording is then used to generate speckle image pairs, which are correlated to produce the local velocity field. The LSV technique was used with much success within the fluid mechanics community for the study of a wide range of flow phenomena. However, the requirement for high seed density to generate speckle patterns is a shortcoming of this technique since the seed particle loading can affect the flow behaviour under study³¹. Furthermore, the LSV speckle patterns can be difficult to correlate when out-of-plane flow motions are present, as is the case in highly turbulent flows³².

As the imaging of particles rather than speckle became recognised as a better alternative for the study of turbulent flow structures, the basic foundations of PIV as a technique for flow visualisation and quantification were laid by the work of Adrian³³ and Pickering and Halliwell³⁴. In principle, PIV is equivalent to LSV, apart from the seed particle density which is much lower in PIV, and which subsequently produces tracer image pairs instead of speckle image pairs. In this way, the local flow velocity can be determined by measuring the fluid displacement, from particle images, and dividing this by the time interval between the exposures. As the exposure time interval and the spatial resolution of the imaging system are small when compared to the time and length scale of the flow, instantaneous and accurate velocity maps can be obtained.

The fluctuating accelerations of a turbulent flow require that tracer particles be small (of the order of micrometer diameter for experiments in gas flow) so that they can follow the flow without excessive slip. The associated small light-scattering cross-section combined with the required short-time exposure recording (when imaging

turbulent flow), means that powerful, pulsed lasers are needed for producing good quality particle images. In its early stage, PIV experiments relied on the use of continuous wave (CW) lasers (typically argon-ion) for flow illumination with the pulsed laser light sheet (LLS) generated using diverse strategies³⁵ such as: rotating multi-facet prisms, rotating mirrors and mechanical shutters. The technical limitations and the light intensity loss inherent to the implementation of CW lasers for pulsed LLS, constrained PIV to the study of low velocity air flows³⁶ until the arrival of double-pulsed solid-state lasers and particularly the Nd:Yag laser which saw its first application in 1986 in the work of Kompenhans *et al.*³⁷

The high pulse energy (typically 0.4 J at 532 nm), short pulse duration (5-10 ns) and high repetition rate (10 – 50 Hz) made the Nd:Yag laser the ideal PIV laser, delivering enough light intensity to produce good particle images from micron-sized tracers. Particle images can be recorded either on a photographic film or on a CCD camera sensor. The large dynamic range and the high resolution needed for the study of turbulent flows meant that photographic films were well suited to that purpose until CCD cameras with sufficient resolution became available. High-resolution photographic films such as the Kodak Technical Pan (300 lines/mm) – now discontinued – were very popular as their fine grain could store the equivalent of up to 80 Mbytes of data on a 35 mm film. However, due to the digitisation resolution limit of the typical image scanner, the final exploitable digital data for correlation analysis was limited to approx. 8 Mbytes³⁸.

The transition from film to CCD-based PIV was initiated in the early 1990 by the work of Willert *et al.*³⁹ which demonstrated that it was possible to generate PIV results from particle images recorded directly from a low resolution CCD camera (512x480). The theory behind this work, which became known as digital PIV (DPIV), was further extended by Westerweel⁴⁰ which applied sub-pixel interpolation techniques to low resolution images in order to estimate sub-pixel particle displacements. An in depth review on the fundamentals of DPIV can be found in reference 41, published by the same author⁴¹.

It was not long before the technological limitations of DPIV had been overcome (spatial resolution and frame rate) and today's PIV is exclusively DPIV. Common CCD sensors offer resolution over 12 Megapixels (equivalent to a 120 lines/mm 35 mm film) as well as many added advantages such as higher light sensitivity, linear light intensity response (as opposed to the logarithmic response of a film) and near real-time flow visualisation/computation³⁸.

PIV data processing, along with DPIV, saw tremendous development with the advancement in computer processing power. In order to extract velocity information from the flow, the double exposure particle image pairs were divided into a grid of interrogation windows/spots to which Fourier-transform-based algorithms were applied. In early algorithms, Young's fringe analysis methods were used where, from the amplitude and the orientation of the fringe spacing, it was possible to infer the image spot displacement. An alternative method was proposed by Sutton *et al.*⁴² and Adrian *et al.*³³ which consisted of applying an auto-correlation method to the image interrogation spots resulting from single-frame/double-pulse recording⁴³. In this method, a small group of particles belonging to an interrogation spot of the first image are statistically correlated (auto-correlation function) with the same ones (in the same spot) from the second image. The correlation function (or field) yields to a set of correlation peaks*, which corresponds to the shift in pixels from which the velocity values are inferred. However, the fact that the auto-correlation function is rotationally symmetric means that it suffers from directional ambiguity, i.e. the direction of the flow could not be determined. To resolve this, several techniques were employed such as spatial artificial shift⁴⁴, image de-rotation⁴⁵ and pulse coding⁴⁶.

Cross-correlation is another correlation method that has been developed by Keane and Adrian⁴⁷ and which relies on a different recording strategy, double-frame/single pulse. In this method, the first and the second image are recorded separately and then

*The spatial auto-correlation field results in a main peak at the origin (self-correlation peak) corresponding to the perfect correlation of an image superposed upon itself and two smaller symmetric peaks. The position of these two peaks with respect to the self-correlation peak provides the x and y components of the particles displacement (see Chapter 2).

cross-correlated. Cross-correlation presents many benefits compared with auto-correlation methods, such as the absence of directional ambiguity (since the recorded image order is known), self-correlation peak* and improved signal-to-noise ratio. There is no doubt that cross-correlation methods benefited tremendously from the advances in interline transfer camera technology (also known as cross-correlation cameras) which streamlined even more the image processing step^{38,48}. Although other PIV data processing techniques exist^{48,49}, cross-correlation is a well-established and proven PIV processing method which appears today as a standard tool in many commercially available PIV packages.

PIV can be applied not only to extract the planar velocity field of a flow (2D-PIV), but can also be implemented to perform volume velocity measurements (3D-PIV)⁵⁰. The simultaneous measurement of three velocity components (3C) can be approached by various methodologies such as stereographic⁵¹, holographic⁵² and multiple-plane methods⁵³. Most 3D-PIV methods involve a certain level of experimental and processing complexity, however stereographic PIV (stereo-PIV) is the most widely implemented method⁵⁴ due to its relative ease of setup, given that it only requires two cameras. In this setup, the cameras are arranged in a configuration that fulfils the Scheimpflug condition⁵⁵ where each camera is observing the same flow field at a different angle. In this manner, the imaging setup acquires a stereo-like vision, which allows, after camera calibration, the determination of the out-of-plane velocity components from the measurement of the in-plane (2-D) components at each camera. However, although stereo-PIV is a common methodology for 3D velocity measurement, the accuracy of the velocity in-plane components is much better than that out-of-plane and current research is still driven toward improving the latter⁵⁶.

4.2. Multiphase PIV

A multiphase flow can be described in terms of two topologies, dispersed and separated⁵⁷. Dispersed multiphase flows are defined by the presence of a continuous gaseous (or liquid) phase flow in which the dispersed liquid/solid (or solid/bubble)

phase is laden. On the other hand, separated multiphase flows are defined by two or more continuous streams of flow separated by interfaces. In multiphase flows, the respective phases are mixed macroscopically (i.e. well above the molecular level) with each one having its own velocity field⁵⁷.

Multiphase flows occur in many industrial, environmental and biological processes, such as automotive combustion, sprays, powder mixing, cavitating flows, meteorological systems and blood flow. For some multiphase flow systems, it is important to understand their behaviour in order to predict the consequences, while for others the characterisation and the understanding of the phases interaction(s) are critical to improve the efficiency of the system. PIV is powerful in this respect owing to its potential to provide simultaneous velocity field measurements in both phases.

In PIV, a laser beam is focused into a light sheet, which illuminates tracer particles in the flow. Light from the tracers is then elastically scattered and imaged onto a CCD camera. After correlation analysis, a 2D/3D vector map of the fluid flow is produced. This approach is well established for single phase flows but its implementation in multiphase flows generates images from the tracers in both phases (or constituents) resulting in velocity vectors across the overall image field. This does not allow quantification of the flow fields in each phase of the flow and hence further parameters such as relative velocity and mixing cannot be quantified. Therefore, for multiphase PIV, sufficient phases discrimination is a requirement.

Typically, in a dispersed multi-phase flow, the continuous phase (e.g. gas) can be seeded with tracer particles whose sizes are much smaller than the laden dispersed phase (e.g. liquid droplets). Phase discrimination can then be achieved by separation methods such as spot intensity⁵⁸, spot size thresholding^{59,60} and masking⁶¹, spatial frequency filtering⁶², spot shape discrimination by median filter⁶³ and phase correlation peak properties⁶⁴. However, separation methods suffer limitation from the noise that each phase introduces to the other⁶⁵ or because they are difficult to apply in applications when there is a size overlap between tracers and dispersed phase particles (droplets), such as in fuel sprays for automotive combustion. Furthermore, size-based separation algorithms cannot be applied in separated multiphase flows

since both phases will need similarly sized seed particles to achieve adequate flow following.

Another approach can be envisaged for phase discrimination and which consists of colour tagging of either one or both phases with the aid of optically active tracers that produce fluorescent or phosphorescent emissions over a range of wavelengths different from that of the illuminating laser beam. In the case of laser-induced fluorescence-PIV (LIF-PIV), or more simply fluorescence-PIV (FPIV), the optical signal from the tracers is the fluorescence induced by excitation from the illuminating laser.

Optically active tracers were first used in full field instrumentation in 1985 where Gharib *et al.*⁶⁶ used phosphorescent coated particles to show the direction of motion of tracers within a flow. These tracers emitted phosphorescence for a short time after exposure, with the phosphorescence intensity gradually decaying, allowing the direction of the velocity vector to be inferred from a single exposure photograph.

Two groups have addressed the application of PIV to gasoline direct injection (GDI) sprays using 532 nm laser light sheets with conventional tracers in one phase and fluorescent tracers in the other^{19,67}. Boedec *et al.* employed incense solid particles (0.3 to 3 μm) to seed the gas phase while the high pressure spray delivered rhodamine 6G doped water droplets. Conversely, Rottenkolber *et al.* seeded the air phase with aerosol droplets (diameter < 3 μm) of a solution of DCM dye in propylene carbonate, while the other phase was made of sprayed droplets of a hollow-cone injector. In these works, the emission spectrum of the fluorescent dye was selected to be separate from the excitation and hence combinations of filters were used on the CCD cameras. Whilst multi-phase velocity vectors were produced, the data suffered from either poor validation rates⁶⁷ or required the phases to have differing velocities¹⁹ implying that the optical discrimination of the fluorescent tracers from the conventional tracers was not completely successful.

In a previous study of multi-constituent flows, Towers *et al.*⁶⁸ used optically active tracers, in the form of rhodamine-doped droplets, in one phase and conventional tracers in the other. The mixing flows were illuminated with a first pulse at 532 nm

and a second from a pulsed dye laser at ~ 640 nm. Images were obtained on 2 monochrome cameras with filters, such that one camera only imaged Mie scattering from the 2nd pulse and fluorescence emission from the first pulse, with the other recording Mie scattering from the first pulse. However, as high 532 nm energy pulse was required (>100 mJ) in order to obtain sufficient fluorescence signal, from fluorescent droplets of a size < 5 μm , this generated intense Mie scattering signal that saturated the camera CCD chip. This setup required the use of dense filters that generated image distortions. Therefore, to avoid signal intensity mismatch between the fluorescence and Mie scattering and the need to use optically dense filters to accommodate the camera dynamic range, a different approach was envisaged by Kosiwczuk *et al.*⁶⁹ where only LIF is used to discriminate between the phases of a turbulent two-phase flow. The dispersed phase was doped with a fluorophore emitting at different wavelength from that of the tracer particles of the continuous phase, when both phases were illuminated by a laser light sheet at 355 nm. A pair of synchronised cameras were then used to record simultaneously the fluorescence signal of each phase. A potential source of errors resides in this approach in correctly aligning the cameras so that each camera records the same image.

In order to free the experimental setup from camera alignment and synchronisation difficulties a strategy employing a single colour CCD camera can be envisaged. For each phase of the flow, a fluorescent dye can be chosen to emit light at a particular wavelength in order to discriminate between the phases. The adopted philosophy is to exploit the inherent co-registration offered by a 3-chip colour CCD camera with the images recorded in the 3 colour channel enabling flow phase to be determined as well as pulse order.

This strategy relies on seeding each of the two flow phases with two different optimised micron-sized fluorescent tracers (see Chapter 4). One with red emitting dye tracers and one with blue emitting dye tracers, for which simultaneous excitation using 355 nm excitation from one laser cavity, will produce separate images in the blue and red channels of a colour camera, thereby achieving flow constituent discrimination. A second pulse at 532 nm from the second laser, will generate Mie

scatter from both types of tracer in the green channel and a red signal from the phase tagged with the red emitting tracers. Cross-correlation between the red and green layer should therefore produce vectors for one flow phase, and between the blue and green layer the vectors for the other phase. This approach is further discussed in the Chapter 5 of this thesis.

Prior to using fluorescent droplets in PIV experiments it was attempted to quantitatively correlate the fluorescence intensity from airborne micron-sized fluorescent droplets (0.5 to 5 μm) with their diameter. However, because of technical difficulties this provided limited success. This work is summarised in Appendix I.

4.3. Use of Emulsions for Fluorescent Tracer Optimisation

In LIF-PIV multiphase experiments, tracer particles consist of dye-doped liquid droplets generated by an atomiser. It is generally accepted⁷⁰ that for proper flow following, tracer particle size needs to be below 5 μm in order to minimise tracer slip and settling. This size requirement renders the detection of the fluorescent tracers difficult by the imaging system and therefore the recourse to the use of high dye concentrations. However, the use of high concentrations can result in concentration-related quenching effects⁷¹, thus leading to a decrease in the fluorescence signal as the concentration is increased beyond some optimum value.

In the literature, no explicit work has been reported on the investigation of concentration quenching effects in highly concentrated fluorescent tracers for phase tagging. It is not possible to investigate concentration quenching effects at high dye concentration by conventional spectrofluorometry of bulk dye solution because of the inner filter effect⁷² and self-absorption⁷² (see Chapter 2). Therefore a novel approach has been developed, as described in Chapter 4 of this thesis. This approach consists of mimicking tracer droplets by forming an emulsion system in which the micron-sized doped droplets are dispersed within a non-fluorescent and non-miscible continuous phase. In this manner, quantitative spectroscopic measurements can be made on the emulsion droplets in a stable and controlled laboratory environment. This methodology has enabled the development of optimized fluorescent tracers.

4.4. Flare Removal in Gas Phase PIV

One of the major problems in practical PIV experimental systems has been unwanted ‘flare’ in the recorded images. Flare is caused when the light used to illuminate the tracers also impinges on surfaces within the experimental setup. The light that is scattered from a solid surface is much more intense than that scattered from the tracer particles, giving saturation in the recorded images near these regions and therefore particle images and flow vectors are lost³⁸. This is particularly problematic in a number of industrially important applications, for example, in turbomachinery⁷³⁻⁷⁵, studies of flow and spray dynamics in automotive engine cylinders⁷⁶ and in chemical engineering reactors^{77,78}.

Various approaches have been explored to reduce the effects of flare. Surface preparations with matt black finish have been carried out and have shown to be beneficial for a short period⁷⁹ or more recently, surface coating with a paint containing optical absorbers have been reported for flare removal⁸⁰. However, with pulsed laser illumination the surface layer can rapidly become ablated, which requires the use of paint formulations capable of withstanding high energy pulses and be chemically inert with respect to the seeding substance.

An alternative approach will be discussed in Chapter 6 of this thesis. It involves the use of optimised fluorescent tracers which emit light at wavelengths longer than that of the illumination laser. If sufficient chromatic separation exists between the excitation and emission wavelengths, filters can be used to prevent the intense light scattered (flare) from any solid surfaces from being imaged.

5. MICRO-PIV USING NOVEL FLUORESCENT DROPLET EMULSIONS

Microfluidic devices have seen rapid development in a wide range of applications such as drugs and materials screening and delivery, lab-on-a-chip integrated diagnostic medical tools and inkjet printing heads. Their adoption and scaling up to industrial products, however, demands robust diagnostic tools to measure the flow performance and the reliability of microfluidic devices.

Micro-Particle Imaging Velocimetry (Micro-PIV) constitutes a powerful tool to characterise diverse flow behaviour in microfluidic devices. The principle of this method stems from macro-PIV and has gained widespread acceptance since its application by Santiago *et al.*⁸¹ In that work, tracer images were obtained from the light scattering of monodisperse micro-sized solid polystyrene particles. The low scattered light level from the particles meant that the exposure times were long which limited the system to low velocity flow.

In order to increase the contrast and facilitate image treatment, polystyrene or latex particles coated with a fluorescent dye are generally used⁸². An alternative solution to enhance the contrast is to use polymeric particles having the fluorophore dissolved in the bulk⁸³. From a practical point of view, the large volume fraction of particles in the carrying fluid often leads to clogging of channels and particles tend to adsorb onto the surfaces, where they cannot be removed easily. To reduce uncertainties, such as motion parallax, the particles should have a density close to the carrying fluid to avoid buoyancy effects, as these appear to be important at low flow rates.

To overcome these problems, a novel approach will be discussed in the Chapter 7 of this thesis in which an emulsion of fluorescent droplets has been developed as a micro-PIV tracers medium and applied to the characterisation of rectangular microchannels.

6. REFERENCES

- 1 P. Kageson, T&E - European Federation for Transport and Environment Publications, Brussel, Belgium. <http://www.transportenvironment.org> (2005).
- 2 EU Commission, The Auto-Oil II Programme: a report from the services of the European Commission. Report by the Directorates General for: Economic and Financial Affairs, Enterprise, Transport and Energy, Environment, Research and Taxation and Customs Union. Final version (2000).
- 3 Communication from the Commission to the Council and the European Parliament: Implementing the Community Strategy to Reduce CO₂ Emissions from Cars: (Sixth annual Communication on the effectiveness of the strategy) SEC(2006) 1078, (2006).
- 4 F. Zhao, D. L. Harrington, and M. Lai, *Automotive Gasoline Direct-Injection Engines*. (Society of Automotive Engineers, 2002).
- 5 H. N. Gupta, *Fundamentals of Internal Combustion Engines*. (Prentice-Hall of India, 2006).
- 6 Y. Iwamoto, K. Noma, O. Nakayama, T. Yamauchi, and H. Ando, *Progress in Technology* **80**, 19 (2000).
- 7 F. Q. Zhao, M. C. Lai, and D. L. Harrington, *Progress in Technology* **80**, 105 (2000).
- 8 M. R. Frank and J. B. Heywood, SAE Technical Paper 892058 (1989).
- 9 M. Castagne, J. P. Dumas, S. Henriot, and P. Pierre, *Oil & Gas Science and Technology-Revue de l'institut Francais du Petrole* **58** (1), 79 (2003).
- 10 O. Aoki, H. Yamashita, H. Fujimoto, N. Ohta, T. Nakagawa, and H. Yamamoto, *JSAE Review* **24** (1), 25 (2003).
- 11 K. H. Lee, C. H. Lee, and C. S. Lee, *Atomization Sprays* **14** (6), 545 (2004).
- 12 S. Park, H. Cho, I. Yoon, and K. Min, *Meas. Sci. Technol.* **13** (6), 859 (2002).
- 13 M. Yamakawa, S. Isshiki, T. Yoshizaki, and K. Nishida, *Jsmc International Journal Series B-Fluids and Thermal Engineering* **46** (1), 25 (2003).
- 14 J. J. Kang and D. J. Kim, *Ksme International Journal* **17** (12), 2027 (2003).

- 15 W. Q. Long, H. Ohtsuka, and T. Obokata, *Jsmc International Journal Series B-Fluids and Thermal Engineering* **39** (3), 554 (1996).
- 16 G. Wigley, J. Heath, G. Pitcher, and A. Whybrew, *Particle & Particle Systems Characterization* **18** (4), 169 (2001).
- 17 G. de Sercey, M. Heikal, M. Gold, S. Begg, R. Wood, G. Awcock, and O. Laguitton, *Proceedings of the Institution of Mechanical Engineers Part C- Journal of Mechanical Engineering Science* **216** (10), 1017 (2002).
- 18 J. Lee and P. V. Farrel, SAE paper 930480 (1993).
- 19 G. Rottenkolber, J. Gindele, J. Raposo, K. Dullenkopf, W. Hentschel, S. Wittig, U. Spicher, and W. Merzkirch, *Exp. Fluids* **32** (6), 710 (2002).
- 20 E. Rouland, A. Floch, A. Ahmed, D. Dionnet, and M. Trinite, in *Proceedings of the Eighth International Symposium on Flow Visualization*, pp. 195.1.
- 21 G. Valentino, D. Kaufman, and P. Farrel, SAE paper 932700 (1993).
- 22 H. H. Bruun, *Hot-wire anemometry : principles and signal analysis*. (Oxford University Press, Oxford, 1995).
- 23 A. E. Perry, *Hot-wire anemometry*. (Clarendon, Oxford, 1982).
- 24 A. V. Smol'iakov, V. M. I. Tkachenko, and P. Bradshaw, *The measurement of turbulent fluctuations : an introduction of hot-wire anemometry and related transducers*. (Springer-Verlag, Berlin ; New York, 1983).
- 25 F. Durst, A. Melling, and J. H. Whitelaw, *Principles and practice of laser-doppler anemometry*, 2nd ed. (Academic Press, London, 1981).
- 26 F. Durst, J. H. Whitelaw, and A. Melling, *Combust. Flame* **18** (2), 197 (1972).
- 27 Y. Yeh and H. Z. Cummins, *Appl. Phys. Lett.* **4** (10), 176 (1964).
- 28 D. B. Barker and M. E. Fourney, *Spie Milestone Series Ms* **99**, 105 (1994).
- 29 T. D. Dudderar and P. G. Simpkins, *Nature* **270** (5632), 45 (1977).
- 30 R. Meynart, *Appl. Opt.* **22** (4), 535 (1983).
- 31 R. A. Gore and C. T. Crowe, *Int. J. Multiphase Flow* **15** (2), 279 (1989).
- 32 P. Jacquot and P. K. Rastogi, *Optics and Lasers in Engineering* **2** (1), 33 (1981).

- 33 R. J. Adrian, *Appl. Opt.* **23** (11), 1690 (1984).
- 34 C. J. D. Pickering and N. A. Halliwell, *Appl. Opt.* **23** (17), 2961 (1984).
- 35 I. Grant, *SPIE Milestone Series MS 99* (1994).
- 36 C. Brucker, (Lisbon, 1996).
- 37 J. Kompenhans and J. Reichmuth, in *Proceedings of the IEEE Montech86 conference* (Montreal), 1986).
- 38 A. K. Prasad, *Curr. Sci.* **79** (1), 51 (2000).
- 39 C. E. Willert and M. Gharib, *Exp. Fluids* **10** (4), 181 (1991).
- 40 J. Westerweel, *Proceedings- Spie the International Society for Optical Engineering*, 624 (1993).
- 41 J. Westerweel, *Meas. Sci. Technol.* **8** (12), 1379 (1997).
- 42 M. M. Sutton, W. J. Wolters, W. H. Peters, W. H. Ranson, and S. R. Macneill, *Opt Eng* **1**, 113 (1983).
- 43 R. J. Adrian, *Annual Review of Fluid Mechanics* **23**, 261 (1991).
- 44 R. J. Adrian, *Appl. Opt.* **25** (21), 3855 (1986).
- 45 D. W. Swift, *Optics and Laser Technol.* **4**, 175 (1972).
- 46 I. Grant and A. Liu, *Exp. Fluids* **10** (2-3), 71 (1990).
- 47 R. D. Keane and R. J. Adrian, *Appl. Sci. Res.* **49** (3), 191 (1992).
- 48 R. J. Adrian, *Exp. Fluids* **39** (2), 159 (2005).
- 49 I. Grant, *Proceedings of the Institution of Mechanical Engineers Part C- Journal of Mechanical Engineering Science* **211** (1), 55 (1997).
- 50 K. D. Hinsch, *Meas. Sci. Technol.* **6** (6), 742 (1995).
- 51 T. P. Chang, N. A. Wilcox, and G. B. Tatterson, *Spie Milestone Series Ms 99*, 471 (1994).
- 52 K. D. Hinsch, *Meas. Sci. Technol.* **13** (7), R61 (2002).
- 53 T. Utami and T. Ueno, *Spie Milestone Series Ms 99*, 463 (1994).
- 54 N. J. Lawson and J. Wu, *Meas. Sci. Technol.* **8** (12), 1455 (1997).
- 55 A. K. Prasad and K. Jensen, *Appl. Opt.* **34** (30), 7092 (1995).
- 56 R. Fei and W. Merzkirch, *Exp. Fluids* **37**, 559 (2004).

- 57 C. E. Brennen, *Fundamentals of multiphase flow*. (Cambridge University Press, Cambridge [England] ; New York, 2005).
- 58 J. Sakakibara, R. B. Wicker, and J. K. Eaton, *Int. J. Multiphase Flow* **22** (5), 863 (1996).
- 59 R. C. Chen and L. S. Fan, *Chem. Eng. Sci.* **47** (13-14), 3615 (1992).
- 60 Y. A. Hassan, T. K. Blanchat, C. H. Seeley, and R. E. Canaan, *Int. J. Multiphase Flow* **18** (3), 371 (1992).
- 61 L. Gui, Merzkirch, W., in *Proceedings of the 7th International Conference on Laser anemometry advances and applications* (Karlsruhe, Germany, 1997).
- 62 K. Kiger and C. Pan, in *The third international workshop on PIV*, edited by R. J. Adrian (Santa Barbara, California), 1999), pp. 157.
- 63 K. T. Kiger and C. Pan, *J. Fluids Eng. Trans. ASME* **122** (4), 811 (2000).
- 64 E. Delnoij, J. Westerweel, N. G. Deen, J. A. M. Kuipers, and W. P. M. van Swaaij, *Chem. Eng. Sci.* **54** (21), 5159 (1999).
- 65 D. A. Khalitov and E. K. Longmire, *Exp. Fluids* **32** (2), 252 (2002).
- 66 M. Gharib, M. A. Hernan, A. H. Yavrouian, and V. Sarohia, *AIAA 23rd Aerospace Sciences Meeting Paper No. 85-0172*, 6 (1985).
- 67 T. Boedec and S. Simoens, *Exp. Fluids* **31** (5), 506 (2001).
- 68 D. P. Towers, C. E. Towers, C. H. Buckberry, and M. Reeves, *Meas. Sci. Technol.* **10** (9), 824 (1999).
- 69 W. Kosiwczuk, A. Cessou, M. Trinite, and B. Lecordier, *Exp. Fluids* **39** (5), 895 (2005).
- 70 A. Melling, *Meas. Sci. Technol.* **8** (12), 1406 (1997).
- 71 R. J. Lakowicz, *Principles of Fluorescence Spectroscopy*, 2nd ed. ed. (Kluwer Academic/Plenum Publishers, New York, 1999).
- 72 B. Valeur, *Molecular Fluorescence: Principles and Applications*. (Wiley-VCH, Weinheim, New York, 2002).
- 73 B. Liu, X. Yu, H. Liu, H. Jiang, H. Yuan, and Y. Xu, *Exp. Fluids* **40** (4), 621 (2006).
- 74 M. P. Wernet, *Optics and Laser Technology* **32** (7-8), 497 (2000).

- 75 X. J. Yu and B. J. Liu, *Exp. Therm Fluid Sci.* **31** (8), 1049 (2007).
- 76 P. G. Aleiferis, Y. Hardalupas, A. M. Taylor, K. Ishii, and Y. Urata, *Exp. Fluids* **39** (5), 789 (2005).
- 77 A. Kumar, P. R. Gogate, and A. B. Pandit, *Ind. Eng. Chem. Res.* **46**, 4368 (2007).
- 78 E. Rodriguez, A. H. Castillejos, and F. A. Acosta, *Metall. Mater. Trans. B* **38**, 641 (2007).
- 79 A. Arnott, G. Schneider, K. P. Neitzke, J. Agocs, B. Sammler, A. Shroder, and J. Kompenhans, in *ICIASF '03* (2003), pp. 44.
- 80 R. Konrath, C. Klein, A. Schröder, and J. r. Kompenhans, *Exp. Fluids* **44** (3), 357 (2008).
- 81 J. G. Santiago, S. T. Wereley, C. D. Meinhart, D. J. Beebe, and R. J. Adrian, *Exp. Fluids* **25** (4), 316 (1998).
- 82 C. D. Meinhart, S. T. Wereley, and J. G. Santiago, *Exp. Fluids* **27** (5), 414 (1999).
- 83 R. Lima, S. Wada, K. Tsubota, and T. Yamaguchi, *Meas. Sci. Technol.* **17** (4), 797 (2006)

CHAPTER 2: BACKGROUND

1. ABSORPTION AND FLUORESCENCE

When a molecule is excited via light absorption, the consequent relaxation process when it emits light is known as photoluminescence. There are different pathways for a molecule to de-excite and fluorescence is one particular case.

1.1. Light Absorption

1.1.1. Generalities

Prior to the absorption, the large majority of molecules in the electronic ground state lie in the vibrational level $m=0$ known as the zero-point vibrational level.

When a molecule absorbs light, several vibronic transitions can occur between the ground state and the excited state, the lowest energy vibronic transition, the 0-0 transition, corresponds to the transition between the zero-point levels of the ground and excited states.

For most organic molecules, the ground electronic state consists of a closed shell with all bonding orbitals doubly occupied. In such situation, the spin multiplicity equals to 1 ($M=2S + 1$) and the ground state is described as a singlet state (S_0). When an electronic transition occurs, the resultant excited electronic states are called singlet $S_1, S_2, S_3...$ if the promotion of the electron leads to a conservation of the quantum spin number with $S=0$. On the other hand, if the transition results in the electron spins being parallel so that the multiplicity is 3, these excited states are described as triplet states $T_1, T_2, T_3...$

In the triplet state, as the Pauli's exclusion principle forbids two electrons with parallel spin of occupying the same orbital overlap zone, the electrons are further

apart than in the singlet state and are subjected to lesser repulsive interactions. Thus, the triplet state lies lower in energy than the singlet state.

1.1.2. Transition probability and absorption coefficient

The lowest transition in energy involves a transition between the singlet ground state and the first triplet excited state. However, this transition is forbidden and therefore it is rather transitions between S_0 and S_n states which are generally observed.

1.1.2.1. Selection rules for a transition

A transition between two states is likely to occur only if a dipole moment is created as results of the interaction of light with the molecule¹. The resulting transition dipole moment is a purely quantum mechanical quantity that describes the transient electric dipole resulting from the shift of charge during a transition². This fact can be quantified in terms of transition probability which is proportional to the square of the scalar product of the transition dipole moment and the cosine of the angle between the vectors of the dipole moment and the light polarisation direction. Therefore, the probability of transition is maximum (transition allowed) if the two vectors are parallels and nil if they are perpendicular (transition forbidden)³.

Several factors can contribute to the vanishing of the transition dipole moment and their effect can be summarised in a set of rules known as selection rules for a transition. These rules are not strict if appropriate perturbations (spin-orbit coupling, molecular vibrations) are introduced and can be summarised in two main selection rules:

- Spin-forbidden transitions: Transitions between states of different multiplicity such as singlet-triplet are forbidden. However, this rule can be relaxed through spin-orbit coupling which could result in ISC. The probability of observing ISC is increased by the presence of heavy atoms as the extent of spin-orbit coupling increases with the atomic number.
- Symmetry-forbidden transitions: Transitions between states of the same symmetry are forbidden. This rule can be relaxed through molecular vibrations which induce a departure from the molecule's perfect symmetry

(vibronic coupling) such as in the case of benzene which displays long-wavelength absorption bands.

1.1.2.2. Absorption coefficient

The absorption coefficient is a molecular property that is independent of the concentration of the absorbing species and the optical path length. Experimentally, when a monochromatic beam of light (of intensity I and cross-section S) traverses a sample of thickness dl containing dN molecules, the portion of light $-\frac{dI}{I}$ getting absorbed is equivalent to the probability of capturing a photon:

$$-\frac{dI}{I} = \frac{\sigma dN}{S} = N_a \sigma C dl \quad (2.1)$$

$$\text{where } dN = N_a CS dl \quad (2.2)$$

where C , σ and N_a are the sample concentration, the molecular cross-section and the Avogadro's number, respectively.

As the initial beam intensity (I_0) decreases exponentially as it progress through the light path, the sample absorbance, A , follows the Beer-Lambert law:

$$A = \log \frac{I_0}{I} \quad (2.3)$$

Following the integration of Eq. 2.1, the absorbance is re-expressed as:

$$A = \log \frac{I_0}{I} = \frac{N_a \sigma C l}{2.303} \quad (2.4)$$

where the quantity $\frac{N_a \sigma}{2.303}$ can be defined as the molar absorbance coefficient ϵ

which lead to the well-known Beer-Lambert law for the absorbance:

$$A = \epsilon C l \quad (2.5)$$

1.1.3. Franck-Condon principle

The Franck-Condon principle⁴ states: *electronic transitions are so fast in comparison to the nuclear motion that immediately after the transition, the nuclei have nearly the same relative position and momentum as they did before the transition*². Such a transition is represented on potential energy diagram (Figure 2.1. a & c), by a vertical transition.

The relative intensities of the vibronic transitions is determined by the Franck-Condon factor which is the square of the vibronic overlap integral $f_v \equiv |\langle \chi^{gr} | \chi^{ex} \rangle|^2$.

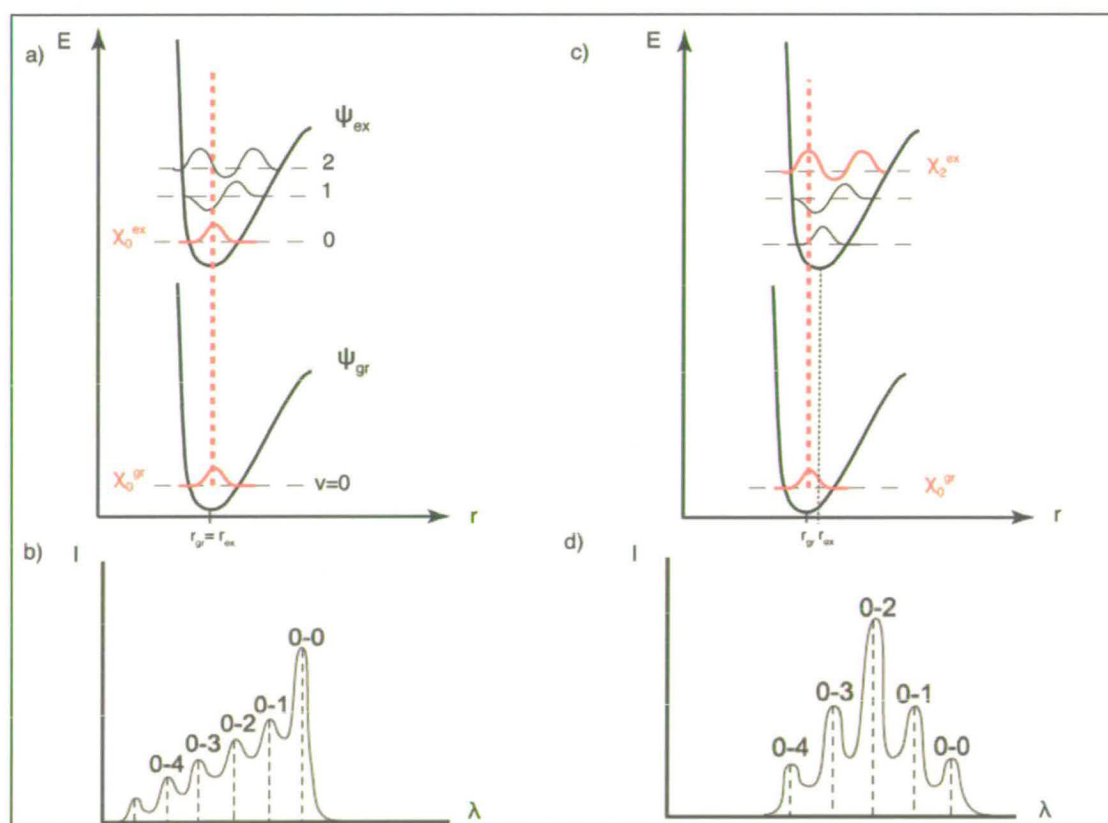


Figure 2.1: a, c) Schematic representation of the potential energy curve as a function of nuclear separation r . The vibronic wave functions (χ) are represented as Morse functions. b,d) Depiction of the absorption spectrum. The vertical lines represent the observed absorption bands as in the gas phase, whereas the solid line represent the shape of the spectrum due to broadening effects.

Considering the situation where the equilibrium nuclear separation is the same in both the ground and the excited states ($r_{gr}=r_{ex}$, Figure 2.1-a), the most intense transition will correspond to the 0-0 transition ($|\langle \chi_0^{gr} | \chi_0^{ex} \rangle|^2 = \max$). On the other hand, if the equilibrium nuclear separation of the excited state differs from that of the ground state to a higher vibronic transition. For example, in Figure 2.1.c where $r_{ex} > r_{gr}$, the 0-2 transition is most intense. Consequently, the shape of the absorption spectrum and the intensities of the vibronic band reflect the relative position of potential energy curves and the corresponding Franck-Condon overlap integrals (Figure 2.1.b & d).

1.2. Fluorescence

1.2.1. Fluorescence characteristics

The energy received from light absorption is dissipated by radiative and non-radiative transitions. For polyatomic molecules, luminescence (fluorescence/phosphorescence) are mainly observed from the S_1/T_1 excited states, because of the high rate of non-radiative deactivation processes (internal conversion and vibrational relaxation) of the upper excited states S_n, T_n ($n>1$). This observation is known as Kasha's rule.

1.2.1.1. Radiative and non-radiative deactivation of excited states

The Jablonski diagram (Figure 2.2) is a convenient way to illustrate the possible unimolecular processes for deactivation of the excited states of a molecule.

Internal conversion (IC) describes the non-radiative transition between two isoenergetic vibrational level of two electronic states possessing the same spin multiplicity (e.g. S_n to S_1 and T_n to T_1) and is followed by vibrational relaxation towards the lowest vibrational level of the final electronic state. The S_1 to S_0 internal conversion can compete with the S_1 to S_0 transition (fluorescence) but it is less efficient than S_2 to S_1 conversion because of the larger energy gap between S_1 and S_0 . IC from S_2 to S_1 typically occurs in 10^{-12} s or less.

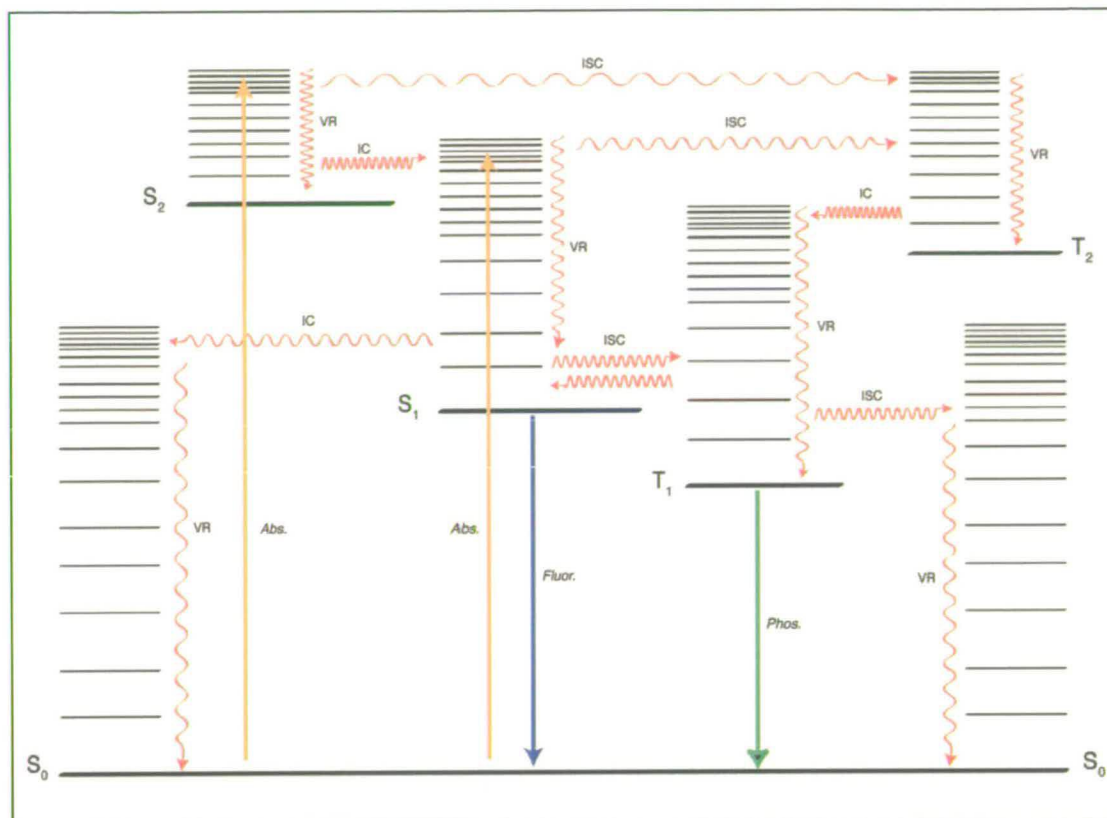


Figure 2.2: Jablonski diagram. The thick horizontal lines depict the electronic states and the thin line the vibrational levels. Radiative transitions are represented by straight arrows. (abs.=absorbance, fluor.=fluorescence, phos.=phosphorescence). Non-radiative processes by wavy arrows (VR=vibrational relaxation, IC=internal conversion, ISC= intersystem crossing).

Fluorescence is a radiative relaxation process, which involves the emission of a photon as a consequence of the S_1 to S_0 transition and its lifetime is in the order of 10^{-10} - 10^{-7} s. Vibrational relaxation to the thermally equilibrated S_1 state is fast (typically 10^{-12} s); hence, the fluorescence emission is from the lowest vibrational levels of S_1 to higher vibrational levels of S_0 . The latter in turn relax vibrationally to the ground state thermal population of vibrational levels. Consequently, three general effects are observed:

- The emission spectrum is a mirror image of the absorption spectrum if the vibrational level is similar in the S_1 and S_2 states.

- The emission spectrum lies at longer wavelengths than the absorption spectrum because of the energy loss from vibrational relaxation in the upper excited state (Stokes shift).
- Fluorescence emission spectra and quantum yield are independent of the excitation wavelength, since excitation to higher vibronic levels is followed by rapid relaxation to the lowest vibrational level of S_1 (Vavilov's rule).

Intersystem Crossing (ISC) is a non-radiative spin-forbidden transition between vibrational levels belonging to electronic states of different multiplicity (e.g. S_n to T_n) and as a result of spin-orbit coupling. ISC has a lifetime of typically 10^{-10} – 10^{-8} s. Typically, ISC from S_1 can involve transitions to higher vibrational level of T_1 or to an upper state T_n state followed by rapid $T_n \rightarrow T_1$ internal conversion. Vibrational relaxation will bring the system to T_1 thermal equilibrium level where the molecule will undergo either phosphorescence or vibrational relaxation to S_0 . The T_1 to S_0 radiative transition is spin-forbidden and thus its radiative rate is low. For instance, in solution and at room temperature, molecular collisions will result in non-radiative transition to S_0 (right hand process in Figure 2.2), whereas at low temperature or in solids, the triplet state lifetime is long enough to allow phosphorescence (typically 10^{-6} – 1 s). Because of T_1 lies below of S_1 , the phosphorescence spectrum is situated at longer wavelength than fluorescence.

The ISC rate constant depends on both the singlet–triplet energy gap and the spin-orbit coupling between these states.

1.2.1.2. Rate constant, lifetime and quantum yield

The rate of the radiative and non-radiative processes can be expressed in terms of their rate constant as defined in Figure 2.3.

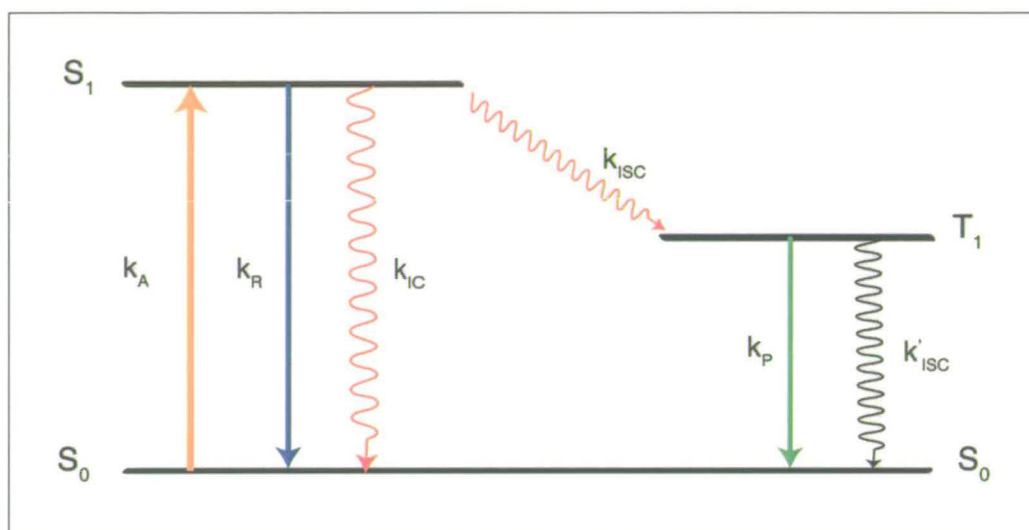


Figure 2.3: Representation of processes and respective rate constants leading to activation and deactivation of the S_1 and T_1 states. Radiative transitions are represented with straight arrows (orange: absorption, blue fluorescence, green phosphorescence). Wavy arrows represent non-radiative processes.

The quantum yield of fluorescence is the rate of emission to the rate of absorption of radiation. Therefore, the fluorescence quantum yield corresponds to the fraction of molecules decaying radioactively, which can be expressed as follows³:

$$\Phi_F = \frac{k_R[S_1]}{k_A} = \frac{k_R}{k_R + k_{IC} + k_{ISC}} \quad (2.6)$$

In the absence of intermolecular quenching and photochemical reactions, the sum of quantum yields for the deactivation processes originating from the S_1 state will be equal unity, $\Phi_F + \Phi_{ISC} + \Phi_{IC} = 1$.

The lifetime of the excited state S_1 which corresponds to the measured fluorescence lifetime, τ_F , is given by:

$$\tau_F = \frac{1}{k_R + k_{IC} + k_{ISC}} \quad (2.7)$$

The radiative lifetime, τ_R , of the S_1 state is the fluorescence emission lifetime in the absence of non-radiative process so that $\tau_R = \frac{1}{k_R}$. Therefore, the fluorescence

quantum yield can be expressed as the ratio of the measured to the radiative lifetimes:

$$\Phi_F = \frac{\tau_F}{\tau_R} \quad (2.8)$$

1.2.2. Fluorescence quenching

In addition to the unimolecular processes such as internal conversion and intersystem crossing deactivating the excited molecule, a wide range of intermolecular photophysical processes can contribute to a decrease of the fluorescence quantum yield. These processes are generally called *fluorescence quenching processes* and frequently involve fast electron, proton or energy transfer.

It is beyond the scope of this thesis to further describe the characteristics of fluorescence quenching processes. However, fluorescence quenching by excimer formation will be given specific mention here, since it is relevant to the quenching of the fluorescence by fluorophore concentration (see Chapter 4).

In some cases, it is observed that an increase in the concentration of a fluorophore results in a decrease in the fluorescence quantum yield. This effect is termed self-quenching or concentration quenching and results from the collisional formation of an excited dimer complex known as an excimer, as follow:



Excimer formation is favoured by an enhanced stabilisation interactions between the ground and excited monomers 1A and ${}^1A^*$ relative to a 1A monomer pair as shown by the potential energy diagram Figure 2.4. Therefore, the excimer fluorescence spectrum generally consists of a broad and structureless peak lying at longer wavelengths than the monomer emission².

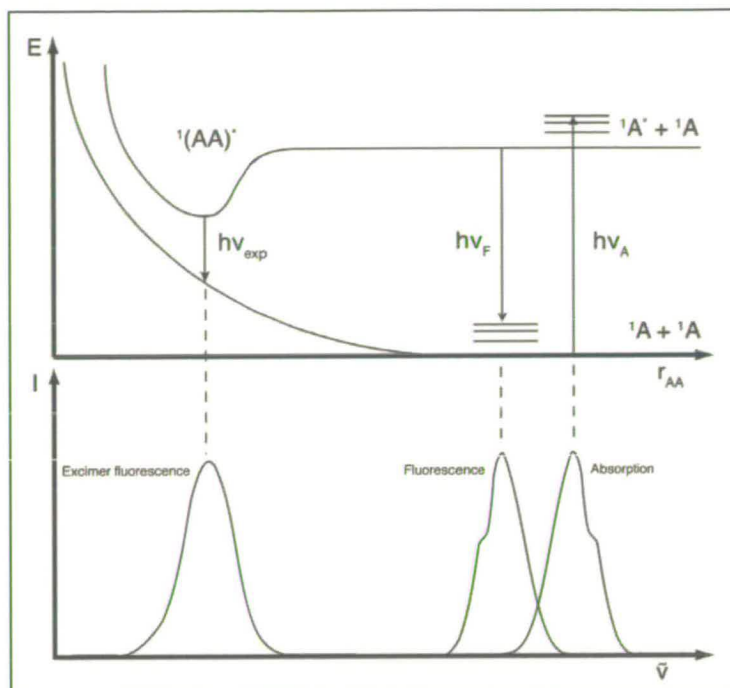


Figure 2.4: Schematic representation of excimer and monomer: Top: potential surfaces. Bottom: absorption and fluorescence emission (Adapted from reference 2).

1.2.3. Solvent effect

As mentioned in section 1.2.1.1, vibrational relaxation results in a Stokes shift between the absorption and emission spectra. However, interactions with the solvent can result in a much increased Stokes shift. This effect is particularly marked if the fluorophore has a larger dipole moment (μ_F) in the excited state (S_1) than in the ground state (μ_G, S_0)⁵. This is illustrated in Figure 2.5.

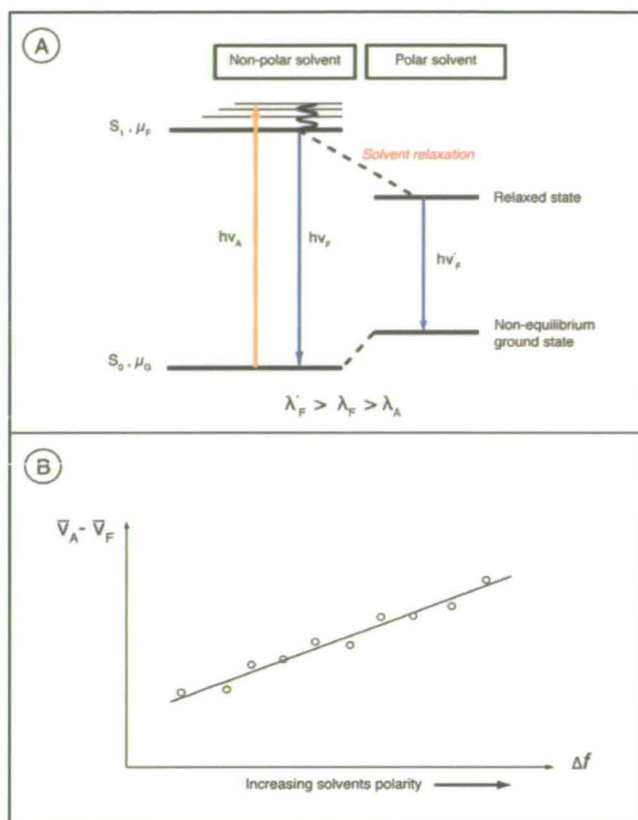


Figure 2.5. A) Sketch of solvent effect on the energy of the excited state and on increasing Stokes shift. B) Representation of a typical Lippert plot for a fluorophore in solvents with increasing polarity (From reference 5).

The timescale of solvent relaxation time is shorter (typically 10^{-12} s) relative to fluorescence lifetime ($\sim 10^{-8}$ s), hence when a molecule is excited to the S_1 level, the solvent dipole moments have time to redistribute and reorient around μ_F . The net result is the stabilisation of the S_1 state by lowering its energy prior to the emission (Figure 2.5 (A)). Therefore, the extended Stokes shift is characteristic of the fluorophore's solvent environment.

The Lippert equation (Eq. 2.10) provides a general quantitative and qualitative description of solvent effect on the fluorophore's spectral properties ⁵.

$$\bar{\nu}_A - \bar{\nu}_F = \frac{2(\mu_F - \mu_G)}{a^3} \Delta f + \text{constant} \quad (2.10)$$

where $\Delta f = \frac{\epsilon - 1}{2\epsilon + 1} - \frac{n^2 - 1}{2n^2 + 1}$ and a the cavity radius in which the fluorophore resides (typically $a \approx 4 \text{ \AA}$ for an aromatic fluorophore).

The fluorophore sensitivity to solvents can then be estimated by plotting the Stokes shift values ($\bar{\nu}_A - \bar{\nu}_F$) against solvent's Δf (Lippert plot, Figure 2.5 (B)).

1.3. Steady-state Spectrofluorometry

1.3.1. The spectrofluorometer

Conventional spectrofluorometers (Figure 2.6) are commonly equipped with a Xenon lamp that offers high intensity, continuous emission from 250 nm to the infrared. An excitation monochromator is used to select the excitation wavelength by a diffraction grating. The fluorescence signal is collected at right angles to the incident beam and detected by an emission photomultiplier via an emission monochromator. The monochromators are motorised to allow automatic wavelength scanning and are controlled via computer.

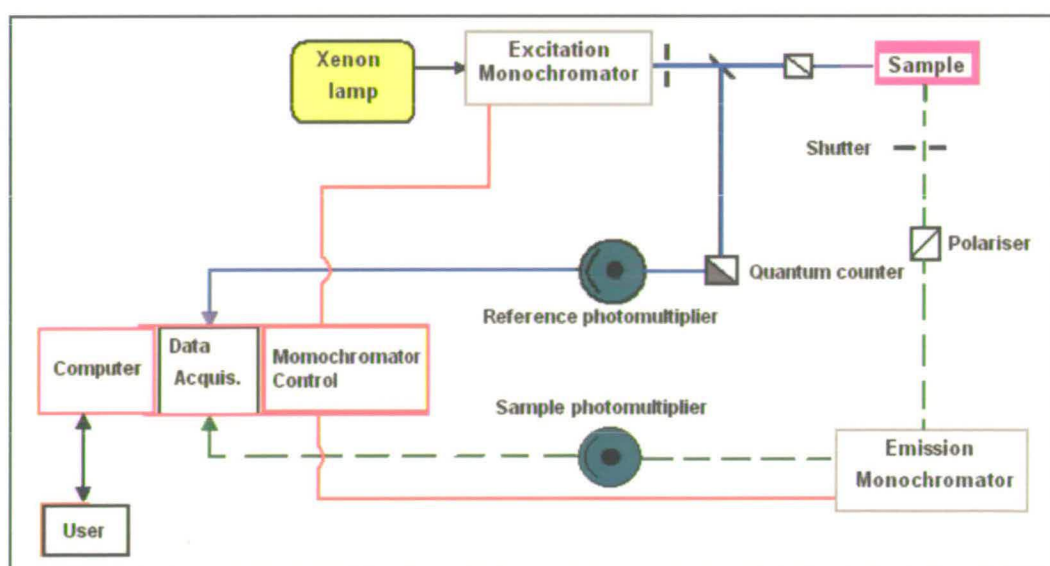


Figure 2.6: General layout of a conventional spectrofluorometer.

To allow compensation for intensity fluctuations and the spectral profile of the lamp, the spectrofluorometer may include a reference channel whereby a photodiode or photomultiplier detector monitors the excitation intensity.

Optical fibres can be interfaced to the spectrofluorometer to allow the study of samples not compatible with the spectrofluorometer sample holder. The use of optical fibres requires the use of an adapter (Figure 2.7) consisting of reflectors and lenses, which focus the light at the exit/entry of the monochromators. Two optical fibres are required for conducting light one for the emission and the other for the excitation.

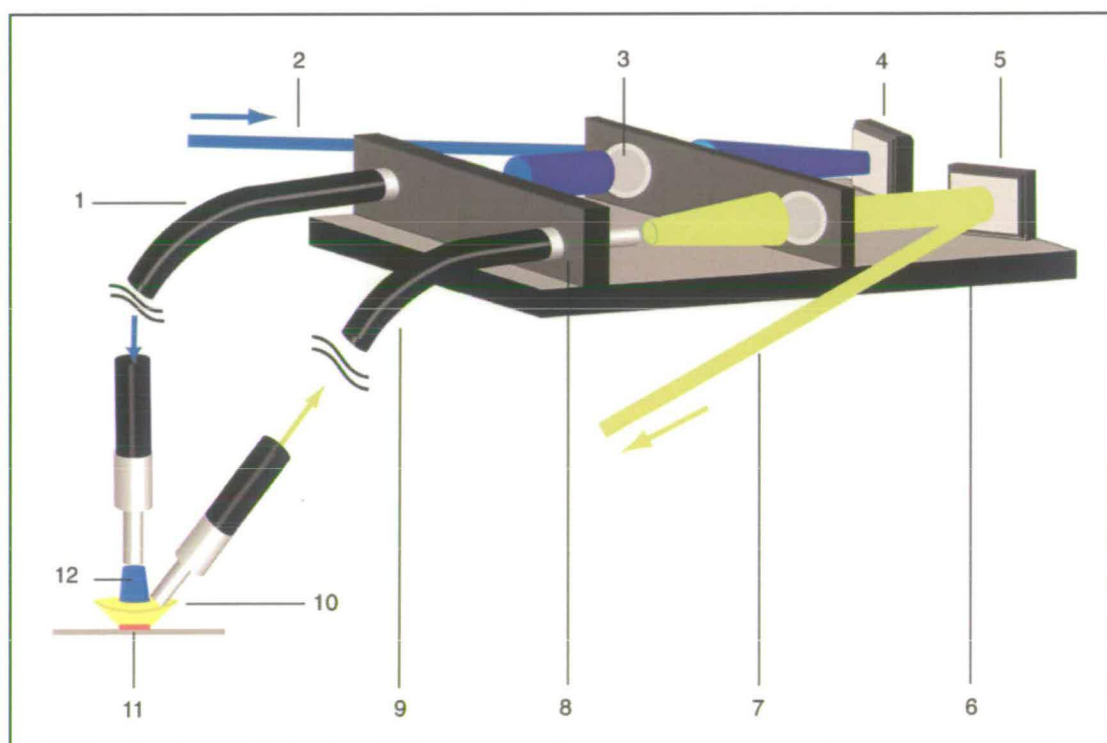


Figure 2.7: Schematic representation of a typical spectrofluorometer optical fibres adapter: 1- Excitation fibre. 2- Incoming excitation monochromator light 3- Collimating lens. 4- Excitation mirror. 5- Emission mirror 6- Optical fibres adapter. 7- Fluorescence directed to the emission monochromator. 8- Optical fibre holder. 9- Emission fibre. 10- Fluorescence from sample. 11- sample. 12- Excitation light.

1.3.2. Steady-state fluorescence

The steady-state fluorescence intensity, I_F , per absorbed photon, is the fluorescence quantum yield of the fluorophore³, since:

$$\Phi = \frac{I_F}{I_A} \quad (2.11)$$

The intensity of the absorbed light is the difference between the intensities of incident light and transmitted light: $I_A = I_0 - I_T$ with I_0 the intensity of the incident photons and I_T expressed using the Beer-Lambert law where ϵ , C , l are the molar absorption coefficient, the sample concentration and the sample path length respectively

$$I_T = I_0 10^{-\epsilon CL} \quad (2.12)$$

Therefore, the fluorescence intensity can be expressed as a function of the sample photophysical properties

$$I_F = \Phi_F I_A = \Phi_F I_0 (1 - 10^{-\epsilon CL}) \quad (2.13)$$

If the sample solution is dilute enough so that its absorbance is small (typically⁶ < 0.05), a Taylor series expansion for the exponential function can be used where $e^{-x} \approx 1 - x$.

Thus equation (2.13) for the fluorescence intensity takes the form:

$$I_F \propto I_0 \Phi_F \epsilon CL \quad (2.14)$$

A plot of the fluorescence intensity against the concentration should therefore be linear for solution with low absorbance.

1.3.3. The inner-filter effect

The fluorescence intensity is proportional to the sample concentration, but this proportionality is only valid for dilute solutions.

A right-angle detection geometry sample holder (Figure 2.8) is commonly found in conventional spectrometers. When the concentration is too high, most of the incident light is absorbed before reaching the central part of the cuvette, which leads to a diminution in the detected fluorescence intensity.

This is known as the inner filter effect and results in a non-linear dependence of detected fluorescence on concentration.

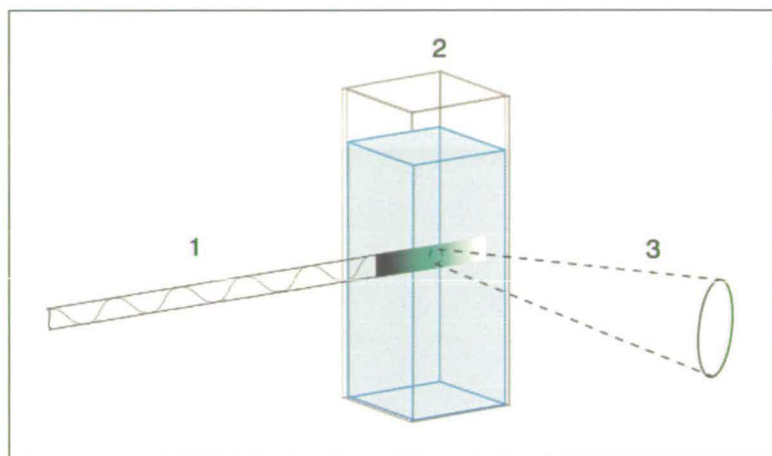


Figure 2.8: Sketch of inner-filter effect in conventional cuvette in a right-angle detection setup. 1: Incoming excitation light, 2: Cuvette containing a concentrated fluorophore solution, 3 Aperture of the emission monochromator detector.

2. PARTICLE IMAGE VELOCIMETRY

Particle image velocimetry (PIV) has seen a tremendous development since the late 1980s when the principles of PIV theory were proposed. The development of lasers and camera technology helped open the way for crucial advances in flow visualisation and flow field velocity measurements, which broadened the range of PIV applications.

2.1. Principle of Particle Image Velocimetry

The principle of PIV consists of recording images from a light sheet illuminating micron-sized particles “tracers”, seeded in the flow. The local flow velocity can be determined by measuring the fluid displacement from sequential particle images and dividing this by the time interval between the exposures. As the time interval and spatial resolution of the imaging system are high, when compared to the time and length scale of the flow, instantaneous and accurate velocity maps can be obtained.

A typical arrangement for a PIV experiment would incorporate a pulsed laser light sheet illuminating a cross section of the seeded flow, a CCD camera recording particle images and software for image analysis, as shown in Figure 2.9. Hence, the success of PIV experiments depends on the careful choice of laser source, tracers, camera and the image processing algorithms.

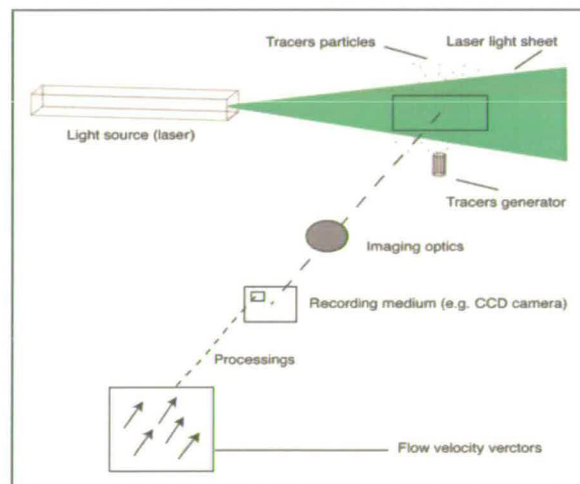


Figure 2.9: Representation of a simple particle image velocimetry experimental setup.

2.2. Laser source and laser light sheet generation

An optimum spatial resolution and field of view is a prerequisite for PIV experiments; hence, as a source of illumination, lasers are ideal. As opposed to white light, lasers output a bright, monochromatic, coherent and directional beam that can be converted into a thin laser light sheet (LLS).

2.3. PIV Laser

Because the acquisition of particle images is done by short exposure of the tracers to the LLS, pulsed lasers are more suitable than continuous wave (CW) lasers. These latter require an additional shutter mechanism to generate the pulsing effect, which limits their applicability to slow flow velocities.

The Nd:YAG (Neodymium:Yttrium Aluminium Garnet) laser is a repetitive pulsed laser commonly used in PIV applications. This solid-state laser consists of a rod of $\sim 1\%$ Nd³⁺ doped YAG crystal ($Y_3Al_5O_{12}$)⁷ enclosed in a cavity where it is flashlamp-pumped. This results in lasing at 1064 nm.

The good optical quality and thermal conductivity of the Nd:YAG crystal⁸, allow the use of techniques such as Q-switching to produce short laser pulses with repetition rates and power up to 100 Hz and 200 mJ respectively⁹.

The infrared line at 1064 nm wavelength can be either frequency doubled or frequency tripled (or even frequency quadrupled) by a non-linear crystal in order to produce radiation at 532 or 355 nm wavelengths, respectively. Non-linear crystals operate on the principle of non-linear interaction between light and matter to generate harmonics as multiples (n) of the input frequency. Harmonic generation^{8,10} is accompanied by power loss which increases rapidly as higher harmonics are produced and since the efficiency is proportional to the nth power of input laser intensity, high input power is generally needed¹¹.

In order to generate powerful pulses and control the time interval between pulses, a Q-switch is inserted in the laser cavity¹².

Q-switching is a technique where the quality factor, Q, (energy stored per pass/energy dissipated per pass) of the laser cavity is altered. To generate intense

pulses, the Q value is first set a low value by, for example, blocking light reflection to one of the laser mirrors so that the laser cannot resonate and lasing cannot begin. When a certain energy level is reached (saturated gain), the Q value is rapidly raised, lasing begins and an intense pulse is then delivered.

Q-switching is operated using several types of devices^{8,11}, the most common of which consists of a polariser and a Pockels cell, which is an electro-optic crystal whose light transmittivity is altered according to the voltage applied⁸.

Typical properties and specifications of modern Nd: YAG PIV laser are summarised in Table 2.1:

Repetition rate	10 Hz
Pulse energy 1064/532/355 nm	650/300/160 mJ
Beam spatial profile: near field (<1m)	70%
Beam spatial profile: far field (∞)	95%
Delay between two laser pulses*	0 to 10 ms
Resolution (pulse duration)	4-6 ns

Table 2.1: Specifications of Nd:YAG laser (Continuum surelite II-10), reproduced from reference 13.

2.3.1. Laser light sheet generation

Tracer particles in the flow are illuminated using a laser light sheet generated by passing the laser output beam through a set of cylindrical and/or spherical lenses. Depending of the application, laser light sheets with different shapes can be produced using a combination of different types of lenses as shown in Figure 2.10.

Generally, one cylindrical lens (c, f) is sufficient for generating the LLS and control of the height is done via the focal length of a second lens (b, e). Also, in order to avoid focal lines¹², a diverging lens (a,d) is used in front the incident laser beam.

The LLS properties such as thickness, beam waist and intensity profile can be predicted using Gaussian optics laws, but the calculations are generally based on assumptions that can lead to imprecision^{12,14}. Therefore, the LLS thickness and beam

profile are generally measured experimentally using a detector such as a monochrome camera fitted with an appropriate density filter.

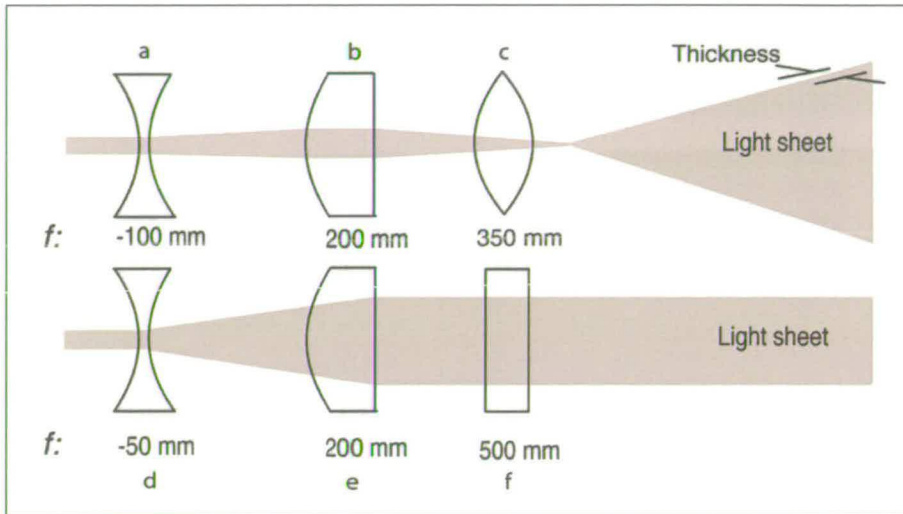


Figure 2.10: Side view of laser light sheet optics with examples of lens focal lengths. Top- Two spherical lenses (a, b) and one cylindrical lens (c). Bottom-Three cylindrical lenses (d,e,f) (Adapted from reference 12).

2.4. Tracer Particles

To be perfect flow tracers, seeding particles should be homogeneously distributed in the flow and be small enough to reflect the motion of the fluid; but since the ability of a particle to scatter light decreases with its diameter, there is compromise between the intensity of the light scattered from the particle and the response to flow fluctuations.

2.4.1. Tracers in a Flow

As PIV relies on measuring the velocity of particles seeded in the flow rather than the flow itself, it is important that the tracer follows the flow characteristics with a minimum of velocity lag, due to drag and gravity effects. The response of the tracers to the fluid accelerations can be assessed through the particle frequency response f_p , which is a convenient way to assess the particle's ability to establish velocity equilibrium with the fluid¹⁶.

$$f_p = \frac{18\mu}{d_p^2 \rho_p} \quad (2.15)$$

where μ , d_p and ρ_p are the dynamic viscosity of the fluid, the particle diameter and density respectively.

A water droplet in air ($\mu_{air} = 1.82 \cdot 10^{-5} \text{ kg.m}^{-1}.\text{s}^{-1}$ at 293 K and $\rho_p = 1000 \text{ kg.m}^{-3}$) with a diameter of 5 μm will give a frequency response of $f_p \approx 15 \text{ kHz}$, which is low considering that typical¹⁵ flow turbulence frequencies are in the range of 1 – 10³ kHz. On the other hand, a 1 μm droplet will present better flow tracking behaviour with $f_p \approx 300 \text{ kHz}$.

2.4.2. Light scattering from particles

The treatment of light scattering from particles with a diameter larger than the wavelength of the incident light, is best described within the framework of Mie theory. The theory provides a rigorous solution of Maxwell's equations for a light field generated by a plane monochromatic wave propagating in a homogeneous medium and impinging on a spherical, isolated, homogeneous particle¹⁴. In the Mie regime, the scattering of light by a particle suspended in a given medium can be characterised in term of its size parameter, $q = \pi n_{med} d_p / \lambda$, where n_{med} and λ correspond to the medium refractive index and the incident wavelength respectively. Detailed derivations of Mie scattering equations can be found in the relevant literature.

Light scattering intensity is proportional to the square of particle diameter¹⁷, $I_M \propto q^2 \propto d_p^2$, and also strongly varies with the observation angle (Figure 2.11). The latter must be taken into account in PIV experiments since measurements are mainly made perpendicular to the light sheet where the scattering intensity is a factor of 100 lower than the forward scattering.

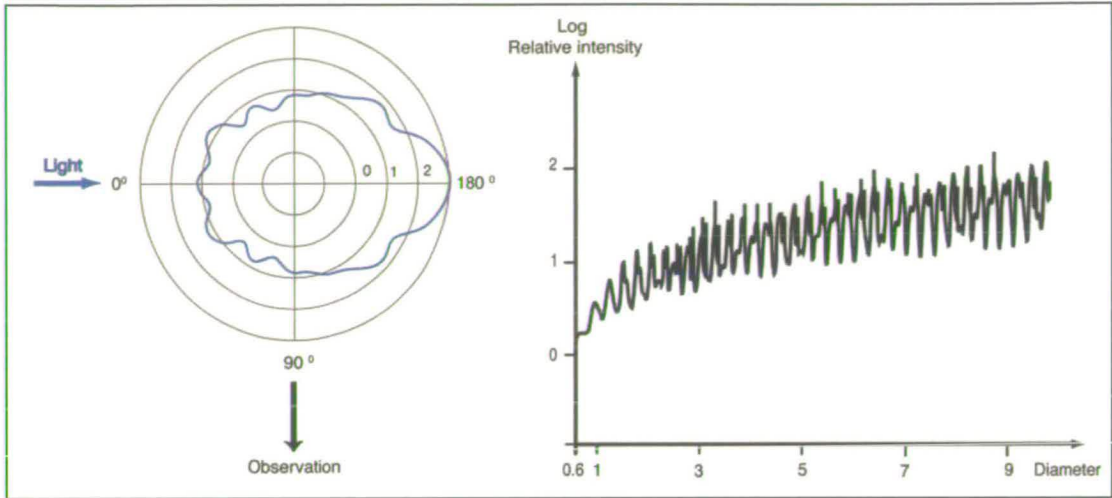


Figure 2.11: Light ($\lambda = 532 \text{ nm}$) scattering by an oil particle ($n = 1.46$) in air. Left– polar plot of the logarithm intensity against the scattering angle for a $1 \mu\text{m}$ oil particle. Right– logarithm relative intensity against particle diameter for a 90° observation angle.

In PIV tracer images, the intensity of each pixel contains the Mie scattering intensity contributions from a number of particles. The scattering intensity signal corresponds to:

$$S_M = C_M \sum_0^m d_k^2 \quad (2.16)$$

$$\text{where } C_M = \frac{K_M I_M V}{\pi r^2} \lambda^2 \quad (2.17)$$

and m is the total number of particles contributing to a given pixel and K_M an experimental constant. d_k , I_M , λ , V and r are the diameter of droplet k , the incident laser intensity and wavelength, the detection volume V and the LLS–CCD camera distance, respectively. Therefore:

$$S_M = \frac{K_M I_M V \lambda^2}{\pi r^2} \sum_0^m d_k^2 \quad (2.18)$$

2.4.3. Fluorescence from tracer droplets

Fluorescence intensity from tracer droplets containing a fluorophore can be calculated using geometric optics and the Beer-Lambert law. When an incident light

ray reaches the curved surface of a droplet it is refracted inside it until reaching a point on the internal surface where it is then reflected towards another point on that surface (Figure 2.12). The process is then repeated and the incident ray intensity is attenuated by the successive reflections/refractions.

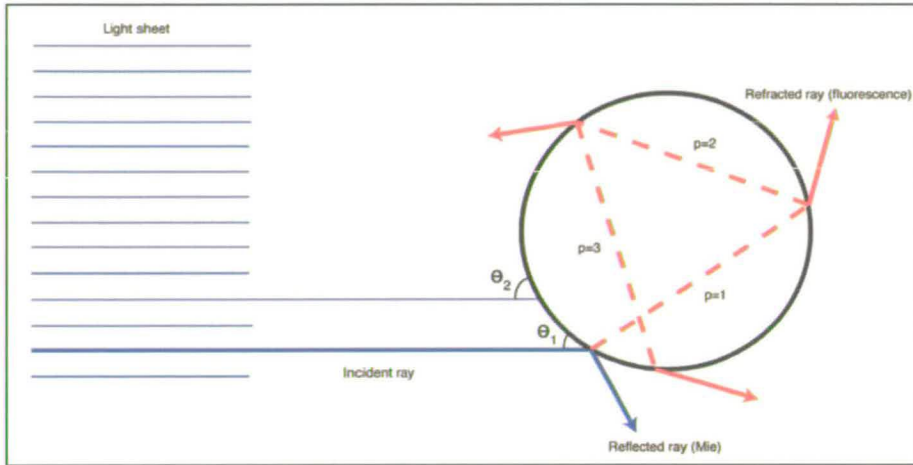


Figure 2.12: Schematic representation of the path of a ray inside a droplet.

Therefore, the fluorescence intensity I_f emitted by a tracer droplet, consists of the sum of the of the fluorescence intensities $i_f(p)$, resulting from the light absorption along the different light paths ($L_p(\theta)$ with $p = 1, 2, 3, \dots$) and over all the incidence angles θ_n ($n = 1, 2, 3, \dots$).

$$i_f(p, \theta) = I_0 \Phi (1 - e^{-\epsilon C L_p(\theta)}) \quad (2.19)$$

A more in depth discussion on the application of geometric optics and calculation of the integrated fluorescence intensity for a droplet larger than the incident light wavelength can be found in reference 42.

For sufficiently low fluorophore concentrations, the fluorescence intensity emitted by a droplet is proportional to its volume and, at the pixel level, the fluorescence signal captured by the CCD camera can be expressed as⁴³:

$$S_F = \frac{K_F I_0 V \Phi}{r^2} N \quad (2.20)$$

where the number density of fluorescence species $N = \frac{4}{3} \pi \frac{\sum_0^m d_k^3}{m} C$ and K'_F is an experimental constant. This leads to:

$$S_F = \frac{K'_F I_0 V \Phi C}{m r^2} \sum_0^m d_k^3 \quad (2.21)$$

2.4.4. Generation of tracers

When gas flows are studied, seed particles are either liquid droplets or solid particles. Although, the choice of the particle type will generally depend on the specific PIV application, droplet generators are often preferred over particle generators because of the ability to produce steadier seeding rate, the availability of a wide range of atomisation fluids with known physical properties¹⁶ and the ability to incorporate a fluorophore for laser induce fluorescence-PIV (LIF-PIV) applications such as multiphase PIV and flare removal. Droplet generators should, however, produce droplets with nearly monodisperse size distributions in order to avoid image bias towards the larger droplets that may not be following the flow¹⁸.

Air nebulisers also known as air-assist atomisers can produce monodisperse droplet distributions in the 1–5 μm range in diameter. Air nebulisers come in different designs but they are generally based on the same principle as illustrated in Figure 2.13. The fluid contained in the nebuliser reservoir is drawn upstream by the depression created by the air jet and form a thin liquid film which is then atomised by the vertical air jet. The function of the impactor is to remove the largest droplets which condense back to the reservoir, whilst the smallest ones are dragged by the airflow.

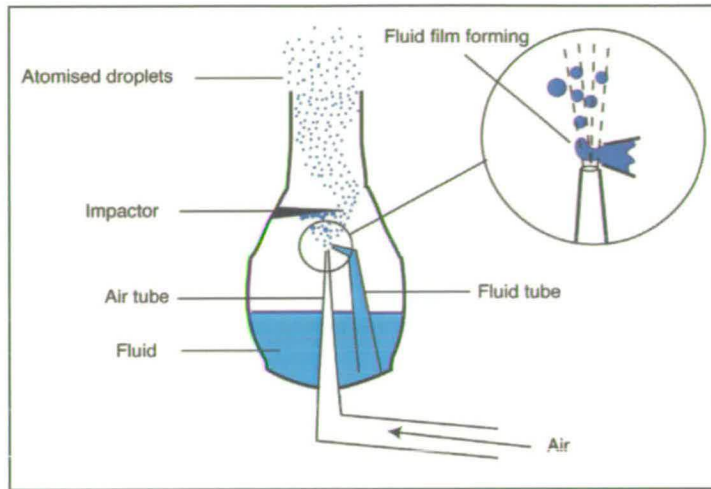


Figure 2.13: Schematic representation of an air nebuliser (Adapted from reference 19).

For air nebulisers presenting a configuration where the liquid film is impinging perpendicular to the air jet, the mean diameter of the atomised droplets depends mainly on the nebuliser geometry^{19,20}.

2.5. Data and Image Processing

In PIV, the particle density in the flow is too high to allow the particles be tracked individually and thus statistical methods are employed to extract velocity measurements. The general approach consists of dividing an image into a grid of small areas called interrogation spots, which can then be analysed by either of two Fast Fourier Transform (FFT) based methods, auto-correlation and cross-correlation analysis²¹⁻²³

In auto-correlation, two exposures from two laser pulses of seed particles are captured on a single frame as shown in Figure 2.14– left scheme. The resulting auto-correlation field consists of a large central peak and two smaller peaks symmetrical to it. The large peak (S) represents the perfect correlation of an image superimposed upon itself. The two other peaks (S^+ , S^-) correspond to the mean displacement within the interrogation area. There are two peaks because of the directional ambiguity in the image: it is not possible to determine which particle images were recorded in the first exposure. The ambiguity can be lifted by using image-shifting techniques²⁴, but

this adds to the experimental difficulties. The auto-correlation method also suffers from poor resolution for small displacements since the two peaks tend to overlap with the large peak. These are the two main reasons why cross-correlation analysis is preferred in PIV.

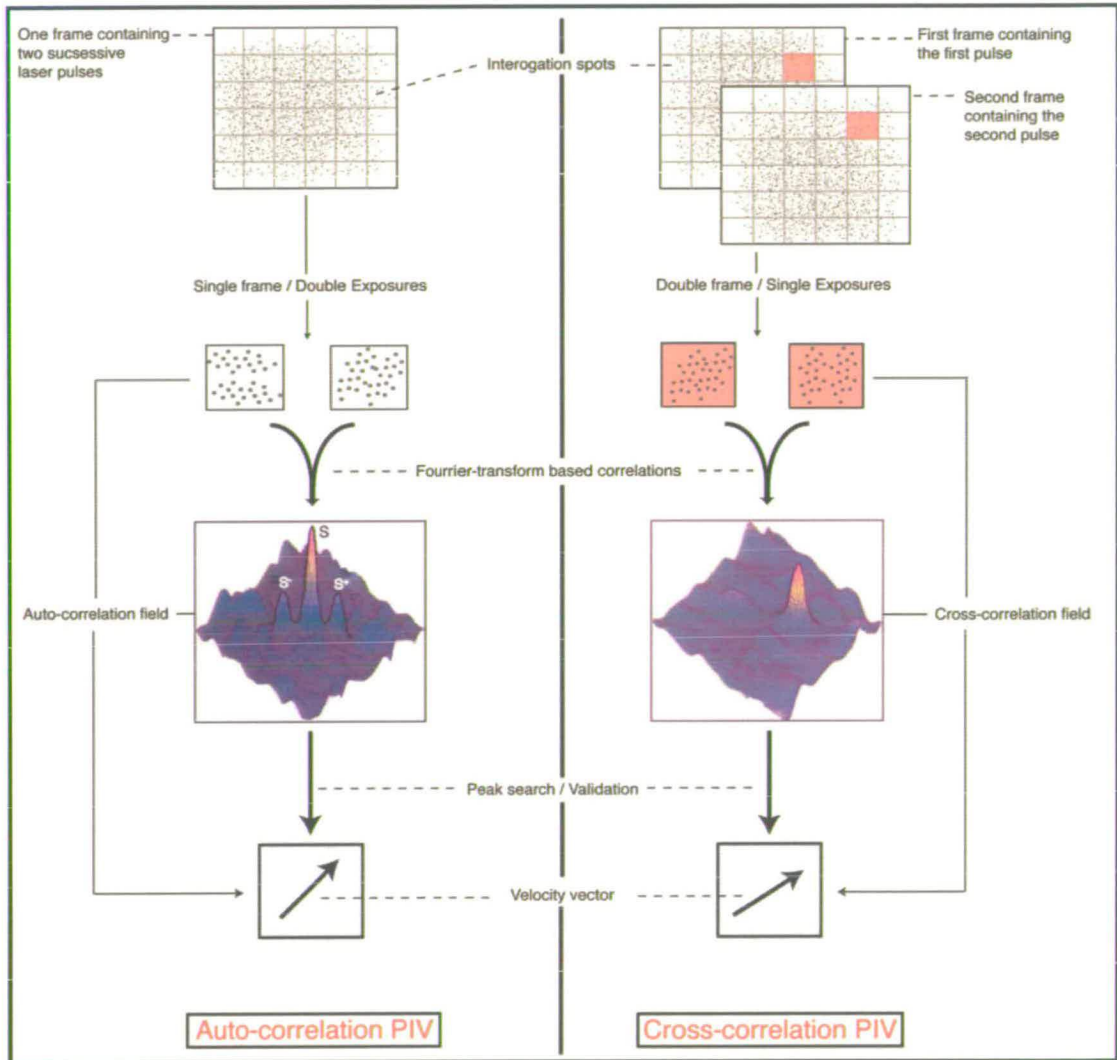


Figure 2.14: Schematic representation of velocity vector generation by single frame/double exposure and double frame/single exposure for auto-correlation and cross-correlation PIV respectively (correlation fields adapted from reference 25).

Cross-correlation analysis is based on the capture of two images on two separate frames, as shown in Figure 2.14 – right scheme. It consists of correlating the same interrogation spots between the two frames. In this way, because pulse order/image is

known, the cross-correlation field yields a single large peak and the directional ambiguity is lifted. The raw data obtained from cross-correlation need to be processed (validated) before the statistical velocity vectors can be extracted and a range of validation techniques are employed such as correlation peak-height and moving-average validation^{23,26,27}.

Several parameters affect the spatial /temporal resolution, dynamic range and the signal to noise ratio of the cross-correlation analysis. Although the list is too extensive to be presented here, three main parameters can be highlighted:

- Seed density.

In order to achieve a high probability of valid measurement, each interrogation spot needs to contain a minimum number of seed particles, defined as the seed density, for which a value of 7–10 produces a near 100% probability of making valid correlations²³.

- Laser pulse separation.

In cross-correlation PIV the laser pulse/image recording sequence is synchronised with respect to the pulse separation (Δt). The dynamic range of the measurement increases with Δt but the probability of finding the same group of particles in the same interrogation spot decreases and therefore so does the signal-to-noise ratio (SNR).

- The interrogation spot size.

The spatial resolution of PIV measurements increases with decreasing interrogation spot size. Accordingly, the seed density will decrease and likewise the probability of valid correlations.

2.6. Image Recorder and Optical System

2.6.1. Cross-correlation PIV camera

For cross-correlation PIV analysis, cross-correlation CCD cameras are the preferred method of sampling data. The cross-correlation cameras use high-performance

progressive-scan interline CCD chips. Such chips include $m \times n$ light sensitive cells and an equal number of storage cells as shown in Figure 2.15.

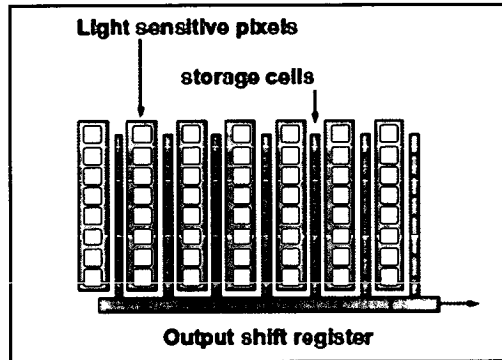


Figure 2.15: Schematic illustration of light-sensitive pixels and storage cell layout of a cross-correlation PIV camera (Adapted from reference 28).

As noted in the previous section, the camera is synchronised with the first laser pulse which exposes the seed particles to the LLS, this produce the first frame. Immediately after, the frame is transferred from the camera's light-sensitive cells to the storage cells (buffer). The same process is applied for the following pulse(s). Once the storage cells contain the frames from the first and the second pulses showing the initial and final position of seed particles, these are transferred sequentially to the camera outputs for acquisition and cross-correlation processing.

2.6.2. Recording optics

The CCD camera, as the recording medium for particle images, is used in conjunction with an optical system for image formation which consists generally of a set of lens. The optical system parameters such as the magnification, M , focal length, f , and aperture, D , affect the dynamic range of a given PIV experiment and particularly the particle image size and the depth of field (DOF) as shown in Figure 2.16.

2.6.2.1. Particle image size

The diameter of tracer particle/droplet is generally in the order of a couple of micrometers, therefore the effective particle image diameter in the image plane is generally governed by the combination of geometric and diffraction effects. Geometric effects imply that the particle image diameter is Md_p , where d_p is the particle diameter in the object plane. But, since the lens is diffraction limited and its point response function is given by an Airy function whose diffraction-limited spot size $d_s = 2.44(1 + M)f^\# \lambda$ with $f^\# = \frac{f}{D}$ the lens f-number. Therefore, the

effective particle image diameter in the image plane is:

$$d_e = \sqrt{M^2 d_p^2 + d_s^2} \quad (2.22)$$

For particle/droplet tracers whose diameters such that $Md_p \ll d_s$, $d_e \approx d_s$, which means that the particle imaging is then governed by diffraction effects and the particle image size is independent of the actual particle diameter.

2.6.2.2. Depth of field

The DOF is the thickness of the region in the object plane where all the particles are in focus. The DOF (Eq. 2.23) needs to be larger than the laser light sheet thickness in order to avoid imaging out-of-focus particles, and can be made thicker by increasing the $f^\#$ at the expense of the image resolution.

$$DOF = 4\left(1 + \frac{1}{M}\right)^2 f^{\#2} \lambda \quad (2.23)$$

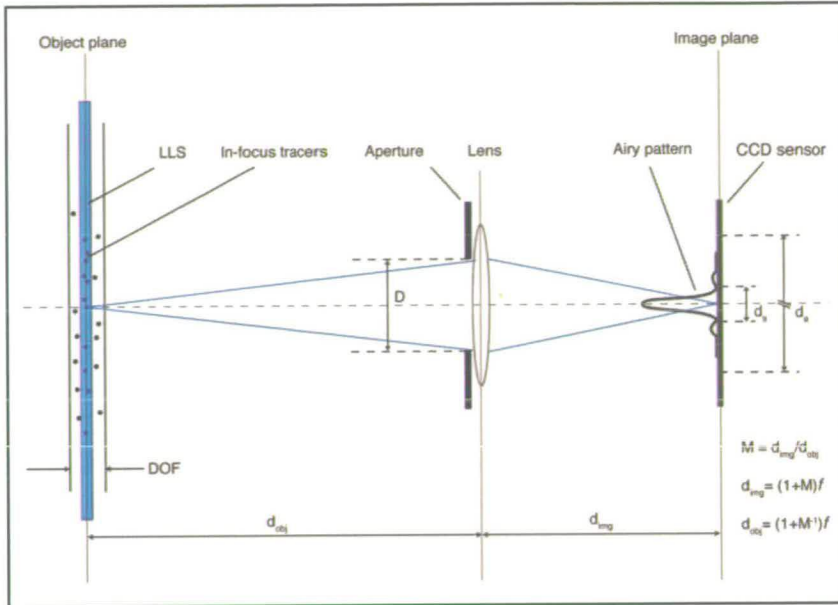


Figure 2.16: Schematic representation of the imaging system and diffraction effect for a particle image recording.

3. EMULSIONS

An emulsion can be defined as at least two immiscible phases, one of which is dispersed in the form of droplets in the other, and can be considered as metastable colloidal systems. As such, emulsions display characteristics of Brownian motion, reversible phase transitions and irreversible transitions leading to complete phase separation. Emulsion destruction is thermodynamically and kinetically favourable and can be hindered by increasing the kinetic barrier via the addition of surface-active species such as surfactants or solid particles. The main role of such surface-active species, which are also known as emulsifiers, is to adsorb at the interface and reduce the interfacial tension between the phases (surfactants) and to form a barrier between the dispersed phase so that drop coalescence does not occur.

Depending on which phase is the dispersed phase, there are two types of simple emulsions, oil-in-water (O/W) and water-in-oil (W/O). The emulsion type is generally controlled by the type of the emulsifier, lipophilic or hydrophilic, which can also control the dispersed phase drop size.

Emulsions can be classified into two main categories, (macro)emulsions, which are thermodynamically metastable systems with a drop size ranging from 50 nm to 50 μm , and microemulsions, which are thermodynamically stable and have a characteristic drop size between 5–50 nm.

In the context of this thesis, only the general aspects of W/O and O/W emulsions stabilised by solid nanoparticles will be discussed.

3.1. Emulsion instability processes

The stability of an oil-in-water emulsion can be affected by several breakdown mechanisms that can be divided into five major categories²⁹, flocculation, coalescence, creaming/sedimentation, Ostwald ripening and breaking. Figure 2.17 illustrates these processes.

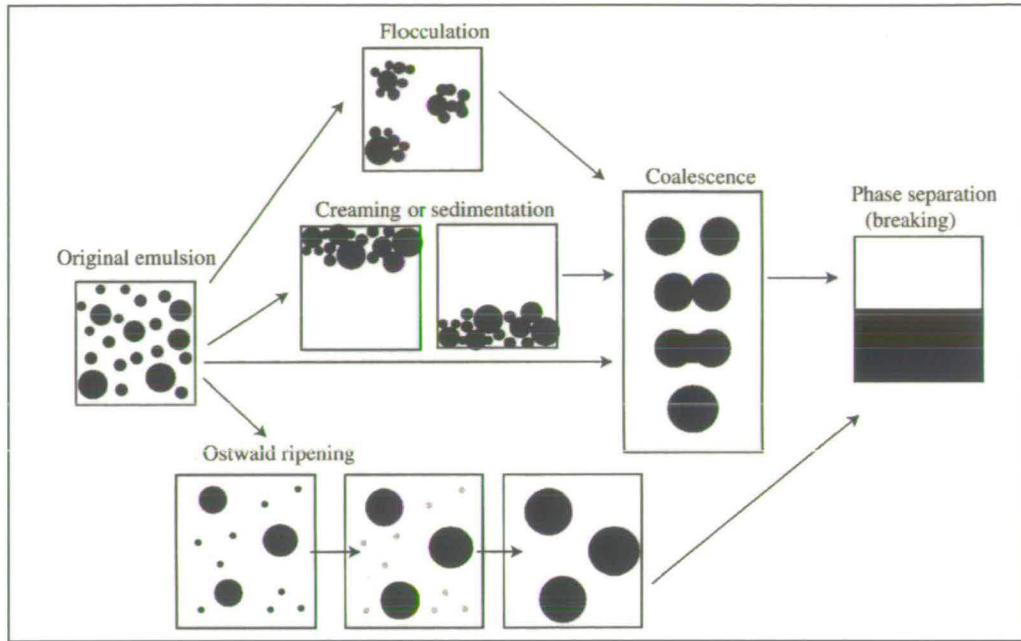


Figure 2.17: Sketch of emulsion instability processes (Adapted from reference 29).

Flocculation & Coalescence. Emulsion flocculation occurs when there is a net attractive force between droplets that is able to overcome the Brownian motion, resulting in either the formation of discrete aggregates called flocs or the formation of structures with expanded networks (or both). During flocculation, the droplets keep their characteristics (size, distribution...) and, generally, the attractive forces are weak enough to allow an easy reversibility to the original emulsion.

Coalescence, on the other hand, involves droplets coming into close contact then irreversibly fusing to create new larger ones. The rate of coalescence is dependent on droplet collision rate and surface properties. This process results in a change in the initial droplet size distribution and the limiting stage is the complete separation of the emulsion into the two immiscible bulk phases.

Creaming/sedimentation, Ostwald ripening & Breaking. Contrary to coalescence and flocculation, these two processes do not involve the droplets coming into contact. Creaming occurs when there is a density difference between the two phases, which by the effect of gravity will separate them. During this process, the less dense

phase will “float” at the top of the vessel (creaming) while the denser phase tends to sink at the bottom (sedimentation).

Ostwald ripening refers to an isothermal diffusion (distillation) process, which has as a driving force the decrease of the droplet’s interfacial area and where smaller droplets are transported through the continuous phase to be re-condensed into larger ones³⁰.

Breaking constitutes the final stage of an emulsion break-up and involves one or more of the processes described above. Since emulsion instability factors influence one another, breaking can occur within minutes or years.

3.2. The Stability of Pickering Emulsions

It has been known for a long time that finely divided particles such as silica can act as stabilising agents for emulsions. These emulsions are often referred to as Pickering emulsions after the early work of Spencer Pickering who observed that particles acted as emulsifiers for O/W emulsions if they were more wetted by water than oil, by residing at the interface³¹.

During the emulsification process, an increase of the interfacial area (ΔA) occurs, due to the formation of dispersed droplets, and it is accompanied by an increase of the interfacial free energy $\Delta G_{\text{int}} = \gamma \Delta A$. Therefore, in the absence of surface-active agents, the system tends towards the emulsion destruction. Whereas the role of surfactants in stabilising emulsions is to decrease the surface tension (γ) so that the interface free energy is small, this is not the case for solid particles which have no impact on the surface tension^{32,33}. Stabilisation in this case, is achieved by reducing the interface area of the drop that is exposed to the continuous phase, since the particles are irreversibly adsorbed at the oil/water interface. The energy of adsorption with which a particle is held at the oil-water interface is function of the particle-interface contact angle (θ) (a quantitative measure of wettability of the particles by either phase) which is $< 90^\circ$ for hydrophilic particles and $> 90^\circ$ for hydrophobic ones. As the energy of adsorption is smaller than the energy of desorption for all contacts angles, except for 0 and 180° , particle adsorption at the interface is

spontaneous and thermodynamically favourable. However, for an emulsion to be stable, particles should be wetted by both the water and oil phases, which means that they should be neither too hydrophobic nor too hydrophilic (i.e. the contact angle is not too far from 90°). In this way, stable W/O (O/W) emulsions can be prepared as the hydrophobic (hydrophilic) particles penetrate the water (oil) drops and curve its layer in order to expose the largest fraction of the particle surfaces to the oil (water) phase³³.

Although, the exact mechanism for emulsion stabilisation by solid particles is still an ongoing debate³², two general mechanisms have been proposed³⁴.

The particles adsorb irreversibly at the oil/water interface and form either a dense monolayer or multilayer film around the droplets. The resulting steric hindrance prevents drops coalescence. Additional stabilisation is provided by particle/particle interactions that create a three-dimensional particle's network extending in the continuous phase and keeping the dispersed drops apart.

Emulsion stability, structure and formation are also influenced by other factors such as particle concentration, pH, system electrolyte, emulsification time and the liquids phase volume fractions. However, these factors can be very specific to a given emulsion system^{33,35-37}, therefore only some generalisations will be presented here:

Effect of particle concentration on droplets size. For many solid stabilised emulsions, dispersed phase droplets size decreases as the concentration of solid particle increases in order to allow more particles to be adsorbed at the interface³⁴. However, if the concentration is further increased until a limiting drop size is reached, then the particles are no longer adsorbed and rest in the continuous phase. Subsequently, a 3-D network of particles may form and provide extra emulsion stability³². One of the advantages in increasing particle concentration is an improvement in emulsion stability against creaming, since smaller droplets will have less tendency to "float" to the surface, but this is generally accompanied by an increase in emulsion viscosity which can be unsuitable for some applications³⁴.

Effect of particle type, pH and electrolyte. There are two main types of silica particles, precipitated silica particles that are prepared by alkaline hydrolysis of

sodium silicate solutions³⁸ and pyrogenic or fumed silica such as Aerosil 200 (300 and R972).

In aqueous dispersions, it has been shown that emulsion stability can be improved when the particles are weakly flocculated prior to emulsification³⁹. Flocculation can be controlled by the addition of salt and/or by adjusting the pH, which decreases the particle's surface potential and electric charge respectively. For some silica particles, the silanol (Si-OH) groups present on the surface can be ionised at the appropriate pH and their surface rendered negative, this lead an increase in the repulsive forces between the particles that decreases the extent of the flocculation³⁷.

3.3. Emulsification Processes

There are numerous emulsification tools and techniques that can be used to create emulsions. Only the following two techniques are relevant to the present work.

3.3.1. Emulsification with Rotor-stator processors

Rotor-stator processors for continuous operation are called colloidal-mills. The processor head consists of a smooth or toothed rotor and a stator comprising slits (Figure 2.18). The large inertial forces and shearing generated by the motion of the rotor create turbulent micro-eddies on the droplet interface which divide large drops into smaller ones. The amount of shear by the processor depends on the number of revolutions and/or the emulsification time and the geometry of the rotor-stator systems⁴⁰.

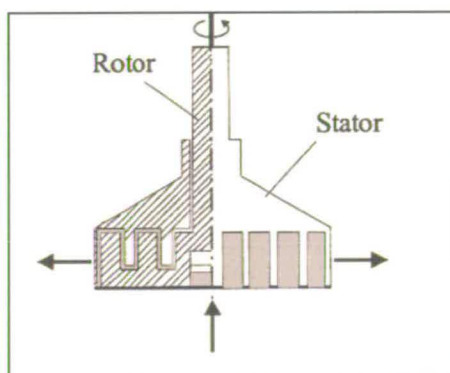


Figure 2.18: Representation of the rotor-stator head (Adapted from reference 40).

3.3.2. Emulsification with Ultrasonic processors

The deformation of two immiscible bulk phases can be achieved by applying mechanical energy which can be dispensed by a wide range of homogenisation techniques. In ultrasonic emulsification, the processor metal tip delivers intense ultrasound at a typical frequency of 20 kHz. The exact mechanism of droplet disruption is unknown, but it is supposed that the drops oscillate at a natural frequency until they burst²⁹. It has been suggested that the frequency of the shock waves (cavitations) create extensional flows which elongate the droplets to the point where they break-up into smaller ones³⁶. There are correlations between the emulsification time, the position of the metal tip in the bulk and the shear rate (proportional to the frequency) on one hand and the emulsion completeness and droplets size on the other hand; these parameters have been widely investigated and reviewed in the literature^{29,41}.

4. REFERENCES

- 1 K. K. Rohatgi-Mukherjee, *Fundamentals of photochemistry*. (Wiley Eastern, New Delhi, 1978).
- 2 M. Klessinger and J. Michl, *Excited states and photochemistry of organic molecules*. (VCH, New York, 1995).
- 3 B. Valeur, *Molecular Fluorescence: Principles and Applications*. (Wiley-VCH, Weinheim, New York, 2002).
- 4 E. U. Condon, *Phys. Rev.* **32** (6), 0858 (1928); J. Franck, *Transactions of the Faraday Society* **21** (3), 0536 (1926).
- 5 R. J. Lakowicz, *Principles of Fluorescence Spectroscopy*, 2nd ed. (Kluwer Academic/Plenum Publishers, New York, 1999).
- 6 G. G. Guilbault and R. F. Chen, *Practical fluorescence; theory, methods, and techniques*. (M. Dekker, New York, 1973).
- 7 W. Koechner, *Solid-state lasers : a graduate text*. (Springer, New York ; London :, 2003).
- 8 C. C. Davis, *Lasers and electro-optics : fundamentals and engineering*. (Cambridge University Press, Cambridge, 1996).
- 9 W. T. Silfvast, (Cambridge University Press, Cambridge :, 2004), Vol. 2nd ed, pp. 450.
- 10 D. Meschede, *Optics, light and lasers : the practical approach to modern photonics and laser physics*. (Wiley-VCH, Weinheim ; [Cambridge], 2004).
- 11 J. Hecht, *The laser guidebook*, 2nd ed. (Tab Books, Blue Ridge Summit, Pa., 1992).
- 12 M. Raffel, *Particle image velocimetry : a practical guide*, 2nd ed. (Springer, Berlin, 2007).
- 13 Continuum Inc., <http://www.continuumlasers.com>.
- 14 M. Stanislas and J. C. Monnier, *Meas. Sci. Technol.* **8** (12), 1417 (1997).

- 15 C. T. Crowe, M. Sommerfeld, and Y. Tsuji, *Multiphase flows with droplets and particles*. (CRC Press, Boca Raton, Fla., 1998).
- 16 A. Melling, *Meas. Sci. Technol.* **8** (12), 1406 (1997).
- 17 H. C. v. d. Hulst, *Light scattering by small particles*, Dover ed. (London : Dover ; Constable, New York, 1981).
- 18 R. J. Adrian, *Annual Review of Fluid Mechanics* **23**, 261 (1991).
- 19 D. Durox, S. Ducruix, and F. Lacas, *Exp. Fluids* **27** (5), 408 (1999).
- 20 J. M. Hespel, Y. Brunet, and A. Dymont, *Exp. Fluids* **19** (6), 388 (1995).
- 21 R. J. Adrian, *Optics and Lasers in Engineering* **9** (3-4), 317 (1988).
- 22 J. Westerweel, *Meas. Sci. Technol.* **8** (12), 1379 (1997).
- 23 R. D. Keane and R. J. Adrian, *Appl. Sci. Res.* **49** (3), 191 (1992).
- 24 R. J. Adrian, *Appl. Opt.* **25** (21), 3855 (1986).
- 25 A. K. Prasad, *Curr. Sci.* **79** (1), 51 (2000).
- 26 A. host-Madsen and R. D. McCluskey, *Seventh International Symposium on the Application of Laser Techniques to Fluid Mechanics*, 1-11. Lisbon. (1994).
- 27 J. Westerweel, D. Dabiri, and M. Gharib, *Exp. Fluids* **23** (1), 20 (1997).
- 28 K. D. Jensen, *J. of the Braz. Soc. of Mech. Sci. & Eng.* **26** (4) (2004).
- 29 P. Becher, *Encyclopedia of emulsion technology*. (New York : Marcel Dekker, 1983).
- 30 A. S. Kabalnov, A. V. Pertzov, and E. D. Shchukin, *J. Colloid Interface Sci.* **118** (2), 590 (1987).
- 31 S. U. Pickering, *J. Chem. Soc.* **91**, 2001 (1907).
- 32 B. P. Binks and T. S. Horozov, *Colloidal particles at liquid interfaces*. (Cambridge University Press, Cambridge ; New York, 2006).
- 33 B. P. Binks and C. P. Whitby, *Langmuir* **20** (4), 1130 (2004).
- 34 R. Aveyard, B. P. Binks, and J. H. Clint, *Adv. Colloid Interface Sci.* **100**, 503 (2003).
- 35 B. P. Binks and S. O. Lumsdon, *Phys. Chem. Chem. Phys.* **1** (12), 3007 (1999).

- 36 B. P. Binks and S. O. Lumsdon, *Phys. Chem. Chem. Phys.* **2** (13), 2959 (2000).
- 37 B. P. Binks and C. P. Whitby, *Colloids Surf., A* **253** (1-3), 105 (2005).
- 38 W. Stober, A. Fink, and E. Bohn, *J. Colloid Interface Sci.* **26** (1), 62 (1968).
- 39 R. Aveyard, B. P. Binks, J. Esquena, P. D. I. Fletcher, R. Buscall, and S. Davies, *Langmuir* **15** (4), 970 (1999).
- 40 K. Urban, G. Wagner, D. Schaffner, D. Roglin, and J. Ulrich, *Chem. Eng. Technol.* **29** (1), 24 (2006).
- 41 R. Rajan and A. B. Pandit, *Ultrasonics* **39** (4), 235 (2001).
- 42 R. Domann and Y. Hardalupas, *Appl. Opt.* **40** (21), 3586 (2001).
- 43 M. C. Jermy and D. A. Greenhalgh, *Appl. Phys. B: Lasers Opt.* **71** (5), 703 (2000).

CHAPTER 3:

EXPERIMENTAL

This chapter describes generic experimental methods. Precise experimental details including preparative methods are found in the corresponding chapters.

1. SPECTROSCOPY

1.1. Steady state Fluorescence measurements

Steady state fluorescence spectra were recorded using a Horiba Jobin Yvon Fluoromax fluorometer, fitted with a 150 W Xenon lamp.

An emission spectrum is measured by selecting the relevant excitation wavelength λ_{ex} at the excitation monochromator. The emission intensity signal is recorded by setting the emission monochromator scanning range between $\lambda_{\text{ex}} + 15$ nm and $2\lambda_{\text{ex}} - 15$ nm. An excitation spectrum is measured by selecting the relevant emission wavelength λ_{em} at the emission monochromator. Emission intensity signal is recorded by setting the excitation monochromator scanning range between $\lambda_{\text{em}}/2 + 15$ nm and $\lambda_{\text{em}} - 15$ nm.

For bulk solutions measurements, the slit width was set for both monochromators at 5 nm-wavelength resolution and the integration times were set at 0.1 s per wavelength increment.

Bulk dye solutions were measured in 1 cm path-length disposable PMMA cuvettes. Fluorescent dyes powder were fully dissolved in the appropriate solvent and diluted so that the final concentration does not exceed a corresponding absorbance of 0.05.

Fluorescence measurements on emulsion samples were carried out in disposable borosilicate glass microcapillary tubes using liquid light-guide optical fibres which directed the excitation beam and the fluorescence emission. The emulsion sample

was flown through the microcapillary at a fixed flow rate using a KDS250 syringe pump (KD Scientific). The microcapillary and the optical fibres were placed in a custom build holder (see section 3.2.4). The excitation monochromator slit width was set to 9 nm, while the emission monochromator was set to 7 nm. The integration times were set to 0.5 s wavelength per increment so that satisfactory smooth spectra are recorded.

The DataMax software (Instruments SA, Inc.) that pilots the fluorometer was used to correct the measured signal intensities against wavelength-dependant lamp performance.

1.2. UV-VIS Measurements

Absorption measurements of dye solutions were carried out in fused silica cuvettes with 1 cm path length using a Cary 300 (Varian) double beam spectrometer. The fluorophore dye powder was fully dissolved in the appropriate solvent and diluted so that the final concentration does not exceed a corresponding absorbance of 0.1.

2. EMULSION PREPARATION, CHARACTERISATION AND IMAGING

2.1. Emulsions preparation

The material required for the preparation of dye-doped oil-in water (O/W) and water-in-oil (W/O) emulsions stabilised by silica nanoparticles are detailed in Chapter 4 section 2. Depending on the solubility of the fluorophore in a given phase, an emulsion type is preferred: O/W emulsion for a dyes soluble in non-polar solvent and W/O for a dye soluble in polar solvent. The preparative method and emulsification process for each emulsion type can be found in Chapter 4 sections 3.2.1 and 3.2.2.

2.2. Microscope imaging

Stock O/W and W/O emulsions were diluted at 1% vol. in water and oil respectively. An aliquot of the diluted emulsion was placed in a Haemocytometer cell

(Marienfeld). Micrographs were taken using a TE2000 inverted microscope (Nikon) fitted with a high-performance computer-controlled Imager QE CCD camera (La Vision). Three Nikon objectives were used for imaging: 10X plan apo (NA= 0.45), 50X Lu Plan (NA=0.80) and 100X plan apo (oil immersion, NA= 1.40).

A haemocytometer cell is a special microscope slide for cells counting (Figure 3-1). It has the advantage, over a conventional microscope slide, of containing a chamber with a fixed depth (0.1 mm) in which the sample solution is introduced through a small slot between the cover and the cell. This avoids the introduction of air bubbles, which could be imaged and confused with the emulsions droplets.

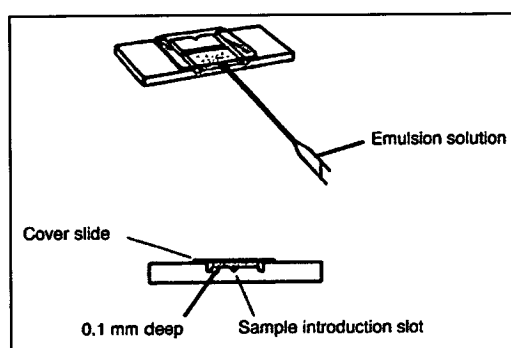


Figure 3.1: Sample introduction in a Haemocytometer cell.

2.3. Emulsion droplet size distribution

Stock O/W and W/O emulsions were diluted at 1% vol. in water and oil respectively and passed into a laser diffraction particle size analyser (LS 230, Beckman Coulter). The volume of sample required for measurements is determined automatically by the analyser.

Prior to the measurements, the sample's background was measured by carefully -so that no air bubbles could form- passing the emulsion continuous phase (either water or oil) in the analyser.

2.4. Flow Cytometry

Flow cytometry allows simultaneous measurements and analysis of multiple physical characteristics of dye-doped particles or tagged cells as they flow in a fluid stream through a beam of light. By measuring visible and fluorescent light emission, properties such as particle's relative size, relative population, and relative fluorescence intensity can be measured.

A flow cytometer (BD FACS) was used to assess how many size populations of the emulsion's doped droplets contribute to the overall fluorescence. The excitation filter was set at 380 nm and the fluorescence signal collected at 450 nm. The measured samples consisted of stock emulsions diluted at 1% vol. in the corresponding continuous phase.

3. PARTICLE IMAGE VELOCIMETRY

3.1. Macro-PIV

3.1.1. Tracer droplets generation

Seed droplets were generated with a pressure-driven medical nebuliser (Andy Flow, Med2000). The nebuliser is equipped with three removable nozzles (A, B and C) which control the nebulised droplets size distribution (Figure 3.2). Nozzle C with a nominal size distribution of 1-3 μm was used. The reservoir was filled with the solution to be nebulised and the seed density was controlled by a pressure-regulated flow of nitrogen.



Figure 3.2: Representation of the Andy flow nebuliser.

3.1.2. Lasers

PIV illumination was provided by two pulsed Nd:YAG lasers (Continuum Surelite II-10) (Figure 3.3). The lasers were triggered from an external pulse generator (Stanford DG535), running at a frequency of 10 Hz. This allows the Q-switch timing of both lasers to be controlled independently, while accurately controlling the pulse separation. The laser cavities were either frequency doubled (532 nm) or tripled (355 nm) by fitting appropriate harmonic generators (Continuum) in the cavity. The maximum output energy of the cavities was measured to be approximately 300 mJ at 532 nm and 110 mJ at 355 nm, in a pulse duration of 6 ns.

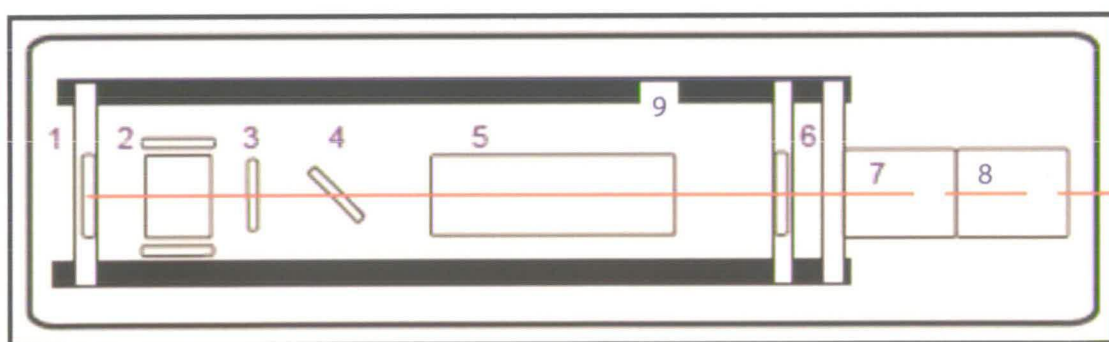


Figure 3.3: Surelight II-10 layout. 1- Rear mirror. 2- Pockels cell. 3- $\lambda/4$ plate. 4- Dielectric polariser. 5- Oscillator rod. 6- Gaussian output coupler. 7- Frequency doubled harmonic generator emplacement. 8- Frequency tripled harmonic generator emplacement. 9- Graphite resonator structure.

3.1.3. Imaging system

The imaging system was composed of a 105 mm Nikon macro lens mounted on the CCD camera using a Nikon to C-mount adaptor. The depth of field and tracer's sharpness was controlled with the lens's selectable $f^\#$ dial.

3.1.4. Recording medium

Depending on the application (Chapter 5 & 6), particle images were recorded on either an Imager QE CCD camera (La Vision) with a resolution of 1376 x 1040 pixels or a HV-F22F 3 CCD-chip colour camera with a resolution of 1280 x 960 pixels. The Imager QE camera possesses a 12 bit dynamic range chip with a high quantum efficiency ($> 62\%$) as well as double exposure function with an interframe time of 500 ns to enable PIV measurements of high velocities. Double frame images capture was done by triggering the camera with an external pulse generator (Stanford DG535). The image recording was done using the Davis Version 7 (La Vision) PIV software package.

The HV-F22F camera is a high precision 3 colour channels (Red, Green and Blue) camera with 8 bit dynamic range per channel. For image capture, the camera was triggered internally at 7.5 frames per seconds. HV-F22F Viewer software (Hitachi) was utilised for image recording.

3.1.5. Data Processing

PIV velocity vector field were generated from the captured double frame images using the adaptive multi-grid cross correlation algorithm in Davis software. The general processing workflow consist of a pre-processing stage for noise subtraction, a multi-pass cross-correlation stage where the interrogation window sizes are defined and a post-processing stage where the validity of the vector fields are assessed.

3.2. Micro-PIV

Micro-PIV measurements were carried out with T- and Y- junction micro-fluidic channels chip. The chip was held in a sample holder with the inlets and outlet

connected to flexible PVC tubes. The measurement fluid consisted of a dilute solution of an emulsion. The emulsion's dispersed phase fluorescent droplets acted as micro-PIV tracers. Continuous pumps (Milligat) were used together with their valve system to alternate between feed solution (the emulsion solution) and the flush solution (wash solution). A Nanoflow sensor was connected to the outlet to monitor the throughput of the pumps. The micro-PIV system consisted of a high intensity light emitting diode as illumination source, controlled by a Flowmap System Hub, illuminating the chip from 5 mm below the surface with 90 ns pulses at 532 nm. The time lapse between two images in a pair was 100 μ s, and each measurement consisted of 25 image pairs recorded at intervals of 1s with an interline transfer CCD monochrome camera (Hisense MKII, Strobe double frame). The experimental set-up and a representation of the microfluidic T-junction chip are represented in Figure 3.4 & Figure 3.5 respectively.

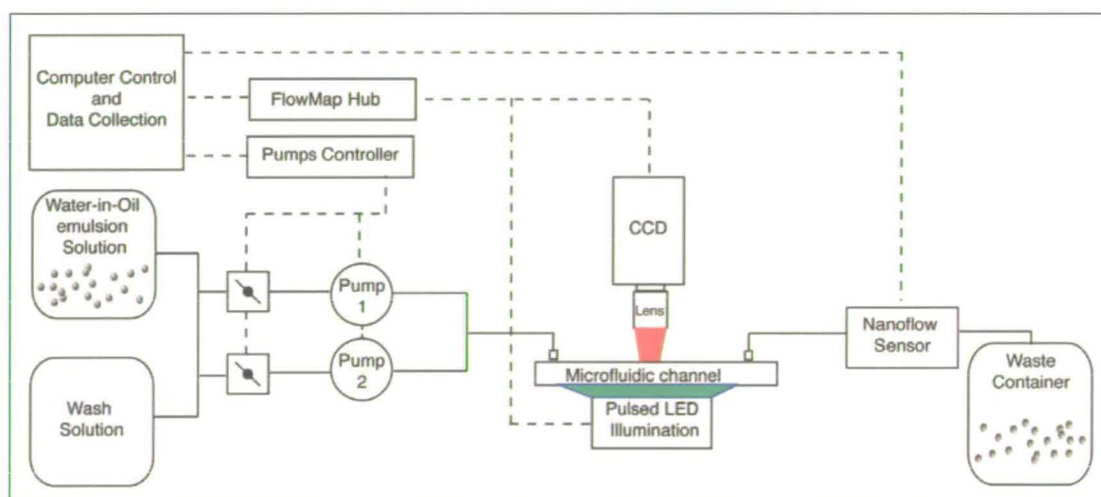


Figure 3.4: Schematic representation of the micro-PIV experimental setup.

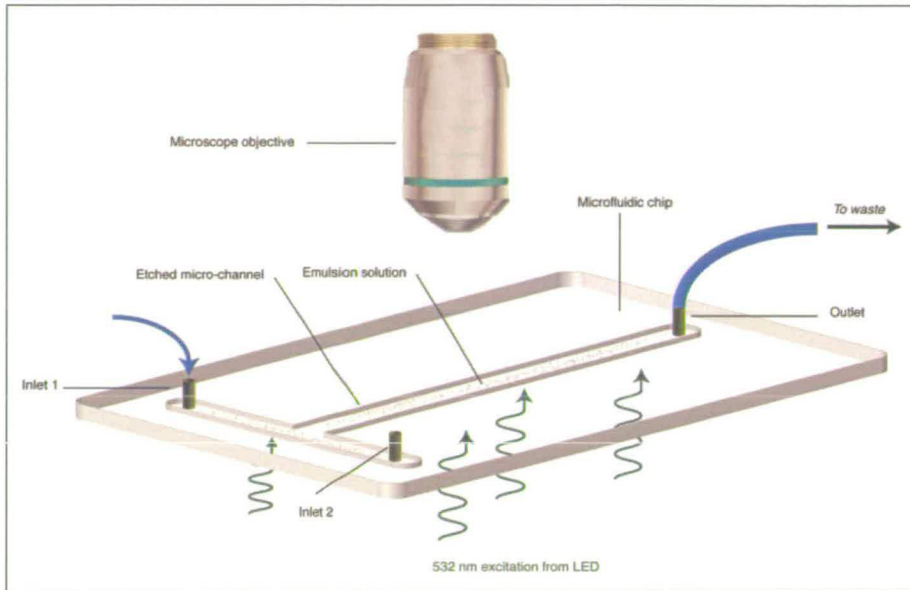


Figure 3.5: Sketch of the microfluidic T-junction chip. The emulsion solution is flown through the chip inlets 1 & 2.

CHAPTER 4:

IDENTIFICATION AND CHARACTERISATION OF AN OPTIMUM FLUOROPHORE FOR PRODUCTION OF DOPED TRACER DROPLETS

1. INTRODUCTION

The study of turbulent two-phase flow systems such as fuel sprays in automotive applications, with a PIV technique that is based solely on Mie scattering is not straightforward. This is mainly due to the difficulty of discriminating between the signals of the seed particles in the gas flow from the one belonging to the spray droplets.

In order to overcome the phase separation difficulty, various methods could be employed such as the application of masking algorithms based on seed image size and intensity¹, spatial frequency² and spot shape filtering³ or by peak properties correlation technique⁴ (see Chapter 2). However, the majority of the separation techniques can be challenging to implement in situations where the signal from seed particles is hard to detect because of the intense scattering from high density spray and/or reflective geometric boundaries. Moreover, discrimination algorithms can introduce some level of noise in one of the phases, which can diminish the quality of the measurements.

Fluorescence PIV (FPIV), which takes advantage of the red-shift of the fluorescence emission signal of the tracer with respect to the laser light, constitutes a strong approach for tackling phase discrimination for simultaneous PIV measurements in multiphase flow. On the other hand, while the requirements for small size seed particles ($< 3\mu\text{m}$) for proper flow following is satisfactory in terms of Mie scattering

signal detection, this is not the case for the fluorescence signal which tends to be weaker since its intensity being proportional to the cube of the doped seed droplet diameter. Previously, Towers *et al.*, have shown that in their setup there was a difficulty in acquiring both fluorescence and Mie scattering images from seed droplets smaller than 3 μm image because of the fluorescence signal being up to 60 times weaker than the corresponding Mie signal⁵.

Therefore, high dye concentrations and high energy laser power are often required in order to produce satisfactory fluorescence images from seed droplets, such as in the work of Driscoll *et al.*⁶ and Kosiwczuk *et al.*⁷, where although the dye spectral properties have been studied, combination of high dye concentration and 355 nm pulse energies of 100 mJ were used.

In highly doped seed droplets, concentration quenching can take place resulting in fluorescence intensity signal being actually reduced. Hence, it is critical that investigations in such effect be carried out in order to produce optimised doped seed droplets which in return would require less illumination power (see Chapters 5 and 6).

For PIV experiments in multi-constituent/multi-phase systems discussed in this thesis a single colour camera is used for image acquisition. It is therefore desirable for the fluorescence emission bandwidth to be contained within one of the primary colour bands corresponding to a detection channel of a colour CCD. The desired properties of the dyes for the PIV applications treated in this thesis are intense absorption at 355 nm, high fluorescence quantum efficiency and a fluorescence emission wavelength centred in the high sensitivity range of the blue channel (≈ 450 nm) and the red channel (≈ 620 nm) of the silicon based CCD cameras, for the blue emitting dyes and the red emitting dye respectively.

1.1. Required Properties of the Fluorophore

In the context of this research, the seed material consists of fluorescent-dye-doped liquid droplets with a size distribution in the range of 0.7-3 μm generated by a nebuliser. The properties of the dye so that optimum fluorescent signal is obtainable must satisfy several requirements:

- The dye must absorb strongly at the laser wavelength.
- The fluorescence emission bandwidth must be appropriate to the spectral sensitivity of the camera. The dye must have a peak emission intensity in a wavelength range where the CCD camera has high quantum efficiency.
- The dye quantum yield must be sufficiently high to achieve good visibility of seed droplets.
- The dye must be soluble in the nebulisation solvent over a range of concentrations. In practice, cross-correlation is carried out at the pixel level, and not on individual droplets, where the intensity of each pixel intensity contains contributions from a number of fluorescing droplets. The laser induced fluorescence (LIF) captured by the CCD can be expressed as⁸:

$$S_{\text{LIF}} = \frac{K_1 I_0 V \Phi N}{r^2} \quad (4.1)$$

where K_1 is an experimental constant, I_0 is the laser intensity, V is the probed volume, Φ is the quantum yield of the fluorophore, r is the distance from the laser light sheet to the camera and N is the number density of the fluorescing species. N is defined as:

$$N = \frac{\frac{4}{3} \pi C \sum_0^m d_k^3}{V \cdot m} \quad (4.2)$$

in which C is the fluorophore concentration, d_k is the diameter of the droplet, k , m is the total number of droplets contributing to the intensity of a particular pixel. Therefore, the fluorescence signal intensity per pixel can be expressed as:

$$S_{\text{LIF}} = \frac{KI_0\Phi}{r^2 \cdot m} C \sum_0^m d_k^3 \quad (4.3)$$

Once all the experimental parameters have been fixed and assuming that the seeding is monodisperse with a constant seed density, the fluorescence intensity from the seed droplets can be adjusted by either changing the laser intensity or the fluorophore concentration. Power adjustments of Nd:YAG lasers commonly used for PIV can be impractical, as the lasers are designed to operate at a nominal frequency and output power. Increasing the pumping power to achieve more laser intensity tends to have a detrimental effect on the spatial properties of the beam and hence the quality of the generated laser light sheet. Laser power attenuation can be achieved by decreasing the Q-switch delay but not without affecting the pulse temporal profile. Alternatively, neutral density filters may be used for beam attenuation without affecting the temporal or the spatial profile⁹.

The adjustment of fluorophore concentration does not require modification of the optical setup and hence provides a convenient way to vary droplet fluorescence intensity according to the available CCD dynamic range.

Generally, the detection of micron-sized fluorescent seed droplets can be difficult, especially when UV-excitable dyes are employed. The generation of Nd:YAG laser third and fourth harmonics (355 nm and 266 nm, respectively) are accompanied by significant laser power losses due to the low conversion efficiency of the harmonic generator crystal, which in return requires the use of high dye concentrations (in the order of 10^{-2} M) to achieve a satisfactory fluorescence signal. However, high dye concentrations can be accompanied by concentration-related quenching effects^{10,11}, such as the formation of dye aggregates or excimers, leading to a decrease in the fluorescence signal. Such effects need to be assessed, in order to optimise the dye concentration in seed droplets.

Fluorescence concentration quenching effects are usually investigated using a standard steady state spectrofluorometry to investigate the relationship between the fluorescence intensity and the fluorophore concentration. In the absence of concentration quenching, a linear relationship should exist between dye

concentration and fluorescence intensity. However, this relationship holds true in bulk solution only for dilute solutions such that the inner filter effect and self-absorption are avoided, as explained in Chapter 2. It is therefore not possible to investigate concentration quenching at the relatively high concentrations that would be found in spray droplets using conventional spectrofluorometry.

Although instrumentation such as aerosol fluorescence analysers are reported to record emission spectra of a variety of airborne micron sized particles^{12,13}, low signal-to-noise, uneven excitation illumination, scattering, spray fluctuations and fluorescence intensity variation with the drop size render quantitative intensity measurements difficult.

In the present work, another approach to evaluate concentration quenching in doped PIV tracers has been developed, whereby an emulsion is formed in which the continuous phase is non-fluorescent and immiscible with the dispersed phase consisting of micron sized droplets containing the fluorophore at the desired concentration. In this way, the continuous phase of the emulsion emulates the air phase in which the doped PIV tracers are seeded and the tracers are emulated by the droplets of the dispersed phase. This approach enables quantitative intensity measurements to be made on highly doped emulsions in a stable and controlled environment and without the limitations of the inner filter and self-absorption, given the small path length of the emulsion droplets (2-4 μm).

2. MATERIALS

Refined olive oil, *o*-xylene, dimethyl sulfoxide (DMSO), *n*-dodecyltrimethylammonium bromide (DTAB) and the fluorescent dyes: 7-amino-4-methylcoumarin (Coumarin 120), 7-amino-4-trifluoromethylcoumarin (Coumarin 151), 1,4-bis(2-methylstyryl)benzene (Bis-MSB), 1,4-bis(5-phenyl-2-oxazolyl)benzene (POPOP) and 4-dicyanmethylene-2-methyl-6-(*p*-dimethylaminostyryl)-4H-pyran (DCM) were obtained from Aldrich Ltd. Silicone oil, poly(dimethylsiloxane-fluid 200, 50 CSt, (PDMS) was obtained from Dow Corning Inc. Water (analytical reagent grade) and sodium hydroxide (NaOH) were obtained from Fisher Ltd. Silica nanoparticles (Aerosil 200; $d_p=12$ nm, Aerosil 300; $d_p=7$ nm, Aerosil R972; $d_p=16$ nm) and ethyl cellulose (Ethocel) were kindly donated by Degussa and Dow Chemicals respectively. All the materials were used as received without further purification and the solvents were of spectrophotometric grade or equivalent.

3. EXPERIMENTAL

3.1. Fluorescence and Absorption Measurements on Bulk Solutions

Fluorescence measurements were carried out using a Fluoromax spectrofluorometer (Jobin Yvon). Solutions were contained in Disposable PMMA cuvettes (100% transmission above 320 nm) were used. Excitation and emission spectra were recorded using dye solution concentrations of 6×10^{-8} M with an estimated error on the molarity not exceeding 1%. Absorption measurements of dye solutions were carried in fused silica cuvettes with 1-cm path length using a Cary 300 (Varian) double beam spectrometer.

Details of the instruments and the measurements methodology are found in the relevant section in Chapter 3.

3.2. Emulsion Preparation

As olive oil is a common nebulisation fluid in PIV experiment, it was sought to carry out emulsions quantitative intensity fluorescence measurements for concentrations of Bis-MSB in olive oil up to the saturation limit ($\sim 10^{-3}$ M). This led to preparation of emulsions based on formulation 1.

However, as *o*-xylene was found to afford higher concentrations of Bis-MSB ($\sim 10^{-2}$ M) than refined olive oil, emulsions based on formulation 2 were therefore prepared.

3.2.1. Preparation of oil-in-water emulsions

Formulation 1

A typical method for preparing oil-in-water emulsions based on the formulation 1 consisted in dispersing 2.5 % wt. of hydrophilic Aerosil 200 in 95 ml of water containing 10^{-4} M of the surfactant DTAB, using an ultrasonic processor (Microson XL2000) fitted with a 3.2 mm tip, using a power of 10 W for 2 minutes at 22.5 KHz. The pH of the aqueous phase was adjusted to 4.5 by the addition of a 1 M solution of NaOH. The oil phase (olive oil) was then added (5 ml) followed by further

sonication for 2 minutes at 20 W and 22.5 KHz. The vessel containing the emulsion was cooled in an ice bath during all sonication processes to avoid excessive heating leading to evaporation of the liquid phases.

Formulation 2

For a typical emulsion based on formulation 2, hydrophilic Aerosil 300 particles (4% wt.) were dispersed in 10 ml water containing 10^{-4} M of the surfactant DTAB, using an ultrasonic processor (Microson XL2000) fitted with a 3.2 mm tip, using a power of 10 W for 2 minutes at 22.5 KHz. A 2% wt. solution of ethylcellulose in o-xylene was prepared. Setting the high shear homogeniser speed at ~ 11000 rpm, 20% of total volume of the oil phase (18 ml) was added to the water phase and emulsification carried out for 1 minute. The remaining of the oil phase volume (72 ml) was then added slowly to the pre-emulsified mixture and the processor speed was set to ~ 20000 rpm. The emulsification was carried out for 3 minutes.

3.2.2. Preparation of water-in-oil emulsions

A typical water-in-oil emulsion is prepared by pre-dispersing 2% wt. of the hydrophobic silica particles Aerosil R972 in 40 ml of PDMS oil using a vortex mixer for 1 minute then sonicating for 3 minutes at 40 W at 22.5 KHz. The resulting oil phase was then pre-homogenised with 60 ml of the 'water' phase which was DMSO using the vortex mixer. The resulting emulsion was then further emulsified using a high shear homogeniser for 3 minutes at 24500 rpm.

3.2.3. Characterisation of Emulsions

Emulsion stability was assessed by storing the emulsion for 24 hours and visually monitoring the evolution of the onset of creaming and settling. Qualitative assessment of droplets size distribution and the extent of droplets flocculation was carried out by light microscopy. Emulsion drop sizing was carried out by laser diffraction scattering. A flow cytometry was used to investigate the contribution of different drop size populations within the emulsion to the overall emulsion fluorescence.

3.3. Fluorescence Measurements on Emulsions

The fluorescence measurements on emulsion samples were carried out using a custom build setup as shown in Figure 4.1. The same spectrofluorometer as used for the bulk solutions measurement (*vide supra*), was coupled with two liquid-guide optical fibre bundles (Edmund), one to carry excitation light from the spectrometer to the sample and one to carry emission from the sample to the spectrometer. A custom build holder was devised to hold the optical fibres and a flow cell consisting in a disposable borosilicate glass microcapillary tube (Kimble/Kontes) of N-51A grade (> 90% transmission above 350 nm) for which the volume capacity and inner diameter were 25 μL and 0.5 mm respectively.

The optical fibres were placed above the capillary tube and along its longitudinal axis. The excitation optical fibre was placed perpendicularly to the capillary so that the elastic scattering reaching the emission fibre is minimised. An angle of $\sim 30^\circ$ between the emission and the excitation fibres was found to allow a maximum of fluorescence signal to be gathered (Figure 4.2).

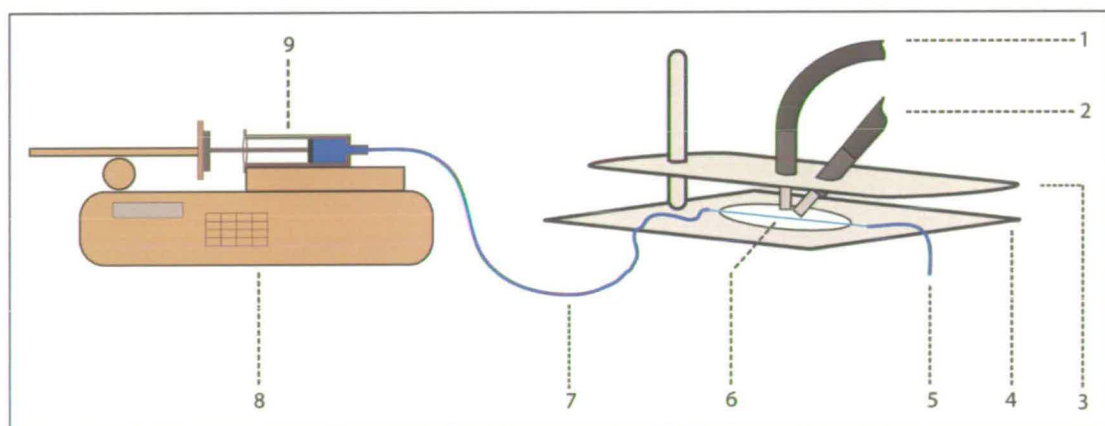


Figure 4.1: Experimental setup for the emulsion fluorescence study. 1- Excitation liquid-guide optical fibre. 2- Emission liquid-guide optical fibre. 3- Support plate for liquid-guide optical fibres. 4- Support plate for the microcapillary tube. 5- Outlet silicon tube. 6- microcapillary glass tube. 7. Silicon tube. 8- syringe pump. 9- Dispensing syringe containing the sample.

Previous experiments have shown that fluorescence measurements of emulsion samples in static forms, such as a thin sample layer on a cover slip, did not allow the acquirement of repeatable and quantitative data.

This is because on the one hand, it was difficult to control the volume of sample being measured (mainly error on sample volumes and vaporisation effects) and on the other, as measurements were made, photoquenching decreased the overall sample fluorescence. Therefore, a solution to the above difficulties was sought and consisted in flowing the emulsion samples through a fixed volume cell. In this way, at relatively high flow rate, the sample is homogenised and the likelihood of its photoquenching is suppressed. Also, the use of a fixed volume cell such as calibrated microcapillaries allowed carrying measurements at known sample volume while avoiding evaporation.

The emulsion samples were prepared by diluting stock emulsion in water at 1% vol. and then flowed through the capillary tube at a fixed flow rate of 0.5ml/min. via a silicon tube (Altec) connected to a KDS250 syringe pump (KD Scientific).

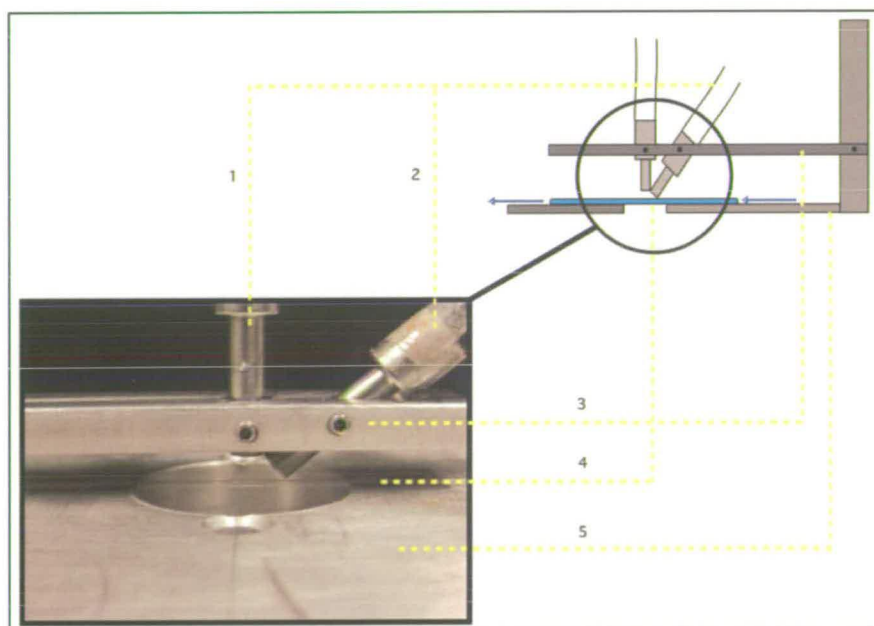


Figure 4.2: Side view of the custom build sample and optical fibres holder. 1- Excitation liquid-guide optical fibre. 2- Emission liquid-guide optical fibre. 3- liquid-guide optical fibre holder plate. 4- Microcapillary cell tube . 5. Microcapillary cell tube holder plate. The arrows are displaying the direction of the flow.

4. RESULTS AND DISCUSSION

As noted in the Introduction to this chapter, it is desired to identify dyes with high fluorescence quantum yield, intense absorption at 355 nm and fluorescence emission wavelength centred either in the high sensitivity range of blue channel (≈ 450 nm) or the red channel (≈ 620 nm) of silicon based CCD cameras.

4.1. Fluorescence of Bulk Solutions

4.1.1. *Blue emitting dyes*

Four candidate dyes, Coumarin 120 (C120), Coumarin 151 (C151), Bis-MSB, and POPOP, were characterised by fluorescence spectroscopy. Initial studies were made by dissolving the dyes in olive oil which is routinely used for gas phase flow seeding. The excitation and emission spectra are shown in Figure 4.3.A, together with those of undoped olive oil Figure 4.3.B. The emission spectrum of olive oil shows: a broad peak at 430 nm, which is due to vitamin E and a second weak peak at 671 nm due to chlorophyll. Work by Kyriakidis and Skarkalis.¹⁴ showed that the chlorophyll acts as a quencher for the vitamin E and that it is possible to increase the intensity of the 430 nm peak by heating the olive oil to degrade the chlorophyll.

The fluorescence spectrum of Bis-MSB shows clear vibronic structure with two peaks at 400 and 421 nm (maxima) and a shoulder at 448 nm. The excitation spectra consist of a single peak with vibronic structures absent.

In olive oil, the coumarin dyes C151 and C120 display a broad emission peak with no discernable vibronic structure with fluorescence maximum at 434 nm and 407 nm. Similarly, the excitation spectra of these dyes show no vibronic structure and display a single peak, apart in the case of C120 where a shoulder is present at 315 nm. The latter is due to the absorption band of olive oil.

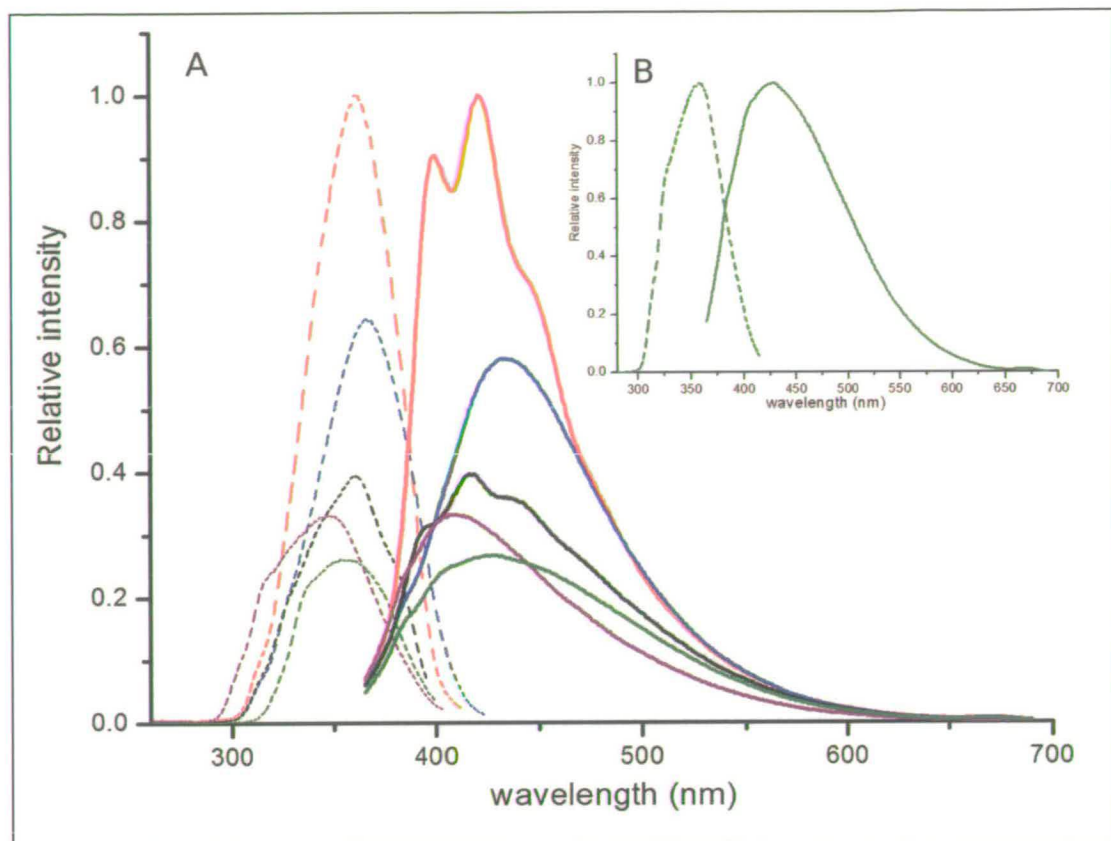


Figure 4.3: A – Excitation (dashed lines) and emission spectra (solid lines) of Bis-MSB (red), C151 (blue), POPOP (black), C120 (purple) in olive oil ($6 \times 10^{-8} \text{M}$) and undoped olive oil (green). B- Enlarged view of excitation and emission spectra of undoped olive oil. Emission spectra were acquired using an excitation wavelength of 355 nm. Intensities have been normalised to the maximum.

The excitation and emission spectra of POPOP in olive oil show clear vibronic structures. The fluorescence spectrum consists of a main peak with a fluorescence maximum at 416 nm and two shoulders at 395 and 441 nm.

The comparison of the relative fluorescence intensities of Bis-MSB, C151, POPOP, and C120 in olive oil at the peak sensitivity wavelength (450 nm) of the CCD camera (Table 4.1) shows that the most intense emission was obtained for Bis-MSB and therefore it was selected as the dye of choice.

Dye	Emission maximum (nm)	Relative intensity	Relative intensity at 450 nm
Bis-MSB	400/421/448*	0.90/1/0.68	0.67
C151	434	0.58	0.53
POPOP	395*/416/441*	0.31/0.39/0.35	0.32
C120	407	0.33	0.23
Olive oil	430/670	0.26/0.005	0.24

Table 4.1: Relative maxima fluorescence intensities of Bis-MSB, C151, POPOP and C120 in olive oil along with relative intensities at the peak sensitivity wavelength (450nm) of the CCD camera. * indicates a shoulder.

The emission spectra of the coumarin dyes in refined olive were found to exhibit a lower fluorescence intensity when compared with Bis-MSB, which is surprising since these dyes are noted for their high quantum yield¹⁵⁻¹⁷. Also, the fluorescence emissions of both C151 and C120 (structures 1 and 2 respectively in Figure 4.4) were found to undergo a large bathochromic shift with solvent polarity as shown in Figure 4.5 for C151 where the fluorescence emission maxima is red shifted from 434 nm in olive oil to 481 nm in methanol.

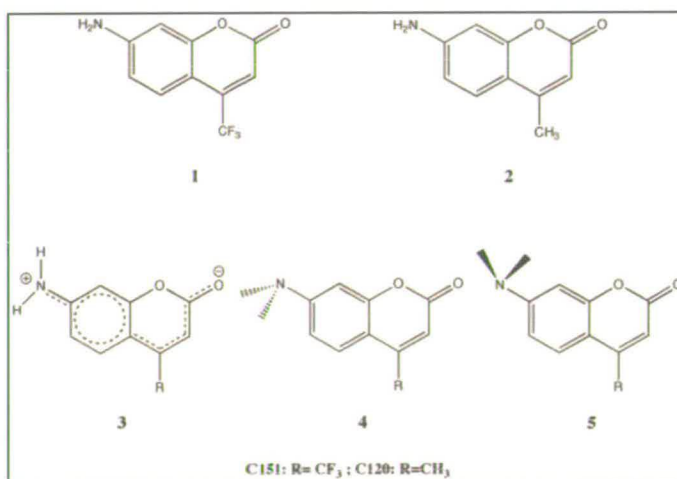


Figure 4.4: Molecular structure of C151 and C120. Intramolecular charge transfer structure of C151 and C120 in polar solvents. Possible conformations for C151 and C120 in non-polar solvents (4 & 5). The structures 3, 4 & 5 were taken from reference 13.

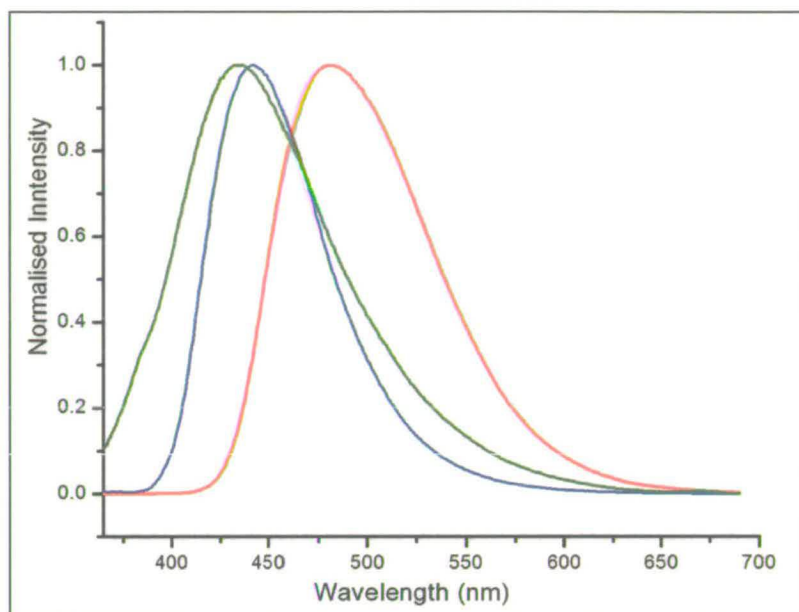


Figure 4.5: Emission spectra of C151 in olive oil (green), dioxane (blue) and methanol (red). Emission maxima: 434nm (olive oil), 441nm (dioxane) and 481nm (methanol). Emission spectra were acquired using an excitation wavelength of 355 nm. Intensities have been normalised to the maximum.

This solvatochromism has been reported by Jones *et al.*¹⁸ for 7-aminocoumarin derivatives and more specifically for C151 by Nad *et al.*¹⁹ and C120 by Pal *et al.*²⁰ where these dyes display not only an unusual low Stokes shift but also a low quantum yield in non-polar solvents when compared with the moderately polar and polar solvents. This behaviour is explained by the fact that in non-polar solvents no specific solute-solution interaction is present. This results in the molecule adopting a non-planar non-polarised structure (structures 4 and 5 in Figure 4.4) in both the ground and the excited states and therefore a low Stokes shift is observed. Furthermore, as in non-polar solvents the 7-NH₂ group is in a free motion, this has the effect of activating a nonradiative deexcitation channel for the excited state (S₁) which dissipates the excess of energy to the solvent. This in turn drastically diminishes the quantum yield.

On the other hand, in more polar environments the dyes adopt planar and polar intramolecular charge transfer (ICT) structure (structures 3 in Figure 4.4) where the flexibility of the amino group is restricted and in resonance with the benzopyrone

moiety. Therefore, and contrary to non-polar solvents the C120 and C151 dyes exhibit a higher quantum yield. In the excited state, the ICT structure lies lower in energy than the non-polarised structure so consequently a larger Stokes shift is observed for these dyes.

Contrary to the dyes C151 and C120, the dye Bis-MSB is a stilbene derivative and a highly efficient blue emitting laser dye^{21,22} for which the quantum yield, close to unity, shows little solvatochromism²³.

In the excited state, substituted stilbenes have been reported²³ to favour a planar conformation which maximises the π conjugation. This explains the presence of resolved vibronic structure in the emission spectra of Bis-MSB (Figure 4.3 and Figure 4.6). However, for Bis-MSB in the ground state, there is a steric hindrance between ethylenic hydrogens and the methyl group of the terminal phenyls which impede the adoption of the planar conformation. As a result, the ground state consists of an inhomogeneous mixture of pseudo-planar conformations which results in an absorption spectrum without vibronic structures as shown in Figure 4.6.

The ability of some stilbene derivatives (such as Bis-MSB) to achieve planar conformation in the excited state, which is not possible in the ground state, has been attributed to the increase of the bond order (or bond length) of the ethenyl-terminal phenyl single bond (i.e. the single bond linking the double bond and the terminal phenyls). Consequently, the extent of steric hindrance between the above mentioned substituent decreases and allows the adoption of planar conformation²³.

However, recent work by Thipperudrappa *et al.*²⁴ showed that the magnitude of the Stokes shift varies by ~ 8 nm from the least polar solvent (benzene) to the more polar methanol. This tends to indicate the limited effect, in the excited state, of solvent polarity on the bond order of the ethenyl-terminal phenyl single bond.

Therefore, it can be concluded that the Stokes shift in stilbene derivatives show little solvatochromism and it is only as function of the ability of the molecule to achieve a planar conformation in the ground state.

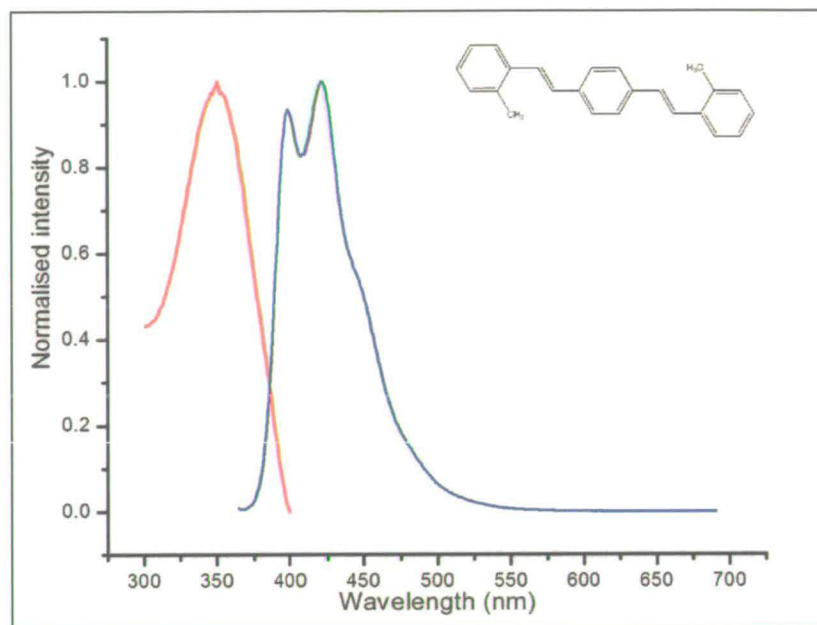


Figure 4.6: Absorption and emission spectra of Bis-MSB in Chloroform along with its structure. Emission spectrum was acquired using an excitation wavelength of 355 nm. Intensities have been normalised to the maximum.

This can be further illustrated as in the case of DSB (1,4-Distyrylbenzene) in which the ortho substituent group of the terminal phenyls are hydrogens. For this derivative the Stokes shift is found to be smaller than Bis-MSB²³.

The solubility of Bis-MSB in polar solvents was found to be very limited (in the order of the micromolar) when compared to the concentration level (10^{-3} – 10^{-2} M) that would be required in PIV tracers for satisfactory visibility. Therefore, the polar solvatochromism of Bis-MSB was not investigated further.

However, the fluorescence intensity that could be achieved for Bis-MSB in olive oil was found to be limited by the maximum solubility of $\sim 10^{-3}$ M (the solubility is even less in paraffin oil, which is also used as a nebulisation solvent in PIV). Therefore, another solvent was sought, in which Bis-MSB is more soluble and which would be suitable for nebulisation to produce tracer particles. *O*-xylene was found to satisfy both the criteria of nebulisation (see chapter 3) and solubility allowing a Bis-MSB concentration of 10^{-2} M to be achieved.

4.1.2. Red emitting dyes

In the multiphase flow PIV application described in this thesis (see Chapters 1 and 5), the red emitting candidate dyes were required to exhibit high quantum yield as well as strong absorption in both 355 nm and 532 nm. However, the list of available dyes displaying such quantum yield and large Stokes shift, i.e. absorption at 355 nm and emission at ~ 620 nm, is far from exhaustive.

The dye DCM is one of the most well known red laser dyes owing to its high efficiency, broad absorption bandwidth and large Stokes shift in polar solvents^{25,26}.

The absorption spectrum of DCM in DMSO (Figure 4.7) was found to present absorptions over a large spectral range with a main broad peak at 478 nm (maximum) and absorbance at 355 and 532 nm of 0.23 and 0.33, respectively.

The photophysical properties of DCM are largely dominated by intramolecular charge transfer (ICT) between the electron-accepting substituents, pyran ring with two cyano groups, and the terminal electron-donating, dimethylamino, group (inset Figure 4.7)²⁷.

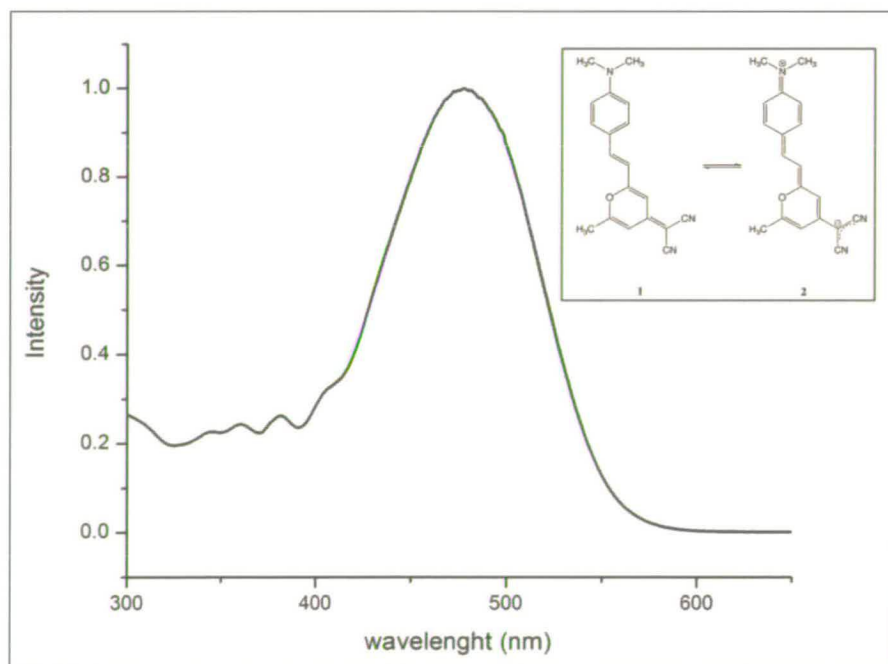


Figure 4.7: Absorption spectra of DCM in DMSO along with its resonance structures. Intensities have been normalised to the maximum.

DCM exhibits marked solvatochromism where the Stokes shift and quantum yield increase with increase of solvent polarity. This is explained as a result of DCM adopting a bipolarised structure (due to ICT), that is stabilised, in the excited state, by polar solvents via the formation of a twisted intramolecular charge transfer (TICT) conformation. Transitions to the latter state occurs from a locally planar untwisted excited state and fluorescence emissions are expected from these two states. However, as the transition between the locally excited and TICT states is fast (100 fs) and occurs at high rate, only fluorescence from the TICT state is observable²⁸ and occurs at longer wavelengths with high quantum yield.

In Figure 4.8 the fluorescence emission of DCM shows a large broad peak with a maximum intensity at 628 nm and with no vibronic structures as a result of transitions from a mixture of TICT conformer states. The ratio between fluorescence maxima at 532 and 355 nm is 1.42 (Table 4.2).

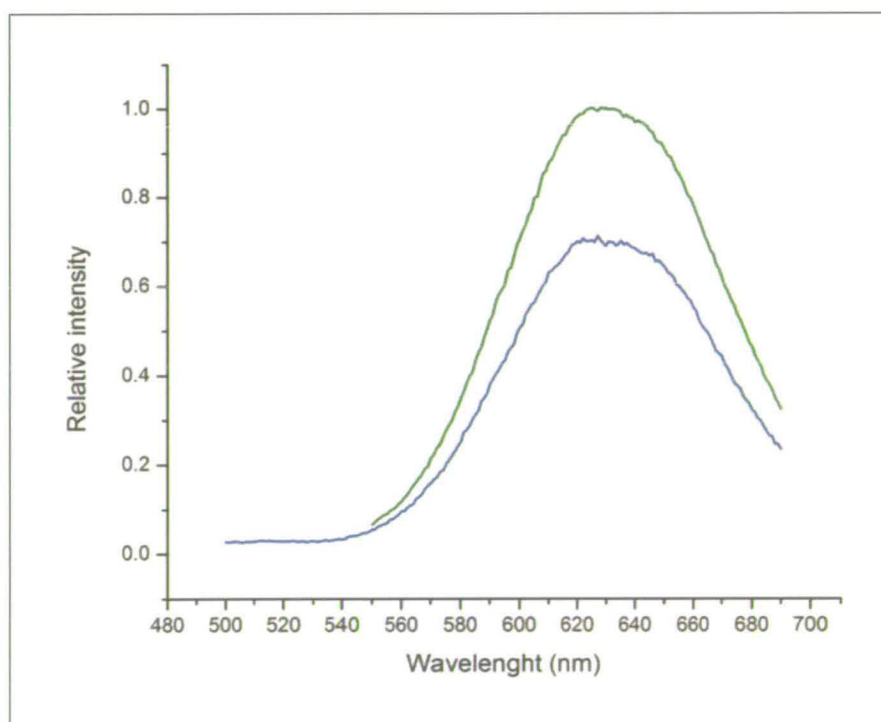


Figure 4.8: Emission spectra of DCM in DMSO (10^{-7} M) from excitation at 355 nm (blue) and 532 nm (green). Intensities have been normalised to the maximum.

Relative intensities	532 nm	355 nm	Ratio (532/355)
Absorbance	0.33	0.23	1.5
Fluorescence (at 628 nm)	1	0.7	1.42

Table 4.2: Absorption and fluorescence relative intensities at 355 nm and 532 nm for DCM in DMSO.

4.2. Optimisation and Characterisation of Emulsions

It was beyond the scope of the work presented here to carry out in depth and/or systematic investigation into the exact mechanism by which the composition of each emulsion affected the final emulsion stability (such as contact angle, conductivity measurements....). A pragmatic approach was adopted, that was based on findings already published on the literature²⁹⁻³² that demonstrated that a given constituents/parameters lead to an improvement of the emulsion stability.

The optimum formulation for emulsion stability was determined by varying the water/oil phase fractions and particle concentration and then visually assessing the emulsions stability after a 24 hours period by monitoring the appearance of any creaming or settling.

4.2.1. Oil in water (O/W) emulsions

4.2.1.1. Formulation 1

For the formulation 1, where the oil phase consisted of olive oil, the water/oil phase fraction was varied between 50% and 5% while keeping the concentration of silica nanoparticles constant (2% wt.) and the aqueous phase pH at 4.5. This led to the preparation of the emulsion A1 to A6 (Table 4.3).

As reported by Binks *et al.*³⁰, emulsions stabilised with Aerosil particles show marked stability at pH around 4 where the particles are slightly negatively charged and displaying enough hydrophobicity to promote their adsorption at the oil/water interface.

Formulation 1: 2% wt. silica nanoparticles, [DTAB]= 10^{-4} M, pH=4.5	
Emulsions	Oil/water fraction (% vol.)
A1	50
A2	40
A3	30
A4	20
A5	10
A6	5

Table 4.3: Definition of emulsions A1 to A6 in which the oil phase fraction was varied.

Therefore, the water-in-oil emulsion aqueous phase was fixed at 4.5, as previous experiments showed that at this pH value stable emulsions were produced.

The addition of cationic surfactant such DTAB was also found to improve the stability of the Pickering emulsion based on Aerosil 200³³ fumed silica. In a recent work by Binks *et al.*³⁴, it has been shown that at low pH there was a strong synergism between solid particles and surfactant molecules in stabilising O/W emulsions. The suggested mechanism consisted in the surfactant rendering silica particles increasingly hydrophobic as well as decreasing the oil/water interfacial tension.

As the surfactant concentrations in the works of Binks *et al.*^{33,34} was in the range of 10^{-4} M, this concentration for DTAB was used in this work.

Once the emulsions A1 to A6 were prepared, they were stoppered and stored for 24 hours. After this time, it was difficult to assess visually the effect on the emulsion stability of varying the oil phase fraction for the formulations A1 to A6 (Figure 4.9). This series of emulsions shows some phase separation with a release of particles in the lower water phase.



Figure 4.9: A picture of the emulsions A1 to A6 displaying the effect of volume fraction on the emulsion stability.

In order to study the impact of silica particle loading on the emulsion stability, the emulsion formulation A6 was used as a model and the emulsions B1 to B6 (Table 4.4) were then prepared with the particle concentration varying from 4% to 0.25%.

Formulation 1: 5% Oil/Water fraction, [DTAB]= 10^{-4} M, pH=4.5	
Emulsions	SiO ₂ (% wt.)
B1	4
B2	3
B3	2.5
B4	1.5
B5	1
B6	0.5
B7	0.25

Table 4.4: Definition of emulsion formulations B1-B7 for which the silica particle loading was varied.

In this series of formulations, the silica particles have an obvious effect on emulsion stability as seen in Figure 4.10.

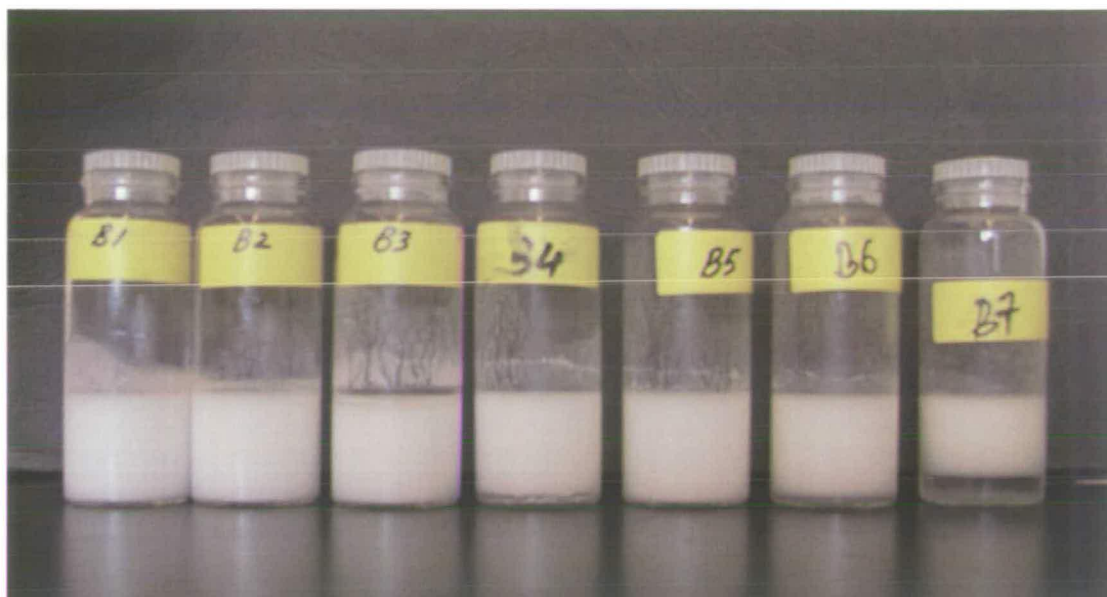


Figure 4.10: A picture of the emulsions B1 to B7 displaying the effect of silica particle loading on the emulsion stability.

However, it is hard to visually assess the effect for the formulations having a particle concentration above 2.5%; the emulsions B1, B2 and B3 were stable for more than a week. The emulsions displayed an increase of viscosity with increased of particle loading, the emulsion B1 was particularly viscous and presented a gel like rheology. The impact of particles concentration on the emulsion viscosity is due to both the coating of drops by the particles and to the aggregation of the excess particles in the continuous phase³⁵.

Below a particle concentration of 2.5%, the emulsions show a gradual phase separation. Emulsion B7 shows a clear phase separation, as the particle concentration was too low to stabilise the emulsion.

Emulsion B3 was subjected to dynamic light scattering measurements and light microscopy examination to investigate both the droplet size distribution and the extent of drop flocculation. The dispersitivity of oil droplets within the emulsion is

critical and the oil droplets must exist individually so that the fluorescence measurements will not report the properties of large drop flocs.

The micrographs (Figure 4.11, 4.12 and 4.13) of a diluted (1% vol. in water) sample of emulsion B3 in water show that the drops are well dispersed within the water continuous phase and do not display any noticeable drop flocculation.

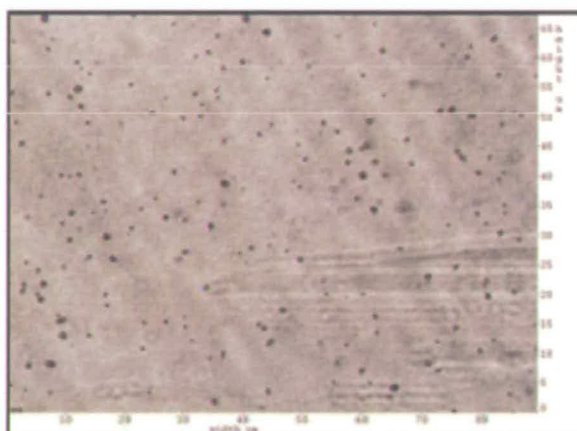


Figure 4.11: Optical micrograph of B3 emulsion diluted in water at 10x magnification. The actual scale is 10x the one displayed.

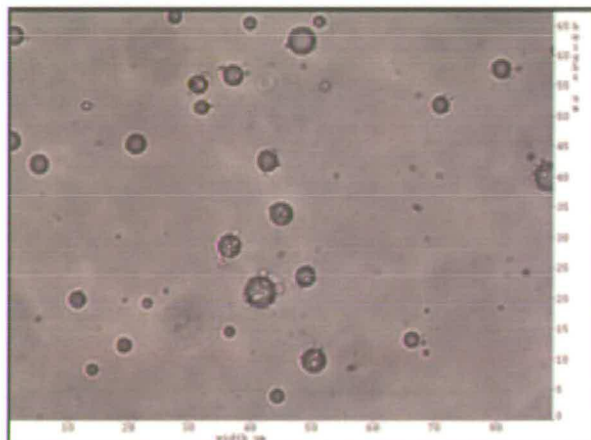


Figure 4.12: Optical micrograph of B3 emulsion diluted in water at 50x magnification. The actual scale is 2x the one displayed.

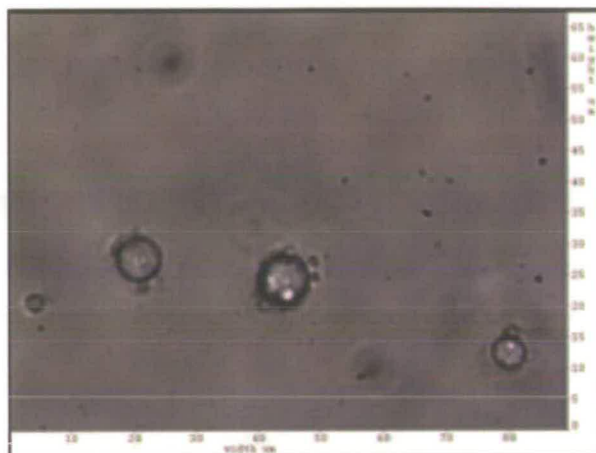


Figure 4.13: Optical micrograph of B3 emulsion diluted in water at 100x magnification.

The emulsion B3 was diluted at 1% vol. in water and subjected to laser diffraction particle size analyser for emulsion drops size measurements. Drop sizing results in Figure 4.14 show that the emulsion B3 contain a single and rather broad monomodal size distribution (mode = 4.4 μm) extending from ~ 1 to ~ 15 μm with a mean and median drop diameter of 4 μm (Table 4.5).

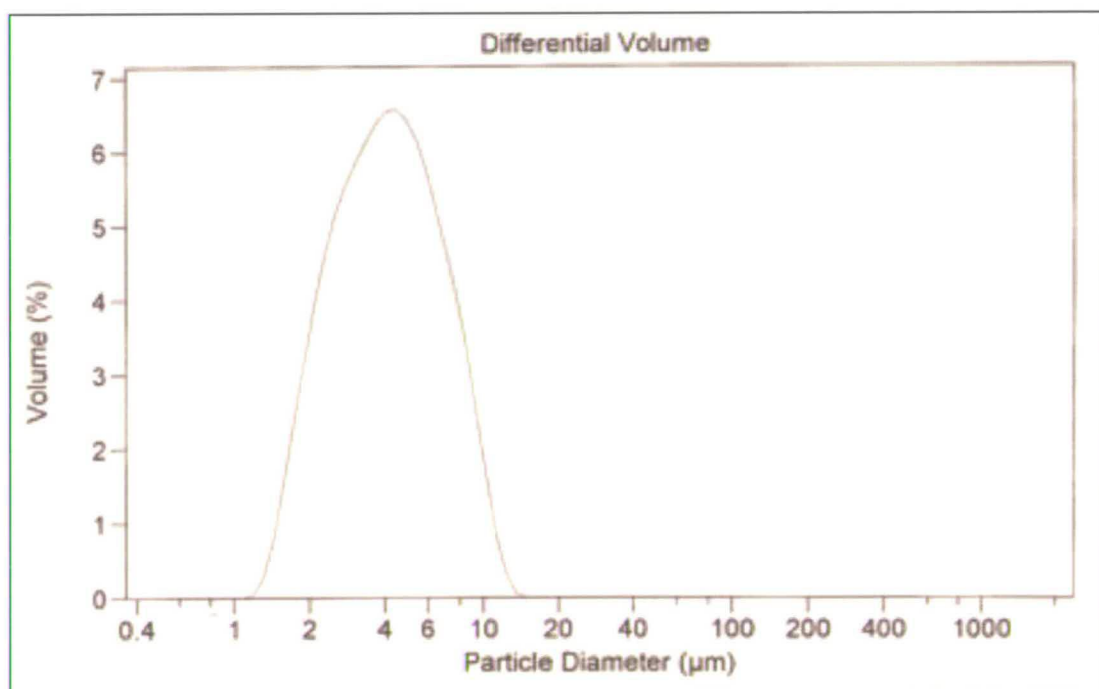


Figure 4.14: Droplet size distribution of emulsion B3.

Mean	4.071 μm
Median	4.097 μm
Mean/Median ratio	0.994
Mode	4.443 μm
Standard deviation	1.635 μm

Table 4.5: Drop sizing statistics for the B3 emulsion.

The ability of the flow cytometry technique to discriminate between fluorescent species according to their fluorescence intensities and size has been exploited to determine the number of fluorescing populations, which contribute to the overall fluorescence intensity. Therefore, in order to substantiate the size distribution results for the emulsion B3, it was sought to find out if the overall recorded fluorescence intensity from emulsion dye doped droplets is due to a single drop size population or at the contrary at the sum of different size populations.

A 1% vol. dilution of the emulsion B3 in water was taken as a reference. Figure 4.15 shows the count number versus the fluorescence intensity at 450 nm. The fluorescence intensity of olive oil droplets in the emulsion, collected at 450 nm, is represented by one broad peak, which suggests the presence of a single fluorescing droplet population. As the fluorescence emission of olive oil is quite weak, the experiments were repeated by preparing the emulsion B3 with an olive oil phase containing 6×10^{-8} M of Bis-MSB.

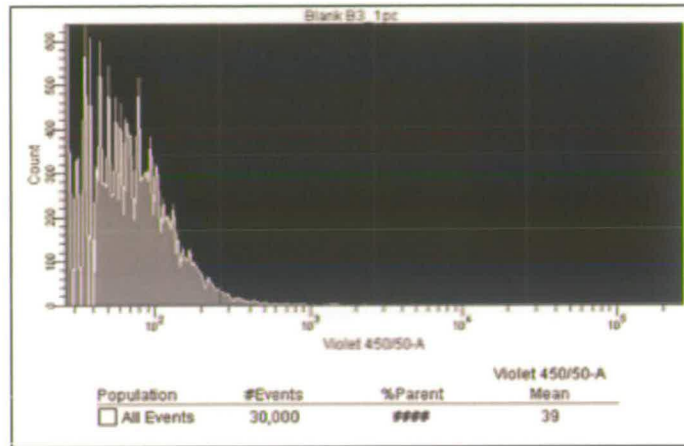


Figure 4.15: Flow cytometry count number versus fluorescence intensity for a 1% dilution of emulsion B3 in water.

The results of the flow cytometry for a 1% dilution of emulsion B3 in water Figure 4.16 shows an increase of ~ 10 fold of the fluorescence intensity at 450 nm in comparison with the fluorescence intensity of the reference emulsion of undoped olive oil (39 vs. 3641). Moreover, there only one large peak (with a shoulder) present, again suggesting that there is one main fluorescent droplet population. However, the presence of the shoulder at higher fluorescence intensity indicates the probable presence of a much smaller population but with larger droplets.

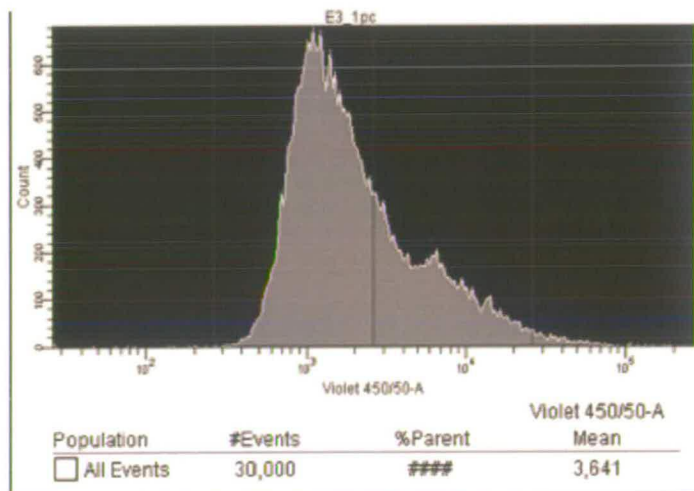


Figure 4.16: Flow cytometry count number versus fluorescence intensity for a 1% dilution of the doped emulsion B3 in water.

The emulsion B3 being the most stable for the emulsions based on formulation 1, it was therefore used as model for fluorescence experiments on emulsions (see section 4.2.1).

4.2.1.2. Formulation 2

In previous experiments it has been noticed that the addition of ethylcellulose in o-xylene improved dramatically the stability of the prepared oil-in-water emulsions. Ethylcellulose is an oil soluble ethyl ether polymeric emulsifier for which the mechanism of stabilisation of O/W emulsions has been proposed by Melzer *et al.*³⁶. According to the authors, ethylcellulose was found to precipitate at the oil/water interface forming colloidal ethylcellulose particles. The latter act in a similar manner in stabilising O/W emulsions as do solid particles in Pickering emulsions.

Hence, it can be suggested that for the emulsions based on the formulation the improvement in stability of the emulsions based on formulation 2 can be attributed to combined effect of ethylcellulose and silica particles as well as to the known interfacial activity of the ethyl ether polymers^{37,38}.

In this work, a trial and error approach has been adopted to determine the amount of ethylcellulose to be used in o-xylene and a value of 2% wt. of was found to produce stable emulsions.

For emulsions with formulation 2, five O/W emulsions have been prepared by varying the liquid phases fractions from 10% to 50% and keeping the concentration of Aerosil 300 particles, DTAB (10^{-4} M) and pH (4.5) constants. Table 4.6 indicated the required components quantities for making a 100 ml emulsion.

% Aerosil 300 (wrt water phase weight)	2				
% Ethylcellulose (wrt oil phase weight)	2				
Emulsions	C1	C2	C3	C4	C5
Oil/Water fraction	0.1	0.2	0.3	0.4	0.5
V(o-xylene+ethylcellulose, ml)	10	20	30	40	50
V(water+DTAB, ml)	90	80	70	60	50
m(Aerosil 300, g)	1.80	1.6	1.4	1.2	1
m(Ethylcellulose)	0.17	0.35	0.53	0.70	0.88

Table 4.6: Definition of formulation 2 emulsions C1-C5 in which the oil phase fraction was varied.

Once the emulsions C1 to C6 have been prepared, they were stoppered and stored for 24 hours. After this period, it was observed (Figure 4.17) that a clear correlated phase separation is occurring as the oil/water fraction was decreased from 50% to 10%. For these emulsions, creaming is generally apparent 1 to 3 hours after emulsion preparation.

It was also observed that the higher the oil/water volume fraction the higher was the viscosity of the emulsion (the emulsion C5 presented a gel like rheology). As the viscosities for the emulsions C4 and C5 were much more pronounced than the one of C1, C2 and C3, it was decided to increase the amount of silica only on the latter emulsions. This is to avoid a further increase in viscosity, that generally occurs in emulsions with high silica particles loading (see Chapter 2), and which will render the emulsions C4 and C5 unusable for the purpose of this work.

Using the same formulation for C1, C2, C3 emulsions the concentration of Aerosil 300 was increased to 4%, this led to the preparation of the emulsions D1, D2 and D3. These emulsions were stored for 24 hours after preparation. In Figure 4.18 it can be seen the effect of particle concentration on emulsion stability.

For all three oil/water fractions, there is a marked stabilisation of the emulsions. The emulsion D1 with 10% oil/water volume fraction and 4% silica particles did not show any creaming after one week, whereas the emulsions D2 and D3 only showed a

limited phase separation after this period. For this reason the emulsion D1 was used as model for fluorescence experiments on emulsions (see section 4.2.1).



Figure 4.17: A picture of the emulsions C1 to C5 displaying the effect of volume fraction on the emulsion stability. Left to right, the O/W volume fraction are 10%, 20%, 30%, 40% and 50%.

The emulsions D1, D2 and D3 were diluted at 1% vol. in water and subjected to laser diffraction particle size analyser for emulsion drops size measurements. Drop sizing results in Figure 4.19 show that the emulsions contain a single and monomodal size distribution ranging from ~ 2 to $6 \mu\text{m}$ and ~ 2.5 to $8 \mu\text{m}$ for D1, D2 and D3 respectively. The drops size mode for the three emulsions is situated between 3 and $5 \mu\text{m}$ while the mean drops diameter range between 4 and $5 \mu\text{m}$ (Table 4.7).



Figure 4.18: A picture of the emulsions C1, D1, C2, D2, C3 and D3 (from left to right) displaying the effect of O/W volume fraction and silica particles concentration on the emulsion stability.

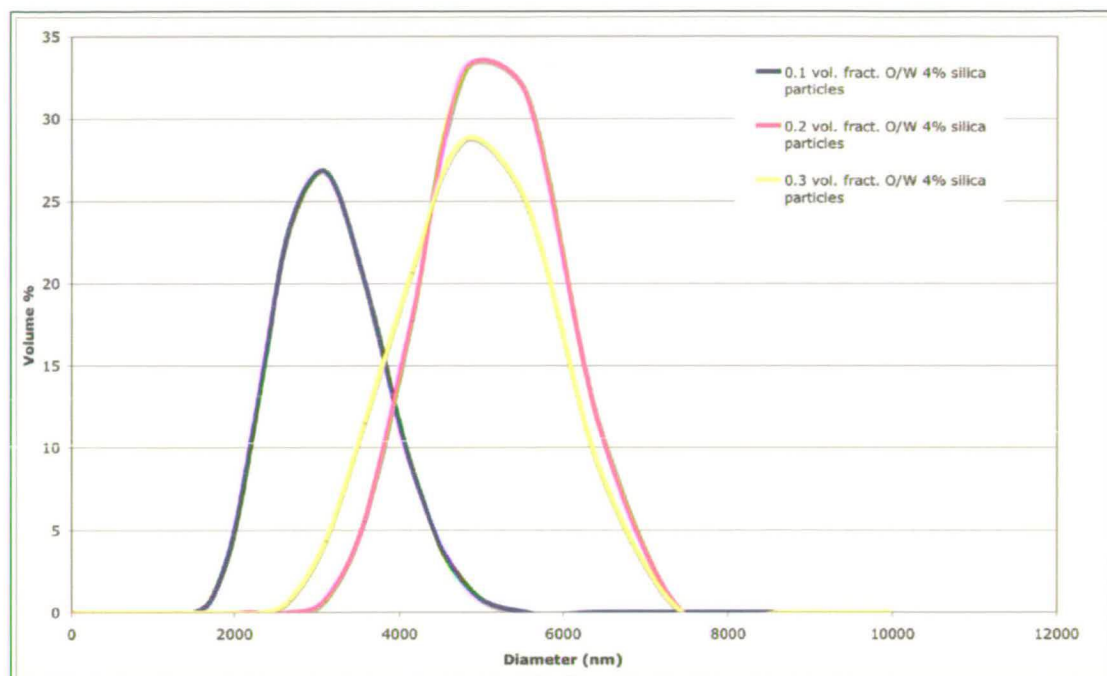


Figure 4.19: Droplet size distribution of emulsion D1 (blue), D2 (purple) and D3 (yellow).

Formulation 2 with 4% wt. Aerosil 300.	Mean drop size (μm)	Mode (μm)
D1	4.1	3.1
D2	4.8	4.8
D3	5.4	4.8

Table 4.7: Drop sizing statistics for D1, D2 and D3 emulsions.

Figure 4.20 displays the appearance of three emulsions based on the D1 formulation where the oil phase has been doped with Bis-MSB at 10^{-3} , 5×10^{-3} and 10^{-2} M.



Figure 4.20: A picture of the formulation D1 emulsions at different doping level of Bis-MSB in o-xylene phase. Left to right: 10^{-3} , 5×10^{-3} and 10^{-2} M.

4.2.2. Water in oil (W/O) emulsion

Four emulsions based on the formulation 2 were prepared where water/oil fraction was varied from 10 % to 40 % (E1 to E4 in Table 4.8) and the concentration of silica particles kept constant at 2% wt. of PDMS.

Once the emulsions have been prepared, they were stoppered and stored for 24 hours. It can be seen from the aspect of the emulsions E1, E2, E3 and E4 (Figure 4.21) that after this period of time, no phase separation occurs when the water/oil fraction is varied.

W/O emulsion, 2% wt. Aerosil R972				
Emulsion	E1	E2	E3	E4
V (DMSO, ml)	10	20	30	40
V (PDMS, ml)	90	80	70	60

Table 4.8: Definition of W/O emulsions E1-E5 in which the water phase fraction was varied.



Figure 4.21: A picture of the emulsions E1, E2, E3 and E4 (left to right displaying the effect of O/W volume fraction).

All four emulsions were stable for more than a week, and no further investigation on the effect of silica particles was carried.

Micrographs of the 1% vol. dilution emulsion E4 in PDMS (Figure 4.22 and Figure 4.23) show that the droplets are well dispersed with little evidence of flocculation. It also shows the presence of very few large droplets. This is confirmed in the results of dynamic laser scattering (DLS) measurement of 1% vol. emulsion dilution in PDMS. The droplet size distribution clearly appears monomodal, with a mean diameter of $3.8 \mu\text{m}$ and a mode of $\sim 3 \mu\text{m}$. The distribution is right skewed towards large diameters in the range of $10 \mu\text{m}$, but less than 10% of the population has a diameter larger than $6 \mu\text{m}$, while 75% of the droplets have a diameter smaller than $3 \mu\text{m}$.

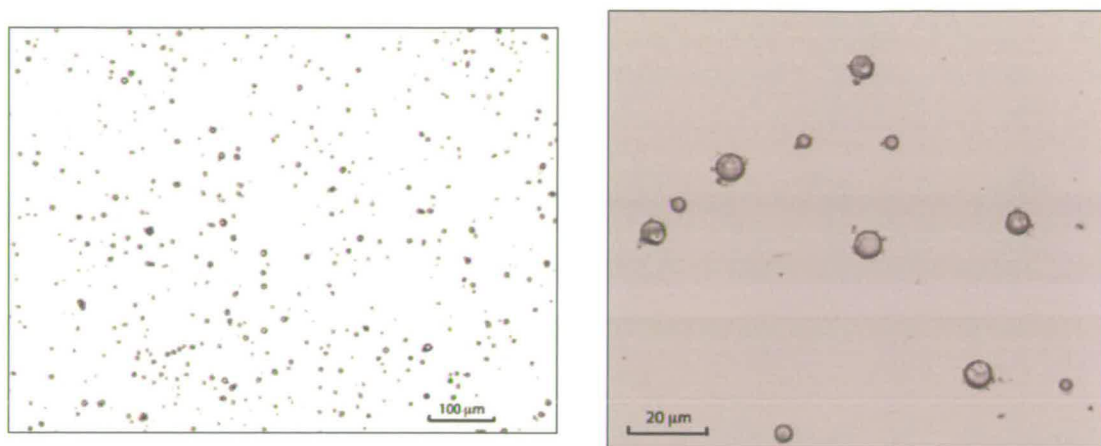


Figure 4.22: Micrographs of E4 water-in-oil emulsion at 10x and 50x magnification (left and right respectively).

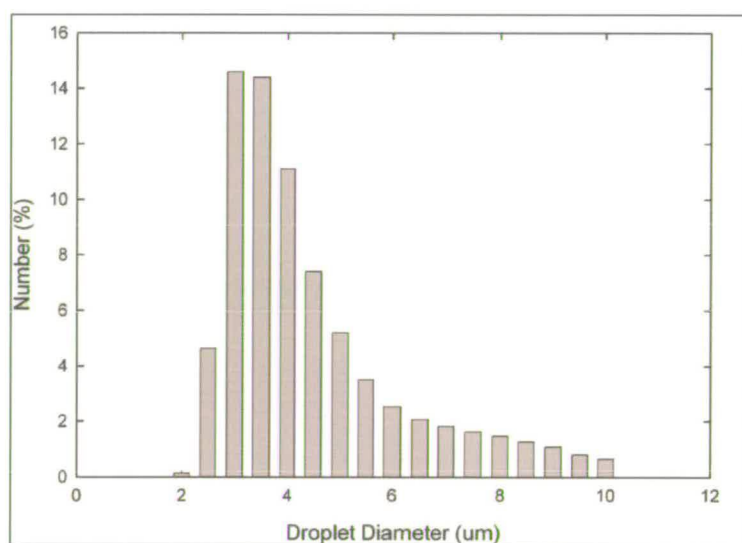


Figure 4.23: Droplets size distribution of E4 water-in-oil emulsion as determined by DLS measurement.

Figure 4.24 displays the appearance of the emulsion E4 where the water phase has been doped with DCM at 10^{-2} M.

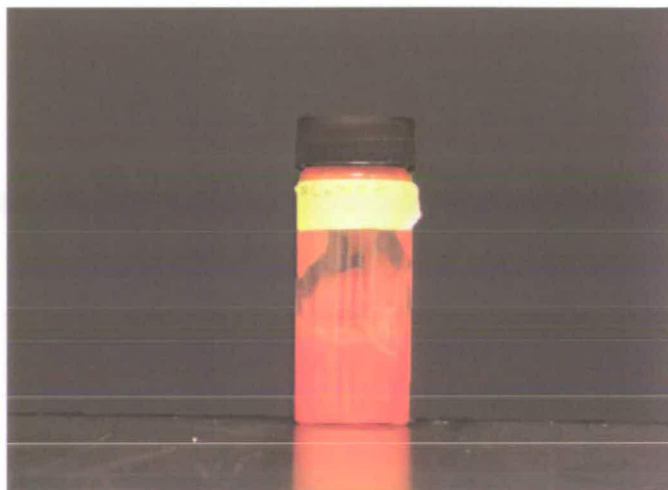


Figure 4.24: A picture of the emulsion E4 with a doping level of DCM in DMSO at 10^{-2} M.

4.3. Fluorescence of Emulsions

4.3.1. Fluorescence of doped O/W emulsions

Fluorescence measurements of both the doped formulations 1 (emulsion B3) & formulation 2 (emulsion D1) were carried out on the custom-built capillary flow cell setup described in 3.2.4 and shown in Figure 4.1. Three B3 emulsions were prepared in which the olive oil phase was doped with Bis-MSB at concentration 10^{-4} , 5×10^{-4} and 10^{-3} M, respectively. In the same way three D1 emulsions were prepared in which the o-xylene phase was doped with Bis-MSB at the concentration 10^{-3} , 5×10^{-3} and 10^{-2} M. Since there must be sufficient dispersion of the dye-doped droplets within the emulsion to ensure that the fluorescence measurements report the properties of individual droplets, not a continuous phase, the original bulk emulsions was diluted in water (1% vol. for formulation 1 and 0.1% for formulation 2) for fluorescence measurements.

The diluted emulsions were stable for the duration of the experiment and the fluorescence emission spectra measured for the two sets of emulsions are shown in Figure 4.25 and Figure 4.26.

A plot of the relative intensity against doping concentration for each emulsion set (Figure 4.27) shows a near-linear increase in the fluorescence intensity with

increasing dye concentration, which is an indication that no concentration quenching is occurring for Bis-MSB tracer droplets up to a concentration limit of 10^{-2} M in o-xylene and 10^{-3} M in refined olive oil.

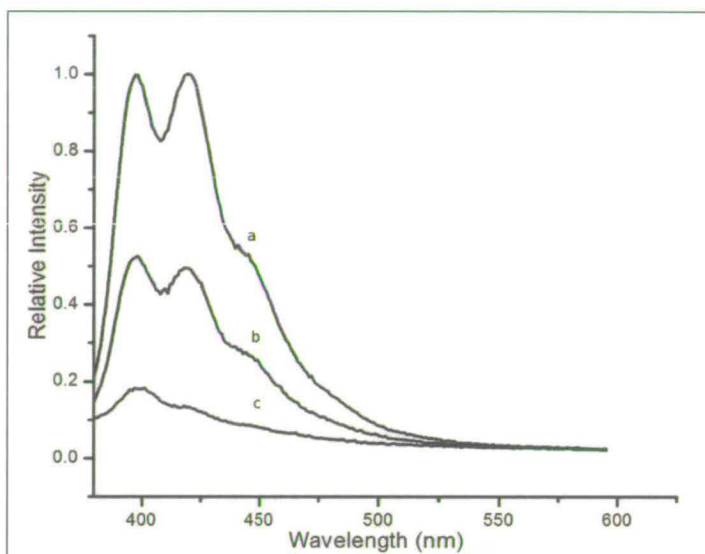


Figure 4.25: Fluorescence emission spectra of aqueous emulsions of $\sim 4 \mu\text{m}$ droplets of olive oil doped with Bis-MSB at a concentration of (a) 10^{-3} M, (b) 5×10^{-4} M and (c) 10^{-4} M. Intensities have been normalised to the maximum.

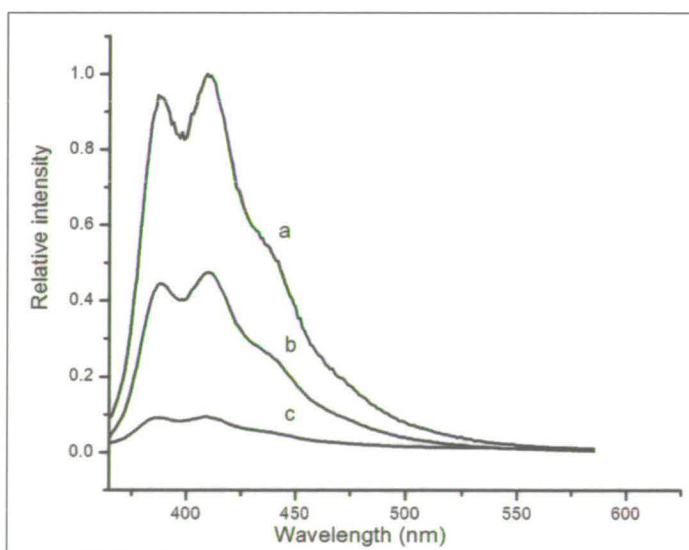


Figure 4.26: Fluorescence emission spectra of aqueous emulsions of $\sim 4 \mu\text{m}$ droplets of o-xylene doped with Bis-MSB at a concentration of (a) 10^{-2} M, (b) 5×10^{-3} M and (c) 10^{-3} M. Intensities have been normalised to the maximum.

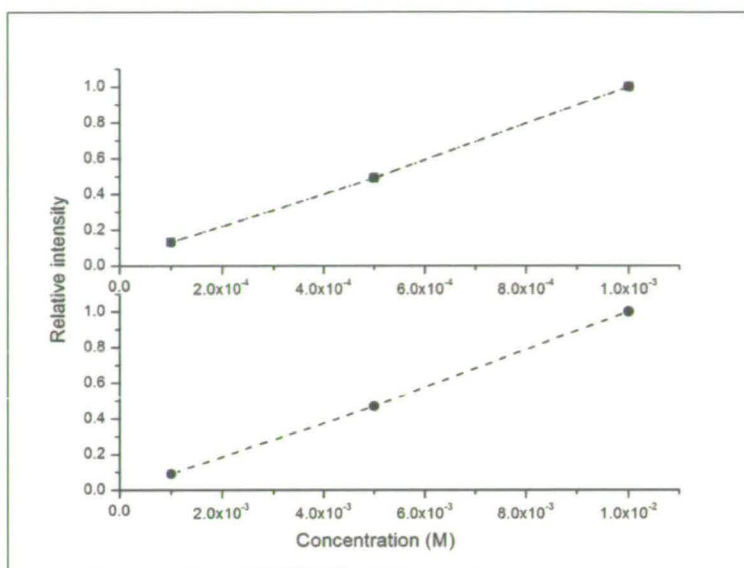


Figure 4.27: Plots of relative fluorescence intensity against Bis-MSB concentrations in olive oil (top) and o-xylene (bottom) droplets in diluted emulsion samples.

4.3.2. Fluorescence of doped W/O emulsions

In the same way as for O/W emulsions (section 4.3.1), fluorescence measurements of doped W/O emulsions were carried on the custom-built capillary flow cell setup. Three E4 emulsions were prepared in which the DMSO phase was doped with DCM at concentration 10^{-3} , 5×10^{-3} and 10^{-2} M, respectively. The emulsions were diluted at 1% vol. in PDMS and were stable for the duration of the experiment.

The fluorescence emission spectra measured for this set of emulsions are shown in Figure 4.28 and Figure 4.29 for 355 nm and 532 nm excitation, respectively.

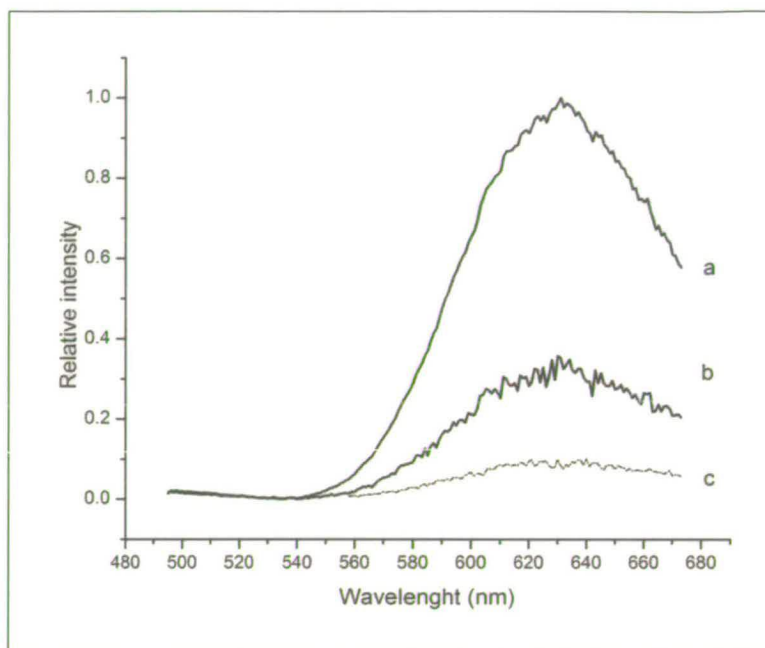


Figure 4.28: Fluorescence emission spectra of oil emulsions of $\sim 4 \mu\text{m}$ droplets of DMSO doped with DCM at a concentration of (a) 10^{-2}M , (b) $5 \times 10^{-3}\text{M}$ and (c) 10^{-3}M . Excitation a 355 nm. Intensities have been normalised to the maximum.

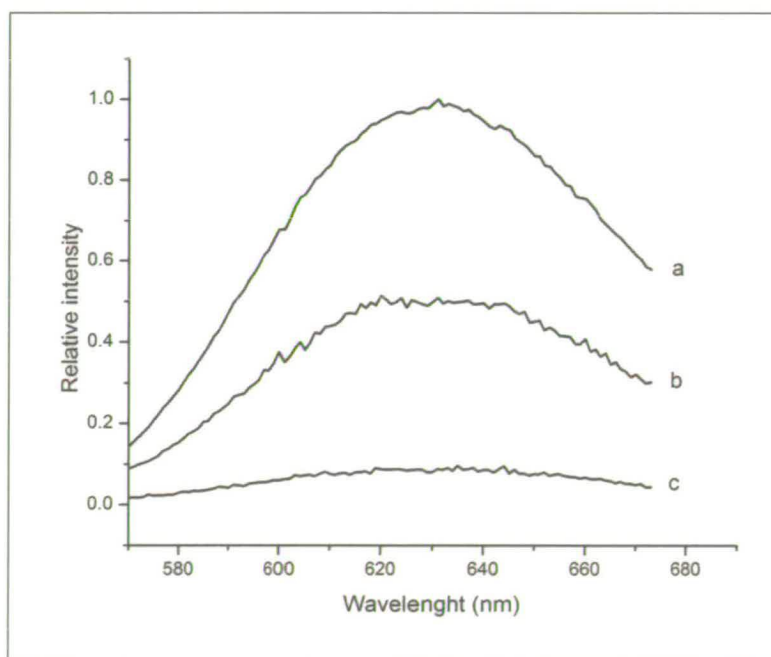


Figure 4.29: Fluorescence emission spectra of oil emulsions of $\sim 4 \mu\text{m}$ droplets of DMSO doped with DCM at a concentration of (a) 10^{-2}M , (b) $5 \times 10^{-3}\text{M}$ and (c) 10^{-3}M . Excitation a 532 nm. Intensities have been normalised to the maximum.

For emulsions excited at 355 nm, the fluorescence spectra (Figure 4.28) were found to be noisy with a weaker than expected fluorescence signals when compared with the sample excited at 532 nm. This can be explained by the low absorbance of DCM the UV, which results in a low fluorescence where ambient scattering (mainly reflections from the cell wall and multiples droplets scattering) are more marked. However, a near-linear increase in the fluorescence intensity with increasing dye concentration is obtained for samples excited at 355 nm (Figure 4.30–top).

For emulsion samples excited at 532 nm, none of the above observation are reported and a linear relationship is obtained for these samples (Figure 4.30–bottom).

Therefore, these results indicate that no concentration quenching is occurring in DCM tracer droplets for concentration in DMSO up to solubility limit of $\sim 10^{-2}$ M.

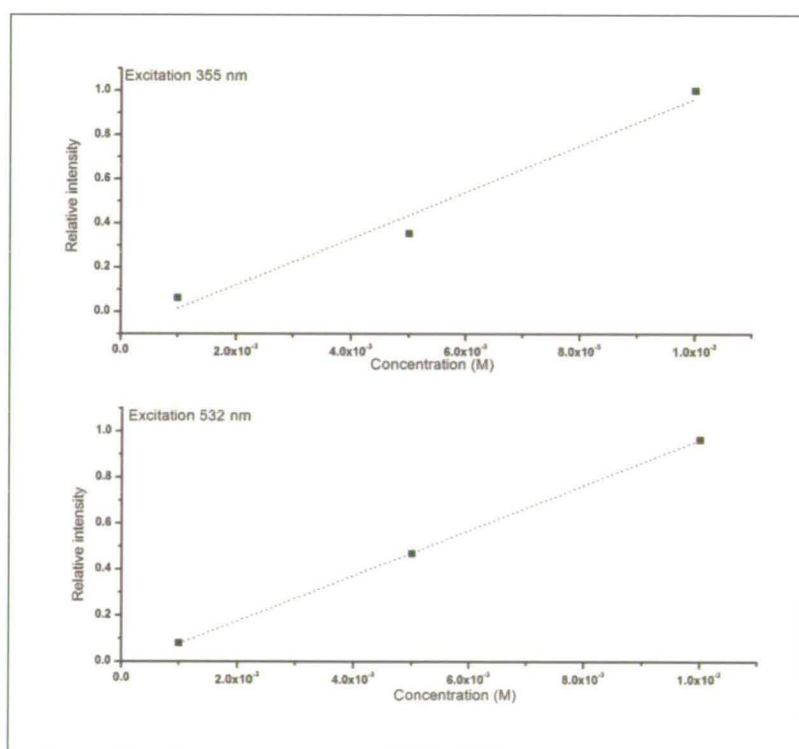


Figure 4.30: Plots of relative fluorescence intensity against DCM concentrations in DMSO droplets in diluted emulsion samples at 355 nm (top) and 532 nm excitation (bottom).

5. CONCLUSIONS

In this work, the importance of fluorescent tracers with optimised spectral properties for fluorescence–particle image velocimetry (FPIV) applications has been discussed. Amongst a set of candidate dyes, Bis-MSB and DCM were identified as suitable blue and red emitting fluorophores exhibiting high quantum yield and high solubility ($\sim 10^{-2}$ M) in *o*-xylene and DMSO, respectively.

A laboratory method, employing stabilised Pickering emulsions with micron-sized dispersed droplets ($\sim 4 \mu\text{m}$) has been devised for assessing and optimising the fluorescence properties of dye-doped droplets for use in particle imaging.

Using this method, quantitative fluorescence spectroscopy can be performed on micron-sized droplets at the high dye concentrations required for successful PIV measurements in gas phase flows. The obtained results have demonstrated that no concentration quenching effects are occurring in Bis-MSB and DCM for concentrations up to the solubility limit ($\sim 10^{-2}$ M) in their respective solvents. This also imply that in principle, even higher fluorescence intensity could be achieved, if a greater concentration could be attained.

6. REFERENCES

- 1 L. Gui, Merzkirch, W., in *Proceedings of the 7th International Conference on Laser anemometry advances and applications* (Karlsruhe, Germany, 1997).
- 2 K. Kiger and C. Pan, in *The third international workshop on PIV*, edited by R. J. Adrian (Santa Barbara, California), 1999), pp. 157.
- 3 K. T. Kiger and C. Pan, *J. Fluids Eng. Trans. ASME* **122** (4), 811 (2000).
- 4 J. Westerweel, D. K., and Y. M., in *49th Annual meeting of the division of fluid dynamics* (APS Syracuse, NY, 1996).
- 5 D. P. Towers, C. E. Towers, C. H. Buckberry, and M. Reeves, *Meas. Sci. Technol.* **10** (9), 824 (1999).
- 6 K. D. Driscoll, V. Sick, and C. Gray, *Exp. Fluids* **35** (1), 112 (2003).
- 7 W. Kosiwczuk, A. Cessou, M. Trinite, and B. Lecordier, *Exp. Fluids* **39** (5), 895 (2005).
- 8 M. C. Jermy and D. A. Greenhalgh, *Appl. Phys. B: Lasers Opt.* **71** (5), 703 (2000).
- 9 M. Stanislas and J. C. Monnier, *Meas. Sci. Technol.* **8** (12), 1417 (1997).
- 10 R. J. Lakowicz, *Principles of Fluorescence Spectroscopy*, 2nd ed. ed. (Kluwer Academic/Plenum Publishers, New York, 1999).
- 11 B. Valeur, *Molecular Fluorescence: Principles and Applications*. (Wiley-VCH, Weinheim, New York, 2002).
- 12 S. C. Hill, R. G. Pinnick, P. Nachman, G. Chen, R. K. Chang, M. W. Mayo, and G. L. Fernandez, *Appl. Opt.* **34**, 7149 (1995).
- 13 S. C. Hill, R. G. Pinnick, S. Niles, N. F. Fell, Y. Pan, J. R. Bottiger, B. V. Bronk, S. Holler, and R. K. Chang, *Appl. Opt.* **40** (18), 3005 (2001).
- 14 N. B. Kyriakidis and P. Skarkalis, *J. AOAC Int.* **83** (6), 1435 (2000).
- 15 G. A. Reynolds and K. H. Drexhage, *Opt. Commun.* **13** (3), 222 (1975).
- 16 E. J. Schimitschek, J. A. Trias, P. R. Hammond, R. A. Henry, and R. L. Atkins, *Opt. Commun.* **16** (3), 313 (1976).

- 17 G. Jones, W. R. Jackson, and A. M. Halpern, *Chem. Phys. Lett.* **72** (2), 391 (1980).
- 18 G. Jones, W. R. Jackson, S. Kanoktanaporn, and A. M. Halpern, *Opt. Commun.* **33** (3), 315 (1980).
- 19 S. Nad and H. Pal, *J. Phys. Chem. A* **105** (7), 1097 (2001).
- 20 H. Pal, S. Nad, and M. Kumbhakar, *J. Chem. Phys.* **119** (1), 443 (2003).
- 21 H. Furumoto and H. Cecon, *IEEE J. Quantum Electron.* **Qe 5** (6), 323 (1969).
- 22 J. T. Warden and L. Gough, *Appl. Phys. Lett.* **19** (9), 345 (1971).
- 23 T. E. Bush and G. W. Scott, *J. Phys. Chem.* **85** (2), 144 (1981).
- 24 J. Thipperudrappa, D. S. Biradar, S. R. Manohara, S. M. Hanagodimath, S. R. Inamadar, and R. J. Manekutla, *Spectrochimica acta Part A, Molecular and biomolecular spectroscopy* (2007).
- 25 P. R. Hammond, *Opt. Commun.* **29** (3), 331 (1979).
- 26 A. A. Turban, S. L. Bondarev, V. N. Knyukshto, and A. P. Stupak, *Journal of Applied Spectroscopy C/C of Zhurnal Prikladnoi Spektroskopii* **73** (5), 678 (2006).
- 27 S. L. Bondarev, V. N. Knyukshto, V. I. Stepuro, A. P. Stupak, and A. A. Turban, *J. Appl. Spectrosc.* **71** (2), 194 (2004).
- 28 W. Rettig and W. Majenz, *Chem. Phys. Lett.* **154** (4), 335 (1989).
- 29 B. P. Binks, *Modern aspect of emulsion science*. (Royal Soc. Cambridge Inf. services 1998).
- 30 B. P. Binks and S. O. Lumsdon, *Phys. Chem. Chem. Phys.* **1** (12), 3007 (1999).
- 31 B. P. Binks and C. P. Whitby, *Langmuir* **20** (4), 1130 (2004).
- 32 B. R. Midmore, *Colloids and Surfaces a-Physicochemical and Engineering Aspects* **132** (2-3), 257 (1998).
- 33 B. P. Binks and C. P. Whitby, *Colloids Surf., A* **253** (1-3), 105 (2005).
- 34 B. P. Binks, J. A. Rodrigues, and W. J. Frith, *Langmuir* **23** (7), 3626 (2007).

- 35 R. Aveyard, B. P. Binks, and J. H. Clint, *Adv. Colloid Interface Sci.* **100**, 503 (2003).
- 36 E. Melzer, J. Kreuter, and R. Daniels, *European Journal of Pharmaceutics and Biopharmaceutics* **56** (1), 23 (2003).
- 37 K. Hayakawa, M. Kawaguchi, and T. Kato, *Langmuir* **13** (23), 6069 (1997).
- 38 K. Yonekura, K. Hayakawa, M. Kawaguchi, and T. Kato, *Langmuir* **14** (12), 3145 (1998).

CHAPTER 5: OPTIMISED FLUORESCENT TRACERS FOR MULTI-CONSTITUENT PIV

1. INTRODUCTION

As PIV has become a powerful tool for measuring fluid velocity owing to its non-intrusive nature¹, one of the challenging application areas for its implementation is in the quantification of multi-phase and multi-constituent flows² (see Chapter 2). The application of conventional PIV techniques to such flows generates images from the tracers in both constituents or phases which does not allow quantification of the flow fields in each component of the flow and hence further parameters such as relative velocity and mixing cannot be quantified.

Previously, flow phases have been discriminated based on particle image size³, or brightness⁴. These techniques require a particle size ratio of ~ 5 for reliable processing⁴. In the case of sprays injected into the gas phase the particle size range of the droplets may extend from the sub-micron to 10 microns and therefore overlaps the micron sized particles typically added to the gas phase⁵. Typical examples are fuel sprays for combustion in automotive and gas turbine engines, agricultural sprays and metered dose inhalers. Furthermore, there are multi-constituent gas phase flows where mixing is important and in such cases both components will need similarly sized seed particles to achieve adequate flow following. Hence flow constituent discrimination by particle size or brightness is not feasible.

In such situations, optically active tracers, normally producing a fluorescent or phosphorescent emission over a range of wavelengths different from that of the illuminating laser beam, provide a means of identifying the origin of a particular tracer particle. Whereas fluorescence persists for only 10–100 ns after excitation,

phosphorescence is much longer lived. These tracers thus emitted phosphorescence for a measurable time after exposure, with the brightness gradually reducing, allowing the direction of the velocity vector to be inferred from a single exposure photograph. Automated analysis was never achieved with this technique and no quantitative data produced.

On the other hand, fluorescent tracers are the mechanism of choice to differentiate the seeding in one phase from that in another in multi-phase and multi-constituent flows gas phase PIV. Two groups have addressed the problem with regard to gasoline direct injection (GDI) sprays using 532 nm laser light sheets with conventional tracers in one phase and fluorescent tracers in the other^{6,7}. The emission spectrum of the fluorescent dopant was selected to be separate from the excitation and hence combinations of filters were used on a pair of monochrome CCD cameras, positioned 180° opposite each other such that each camera only produced images of one type of tracer. Whilst multi-phase velocity vectors were produced, the data suffered from either poor validation rates⁶ or required the phases to have differing velocities⁷ implying that the optical discrimination of the fluorescent tracers from the conventional tracers was not completely successful. In a previous work, Towers *et al.*⁸ used rhodamine-doped droplets and conventional tracers illuminated with a first pulse at 532 nm and a second from a pulsed dye laser at ~ 640 nm. Images were obtained on 2 monochrome cameras with filters, such that one camera only imaged the 2nd pulse and fluorescence emission, with the other recording Mie scattering from the first pulse. By performing logical operations between the images, based on the presence or absence of co-located fluorescence at the same pixel location as the green Mie scatter, it was possible to obtain separate fields for the first pulse tracers for each constituent of the flow. However, the efficiency of the dyes was insufficient to allow fluorescent droplets of <5 µm to be imaged when using 532 nm for both excitation source, requiring high energy >100 mJ, and for Mie imaging, which only requires low energy 1-3 mJ.

All the gas phase multi-constituent and multi-phase flow work reported depends on image processing algorithms to separate the flow constituent information from the two cameras. Therefore, sub-pixel registration is important to increase the reliability of processing, but is experimentally difficult, owing to the different distortions introduced by the filters used on each camera. Furthermore, constituent discrimination errors are introduced when particle images from the two constituents overlap.

Considering that no reliable data has been obtained on two-phase flows with the available techniques, a novel strategy for multi-constituent flow measurement in the gas phase is presented here. It consists in an all solid-state laser, a single 3-chip colour camera and two optimised fluorescent tracers with widely different emission bandwidth. For each constituent of the flow, a fluorescent dye was chosen to emit light at a particular wavelength in order to discriminate between the types of tracer particle and hence flow constituent. The adopted approach is to exploit the inherent co-registration offered by a 3-chip color CCD camera with the images recorded in the 3 color planes, enabling flow constituent / phase to be determined as well as pulse order.

2. FLUORESCENT TRACER SELECTION AND IMAGING SYSTEM

The desired properties of the fluorescent dyes in these applications are strong absorption at 355 nm (frequency tripled Nd:YAG), high quantum efficiency, large Stokes shift (Chapter 2) and a fluorescence bandwidth situated in the high sensitivity range of silicon based CCD cameras. For use with colour cameras in the multi-constituent PIV experiments described here, it is desirable for the fluorescence emission bandwidth to be contained within one of the primary colour bands corresponding to a detection channel of the colour CCD, and for there to be sufficient chromatic separation between the illumination and the fluorescence and between the fluorescence and any wavelengths used for Mie scattering.

In chapter 4, Bis-MSB was found to be the best UV-excitabile candidate dye for blue emission and it was shown that concentration quenching effects were absent for concentration up to 10^{-2} M in *o*-xylene. In the same chapter DCM, which emits in the red (620-660 nm region) when excited at either 355 nm or 532 nm, was also found to show no concentration quenching effects for concentration up to 10^{-2} M in DMSO. Consequently, DCM tracers can be used in one flow constituent whilst the Bis-MSB tracers is used in the other. Simultaneous excitation of both dyes can be achieved using 355 nm excitation from one Nd:YAG cavity (Figure 5.1), giving chromatically separate images in the blue and red channels of a colour camera, thereby achieving flow constituent discrimination. A second pulse at 532 nm will generate Mie scatter signal from both types of tracers in the green channel and a red signal for the constituent tagged with DCM. Cross-correlation between the red and green layer should produce vectors for one constituent, while between the blue and green layer the vectors for the other constituent. The phase/constituent tagging strategy is summarised in Table 5.1.

Dopant/constituent	355 nm (1 st pulse)		532 nm (2 nd pulse)	
	Bis-MSB	DCM	Bis-MSB	DCM
Red channel		●		●
Green channel			●	●
Blue channel	●			

Table 5.1: Flow constituents tagging strategy.

The 3-chip colour CCD Hitachi HV-F22F digital camera utilised in this work internally separates the imaged light into bandwidths of red, green and blue that are directed to the appropriate CCD chip. This allows three co-aligned images to be recorded simultaneously.

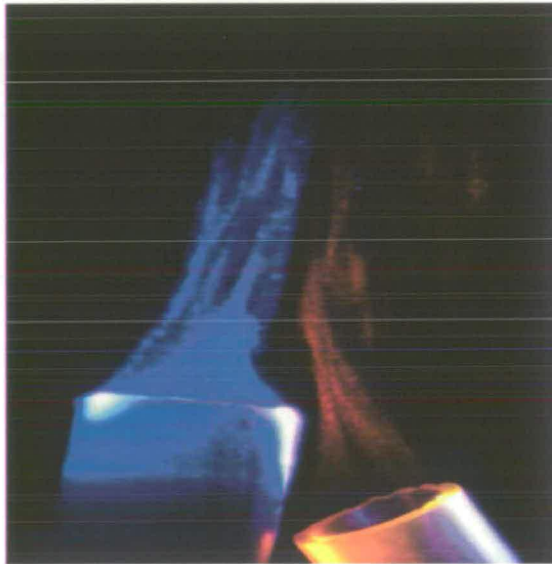


Figure 5.1: An image of the experimental flow, where both the Bis-MSB and DCM doped tracer droplets are illuminated using a sheet of laser light at 355 nm.

3. EXPERIMENTAL

3.1. Material

O-Xylene, Dimethyl sulfoxide (DMSO) and the fluorescent dyes: 1,4-Bis(2-Methylstyryl)Benzene (Bis-MSB, MW= 310.44 g/mol) and 4-Dicyanmethylene-2-methyl-6-(*p*-dimethylaminostyryl)-4H-pyran (DCM, MW= 303.36 g/mol) were obtained from Aldrich. All the materials were used as received without further purification and the solvents were of spectrophotometric grade or equivalent.

3.2. Experimental

3.2.1. Laser light sheet formation

The experimental setup is shown in Figure 5.2 Two single-cavity pulsed Nd:YAG lasers (Continuum Surelite II-10) which were fitted with frequency doubling and tripling crystals, gave a first pulse of 355 nm light and a second one at 532 nm. The pulses separation was set at 50 μ s using a delay box.

It was found that standard high reflectivity dielectric mirrors did not remove the entire second harmonic from the 355 nm pulse; this caused initial problems of crosstalk in the information between the colour channels. The problem was overcome by using a dispersive fused silica 15 mm equilateral prism (Comar) (1, Figure 5.2) to separate the harmonics by refraction.

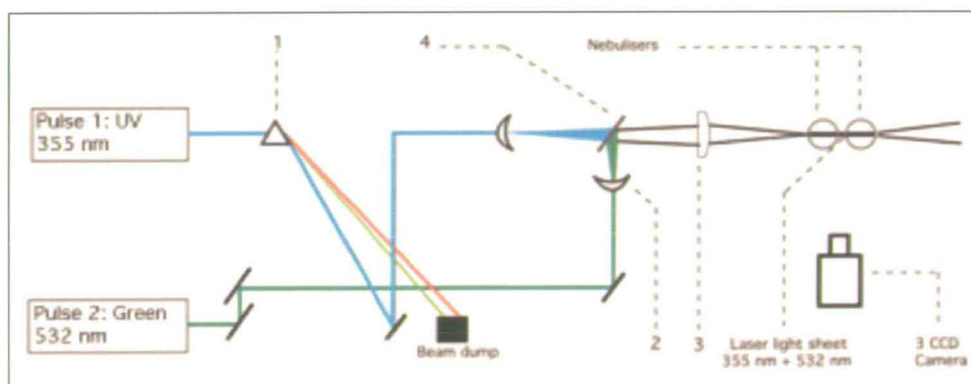


Figure 5.2: Experimental setup (see in text for captions).

The laser beams were formed into light sheets to illuminate the flows using a combination of a negative (2) spherical and positive (3) cylindrical lens.

In order to align the sheets of both wavelengths it was necessary to expand each beam at different distances relative to the cylindrical lens. Expanding plano-concave ($f=-200$ mm) (2) lenses were positioned in each beam and mounted on micro-blocks, giving 3-axes of linear adjustment, to aid the alignment. The beams then met at a 532 nm dichroic mirror (4), which was clear backed, allowing the 355 nm beam to pass through unhindered. The co-aligned expanding beams were directed through a fused silica plano-convex cylindrical lens ($f=300$ mm) (3) to produce a laser sheet of height ~ 30 mm at the focus.

3.2.2. Laser light sheets alignments

The exact alignment of the two light sheets was critical; a JAI CV-A50 1 camera, protected by a neutral density (ND) filter, was placed directly in the sheet. This setup also allows the measurements of the beam profile, thickness and sheet positioning.

3.2.3. Seeding methodology and imaging

Solutions of Bis-MSB in *o*-xylene and DCM in DMSO at 10^{-2} M were prepared by dissolving the required amount of dye powder in its respective solvent. The resulting suspension was then immersed in an ultrasonic bath (50 Hz, Fisherbrand) for up to 30 minutes to ensure full solubilisation of the dye.

The solutions were drawn through separate pressure-driven medical nebulisers (Med2000 Andy Flow) into the sheet. A regulator attached to a N_2 cylinder allowed the pressure and hence seed density to be varied. The atomised droplets were removed from the laboratory environment using an extraction system.

Images were recorded onto a Hitachi HV-F22F 3-chip colour camera and focused by a Nikon 105 mm lens at $f^{#}11$. Brightness and sharpness on the camera were adjusted to reduce background noise level and due to a reduced sensitivity on the red channel (maximum of ~ 0.6 compared to green channel due to the presence of an IR blocking filter) the red gain was increased with all the other options left unchanged. The

camera was used with a resolution of 1280 x 960 pixels and the pixels are 4.65 μm square. The lens aperture was set slightly more closed than in most PIV experiments ($f^{\#}11$) to give sharply focused images in all 3 colour channels, i.e. to overcome any longitudinal chromatic aberration from the imaging optic and manufacturing tolerance on positioning of the CCD chips in the camera.

3.2.4. Tracers droplets sizing

Tracer particle sizing was performed in order to verify that the optimised fluorescently doped tracers were appropriate for satisfactory flow tracking. Each of the nebulisation solutions, 10^{-2} M Bis-MSB in *o*-xylene and 10^{-2} M DCM in DMSO, were drawn through a pressure-driven medical nebuliser (Med2000 Andy Flow) into a 532 nm light sheet and using the same seeding pressure and experimental conditions as those later used for the acquisition of PIV images. The seed density was controlled by a pressure-regulated flow of nitrogen.

An interferometric particle imaging (IPI) setup was developed^{9,10} in which the light directly reflected from the droplet surface and the first-order refracted beam interfere across a de-focused droplet image. Numerical analysis shows that the number of interference fringes across the image is proportional to the droplet size. The experimental setup was formed to give approximately equal intensity of reflected and first-order refracted beams at a scattering angle of 70° and a camera (LaVision Flowmaster 3) was used with a Nikon Plan 20X (NA 0.4) ELWD microscope objective.

Conversion relationships between the number of interference fringes and the drop size are available in the literature¹¹ and have been applied to the imaging setup giving a value of approximately 1.5 fringes per micron. A schematic experimental setup is described in Figure 5.3.

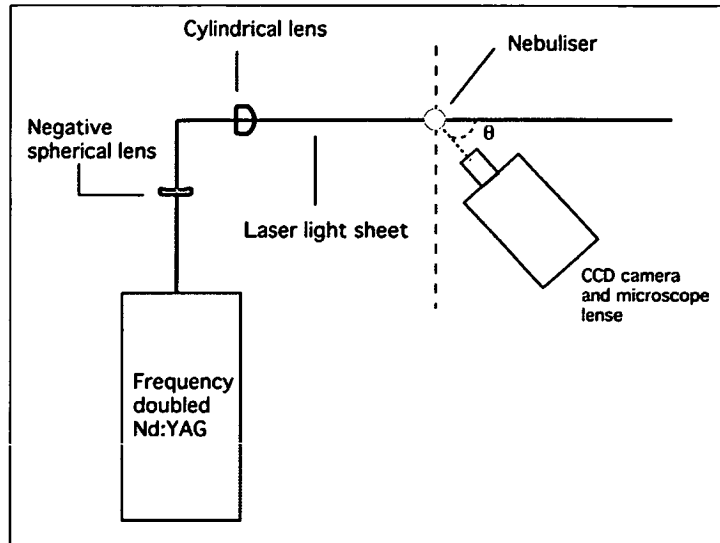


Figure 5.3: Schematic set-up for the interferometric droplet sizing experiment.

4. RESULTS AND DISCUSSIONS

4.1. Light Sheet alignments and Beam Profile

The captured beams images were processed by Towers at Leeds University using the Matlab package (The MathWorks, Inc) in which the *improfile* function allowed to obtain the thickness and intensity profiles of the beams (Figure 5.4). In this image, both laser pulses are visible, the thicker sheet shown is the green pulse, inside which is the 355 nm sheet. The intensity of the laser sheets was significantly reduced to obtain this data (to prevent permanent damage to the camera).

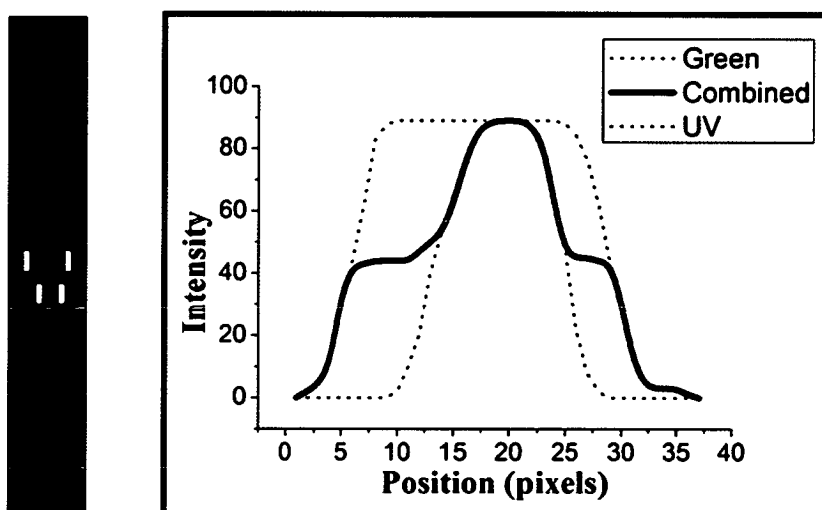


Figure 5.4: Left- Laser Light Sheet imaged on JAI CV-A50, marks show edges of 532 nm (outer) and 355 nm (inner) laser sheets. Right- UV, green and combined horizontal intensity profile (Towers *et al.*).

Because of the difference in sheets thicknesses, the differential error due to the out-of-plane particle's motion between UV and green excitations in the overall 2D velocity field data must be considered. However, it is expected that the laser sheets are more similar in thickness due to the difference in camera sensitivity at the two wavelengths used and the differential error negligible. Moreover, the use of the alignment camera ensured that the centre of each sheet were precisely co-aligned.

4.2. Drop sizing

The fluorescence emission of micron sized droplets, typically used in gas phase PIV for adequate dynamic response, was analysed by exciting both types of tracers simultaneously with a 355 nm pulse. Initial examination of the images recorded showed that Bis-MSB (blue) tracers had sufficient signal-to-noise ratio whereas images from DCM (red) tracers did not. In order to ensure reliable vector processing, a wider drop-size distribution (larger mean drop size) was used for the red tracers by changing the nebulising conditions such that a higher fluorescence signal was obtained on the red channel.

The droplet size distribution using the interferometric method for each solution is shown in Figure 5.5. The mean droplet sizes for Bis-MSB and for DCM was found to be $1.04\ \mu\text{m}$ and $2.25\ \mu\text{m}$, respectively.

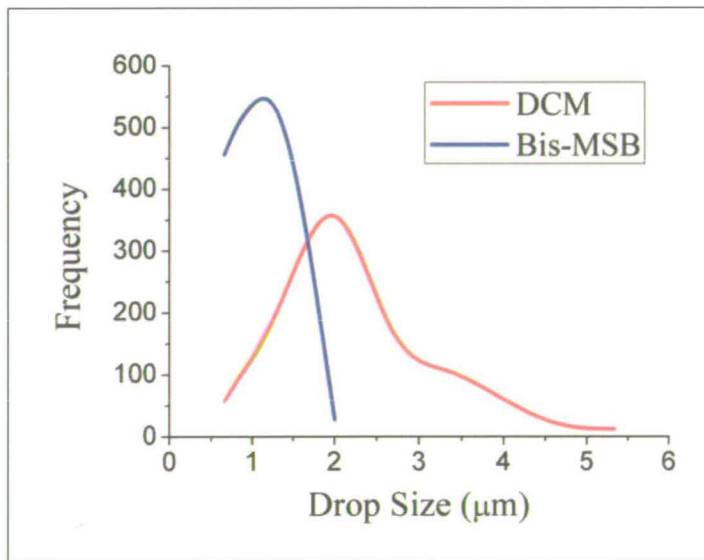


Figure 5.5: Drop size distribution of Bis-MSB and DCM seed droplets (Towers *et al.*).

The drop size distribution for the DCM (red) tracers spans from 1 to 5 μm but it needs to be established which part of the size distribution is recorded by the colour camera on the red channel.

Small particles ($<2\ \mu\text{m}$) will have a considerably lower fluorescence intensity than larger ones ($2\text{-}4\ \mu\text{m}$), due to the power law dependence on particle diameter of the fluorescence signal (expected to be between a quadratic and cubic relationship). For this range of tracer sizes the particle image size is dominated by the diffraction-limited performance of the imaging optic, hence the particle image diameter is approximately constant at $1.8\ \mu\text{m}$ (approximately 6 pixels) for the magnification used (20X). The particle images across the size range of all of the tracers therefore appear with an approximately uniform size and a Gaussian intensity profile of varying intensity for each color channel. Furthermore, to remove crosstalk between the colour channels (see section 4-3), particles with low signal-to-noise ratio will be removed so the bigger droplets are the ones actually contributing to the cross-correlation process.

To quantify the fraction of the DCM-doped tracers with detectable fluorescence, two sets of images of the tracers were recorded separately on the red (fluorescence, 355 nm pulse) and green (Mie, 532 nm pulse) channels using the same seeding pressure of 0.35 bar. It is assumed that the 532 nm laser sheet energy is sufficient to make the entire distribution of tracers visible in the green layer of the colour camera.

A Matlab code was developed by Towers at Leeds University to count the number of particles visible in an image. The ratio of number of red to number of green particles is an indicator of the part of the droplet size distribution being recorded, as only the bigger, more intense red particles will be captured. Based on a particle count evaluated over 30 green and red images an average of 73% of the particles present have sufficient fluorescence intensity to be imaged, indicating that approximately three quarters of the DCM droplet size distribution is recorded on the red channel under experimental conditions. Figure 5.6 shows the cumulative distribution of DCM drop size, highlighting the part of the distribution that is being recorded. Hence the mean drop size of the visible DCM doped tracers was evaluated to be $2.65\ \mu\text{m}$.

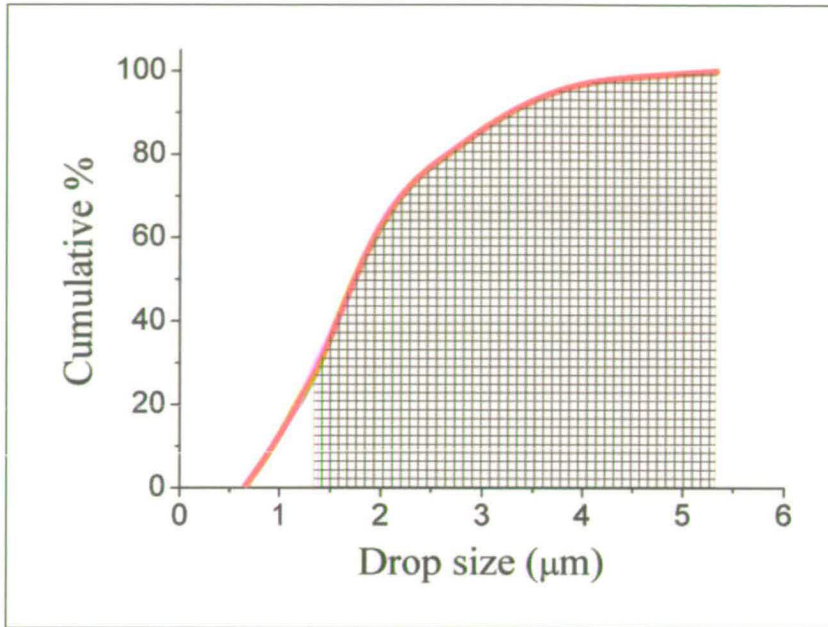


Figure 5.6: Cumulative drop size distribution for DCM tracers highlighting the size range visible on the red channel of a Hitachi HV-F22F 3-chip colour camera (Towers *et al.*).

4.3. Cross-Talk Elimination

In most colour CCD cameras the spectra of the red, green and blue channels are designed to overlap so that there are no colour-blind areas. However, this can also lead to crosstalk between colour channels, for example a ‘red’ fluorescent image produced a low signal in the blue and green channels. In this configuration the most damaging crosstalk is that between the red and blue images representing the separation of the images from the two flow constituents. The green channel still contains low level crosstalk from the other channels and the red and blue channels some low level crosstalk from the green Mie scattering. The potential for the DCM doped tracers to emit red fluorescence from the 532 nm pulse could also generate crosstalk but given the low pulse energy needed to produce the Mie scattered images this is expected to be at a suitably low level.

A typical image obtained from the system is shown in Figure 5.7. In this case the two seeding streams are largely spatially separated, with the Bis-MSB -doped (blue) tracers on the right and the DCM (red) tracers on the left. The image was illuminated

using a pulse of 532 nm followed 50 μ s later by a 355 nm pulse. Careful examination shows green to red particle pairs on the left hand side and green to blue image pairs on the right, with both flows going from the bottom to the top of the image.

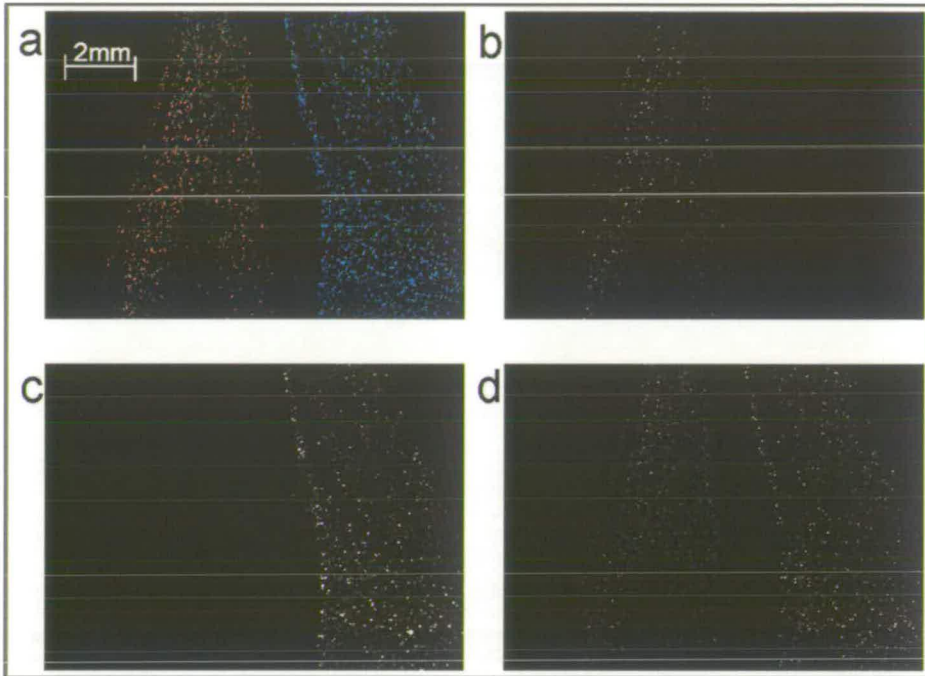


Figure 5.7: RGB image (a) of spatially separate flow streams seeded with DCM doped tracers (left side of image) and Bis-MSB doped tracers (right side). Crosstalk compensated RGB component images are given in greyscales, red: b, blue: c and green: d. Illumination by 532 nm and 355 nm light sheets with pulse separation 50 μ s.

Figure 5.7 shows the original colour image (upper left) and the three separate colour channels shown in grey scales (image splitting was performed in Matlab).

Crosstalk levels can be reduced using an approach initially applied in 3D surface contouring applications using colour imaging¹². This method was then adapted and a Matlab code written by Towers at Leeds University to obtain a quantitative evaluation of crosstalk between colour channels with 3-chip colour CCD cameras for 3D shape measurements¹³. Using this approach the coupling effects can be estimated for each channel respectively as the percentage of the intensity from a particular channel that is detected in the other two channels. For example, for an image in the

red channel, C_{rg} and C_{rb} represent the intensities detected in the green and blue channels expressed as a percentage of the intensity on the red channel. A similar process is used for the other two channels to define the coupling matrix as proposed by Zhang et al.¹³:

$$\begin{bmatrix} C_{rr} & C_{rg} & C_{rb} \\ C_{gr} & C_{gg} & C_{gb} \\ C_{br} & C_{bg} & C_{bb} \end{bmatrix} \quad (5.1)$$

The first suffix for each term indicates the channel of the original image and the second suffix indicates the channel of the detected image. Elements along the diagonal are 1, i.e. $C_{rr}=C_{gg}=C_{bb}=1$.

Images were taken separately of fluorescence emission from both types of tracers (red and blue) and Mie scattering (green) under experimental conditions. Each colour image was split into its RGB channels and a pixel-wise background subtraction performed on each channel. Greyscale intensity of particles in each image was measured on the three channels to obtain the crosstalk coefficients and the coupling matrix in Equation 5-1:

$$\begin{bmatrix} 1 & 0.17 & 0.2 \\ 0.43 & 1 & 0.2 \\ 0.1 & 0.02 & 1 \end{bmatrix} \quad (5.2)$$

Equation 5.2 shows the coupling effects for the experimental setup used. There is a strong coupling effect between the green and the red channels and the green and the blue channels. By inverting the coupling matrix a set of corrected RGB intensities can be determined from a set of measured intensities pixel-wise across the image, thereby accounting for the crosstalk. The method was applied to a raw camera image and the results are shown in Figure 5.7 where crosstalk between colour channels has been considerably reduced. Care was taken in capturing the PIV images from the flow field and in measuring the coupling effects to ensure that the intensities were maintained within the linear range of the camera.

DaVis version 7 from La Vision was used for data processing and cross correlation analysis. A pre-processing stage was employed to perform a background subtraction

of 15 grey scales to remove any residual low level crosstalk and also reduce background noise particularly on the blue channel.

4.4. Image corrections

Chromatic and lens distortions were accounted for in two stages. Firstly, images taken of a white-light-illuminated calibration plate were used to remove the distortions in each colour channel independently with the image de-warping tool in DaVis. Secondly, it is also necessary to estimate the distortions due to the combination of the offset between each of the three colour channels within the camera (since they are not exactly co-aligned) and chromatic lens distortions. For example, taking the green channel as the reference, there is a small offset from the green to the red and from the green to the blue images which produces false displacements on the vector maps.

A simple correction procedure was used in which images taken of a white-light-illuminated rough continuous surface were used to ensure that vectors would be obtained in every interrogation window across the whole field of view. Images were split into RGB channels using Matlab and pairs of images (red to green and blue to green) were cross-correlated in DaVis 7.2 using the same calculation parameters as those later used for the vector calculation of the flow constituents.

The validity and repeatability of the correction procedure were assessed. Different surfaces were used under the same illumination conditions and the maximum difference in displacement in any interrogation region was found to be 20% with the overall offset pattern unchanged for different surfaces. Once a surface had been selected the repeatability was tested by using different light levels. The maximum difference of the average displacement was found to be 4% for different light levels. An average offset of 0.3 pixels was obtained between the red and green images and 0.75 pixels between the blue and green images. The displacements obtained in each interrogation window are then subtracted from the vector maps for the corresponding flow constituent to account for any false displacements.

4.5. Flow Field Velocity Vectors

Following image distortion and crosstalk correction, the data were imported as double frames for green to red and green to blue. Background subtraction was performed and the adaptive multi-grid cross-correlation algorithm in DaVis employed to obtain the velocity vectors for each flow constituent. Finally, the vector fields corresponding to the chromatic distortion and CCD positioning offsets were removed. The resulting vector fields are shown colour coded for each flow constituent in Figure 5.8 corresponding to the RGB image shown in Figure 5.7. In this vector field it is clear that the crosstalk compensation has been successful and spatially separate regions corresponding to each tracer type have been obtained.

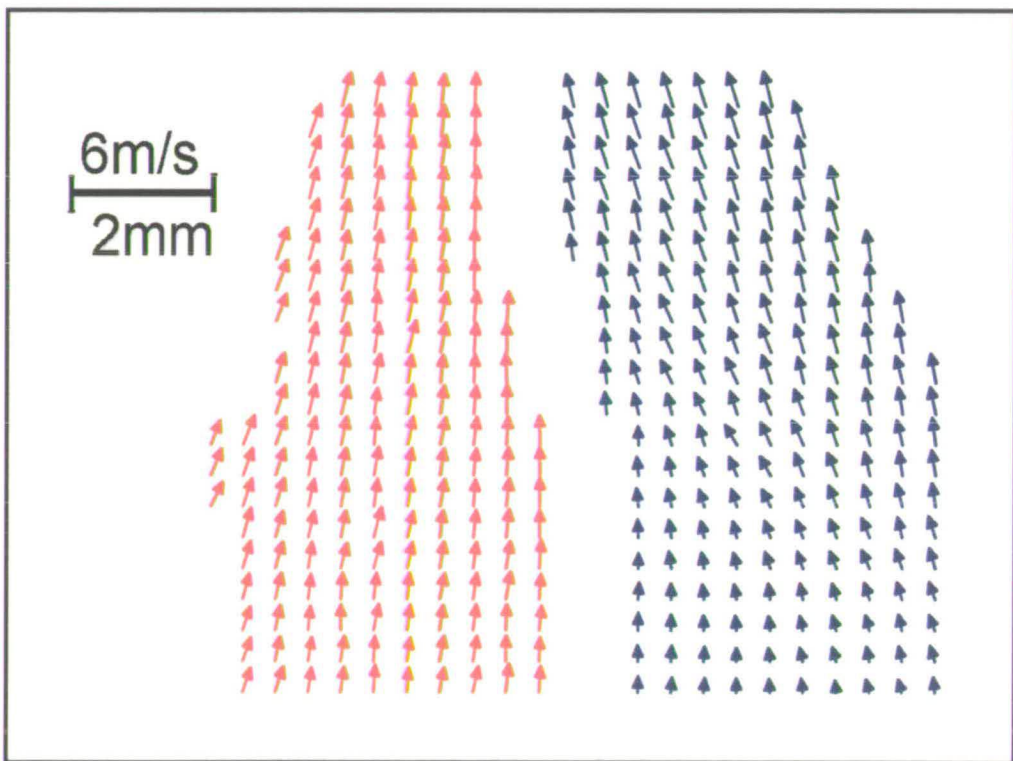


Figure 5.8: PIV vectors found from cross correlation of the data in Figure 5.7. Red vectors from DCM-doped tracers, blue vectors Bis-MSB-doped tracers (Towers *et al.*).

A second example is shown in Figure 5.9, where the flow, generated using four nebulisers (2 for each type of tracer) was brought together using a suitable pipe

before being imaged. This produced a densely seeded image with abundant constituent mixing throughout. The measured region is sufficiently downstream for the two constituents to be considered as well mixed. The vector map is presented in Figure 5.10 showing abundant clear regions of mixed flow where the blue vectors are thicker so that the interrogation regions with vectors from both types of tracers can be easily identified.



Figure 5.9: A second example of a multi-constituent flow. The RGB image shown was produced by illumination with 532 nm and 355 nm laser light sheets and a pulse separation of 50 μ s.

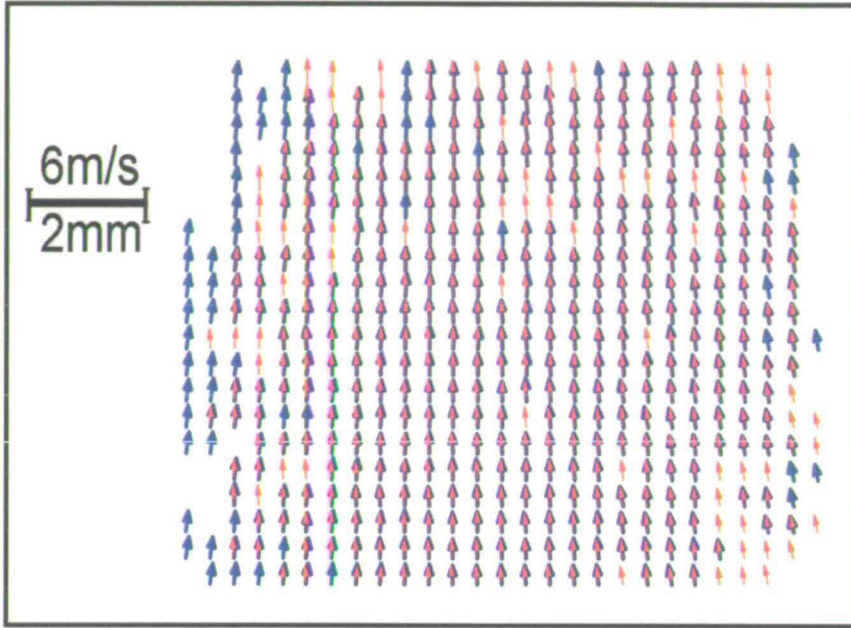


Figure 5.10: PIV vectors found from cross correlation of the data in Figure 5-8. Red vectors from DCM-doped tracers, blue vectors Bis-MSB-doped tracers (Towers *et al.*).

The validity of the vector fields obtained was assessed using the post processing stage in DaVis in which a median filter and a ratio-threshold for the different peaks on the correlation plane were used to discard spurious vectors.

The vector fields in Figure 5.10 were analysed to ensure they are not biased towards integer values due to peak locking effects. DaVis 7.2 provides a numerical estimation of the peak locking effect^{*,15} based on the histograms of the velocities in the x and y directions which were found to be well below the acceptable level of peak locking effects (values of 0.024 and 0.03 were obtained for the Bis-MSB and DCM doped tracers, respectively).

A quantitative comparison of the velocity vectors in each constituent has been generated by taking the resultant velocities (the magnitude of the 2-component vector) from each interrogation region. By sorting the resultant velocities in

* Peak locking is a bias error. The uncertainties associated with PIV measurements can be classified into two categories: random error and bias error. The influence of random error can be reduced by statistical analysis using a sufficiently large ensemble set. The bias error, on the other hand, may still contaminate the results even after averaging, and typically generates a semi-regular, deterministic pattern in averaged results. (Reproduced from reference 14)

ascending order for one constituent (DCM) and plotting the magnitude a continuous distribution is obtained in Figure 5.11.

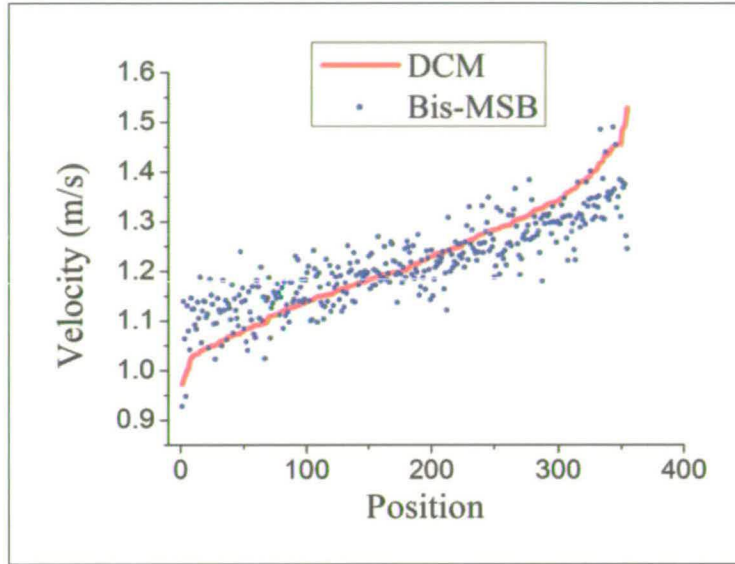


Figure 5.11: Resultant velocity comparison for vector field in Figure 9 with DCM-doped (red) and Bis-MSB-doped (blue) tracers (Towers *et al.*).

The ‘position axis’ refers to locations where vectors in both constituents were obtained and such that the magnitude of the velocity is increasing. The corresponding resultant velocity magnitude for the Bis-MSB tracers is plotted as points for the same positions as for the DCM tracers. It is clear that there is a good correspondence in the velocities measured at the same spatial position in the image.

The average difference between the resultant velocity calculated between both types of tracers was found to be 0.25 pixels (0.046 m/s) equivalent to approximately 3.96% of the average displacement across the image.

As discussed above, larger droplets were required for DCM tracers (red) to ensure the data obtained were reliable. The limiting factors for the recording of red fluorescence are the reduced sensitivity on the red channel (compared to the blue and green channels) of the camera used and the aperture required ($f^{\#} 11$) for a sharp focus on the three colour planes. DCM tracers produced with a Laskin nozzle

(monodisperse droplets, mean size 1 μm) were tested separately with an Imager Intense camera (LaVision, a cooled but not intensified camera) and focused with the same Nikon 105mm lens. The particle images obtained were sufficiently bright to provide reliable PIV data.

5. CONCLUSIONS

Flow direction, displacements and associated velocity vectors have been measured successfully in a multi-constituent gas phase flow using a single 3-chip colour CCD camera and solid state lasers. Direct quantification of the fluid mixing velocities has been achieved and pertinent correction procedures have been implemented to reduce the effects of crosstalk and CCD offset.

The use of optimised fluorescent tracers at high dye concentrations and free from concentration quenching effects allowed to produce seed droplets with strong fluorescence intensity signal which permitted to obtain tracers images with low SNR for cross-correlation analysis. The development of Bis-MSB (blue emitting) and DCM (red emitting) based tracers that are excitable using either frequency doubled or frequency tripled pulses from an Nd:YAG laser, will enable a wide range of flare removal (see Chapter 6) and multi-phase/constituent flow experiments to be performed with standard solid state lasers.

The use of a 3 CCD camera for multi-constituent and multi-phase flows can also be extended to obtain three components of the velocity vector by adding a second colour camera in a stereoscopic imaging setup. This approach would be simpler to implement compared to the conventional method of multiple cameras for each stereo view with different optical filters.

6. REFERENCES

- 1 R. J. Adrian, *Annual Review of Fluid Mechanics* **23**, 261 (1991).
- 2 Y. A. Hassan, in *The Handbook of Fluid Dynamics*, edited by R. W. Johnson (CRC Press, Boca Raton, Fla., 1998).
- 3 M. L. Jakobsen, W. J. Easson, C. A. Greated, and D. H. Glass, *Meas. Sci. Technol.* **7** (9), 1270 (1996).
- 4 K. T. Kiger and C. Pan, *J. Fluids Eng. Trans. ASME* **122** (4), 811 (2000).
- 5 A. Melling, *Meas. Sci. Technol.* **8** (12), 1406 (1997).
- 6 T. Boedec and S. Simoens, *Exp. Fluids* **31** (5), 506 (2001).
- 7 G. Rottenkolber, J. Gindele, J. Raposo, K. Dullenkopf, W. Hentschel, S. Wittig, U. Spicher, and W. Merzkirch, *Exp. Fluids* **32** (6), 710 (2002).
- 8 D. P. Towers, C. E. Towers, C. H. Buckberry, and M. Reeves, *Meas. Sci. Technol.* **10** (9), 824 (1999).
- 9 N. Damaschke, H. Nobach, T. I. Nonn, N. Semidetnov, and C. Tropea, *Exp. Fluids* **39** (2), 336 (2005).
- 10 A. R. Glover, S. M. Skippon, and R. D. Boyle, *Appl. Opt.* **34** (36), 8409 (1995).
- 11 N. Semidetnov and C. Tropea, *Meas. Sci. Technol.* **15** (1), 112 (2004).
- 12 P. S. Huang, Q. Y. Hu, F. Jin, and F. P. Chiang, *Optical Engineering* **38** (6), 1065 (1999).
- 13 Z. H. Zhang, C. E. Towers, and D. P. Towers, *Opt. Express* **14** (14), 6444 (2006).
- 14 J. Chen and J. Katz, *Meas. Sci. Technol.* **16** (8), 1605 (2005).
- 15 J. Westerweel, *Meas. Sci. Technol.* **8** (12), 1379 (1997).

CHAPTER 6:

OPTIMISED FLUORESCENT TRACERS FOR FLARE REMOVAL IN GAS PHASE PIV

1. INTRODUCTION

One of the major problems in practical particle image velocimetry (PIV) experimental systems has been unwanted 'flare' in the recorded images. Flare is caused when the light used to illuminate the tracers also impinges on surfaces within the experimental setup. The light that is scattered from a solid surface is much more intense than that scattered from the tracer particles, giving saturation in the recorded images near these regions, and therefore particle images and flow vectors are lost ¹. This is particularly problematic in a number of industrially important applications, for example, in turbomachinery ²⁻⁴, studies of flow and spray dynamics in automotive engine cylinders ⁵ and chemical engineering reactors ^{6,7}.

Various approaches have been taken to reduce the effects of flare. Matt black surface preparations can be beneficial for a short period ⁸. However, with pulsed illumination the surface layer can rapidly become ablated. More recently, mirror-like paints containing optical absorbers have been reported for flare removal ⁹. An alternative approach is to use fluorescently doped seed particles which emit light at wavelengths longer than that used for illumination. Providing sufficient chromatic separation exists between the excitation and emission wavelengths, filters can be used to prevent the intense light scattered from any solid surfaces from being imaged. The extremely high contrast ratio of commercially available bandpass filters (to $>10^5$) means that fluorescent tracers can be used to produce measurements in close

proximity to surfaces and hence facilitate the study of boundary layers, flow-structure interactions and microfluidics.

In this Chapter, it is described the use of highly Bis-MSB-doped micron-sized tracers compatible with gas-phase flow seeding for recording high contrast PIV images. These highly concentrated tracers are free from concentration quenching effects and discussions of the optimisation of these tracers are detailed in Chapter 4.

UV excitation of Bis-MSB (in o-xylene) seed droplets from a frequency-tripled Nd:YAG laser, is adopted, such that a long-pass (wavelength) filter can remove the unwanted Mie scattered light. Subsequent tests using conventional atomisers have been conducted to assess visibility of the fluorescent tracer particles in conventional PIV imaging geometries. Finally, the application of the optimised fluorescent tracers is demonstrated to quantify a laboratory flow around a metal blade.

2. EXPERIMENTAL

2.1. Materials

O-Xylene, and the fluorescent dye 1,4-Bis(2-Methylstyryl)Benzene (Bis-MSB, MW= 310.44 g/mol) were obtained from Aldrich. All the materials were used as received without further purification and the solvent was of spectrophotometric grade or equivalent.

2.2. Seeding methodology

The required amount of Bis-MSB powder to prepare a solution at 10^{-2} M was dissolved in *o*-xylene. The resulting suspension was then immersed in an ultrasonic bath (50 Hz, Fisherbrand) for up to 30 minutes to ensure full solubilisation of the dye.

The solution was drawn through separate pressure-driven medical nebulisers (Med2000 Andy Flow) into the sheet. A regulator attached to a N₂ cylinder allowed the pressure and hence seed density to be varied. The atomised droplets were removed from the laboratory environment using an extraction system.

2.2.1. Tracers droplets sizing

A concentration of 10^{-2} M Bis-MSB-doped *o*-xylene tracers was nebulised using the same seeding pressure and experimental conditions as those later used for the acquisition of PIV images. Tracer particle sizing was performed using the same interferometric particle imaging method described previously in Chapter 5 (section 3.2.4).

2.3. Experimental setup

2.3.1. Laser sheets alignments

Laser beams were formed into light sheets with a height of circa 40 mm at the focus. The exact alignment of the laser sheets was critical to ensure that the same volume

was illuminated by both the first and second pulse. A similar approach to the one detailed in Chapter 5 (section 3.2.2) was utilised to insure proper alignment of the laser light sheets.

2.3.2. Flow field against a turbine blade surface model

To demonstrate the efficacy of the developed dye solution for PIV, a laboratory experiment was performed to examine the flow against a turbine blade surface. The experiment was setup as shown schematically in Figure 6.1. A flow field was generated using three pressure-driven nebulisers (Med2000 Andy Flow) containing a solution of Bis-MSB at 10^{-2} M in o-xylene. The seeding pressure was set to 0.5 bar with a regulator attached to a N_2 cylinder. The flow from the three nebulisers was collected in a flexible pipe and placed under the metal blade. The blade was tilted such that its entire lower surface was directly visible to the PIV camera and was illuminated by the laser sheet.

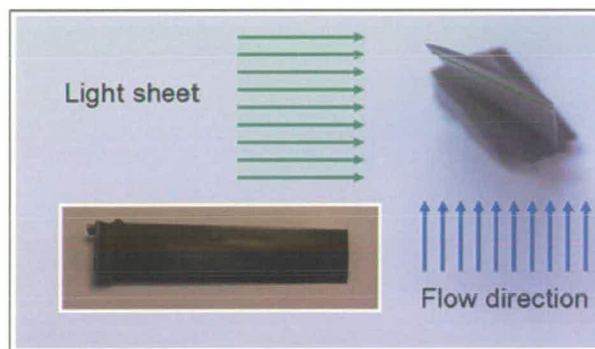


Figure 6.1: Schematic of the camera view and laser sheet orientation for a laboratory flare removal experiment. The inset (lower left) is an image of the gas turbine blade used.

2.3.3. Imaging system and data processing

An Imager camera (LaVision Flowmaster 3, cooled but not intensified) was used with a Nikon 105 mm lens at $f^\#$ 5.6. Images were recorded, corrected and processed using Davis version 7.2 from LaVision. Mie scattered light was recorded by the

camera on double-framed images with a pulse separation of 70 μs between laser pulses; a laser energy of 6 mJ per pulse was used for illumination of the flow.

The double framed images were processed using the adaptive multi-grid cross correlation algorithm in Davis; lens aberrations were accounted for using the de-warping tool available in Davis using images taken of a white light illuminated target.

2.3.4. 532 nm Illumination

The tracers were evaluated using two single-cavity pulsed Nd:YAG lasers (Continuum Surelite II-10). The first set of measurements was performed using conventional 532 nm illumination by fitting doubling crystals to the laser cavities; the two laser beams were combined using a 532 beam splitter with two dichroic mirrors positioned on the beam path to remove any remaining 1064 nm energy.

2.3.5. 355 nm Illumination

To achieve flare removal the Nd:YAG laser was frequency tripled to 355 nm by adding tripling crystals to both laser cavities. It was found that standard high reflectivity dielectric mirrors did not remove all of the second harmonic from the 355 nm pulse. This problem was overcome using equilateral fused silica prisms on both beams to separate the harmonics by refraction. The two beams were combined using a 355 nm half wave plate and a polarisation mixer. Bis-MSB tracers were used at a concentration of 10^{-2} M in *o*-xylene; the imaging lens blocked 355 nm Mie scattered radiation hence no additional filtering was required.

3. RESULTS AND DISCUSSIONS

3.1. Drop Sizing

Drop sizing results for a population of 1000 droplets are shown in Figure 6.2 (left). A mean drop size of $0.94\ \mu\text{m}$ was obtained with the size distribution

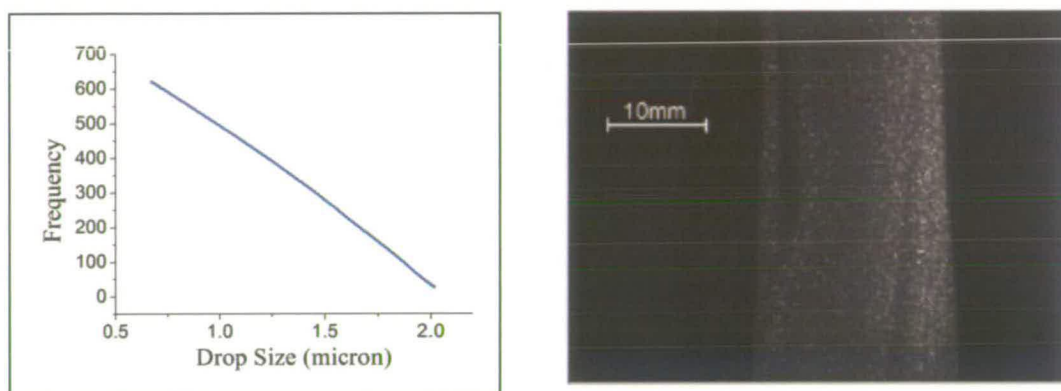


Figure 6.2: Left– Drop size distribution under experimental conditions for *o*-xylene doped with Bis-MSB-doped (10^{-2} M). Right– Image of emission from micron sized Bis-MSB fluorescent tracers (10^{-2} M).

The visibility of these tracers was evaluated with a field of view of the same size as laser sheets typically used for PIV illumination (height ~ 40 mm). It was found that satisfactory images of the fluorescence emission of micron-sized tracers could be obtained with as little as ~ 30 mJ pulse energy of 355 nm laser radiation at $f^\#$ of 4, for Bis-MSB at 10^{-2} M, as shown in Figure 6.2 (right). This compares very favourably with two previous studies in which another stilbene derivative, Stilbene 3 (also known as Stilbene 420), was used in UV-excited tracer droplets for two-phase PIV^{10,11}. In both cases, 355-nm pulse energies of 100 mJ were used. Driscoll *et al.* do not indicate the size of their tracer particles, but Kosiwczuk *et al.* state a diameter range of 1-5 μm . Given the cubic dependence of fluorescence intensity on diameter (see Chapter 2), it is feasible that the images reported in the latter study are dominated by particles at the high end of the diameter range.

3.2. 532 nm Illumination PIV Results

In the PIV experiment where 532 nm was used flare was generated on the surface of the blade as shown in the white saturated areas of Figure 6.3. The laser light directly Mie scattered from the blade surface is many orders of magnitude more intense than that scattered by the 1 μm tracers causing the greyscale range of the detector to be exceeded. Under saturation at particular pixels, charge is leaked out to the neighbouring area thereby generating a region of unusable pixels on the detector where the particle images cannot be observed and hence flow measurements are impossible.

A window size of 128x128 pixels was used for the first pass which was then decreased to 64x64 pixels with 25% overlap for the second pass; these parameters were selected to provide a clear visualisation of the low velocity vectors below the blade. The resulting vector field is shown in Figure 6.4 which has the seeding image as background.

The resulting vector map shows that flare generated on the blade surface prevented seed imaging and velocity measurements within the region with saturated pixels, hence data reporting the interaction of the flow with the surface cannot be obtained. Similarly, light reflected from the surface also produced randomly located spurious vectors.

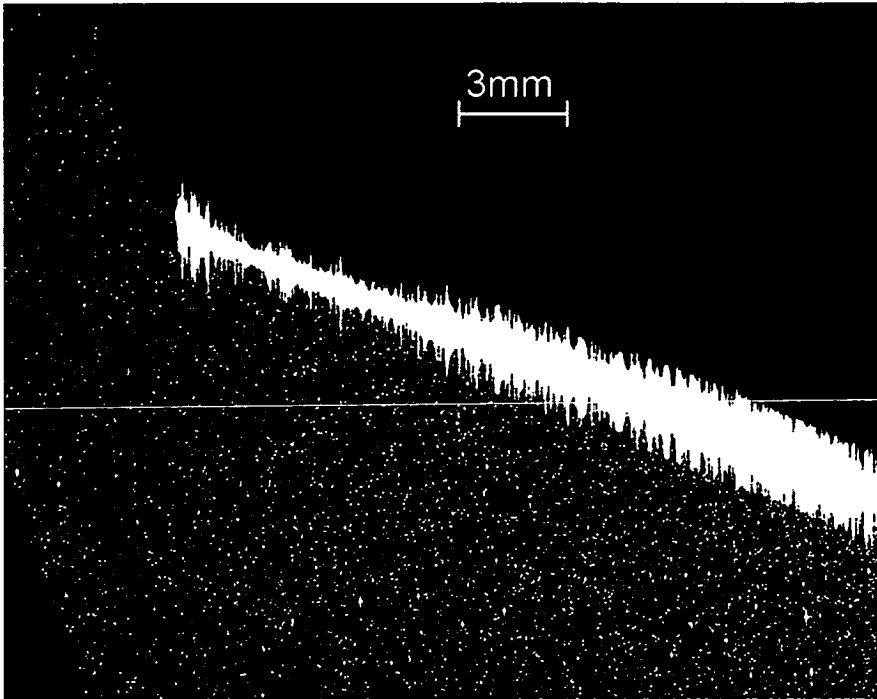


Figure 6.3: Imaging Mie scatter of tracers with 532 nm illumination.

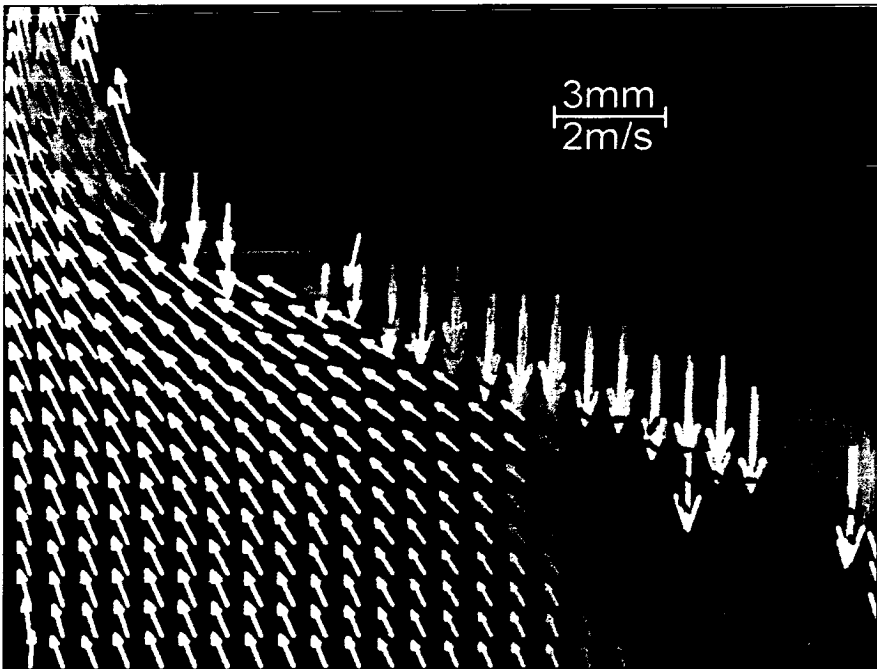


Figure 6.4: Velocity vectors of tracers with 532 nm illumination (Towers *et al.*).

3.3. 355 nm Illumination PIV Results

Measurements on the blade were repeated using 30 mJ UV illumination, acquiring double-framed images with a pulse separation of 70 μs . In this case no flare was produced as shown in Figure 6.5. The lower surface of the blade upon which the laser sheet is incident is visible. Blue fluorescence from the Bis-MSB doped tracers generated high contrast particles within the images. Such images could be obtained for several minutes before agglomeration of the tracers on the blade surface produced a detectable fluorescence.

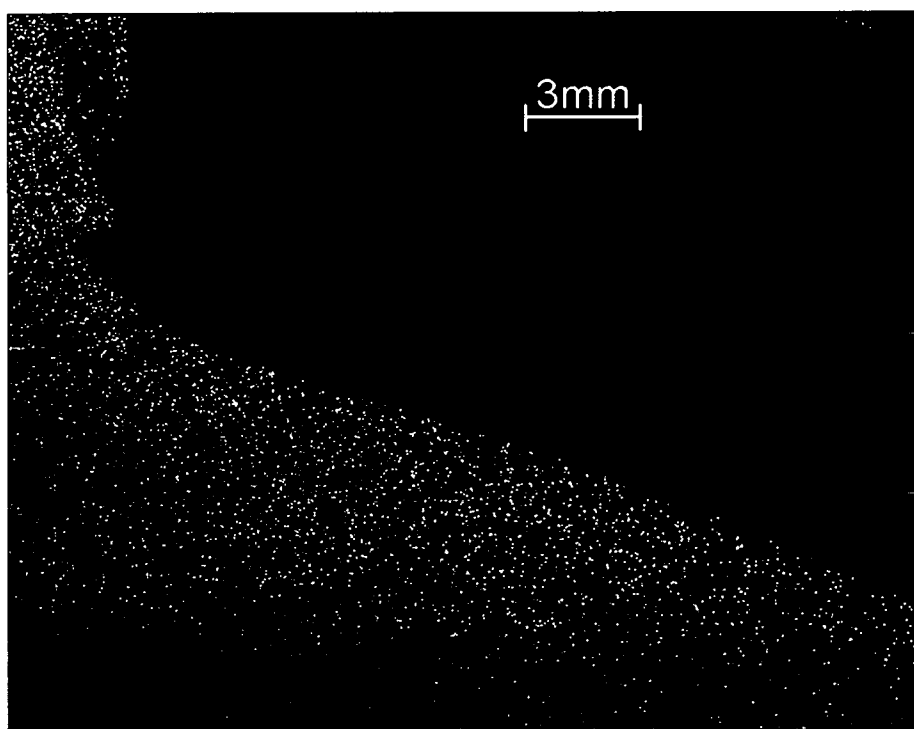


Figure 6.5: Imaging fluorescence of tracers with 355 nm illumination.

After image correction, velocity vectors were calculated with the same cross-correlation parameters used for conventional 532 nm illumination.

The vector map obtained is shown in Figure 6.6. The inset figure demonstrates the ability to measure up to the blade surface. Vectors are obtained within 75 μm of the

surface corresponding to one interrogation window size at 4x4 pixels when the field of view is ~20 mm.

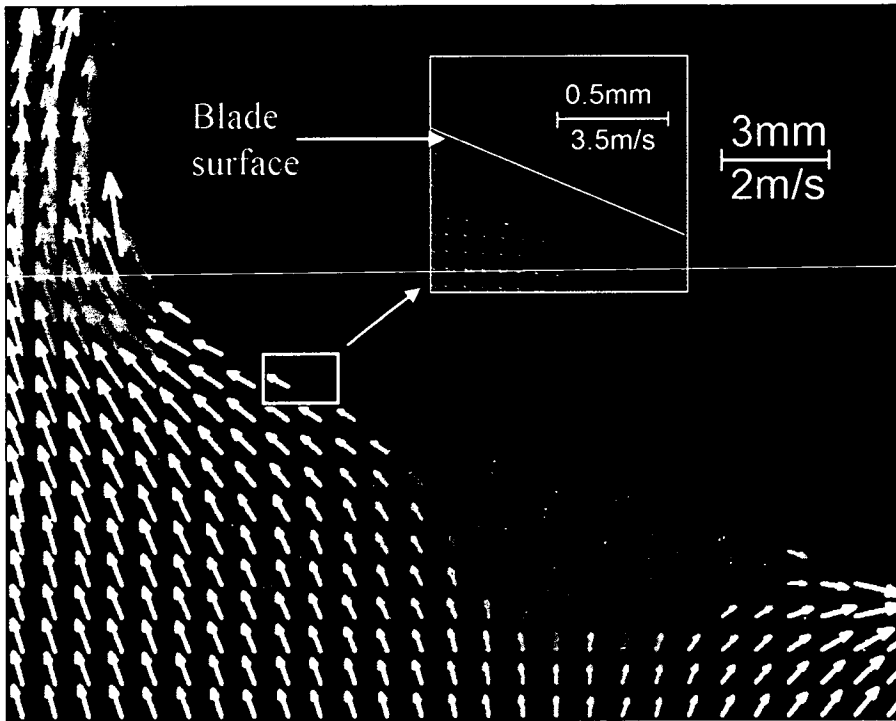


Figure 6.6: Velocity vectors of tracers with 355 nm illumination (Towers *et al.*).

The removal of the image ‘flare’ has enabled velocity vectors to be obtained right up to the surface of the metal blade. It can also be seen that the continuity of the velocity field is considerably improved. With Mie imaging, the presence of flare results in the loss of the vectors from all interrogation regions containing some saturated pixels (Figure 6.4) which increases the size of the region where the velocity information is lost. In contrast, with fluorescence imaging the velocity data shows excellent continuity along the blade surface and around its left hand edge.

4. CONCLUSIONS

A highly concentrated solution of Bis-MSB in o-xylene (10^{-2} M) was utilised to generate tracer droplets (<1 μm mean diameter) free from fluorescence concentration quenching effects. The fluorescence properties of Bis-MSB are such that double pulsed PIV experiments can be successfully conducted with standard solid-state lasers and silicon-based CCD cameras.

The optimised tracers are not only significantly smaller than those developed previously¹¹ but can be imaged with a relatively low laser pulse energy of 30 mJ at 355 nm over a vertical field of view up to 40 mm.

The effectiveness of these fluorescent tracers for flare removal in PIV experiments has been demonstrated, enabling measurements to be made in close proximity (75 μm) to reflective or scattering surfaces. This fluorescent PIV technique is expected to find applications in boundary layer studies and flow structure interactions in turbomachinery, automotive and chemical process industries.

5. REFERENCES

- 1 A. K. Prasad, *Curr. Sci.* 79 (1), 51 (2000).
- 2 B. Liu, X. Yu, H. Liu, H. Jiang, H. Yuan, and Y. Xu, *Exp. Fluids* 40 (4), 621 (2006).
- 3 M. P. Wernet, *Optics and Laser Technology* 32 (7-8), 497 (2000).
- 4 X. J. Yu and B. J. Liu, *Exp. Therm Fluid Sci.* 31 (8), 1049 (2007).
- 5 P. G. Aleiferis, Y. Hardalupas, A. M. Taylor, K. Ishii, and Y. Urata, *Exp. Fluids* 39 (5), 789 (2005).
- 6 A. Kumar, P. R. Gogate, and A. B. Pandit, *Ind. Eng. Chem. Res.* 46, 4368 (2007).
- 7 E. Rodriguez, A. H. Castillejos, and F. A. Acosta, *Metall. Mater. Trans. B* 38, 641 (2007).
- 8 A. Arnott, G. Schneider, K. P. Neitzke, J. Agocs, B. Sammler, A. Shroder, and J. Kompenhans, in *ICIASF '03* (2003), pp. 44.
- 9 R. Konrath, C. Klein, A. Schröder, and J. R. Kompenhans, *Exp. Fluids* 44 (3), 357 (2008).
- 10 K. D. Driscoll, V. Sick, and C. Gray, *Exp. Fluids* 35 (1), 112 (2003).
- 11 W. Kosiwczuk, A. Cessou, M. Trinite, and B. Lecordier, *Exp. Fluids* 39 (5), 895 (2005).

CHAPTER 7: IMPLEMENTATION OF EMULSION DROPLETS AS TRACERS FOR MICRO-PIV MEASUREMENTS

1. INTRODUCTION

The development of microfluidic devices and the expansion of their applications into a wide range of areas, such as micron-scale supersonic propulsion nozzles¹, medical/biological lab-on-chip integrated devices² and inkjet printing, have created an ever growing need for reliable diagnostic techniques to achieve reproducibility, quality control and improved designs.

Micro-Particle Image velocimetry (micro-PIV) is a well-established measurement technique that accommodates the limited optical access that characterises microfluidic devices and at the same time provides high spatial and velocity resolutions. Its development stems directly from the principle of macroscopic PIV³ and was first implemented by Santiago *et al.*⁴ where the velocity field in a Hele-Shaw flow* around a 30 μm elliptical cylinder was measured using an epifluorescence microscope setup.

As in macro-PIV, micro-PIV measurement consists of following the path of particles seeded in the carrying fluid, the velocity being extracted through a digital imaging correlation approach. (In the case of micro-PIV the particles have micron or submicron diameters). Because the average down-stream velocities are usually high due to the small cross-sectional areas of channels, a stroboscopic illumination is

* The Hele-Shaw experiment allows to simulate two-dimensional irrotational flow, i.e. with zero vorticity, past a given object.

used. The image of the pulsed emission from the particles is further captured by a gated, high-sensitivity CCD camera.

A typical micro-PIV setup (Figure 7.1) consists of a microscope equipped with appropriate filters and mirrors, a CCD camera and an illumination source (transillumination or epi-illumination)

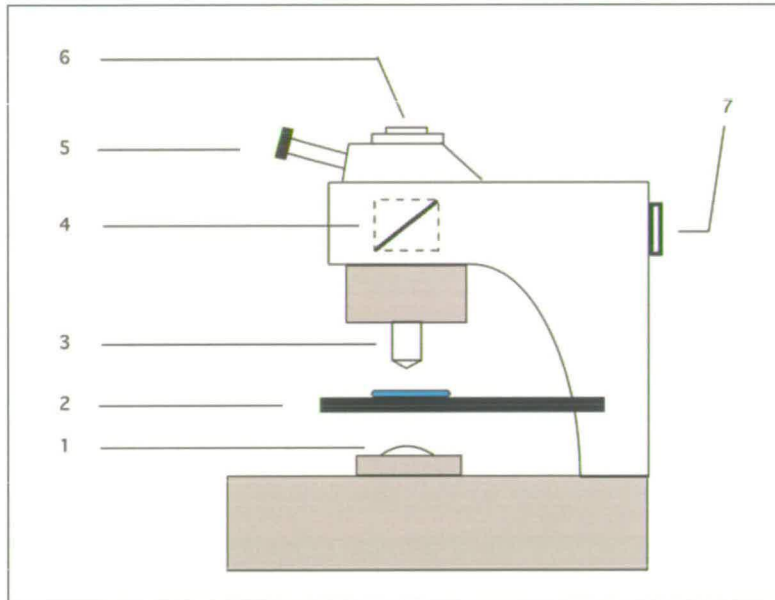


Figure 7.1: Schematic representation of an upright light microscope for micro-PIV measurements: 1- Lamp (transillumination). 2- Translation stage with microfluidic device. 3- Objective. 4- Filter / Dichroic mirror housing. 5- Eyepiece. 6- Camera mount. 7- External illumination aperture (epi-illumination).

Contrary to macro-PIV, flow field illumination in micro-PIV using a thin laser light sheet, where only tracer particles intercepting the sheet are imaged, is experimentally difficult because the limited optical access and the small dimensions of the microfluidic device render the generation of a laser light sheet and its alignment technically challenging. For these reasons, micro-PIV employs wide-field illumination of the flow field volume. Consequently, the use of elastic scattering (reflection) for imaging is impractical because of multiple scattering from tracer particles and reflections from the microfluidic chip surfaces. Instead, fluorescence is the preferred method of imaging tracer particles. As shown in Figure 7.1, the

excitation light is delivered by the illumination source and the dichroic mirror and emission filter serve to eliminate any excitation light from entering the CCD, while transmitting the fluorescence emitted by the fluorescent seed particles.

Monodisperse solid particles of latex or polystyrene, 1 to 5 μm diameter, coated with a fluorescent dye are generally used to obtain a good contrast and facilitate image treatment. An alternative solution to enhance the contrast is to use polymeric particles having the fluorophore incorporated in the bulk. From a practical point of view, the large volume fraction of particles in the carrying fluid often leads to clogging of channels, and particles tend to adsorb onto the surfaces, from which they cannot be removed easily. To reduce uncertainties, such as motion parallax, the particles should have a density close to the carrying fluid which avoids buoyancy effects, as these appear to be important for low flow rates. To overcome these problems, a novel micro-PIV seeding methodology will be described here, in which micron-sized fluorescent droplets of a water-in-oil (W/O) emulsion are used instead of solid particles. These types of tracer offer several potential advantages:

- A significant improvement in image contrast. The fluorescence being proportional to the volume of droplets rather than the area of the tracer as in the case of coated particles.
- Flexibility for matching the densities between the carrying fluid and the tracers, so that no correction is needed.
- Straightforwardness and ease of micro-chip cleaning.
- The use of standardised liquids & reproducible recipes.

2. EXPERIMENTAL

2.1. Material

Dimethyl sulfoxide (DMSO) – ($d=1.1$, $n_D=1.47$) and PDMS oil, poly(dimethylsiloxane), fluid 200 – ($\eta=50$ ctS, $n_D=0.96$) were obtained from Aldrich and Dow Corning, respectively. Silica nanoparticles Aerosil R972 ($d_p=16$ nm) and Lumogen F Red 305 were kindly donated by Evonik-Degussa and BASF, respectively. All the materials were used as received without further purification and the solvents were of spectrophotometric grade or equivalent.

2.2. W/O Emulsion Preparation

A 40% vol. water-in-oil emulsion was prepared. The silica nanoparticles were dispersed in PDMS oil (2 % wt.) by ultra-sonication for 3 minutes (20 kW at 15 Hz). To avoid overheating, the vessel containing the oil was cooled in an ice bath during sonication. To the PDMS nanoparticle dispersion (60 ml), 40 ml of a solution of Lumogen F red 305 (1.1 g/l) in DMSO was added and the solutions pre-emulsified in a vortex mixer for 1 minute. The resulting emulsion was further emulsified using a high shear homogeniser (Ultra Turrax T25, IKA) at 24500 rpm for 2 minutes.

2.3. Micro-PIV System

Microfluidic channels were etched by means of deep reactive ion etching in fused silica (glass channels) and poly(methyl methacrylate) (PMMA). For the glass channels, two 1 mm thick silica wafers were etched with 50 μm deep, 200 μm wide channels and anodically bonded afterwards. The PMMA channels were processed on one side only in 2 mm thick PMMA, the top lid was glued to the bottom etched part for a resulting channel of 90 x 50 μm . The microfluidic chip was mounted in a holder with inlet(s) and outlet connected to a flexible PVC tube by means of Presearch connectors (Presearch Ltd, Basingstoke, Hampshire, UK). A Nanoflow sensor N-565

(Upchurch Scientific, Oak Harbor, WA) was connected to the outlet to monitor the throughput of the pump(s). In these experiments, MilliGAT continuous pumps (Global FIA, Inc, Fox Island, WA) were used together with their valve system to alternate between feed solution (the emulsion described above) and the flush solution (pure PDMS oil). The micro-PIV system consisted of a Dantec Microstrobe (a high intensity light emitting diode) source, controlled by a Flowmap System Hub, illuminating the chip from 5 mm below the surface with 90 ns pulses. The time lapse between two images in a pair was 100 μ s, and each measurement consisted of 25 image pairs recorded at intervals of 1 s with an interline transfer CCD monochrome camera (Hisense MKII, Strobe double frame). The system was operated through Dantec Dynamics FlowManager v4.7.1 software (Dantec Dynamics A/S, Skovlunde, DK). The set-up is shown in Figure 7.2 and Figure 7.3. The recording frequencies were adapted by trial and error following previous work in the literature⁵. Since steady-state flow was studied, the velocity field was supposed constant, and the 25 sets of images were used to present an averaged result with improved statistics. The ensembles of 25 image pairs were treated using the so-called ensemble (or average) correlation method⁶. Each experiment was reproduced five times to obtain the standard deviation of each set of data.

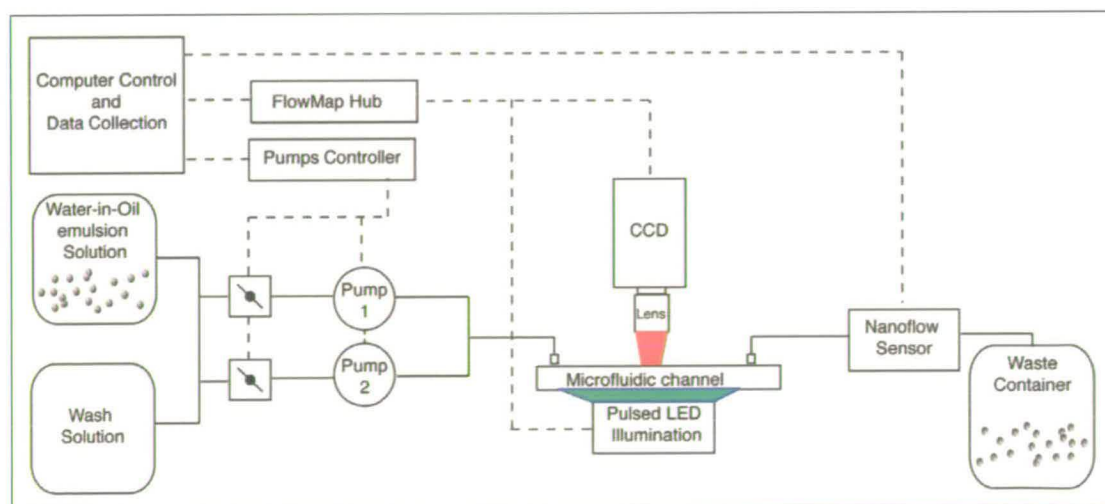


Figure 7.2: Schematic representation of the micro-PIV experimental setup.

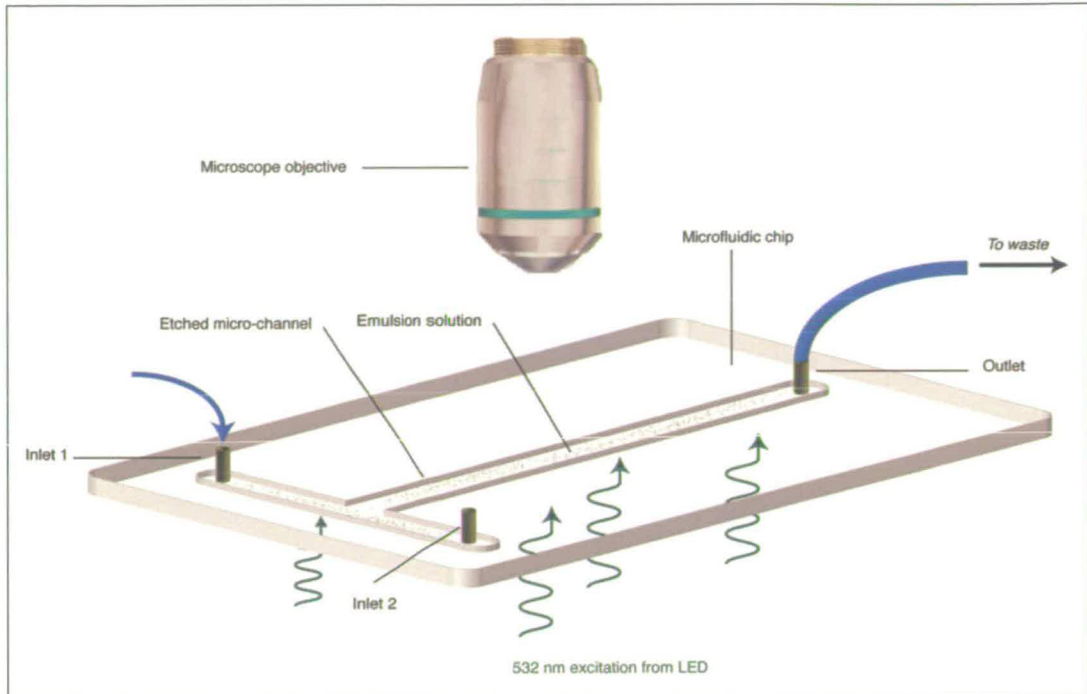


Figure 7.3: Sketch of the microfluidic T-junction chip. The emulsion solution is flown through the chip inlets 1 & 2.

3. RESULTS AND DISCUSSION

3.1. Emulsion Characterisation

Micrographs and the result of a dynamic light scattering (DLS) measurement of 1% v/v emulsion dilution in PDMS are shown in Figure 7.4 and Figure 7.5 respectively. The droplet size distribution (Figure 7.5) clearly appears monomodal, with a mean diameter of 3.8 μm and a half width of 1.35 μm . The distribution is right skewed towards large diameters in the range of 10 μm , but less than 10% of the population have a diameter larger than 6 μm , while 75% of the droplets have a diameter smaller than 3 μm . On the micrographs (Figure 7.4) only a few large droplets can be seen, which is consistent with the DLS results.

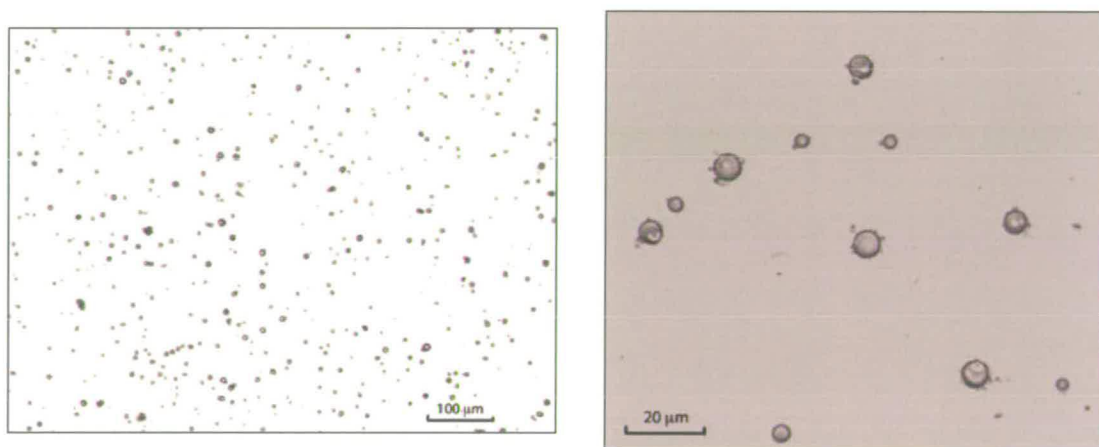


Figure 7.4: Micrographs of 40% v/v water-in-oil emulsion at 10x and 50x magnification (left and right respectively).

The emulsion droplets doped with the Lumogen F red 305 fluorophore were excited with 532 nm light delivered by the microstrobe LED. The fluorophore has its peak absorbance and peak fluorescence at 578 nm and 613 nm, respectively, as shown in Figure 7.6. Images were acquired using a long pass filter with a cut-off value of 590 nm.

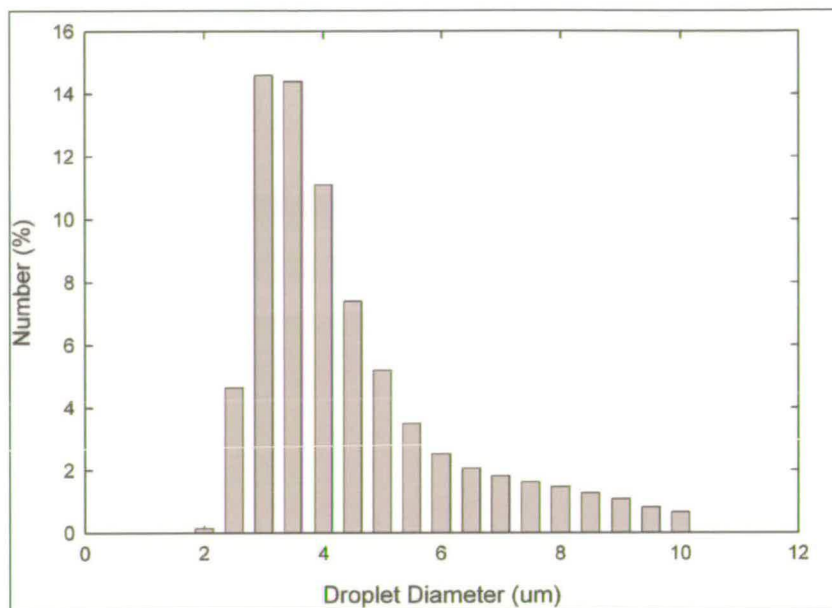


Figure 7.5: Droplets size distribution of 40% v/v water-in-oil emulsion as determined by DLS measurement.

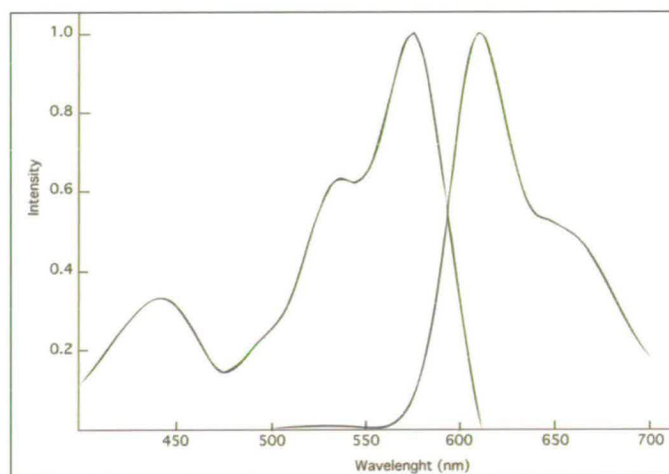


Figure 7.6: Absorption and emission spectra of Lumogen F red 305 in CH₂Cl₂. Intensities have been normalised to the maximum.

3.2. Micro-PIV Results

3.2.1. Validation of water-in-oil emulsion as tracers

In order to validate the use of W/O emulsion droplets as tracers, downstream axial velocity were measured across the width of the channel, far away from the inlet in order to guarantee a fully developed flow. The results of a micro-PIV measurement in a glass microchannel are presented in Figure 7.7 and are plotted against the analytic solution to the flow of a Newtonian fluid in a duct of rectangular cross-section with sides located at $x = \pm a$ and $y = \pm b$, where $a \geq b$

The governing equation of such a flow is:⁷

$$\frac{\partial^2 w}{\partial x^2} + \frac{\partial^2 w}{\partial y^2} = \frac{1}{\mu} \frac{dp}{dz}$$

where $w(x, y)$ is the downstream velocity, μ is the viscosity and dp/dz the constant pressure gradient down the channel. With the boundary conditions $w(\pm a, y) = w(x, \pm b) = 0$, a solution is found in the form:

$$\frac{w}{-(1/2\mu)(dp/dz)b^2} = 1 - \frac{y^2}{b^2} - \frac{32}{\pi^3} \sum_{n=0}^{\infty} \frac{(-1)^n}{(2n+1)^3} \frac{\cosh \lambda_n x}{\cosh \lambda_n a} \cos \lambda_n y$$

where $\lambda_n = (2n+1)\pi/2b$ is the slip length. The through-thickness average

$$\bar{w}(x) = (1/2b) \int_{-b}^b w dy$$

is then given by:

$$\frac{\bar{w}}{-(1/3\mu)(dp/dz)b^2} = 1 - \frac{96}{\pi^4} \sum_{n=0}^{\infty} \frac{1}{(2n+1)} \frac{\cosh \lambda_n x}{\cosh \lambda_n a}$$

A parabolic velocity profile is obtained, characteristic of the laminar flow of a Newtonian fluid in a rectangular channel. The solid line displayed in Figure 7.7 is the through-thickness average of the downstream velocity \bar{w} : in the present case, the depth of correlation as defined by Olsen and Adrian⁸ exceeds 100 μm , the height of the channel.

As a result, the velocities determined by micro-PIV are contributed to by the whole channel, which is reflected by Figure 7.7, as a satisfying agreement is observed.

One last feature deserves additional comment: while the theoretical velocity profile is null at the wall, as required by the no-slip boundary condition, the experimentally determined values are non-zero. This phenomenon, commonly referred to as a partial slip boundary effect, has been observed in a number of micro and nano-fluidic systems (see reference 9 for a recent review). The slip length λ is determined by fitting a parabolic function of the experimental results and determining its intercept. This leads, in the present case, to a value of $\lambda = 10 \pm 4 \mu\text{m}$. The resulting uncertainty is in the range of the experimental error: the micro-PIV results are the average of a measurement in a window of width of 16 pixels, corresponding to $10 \mu\text{m}$ with this magnification.

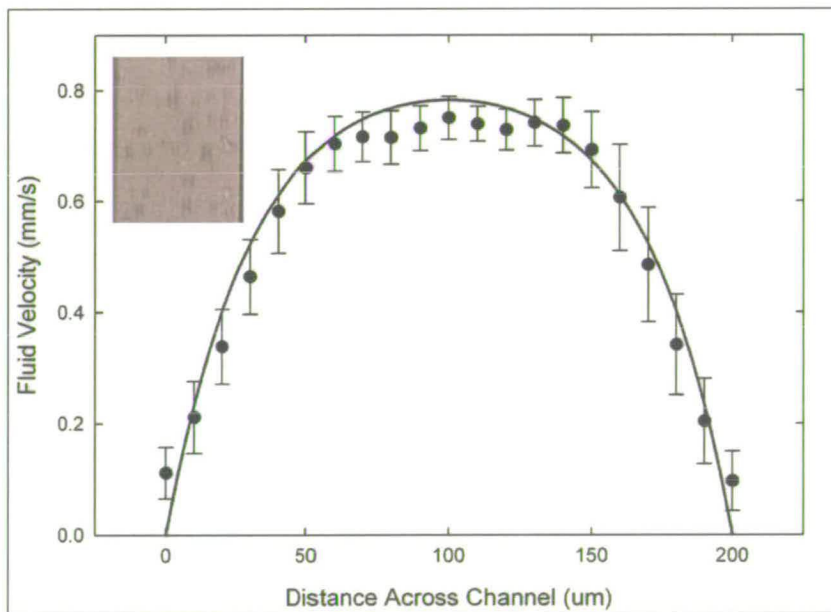


Figure 7.7: Axial flow velocity profile determined by micro-PIV across a glass micro-channel of $200 \times 100 \mu\text{m}^2$ rectangular cross-section with an inlet flow rate of $750 \text{ nl} \cdot \text{min}^{-1}$. Filled circles and error bars respectively represent the average and standard deviation of five replicates of the same experiment; the solid line is the through thickness average velocity determined by the finite volume method, see text for details. Inset: micrograph of the channel measured, width = $200 \mu\text{m}$, showing about 30 fluorescent droplets in motion.

Furthermore, within the set of experimental data determined, four out of the ten measured velocities at the wall were very close to zero, and may represent a better approximation of the slip behaviour.

As a consequence, it is not possible to conclude the existence of a partial slip at the walls from these measurements. Nevertheless, the results are globally satisfying, particularly as no moving average or other smoothing algorithm were used to further treat the data: the data presented is the raw ensemble correlation.

3.2.2. Velocity results

Having validated the use of water-in-oil emulsions as tracers for Micro-PIV in single straight channels, it was proposed to explore the limitations of the technique on other microfluidic devices. Accordingly, T- and Y-junctions were manufactured in float glass and poly(methyl methacrylate) (PMMA), respectively.

Figure 7.8 shows one snapshot taken during the measurement of the glass channel, with the resulting micro-PIV results superposed. As expected, the zones where the fluid has a low velocity do not allow droplets to be carried in, and therefore only a negligible velocity is obtained in the V-shaped exclusion zone at the junction of the two inlet channels of the T junction. The correlation with modelled results of a CFD simulation, similar to that obtained by co-workers and shown in reference 10 appears satisfying, although slight deviations from ideal behaviour are noticed. These are usually attributed to: 1) deviations from the modelled geometry and 2) irregularities in pump throughput. The latter effect has been documented and shown to be a measurable factor in micro-PIV experiments¹¹.

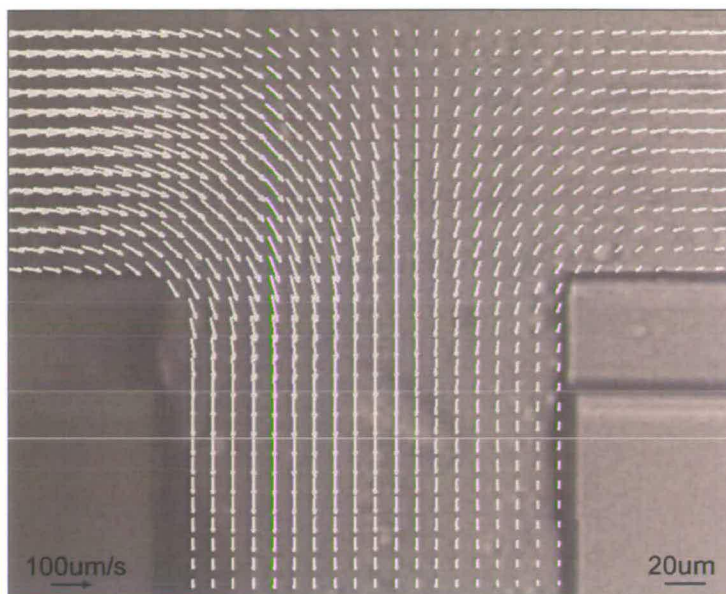


Figure 7.8: Micro-PIV measurement of a glass T-junction where the fluid is driven from the left and right branches with inlet velocities of 75 $\mu\text{m/s}$ to meet head-on in the middle of the T-geometry.

In the present case, neither of these justifications seem to hold, as the flow profiles were found experimentally to compare well in each branch far away from the junction.

Instead, one notices that the computed flow rate is higher in the left branch than in the right branch, which is attributed to a difference of background light intensity and therefore an imbalance of contrast between the droplets and the background from the left to the right of the picture.

This is an effect of the microchip holder which does not allow a homogeneous distribution of light over the microchip. Although it was hoped that the improved signal to noise ratio would overcome this effect, this is not the case. In order to account for such poor illumination conditions, it is necessary to revert to the usual practice, in which the zone is split into a number of areas of interest with homogeneous intensities that are dealt with separately in the micro-PIV analysis. A novel arrangement for the light source has been introduced recently on a similar system, which should overcome this limitation¹².

It can be seen that the flow in the top branch is perfectly defined, while approximately 80% of the velocity information is missing from the bottom one. At the same time, a typical result is observed for this type of junction where the flow is laminar and where the flow from the bottom branch is expected to flow alongside the one originating from the top branch.

The experiments on PMMA Y-junction chip were more problematic than those on the T-junction because previous experiments on the same Y-junction chip using solid particles had resulted in clogging of the bottom inlet channel. This obstruction was found difficult to clean and resulted in dissimilar seeding in the two inlet branches. However, micro-PIV experiments were carried out and the results are displayed in Figure 7.9.

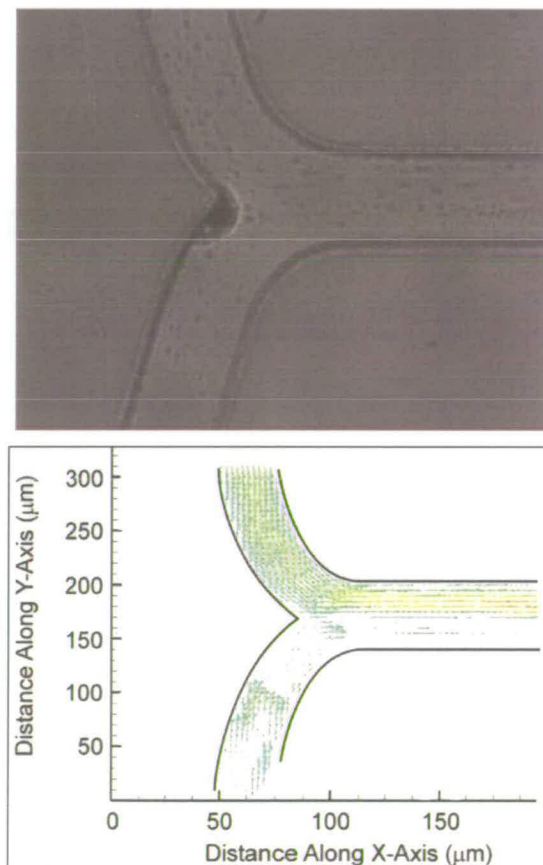


Figure 7.9: Top: A snapshot of fluorescent W/O emulsion droplets flowing through the PMMA Y-junction. Bottom: Micro-PIV measurement of a PMMA Y-junction where the fluid is driven from the top and bottom branches with inlet velocities of 75 nl/min .

4. CONCLUSIONS

A refined experimental method for micro-PIV was applied to the characterisation of rectangular microchannels using doped water-in-oil emulsion droplets as alternative tracers to conventional dye coated solid particles.

Emulsion droplets were validated as suitable micro-PIV tracer as agreements with the analytical description of a Newtonian fluid down a rectangular channel were obtained.

Micro-PIV experiments using this method in T- and Y- junctions were carried out and velocity fields were successfully obtained. Compared to dye-coated particles, the improved contrast from doped emulsion droplets meant that no additional signal treatment was needed after cross correlation analysis.

As proof-of-concept, this type of emulsion based micro-PIV tracers offers the potential of matching the densities between the carrying fluid and the tracers without the need for post processing corrections.

In addition to straightforwardness of micro-chip cleaning and contrary to dye coated particles, emulsion based tracers offers the possibility of choosing within a wide range of fluorophores that can better suit the illumination requirement of a particular micro-PIV.

5. REFERENCE

- 1 R. L. Bayt, A. A. Ayon, and K. S. Breurer, in *33rd AIAA/ASME/SAE/ASEE Joint Propulsion Conference & Exhibit* (Seattle, W.A, 1997), pp. 97.
- 2 M. A. Northup, R. F. Hills, R. Landre, H. D. Lehew, and R. A. Watson, in *Transducers '95, 8th International Conference on Solid State Sensors and Actuators* (Stockholm, Sweden, 1995), pp. 764.
- 3 R. J. Adrian, *Annual Review of Fluid Mechanics* **23**, 261 (1991); M. Raffel, *Particle image velocimetry : a practical guide*, 2nd ed. (Springer, Berlin, 2007).
- 4 J. G. Santiago, S. T. Wereley, C. D. Meinhart, D. J. Beebe, and R. J. Adrian, *Exp. Fluids* **25** (4), 316 (1998).
- 5 L. Bitsch, L. H. Olesen, C. H. Westergaard, H. Bruus, H. Klank, and J. P. Kutter, *Exp. Fluids* **39** (3), 505 (2005); C. D. Meinhart and H. S. Zhang, *Journal of Microelectromechanical Systems* **9** (1), 67 (2000).
- 6 C. D. Meinhart, S. T. Wereley, and M. H. B. Gray, *Meas. Sci. Technol.* **11** (6), 809 (2000).
- 7 M. E. Erdogan, *International Journal of Non-Linear Mechanics* **38** (5), 781 (2003).
- 8 M. G. Olsen and R. J. Adrian, *Exp. Fluids* **29** (7), S166 (2000).
- 9 E. Lauga, M. Brenner, and H. Stone, in *Handbook of Experimental Fluid Dynamics* (Springer, New York, 2005).
- 10 D. A. Mendels, E. Graham, S. Magennis, A. Jones, and F. Mendels, *Microfluid. Nanofluid.* DOI 10.1007/s10404-008-0269-5 (2008).
- 11 K. P. Angele, Y. Suzuki, J. Miwa, and N. Kasagi, *Meas. Sci. Technol.* **17** (7), 1639 (2006).
- 12 S. M. Hagsater, C. H. Westergaard, H. Bruus, and J. P. Kutter, *Exp. Fluids* **44** (2), 211 (2008).

CHAPTER 8:

CONCLUSIONS

The aim of this thesis was to optimise the fluorescence properties of dye-doped tracers for use in gas phase multi-constituent particle image velocimetry (PIV) and in PIV applications where flare removal is required.

Bis-MSB and DCM have been identified as UV-excitabile blue and red emitting dyes exhibiting high quantum yield and peak fluorescence in the respective colour channels of the imaging system.

Novel methodology and instrumentation was developed to establish that tracer droplets with high concentrations of these dyes (up to the solubility limit $\sim 10^{-2}$ M) in *o*-xylene (Bis-MSB) and DMSO (DCM) are free from fluorescence quenching effects. This implies, that although in the PIV applications discussed in this work, tracers were in the range of 1 to 3 μm , it would be possible to utilise even smaller droplets (in the range of 300 nm) if higher dye concentration could be achieved.

The optimised red and blue fluorescent tracers enabled multi-constituent PIV measurements, where relatively low 355 nm and 532 nm illumination energy (2 mJ and 50 mJ, respectively) allowed phase discrimination to be carried on a single colour CCD camera. Flow direction, displacements and associated velocity vectors have been measured successfully as well as a direct quantification of the fluid mixing velocities.

UV excitation of Bis-MSB doped tracers enabled flare removal in PIV experiments. These micron-sized tracers (<1 μm mean diameter) can be excited with relatively low laser pulse energy (30 mJ) and permitted measurements to be made in close proximity (75 μm) to reflective or scattering surfaces. This fluorescent PIV technique is expected to find applications in boundary layer studies and flow

structure interactions such as in turbomachinery, automotive and chemical process industries.

Contrary to the high energy pulses often reported in PIV experiments, the combination of optimised tracers and low laser pulses achieved here has several benefits such as: prolonged lifetime of the optical components, reduced photo-degradability of seed droplets and better control of the dynamic range of the imaging system.

In the devised spectroscopic instrumentation, stabilised water-in-oil (W/O) and oil-in-water (O/W) micro-emulsions were utilised to mimic the fluorescence properties of PIV micron-sized tracers. This instrumentation was also used to quantify the sensing ability of fluorescent microsphere for monitoring the pH in living cells¹.

The doped water-in-oil emulsions also found application as tracers in a novel experimental method for micro-PIV. Emulsion droplets ($\sim 4 \mu\text{m}$) of Lumogen F red dye in DMSO were implemented as alternatives to dye-coated solid particles for the characterisation of rectangular microchannels. As the whole droplet emits, the improved signal-to-noise ratio of these tracers in comparison to dye-coated particles allowed velocity field in T- and Y- junction micro-chips to be successfully obtained without the need for signal treatment after cross-correlation analysis. In future work, doped oil-in-water emulsions tracers could be employed for micro-PIV in biological applications. The potential advantages of emulsion-based tracers over dye-coated particles are numerous, such as being free from dye leakage, the ability to match the fluid/tracers densities, the flexibility to choose within a wide range of probes for sensing or fluorophores that best suit the illumination requirements of a given micro-PIV setup and ease of production, using straightforward and reproducible recipes, without the need for the laborious synthetic route that dye-coated particles require.

¹ M. Bradley, L. Alexander, K. Duncan, M. Chennaoui, A. C. Jones, and R. M. Sanchez-Martin, *Bioorg. Med. Chem. Lett.* **18** (1), 313 (2008).

APPENDIX I:

QUANTITATIVE FLUORESCENCE MEASUREMENT FROM IMAGING AIRBORNE MICRON-SIZED FLUORESCENT DROPLETS

1. INTRODUCTION

In this work, it was attempted to quantitatively correlate the fluorescence intensity from airborne micron sized fluorescent droplets (1 to 5 μm) with their diameter, as this offers numerous potentials such as better laser power tuning, dye concentration optimisation and imaging system dynamic range control.

The theory predict that a cubic relationship exists between the emitted fluorescence intensity (I_f) and the diameter of a doped droplet (d_p), such as:

$$I_f = Cd_p^n$$

with C an experimental constant and $n = 3$

Previously, Le Gal *et al.*¹, Domann *et.al.*² and Park *et al.*³ have established the validity of this relationship for droplets with low dye absorbance and diameters in the range of 50 to 300 μm . However it was found that for high dye concentrations the exponent value, n, lies between 2 and 3.

For the droplet sizes (1 to 5 μm) studied here, the optical path length of small and the absorption effect should therefore be less marked than in larger droplets (> 50 μm). Hence it is expected that the value of n to be close to 3 even for high dye concentrations.

2. BACKGROUND

When imaging small particles, diffraction effects become significant when particle sizes are no longer negligible with respect to the incident illumination wavelength (λ). In such situations, a diffraction pattern from a particle in the object plane will spread out as an Airy function in the image plane (see section 2.1.4.2.1).

The diffraction-limited spot size is $d_s = 2.44(1 + M)f^\# \lambda$ with $f^\# = \frac{f}{D}$ the lens f-number. For a non-infinity corrected microscope objective to:

$$d_s = 1.22(M + 1)\lambda/NA \quad (1)$$

With NA, M and λ being the numerical aperture of the objective, the magnification of the objective and the fluorescence wavelength (taken as 450 nm), respectively.

Therefore, the effective particle image diameter in the image plane is:

$$d_e = \sqrt{M^2 d_p^2 + d_s^2}$$

3. EXPERIMENTAL

Micron-size doped droplets with diameters in the range of 0.5 to 5 μm were imaged with an extra long working distance (ELWD) 20X microscope objective (NA = 0.4) attached to a CCD camera. Three doping concentrations of Bis-MSB were investigated: 10^{-3} , 5×10^{-3} and 10^{-2} M.

Using the following optical setup parameters: M = 20, NA = 0.4 and $\lambda = 450$ nm, the diameter of the point spread function $d_s \sim 28 \mu\text{m}$

Therefore for droplet diameters (d_p) in the object plane, the expected image droplets diameters d_{pix} at the CCD camera (for which 1 pixel = 6.45 μm .) can be found in the table bellow.

dp	Mdp	de (μm)	dpix (pixels)
1	20	35.1	5
2	40	49.3	8
3	60	66.6	10
4	80	85	13
5	100	104.1	16
6	120	123.4	19
7	140	142.9	22
8	160	162.6	25
9	180	182.3	28
10	200	202.1	31

Seed droplets were generated with a pressure-driven medical nebuliser (Andy Flow, Med2000). A 355 nm illumination from a tripled Nd:YAG laser was used as illumination/excitation source.

A large particles images sequence was captured and were processed using a Matlab code developed by Towers at Leeds University which, has two functions:

- 1- to select a droplet within the image and from its intensity profile, determine if drop is in focus (Figure A-1)
- 2- from the selection of an individual focused droplet, the code fits a Gaussian function of the drop greyscale intensity. The fitting result is the determination of the droplet radius as a factor of the Gaussian fit standard deviation (SD). The proportionality factor has been calculated by least squares fit between the Gaussian and the Airy functions (Figure A- 2).

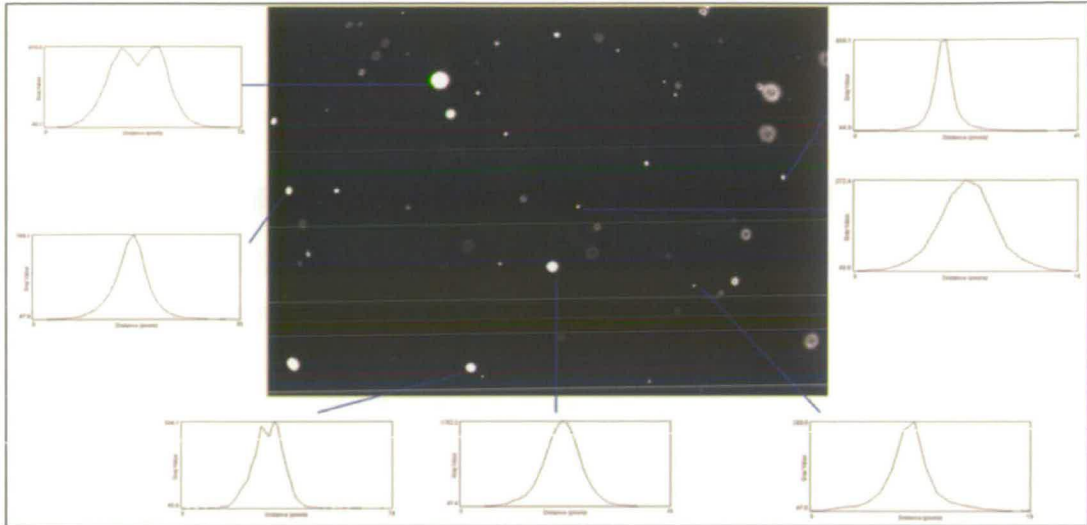


Figure A-1: intensity profiles from different seed droplets.

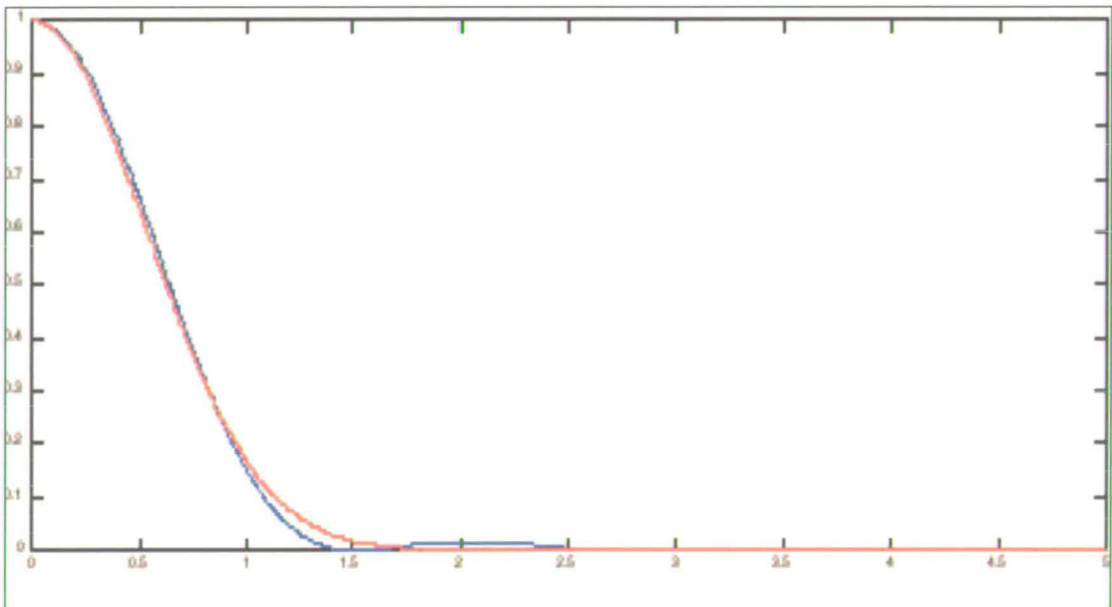


Figure A- 2: Airy (blue) / Gaussian Profile (red) - Linear Least Squares Fit at 2.8678 standard deviations to 1st dark Ring.

4. RESULTS AND DISCUSSIONS

The determination of the droplet radius as a factor of the Gaussian fit standard deviation (SD) has been carried out by linear least squares fit. A value 2.8678 was

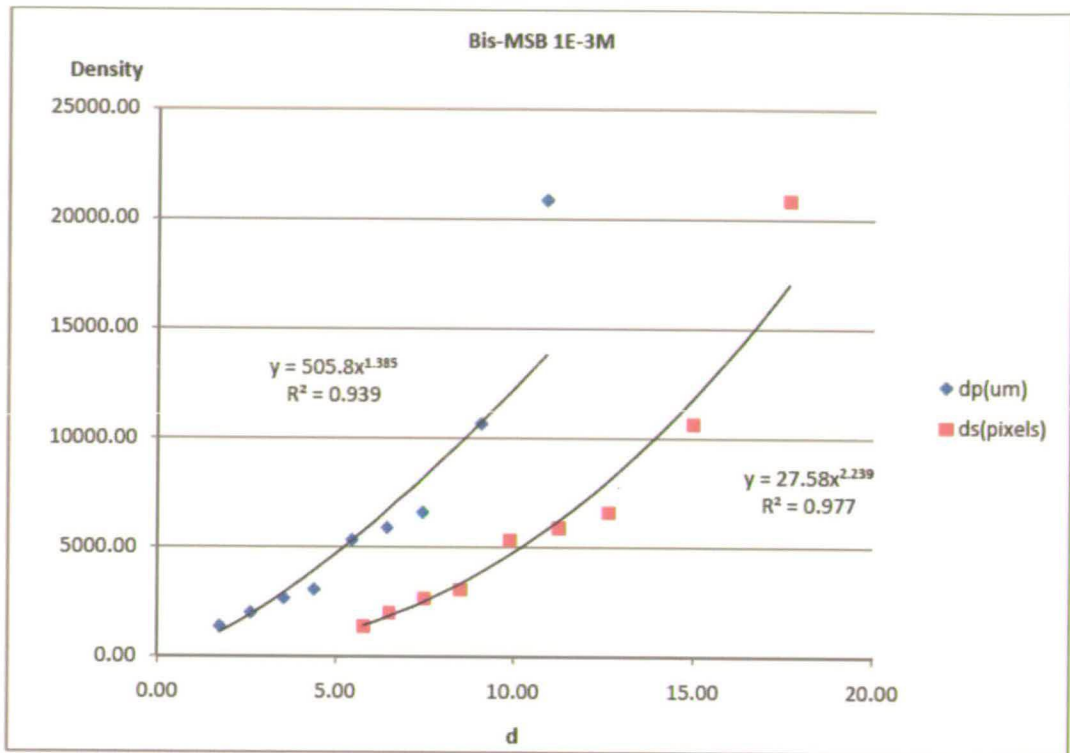
determined so that $r = 2.8678 \cdot SD$. The code then calculates the droplet greyscale by summing the greyscale pixel values (density) contained in an area of πr^2 (with $r = 2.8678 \cdot SD$).

Table 1 represents an example of the data obtained from processing image droplets with the Matlab code where the Gaussian SD/radius ratio is set at 2.86.

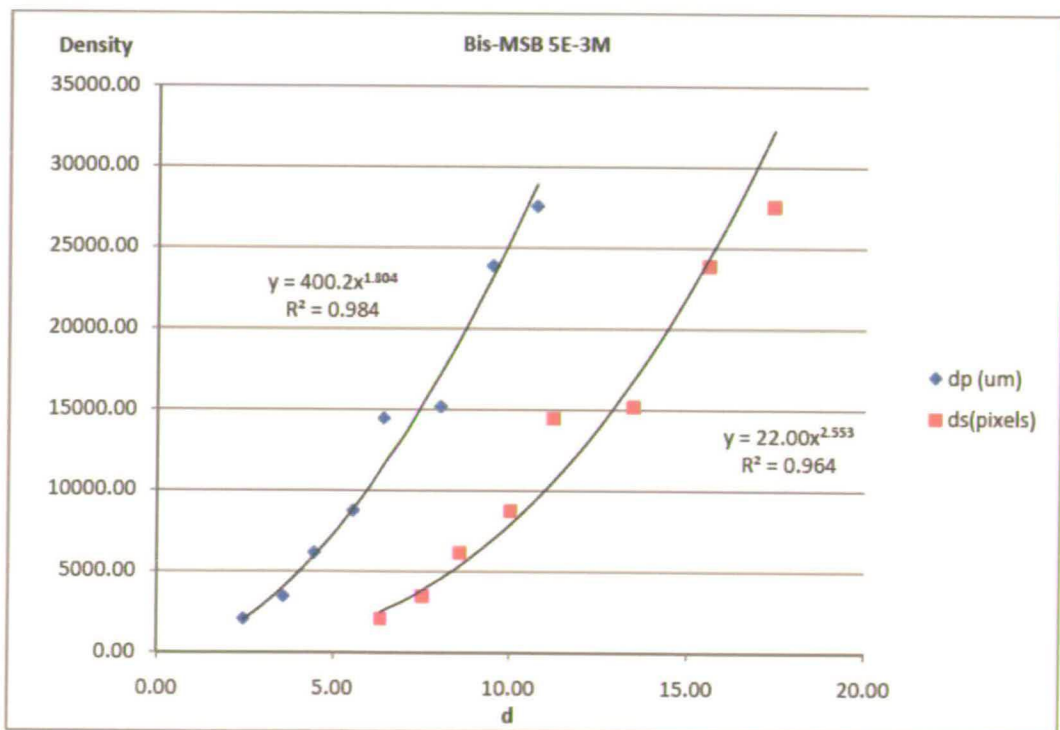
The graphs 1,2 and 3 below are plots of the drop's effective (image plane) and real (object plane) diameters (Table 1).

10 ⁻³ M			5x10 ⁻³ M			10 ⁻² M		
de (pixels)	dp (um)	density	de (pixels)	dp (um)	density	de (pixels)	dp (um)	density
5.78	1.74	1358.30	6.36	2.44	2071.95	6.33	2.41	2841.65
6.51	2.60	1992.73	7.55	3.58	3451.15	7.52	3.55	5023.58
7.50	3.54	2657.15	8.59	4.45	6151.09	8.55	4.42	10215.48
8.52	4.39	3059.27	10.01	5.55	8758.94	9.85	5.43	14130.07
9.88	5.45	5327.81	11.21	6.43	14465.35	11.17	6.41	25496.79
11.23	6.45	5894.33	13.46	8.03	15182.70	13.42	8.00	29593.98
12.62	7.44	6599.21	15.57	9.48	23878.89			
14.97	9.07	10662.51	17.38	10.72	27572.91			
17.63	10.88	20862.88	21.47	13.45	55948.46			
21.25	13.30	35164.42						

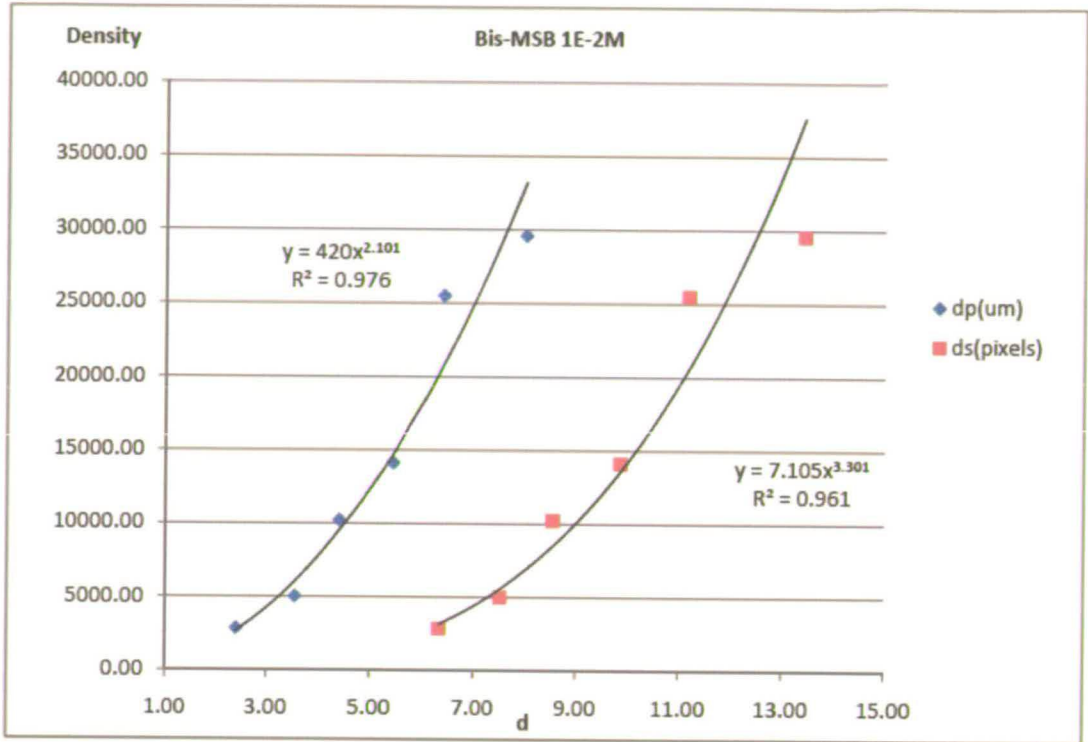
Table 1: Average drop diameters (de, dp) per range and its corresponding densities



Graph 1

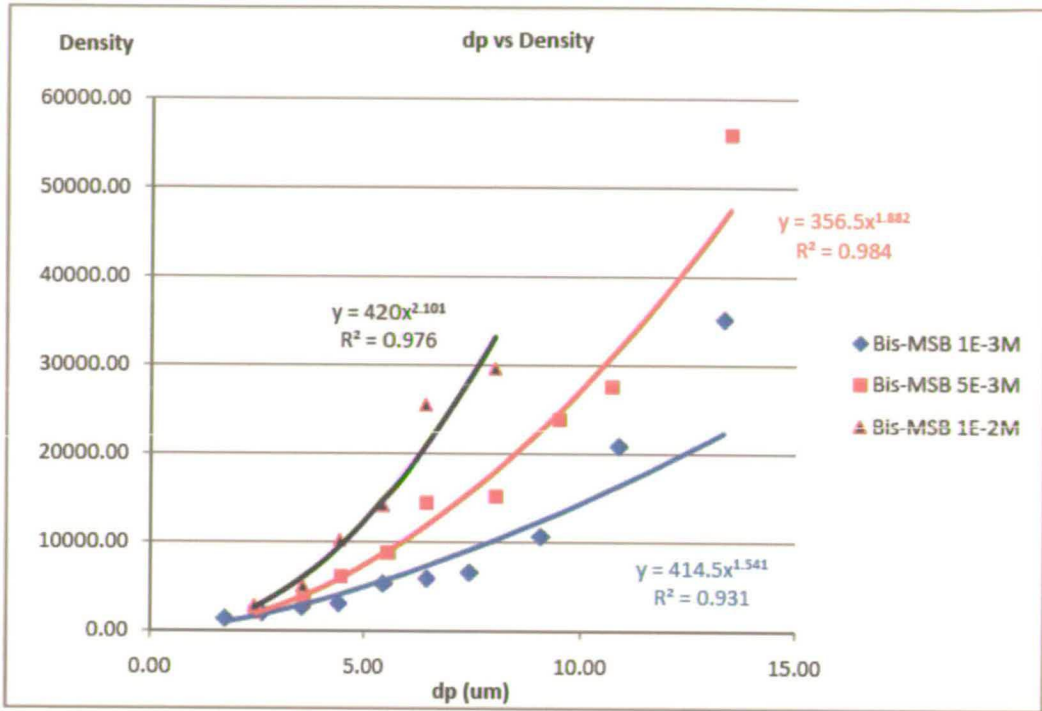


Graph 2

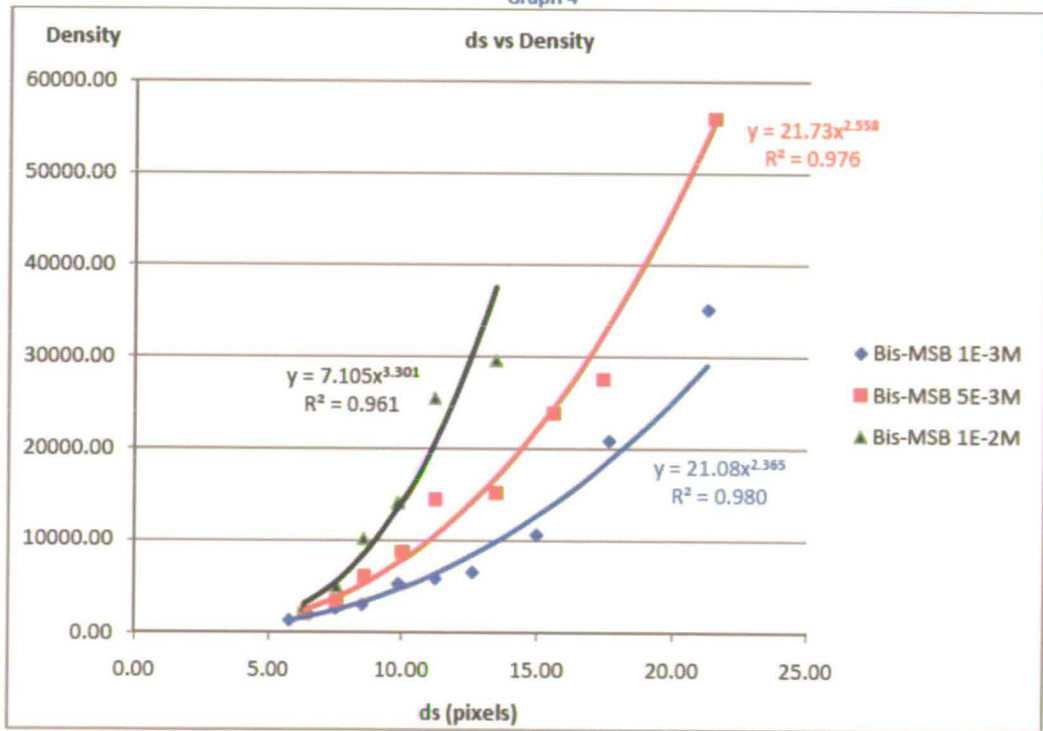


Graph 3

The plots below represent comparison between Bis-MSB at 10^{-3} M, $5 \cdot 10^{-3}$ M and 10^{-2} M drop densities against d_p (graph 4) and d_s (graph 5) from Table 1.



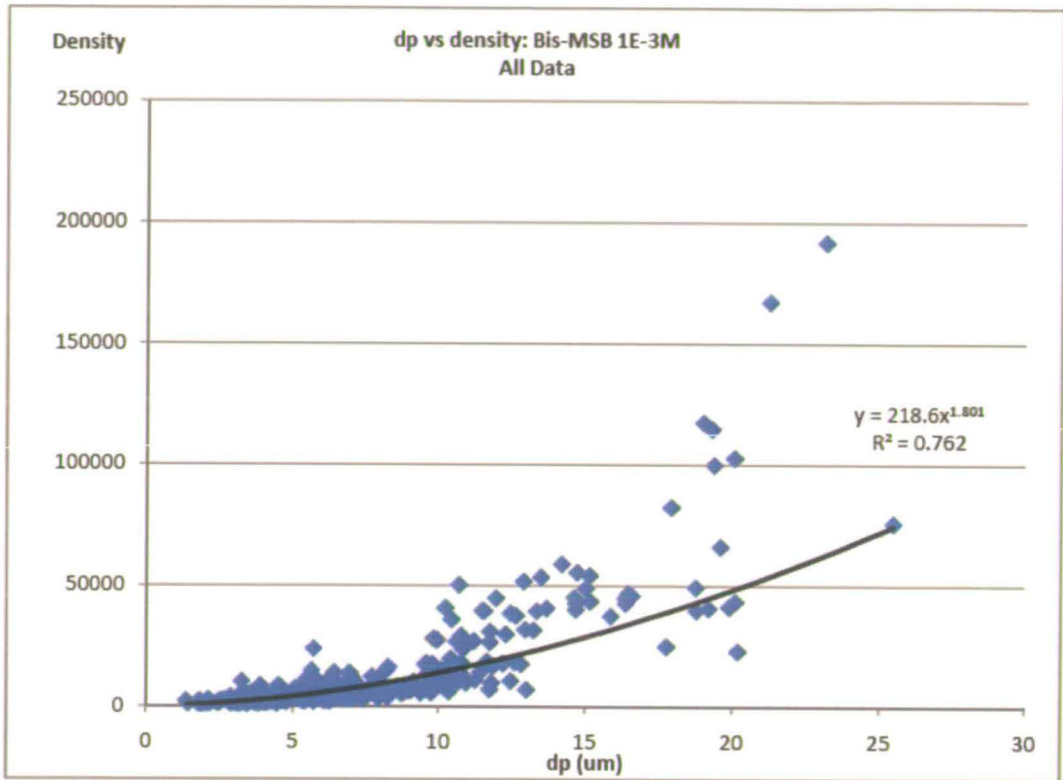
Graph 4



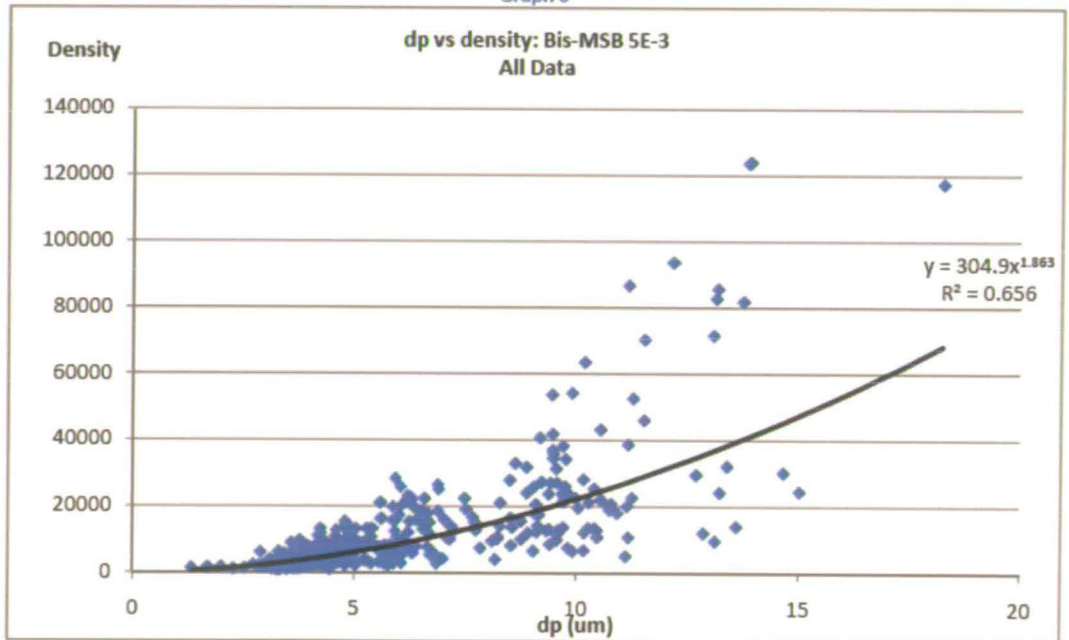
Graph 5

The graphs 6, 7 & 8 represent all the data plotted (without averaging) of the drops density against d_p . The graph 9 is a comparison for all the data fitting.

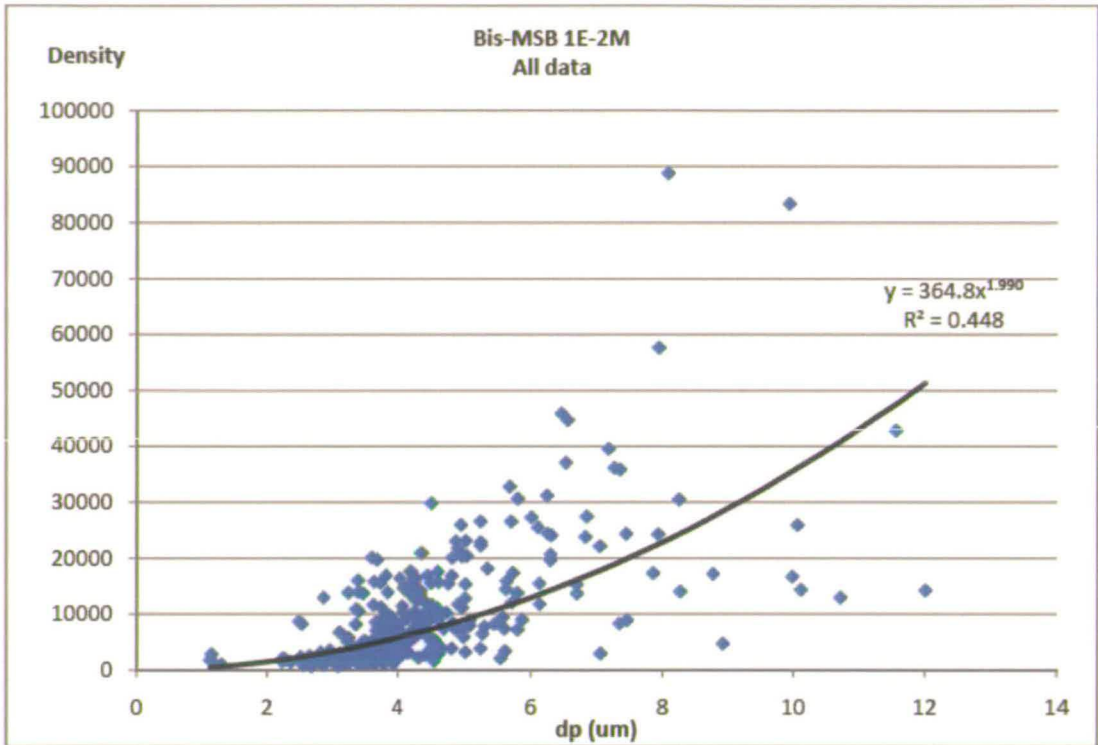
APPENDIX I



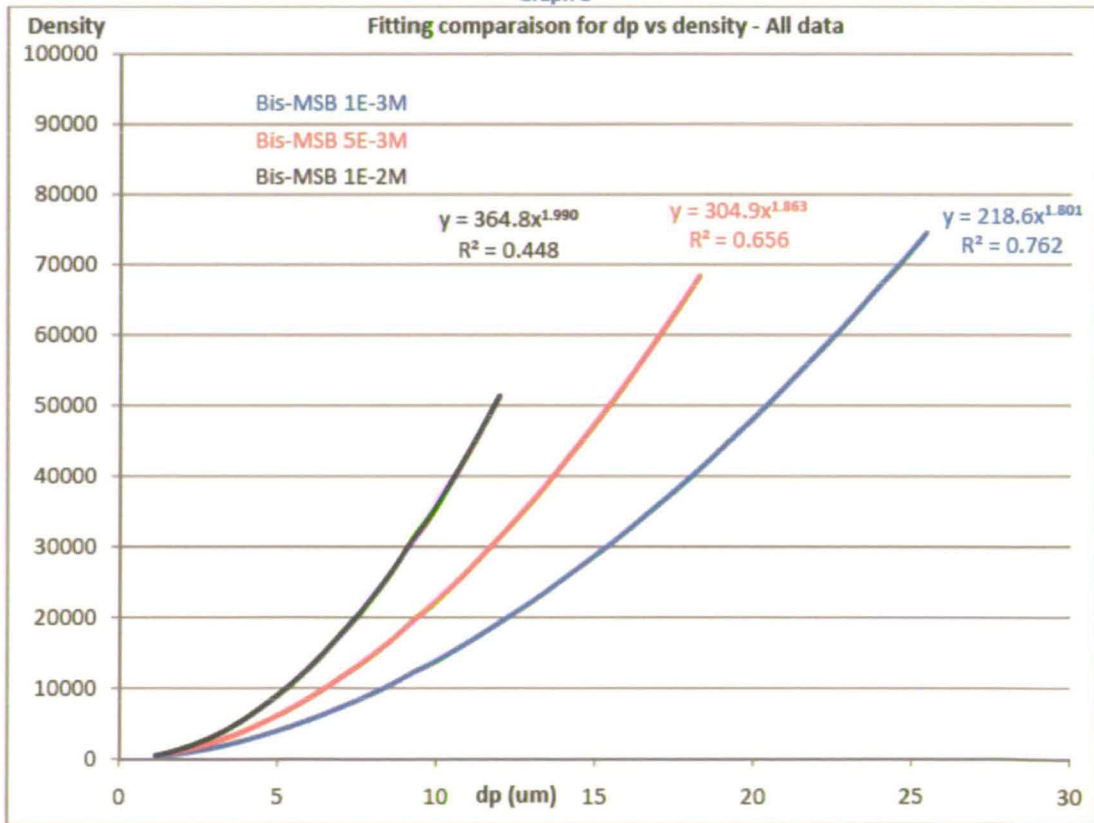
Graph 6



Graph 7



Graph 8



Graph 9

From the results presented here, it seems that it is not possible to correlate the drop's greyscale intensities with the cube of their diameter (d_p). The fitting coefficients do not reflect the linearity between the fitting gradients and the increase of the dye concentration.

The fitting coefficients seem unexpectedly bad ($n < 2$) for the density against d_p plots. Especially that the exponent value (n) decrease as the dye concentration decreases. This is contrary to the trend obtained by Le Gal *et al.*¹ This raises questions on the validity of the obtained results.

Therefore, from the results obtained here it is not possible to reach a conclusion as several experimental difficulties were encountered:

- The diffraction spot size (d_s) is a calculated value (for $\lambda = 450$ nm), while actually the fluorescence emission is broadband (even if it is peaked at 450 nm). Thus the “real” d_s could be slightly different and this could bias the results.
- As the plots show- the large majority of drops diameters (d_p) are below ~ 10 μm , and since the probed droplets diameter is too close to the resolution of the imaging system, some data could be erroneous.
- The imaging system was not optimised to probe such small droplets. The time allocated for this experiment did not allow reproducing this experiment with other sets of microscope objectives (e.g. water or oil immersion) offering better magnification/NA combination for improved resolution.

5. REFERENCES

- 1 P. Le Gal, N. Farrugia, and D. A. Greenhalgh, *Optics and Laser Technology* **31** (1), 75 (1999).
- 2 R. Domann and Y. Hardalupas, *Appl. Opt.* **40** (21), 3586 (2001).
- 3 S. Park, H. Cho, I. Yoon, and K. Min, *Meas. Sci. Technol.* **13** (6), 859 (2002).

APPENDIX II:

LECTURES, CONFERENCES & PUBLICATIONS

5.1. Postgraduate Lectures and Courses

Physical Chemistry Section Seminars

GRAD Schools Management Training Courses

Fluid Mechanic

Digital Image Analysis

Laser Physics

5.2. Conferences and Meetings

MRS Fall Meeting 2007, Material Research Society, *Boston, MA, USA, November 2007.*

PIV 07, 7th International Symposium on Particle Image Velocimetry, *Rome Italy, September 2007.*

Microfluidics Seminar, TUV NEL Ltd., Holiday Inn, *Glasgow Airport, UK, June 2007*

Photon 06, Institute of Physics , *Manchester, UK, September 2006.*

Physical Chemistry Section Meetings, *Firbush Point, Scotland, UK*

Peer-Reviewed Journal Articles

M. Chennaoui, D. Angarita-Jaimes, M. P. Ormsby, N. Angarita-Jaimes, E. McGhee, C. E. Towers, A. C. Jones, and D. P. Towers, *Optimization and evaluation of fluorescent tracer for flare removal in gas-phase PIV*. Meas. Sci. Technol. 19 (11), 115403 (2008).

D. Angarita-Jaimes, M. Ormsby, M. Chennaoui, N. Angarita-Jaimes, C. Towers, A. Jones, and D. Towers, *Optically efficient fluorescent tracers for multi-constituent PIV*. Exp. Fluids 45 (4), 623 (2008).

M Bradley, L Alexander, K Duncan, M Chennaoui, A C Jones, and R M Sanchez-Martin, *pH sensing in living cells using fluorescent microspheres*. Bioorg. Med. Chem. Lett. 18 (1), 313 (2008).

N Angarita-Jaimes, E McGhee, M Chennaoui, H Campbell, S Zhang, C Towers, A Greenaway, and D P Towers, *Wavefront sensing for single view three-component three-dimensional flow velocimetry*. Exp. Fluids 41 (6), 881 (2006).

Reprint of Publications

M. Chennaoui, D. Angarita-Jaimes, M. P. Ormsby, N. Angarita-Jaimes, E. McGhee, C. E. Towers, A. C. Jones, and D. P. Towers, *Optimization and evaluation of fluorescent tracer for flare removal in gas-phase PIV*. Meas. Sci. Technol. 19 (11), 115403 (2008).

D. Angarita-Jaimes, M. Ormsby, M. Chennaoui, N. Angarita-Jaimes, C. Towers, A. Jones, and D. Towers, *Optically efficient fluorescent tracers for multi-constituent PIV*. Exp. Fluids 45 (4), 623 (2008).

M Bradley, L Alexander, K Duncan, M Chennaoui, A C Jones, and R M Sanchez-Martin, *pH sensing in living cells using fluorescent microspheres*. Bioorg. Med. Chem. Lett. 18 (1), 313 (2008).

Optimization and evaluation of fluorescent tracers for flare removal in gas-phase particle image velocimetry

M Chennaoui¹, D Angarita-Jaimes², M P Ormsby², N Angarita-Jaimes²,
E McGhee², C E Towers², A C Jones¹ and D P Towers²

¹ School of Chemistry, University of Edinburgh, UK

² School of Mechanical Engineering, University of Leeds, UK

Received 21 March 2008, in final form 20 August 2008

Published 30 September 2008

Online at stacks.iop.org/MST/19/115403

Abstract

We report the development of optimized fluorescent dye-doped tracer particles for gas-phase particle image velocimetry (PIV) and their use to eliminate 'flare' from the images obtained. In such applications, micron-sized tracer particles are normally required to accurately follow the flow. However, as the tracer size is reduced the amount of light incident on the particle diminishes and consequently the intensity of emitted light (fluorescence). Hence, there is a requirement to identify dyes with high quantum yield that can be dissolved in conventional tracer media at high concentrations. We describe the selection and characterization of a highly fluorescent blue-emitting dye, Bis-MSB, using a novel method, employing stabilized micro-emulsions, to emulate the fluorescence properties of tracer particles. We present the results of PIV experiments, using 1 μm tracer particles of *o*-xylene doped with Bis-MSB, in which elastically scattered 'flare' has been successfully removed from the images using an appropriate optical filter.

Keywords: flare removal, particle image velocimetry, fluorescence

(Some figures in this article are in colour only in the electronic version)

1. Introduction

PIV has become a powerful tool for measuring fluid velocity owing to its non-intrusive nature [1]. In pulsed PIV, a laser beam is focused onto a light sheet which illuminates tracer particles in the flow. Light from the particles or tracers is then elastically scattered and imaged onto a CCD camera or photographic film. In doubled pulsed PIV, the tracers are illuminated twice and their images are recorded either within the same frame or onto separate frames. After correlation analysis, a 2D vector map of the fluid flow is produced. One of the major problems in practical experimental systems has been unwanted 'flare' in the recorded images. Flare is caused when the light used to illuminate the tracers also impinges on surfaces within the experimental setup. The light that is scattered from a solid surface is much more intense than that scattered from the tracer particles, giving saturation in the recorded images near these regions, and

therefore particle images and flow vectors are lost [2]. This is particularly problematic in a number of industrially important applications, for example, in turbomachinery [3–5], studies of flow and spray dynamics in automotive engine cylinders [6] and chemical engineering reactors [7, 8].

Various approaches have been taken to reduce the effects of flare. Matt black surface preparations can be beneficial for a short period [9]. However, with pulsed illumination the surface layer can rapidly become ablated. More recently, mirror-like paints containing optical absorbers have been reported for flare removal [10]. An alternative approach is to use fluorescently doped seed particles which emit light at wavelengths longer than that used for illumination. Provided sufficient chromatic separation exists between the excitation and emission wavelengths, filters can be used to prevent the intense light scattered from any solid surfaces from being imaged. The extremely high contrast ratio of commercially available bandpass filters (to $>10^5$) means that

fluorescent tracers can be used to produce measurements in close proximity to surfaces and hence facilitate the study of boundary layers, flow-structure interactions and microfluidics.

In liquid flows, the use of fluorescent tracers has been established and suitable materials are now available commercially (Dantec [11]). In these cases, the particles can be $\geq 10 \mu\text{m}$ in diameter whilst still giving suitable flow-following performance. Walther *et al* [12] employed fluorescent tracers to quantify the flow of fuel within a diesel injector. The tracers were $2 \mu\text{m}$ in size, and were successfully imaged over a relatively small, sub-mm field of view. However, the efficiency of the fluorescent emission was not quantified and did not need to be optimized owing to the high energy density of the illumination over such a small field. There has also been considerable development of fluorescent tracers for micro-PIV [13, 14], but again the field of view is sub-mm and additionally the flow velocities are sufficiently low to permit longer timed exposures ($\geq \text{ms}$) with a continuous wave laser to be used and hence multiple fluorescence photons can be obtained from individual fluorophore molecules.

In the gas phase, it is generally accepted that micron and sub-micron tracers are required for an adequate dynamic response [15]. Gharib *et al* [16] used larger phosphorescent coated particles to show the direction of motion of tracers within a flow. Whereas fluorescence persists for only 10–100 ns after excitation, phosphorescence is much longer lived. These tracers thus emitted phosphorescence for a measurable time after exposure, with the brightness gradually reducing, allowing the direction of the velocity vector to be inferred from a single exposure photograph. Automated analysis was never achieved with this technique and no quantitative data were produced. Fluorescent tracers have found application as chromatic markers of flow constituent [17] and flow phase [18–20] to enable simultaneous measurement in multiple fluid streams. However, there were limits as to the minimum size of fluorescent tracer that could be imaged [17], the PIV processing gave poor validation rates [18], there had to be a large difference in flow velocity in order for the data in the two phases to be separated [19] or large fluorescent tracers were used for the gas phase [20]. Similarly the use of fluorescent tracers and different timing of the laser pulses to compensate for the difference in velocity of the phases (air/fuel interaction in fuel injection) still required a difference in the velocity range for successful phase separation [21]. Fluorescence and Mie scatter from tracers has also been used to calculate Sauter mean drop size by optimization of the fluorophore concentration to give a cubic intensity function with respect to drop size [22]. The relevant data in this case was obtained from larger droplets in the 10–100 μm range.

In this paper, we describe the development of micron-sized fluorophore-doped tracers compatible with gas-phase flow seeding for recording high contrast PIV images. The approach adopted is to investigate several candidate fluorophores with a high quantum yield that are soluble at high concentration in suitable solvents. Furthermore, excitation in the UV, e.g. from a frequency-tripled Nd:YAG laser, is adopted, such that a long-pass (wavelength) filter can remove the unwanted Mie scattered light. Whilst

there are many commercially available dyes and documented emission spectra, much of this information concerns low dye concentrations and the optical environment of a fluorimeter cell is very different from that of a $1 \mu\text{m}$ droplet. To enable evaluation of a dye's performance at high concentration in micron-sized droplets, stable emulsions have been prepared and studied quantitatively by fluorescence spectroscopy. Subsequent tests using conventional atomizers have been conducted to assess visibility of the fluorescent tracer particles in conventional PIV imaging geometries. Finally, the application of the optimized fluorescent tracers is demonstrated to quantify a laboratory flow around a metal blade.

2. Evaluation of fluorescent dyes as dopants for flow tracers

2.1. Materials

Refined olive oil, *o*-xylene, n-dodecyltrimethylammonium bromide (DTAB) and the fluorescent dyes: 7-amino-4-methylcoumarin (Coumarin 120), 7-amino-4-trifluoromethylcoumarin (Coumarin 151), 1,4-bis(2-methylstyryl)benzene (Bis-MSB), 1,4-bis(5-phenyl-2-oxazolyl)benzene (POPOP) were obtained from Aldrich. Hydrophilic silica nanoparticles (Aerosil 300; dp = 7 nm) and ethyl cellulose (Ethocel) were kindly donated by Evonik Industries and Dow Chemicals, respectively. All materials were used as received, without further purification, and the solvents were of spectrophotometric grade or equivalent.

In the context of gas phase PIV where tracer droplets are airborne, appropriate protective measures (e.g. extractor) must be undertaken in order to avoid breathing the seeded air. Nevertheless, it should be mentioned that Bis-MSB (m.p. 180 °C) presents no significant hazard and displays a low toxicity [23, 24], while *o*-xylene (b.p. 143 °C), as most organic solvents, is classified as hazardous [24]. Both compounds are stable under ordinary conditions of use and storage [24] and no thermal instability has been noted.

2.2. Spectrofluorometric measurements on bulk dye solutions

Fluorescence spectra of bulk solutions were measured using a Fluoromax photon-counting spectrofluorometer (Jobin Yvon). Dye solutions were contained in disposable PMMA cuvettes (100% transmission above 320 nm). Excitation and emission spectra were recorded using dye solutions with concentration of $6.00 (\pm 0.06) \times 10^{-8} \text{ M}$.

2.3. Selection of a suitable dye

The desired properties of the dye for the present flare removal application are intense absorption at 355 nm, high fluorescence quantum efficiency and a fluorescence emission wavelength centred in the high-sensitivity range of silicon-based CCD cameras. For PIV experiments in multi-constituent and multi-phase flows, it is also desirable for the fluorescence emission

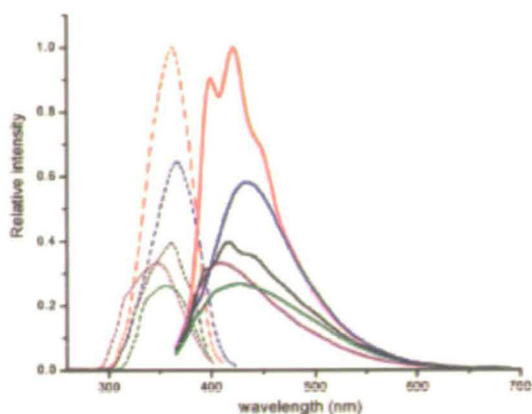


Figure 1. Excitation (dashed lines) and emission spectra (solid lines) from bottom to top of: undoped olive oil, C120, POPOP, C151 and Bis-MSB (the latter four compounds dissolved in olive oil). Emission spectra were acquired using an excitation wavelength of 355 nm. Intensities have been normalized to the maximum intensity of Bis-MSB.

bandwidth to be narrow and either contained within one of the primary colour bands, corresponding to a detection channel of a colour CCD, or located at a defined region within the visible spectrum. To satisfy both sets of requirements, a dye was sought with a strong fluorescence emission around 450 nm. Four candidate dyes, Coumarin 120 (C120), Coumarin 151 (C151), Bis-MSB and POPOP, were characterized by fluorescence spectroscopy. Initial studies were made by dissolving the dyes in olive oil which is routinely used for gas-phase flow seeding.

Excitation and emission spectra of the dye solutions are shown in figure 1, together with those of undoped olive oil. The olive oil has an emission band centred on 430 nm, due to the presence of vitamin E [25].

The coumarin dyes (C151, C120) are potentially good candidates because they are known to have a high quantum yield and a large Stokes shift (wavelength difference between the excitation and emission maxima) [26] in polar solvents [27, 28]. However, their fluorescence properties are solvent-dependent and they display a lower quantum yield and a smaller Stokes shift in non-polar solvents [29, 30], such as olive oil. The most intense emission at 450 nm was given by Bis-MSB (1,4-bis(2-methylstyryl)benzene), a stilbene derivative which has a quantum yield close to unity (0.98 [31]), a fluorescence lifetime of 1.2 ns [31] and a Stokes shift that shows little solvent dependence [31, 32] and is sufficient to enable efficient wavelength discrimination between excitation light and emission. Therefore, Bis-MSB was selected as the dye of choice.

However, the fluorescence intensity that could be achieved for Bis-MSB in refined olive oil was found to be limited by the maximum solubility of $\sim 10^{-3}$ M [33]. (The solubility is even less in paraffin oil, which is also used in PIV.) Therefore, another solvent was sought, in which Bis-MSB is more soluble

and which would be suitable for nebulization to produce tracer particles. *O*-xylene was found to satisfy both criteria, allowing a Bis-MSB concentration of 10^{-2} M to be achieved.

2.4. Use of stable emulsions to mimic the fluorescence properties of tracer particles

Whilst spectrofluorometer measurements of highly dilute bulk dye solutions provide a quantitative comparison of their respective fluorescence intensities, the dye is to be used at near saturated concentration levels in tracer droplets. In order to determine the dye concentration at which maximum fluorescence intensity will be achieved it is necessary to determine whether concentration-related self-quenching effects [34], such as the formation of dye aggregates or excimer formation, or self-absorption will limit the increase in fluorescence intensity with increasing dye concentration in tracer droplets. In a previous study, Kosiwicz *et al* [35] selected optimal fluorescent dyes for tracer droplets in two-phase PIV on the basis of spectroscopic measurements in bulk dilute solution (10^{-6} M solution in a 1 cm path-length cuvette). However, different dyes will show different self-quenching efficiencies, so that the 'optimum dye' selected on the basis of its fluorescence intensity at low concentration may prove not to be optimum at high concentration. Conventional spectrofluorometer measurements of a dye solution in a cuvette do not allow quantitative fluorescence intensity measurements at high concentrations because of the inner filter effect [34] and self-absorption over the relatively long excitation and emission path lengths (mm to cm). Therefore, we have developed a method to mimic tracer droplets by forming an oil-in-water emulsion in which the micron-sized doped droplets are dispersed within a non-fluorescent and non-miscible continuous phase. In this manner, quantitative spectroscopic measurements could be made on the droplets in a stable and controlled laboratory environment.

2.4.1. Emulsion preparation. Oil-in-water emulsions, stabilized by solid nanoparticles [36–38] of hydrophilic silica, were prepared by homogenizing 50% volume fraction of dye solution in *o*-xylene, containing 2% wt of ethyl cellulose, constituting the 'oil' phase, with the water phase containing 10^{-4} M of DTAB and 2.5% wt of dispersed silica nanoparticles. The pH of the aqueous phase was then adjusted to a value of 4.5. There must be sufficient dispersion of the dye-doped droplets within the emulsion to ensure that the fluorescence measurements report the properties of individual droplets, not a continuous phase. To achieve this, emulsions were diluted in water to 0.1% of the original concentration for fluorescence measurements. Characterization of the diluted emulsion by microscopy, laser diffraction and flow cytometry showed that the droplets were well dispersed and had a mean diameter of circa 2 μ m. An optical micrograph of a diluted emulsion sample is shown in figure 2. The diluted emulsions were stable for the duration of the fluorescence measurements.

2.4.2. Fluorescence measurements on emulsions. The fluorescence measurements were carried out using the same spectrofluorometer as used for the bulk solutions measurement

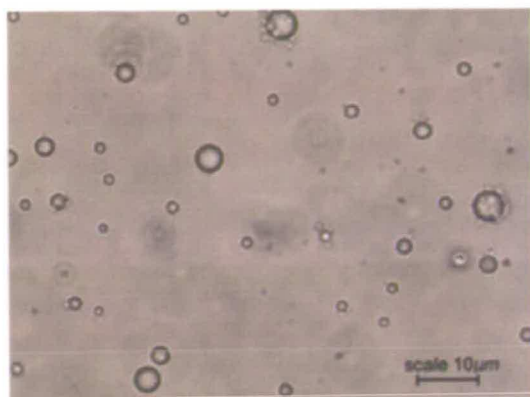


Figure 2. Optical micrograph of an aqueous emulsion of Bis-MSB-doped *o*-xylene at 0.1% dilution in water.

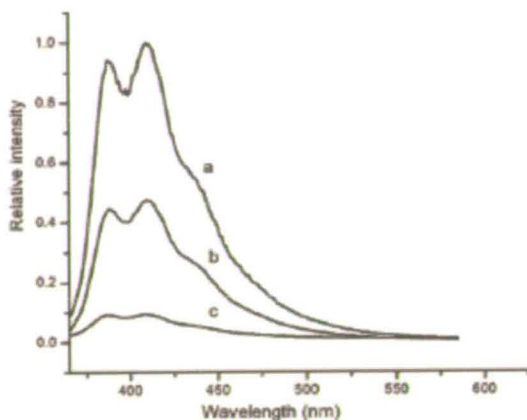


Figure 3. Fluorescence emission spectra of aqueous emulsions of $\sim 2 \mu\text{m}$ droplets of *o*-xylene doped with Bis-MSB at a concentration of (a) 10^{-2} M, (b) 5×10^{-3} M and (c) 10^{-3} M. Emission spectra were acquired using an excitation wavelength of 355 nm. Intensities have been normalized to that of the 10^{-2} M sample.

(*vide supra*), by coupling two optical fibre bundles, one to carry excitation light from the spectrometer to the sample and one to carry emission from the sample to the spectrometer. The emulsion sample was presented in a flow cell, consisting of a glass (N-51A grade with $>90\%$ transmission above 350 nm) microcapillary with a bore of 0.5 mm, fed at a constant rate of 0.5 ml min^{-1} by a syringe pump.

Figure 3 shows the fluorescence emission spectra measured for three emulsions of *o*-xylene droplets doped with Bis-MSB at concentrations of 10^{-3} M, 5×10^{-3} M and 10^{-2} M, respectively. A near linear increase in fluorescence intensity with increasing dye concentration was observed indicating that no concentration quenching is occurring up to a concentration of 10^{-2} M Bis-MSB (the limit of solubility in *o*-xylene). Thus, in principle, even higher fluorescence intensity could be achieved, if a greater concentration could be attained.

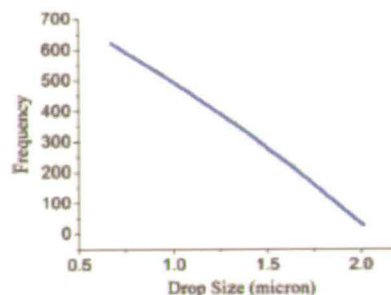


Figure 4. Drop size distribution under experimental conditions for *o*-xylene doped with Bis-MSB-doped (10^{-2} M).

3. Sizing of atomized tracers using Interferometric particle imaging

Tracer particle sizing was performed in order to verify that the optimized fluorescently doped tracers were appropriate for a wide range of gas-phase flows. The nebulization solution, 10^{-2} M Bis-MSB in *o*-xylene, was drawn through a pressure-driven medical nebulizer (Med2000 Andy Flow) into a 532 nm light sheet. The seed density was controlled by a pressure-regulated flow of nitrogen. An interferometric particle imaging (IPI) setup was developed [39, 40] in which the light directly reflected from the droplet surface and the first-order refracted beam interfere across a de-focused droplet image. Numerical analysis shows that the number of interference fringes across the image is proportional to the droplet size. The experimental setup was formed to give approximately equal intensity of reflected and first-order refracted beams at a scattering angle of 70° and a camera (LaVision Flowmaster 3) was used with a Nikon Plan 20 0.4 ELWD microscope objective. Conversion relationships between the number of interference fringes and the drop size [41] are available and have been applied to the imaging setup giving a value of approximately 1.5 fringes per micron.

Bis-MSB-doped *o*-xylene tracers were nebulized using the same seeding pressure and experimental conditions as those later used for the acquisition of PIV images (*vide infra*). For a population of 1000 droplets a mean drop size of $0.94 \mu\text{m}$ was obtained with the size distribution shown in figure 4.

The visibility of these tracers was evaluated with a field of view of the same size as laser sheets typically used with PIV illumination (height circa 40 mm). It was found that satisfactory images of the fluorescence emission of micron-sized tracers could be obtained with as little as ~ 30 mJ pulse energy of 355 nm laser radiation at F# of 4, for Bis-MSB at 10^{-2} M, as shown in figure 5. This compares very favourably with two previous studies in which another stilbene derivative, Stilbene 3 (also known as Stilbene 420), was used in UV-excited tracer droplets for two-phase PIV [21, 35]. In both cases, 355 nm pulse energies of 100 mJ were used. Driscoll *et al* do not indicate the size of their tracer particles, but Kosiwczuk *et al* state a diameter range of 1–5 μm . Given the cubic dependence of fluorescence intensity on diameter,



Figure 5. Image of emission from micron sized Bis-MSB fluorescent tracers.

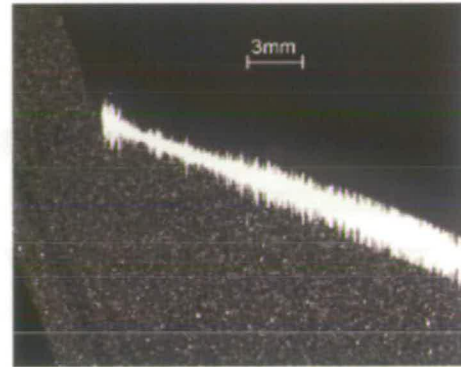


Figure 7. Imaging Mie scatter of tracers with 532 nm illumination.

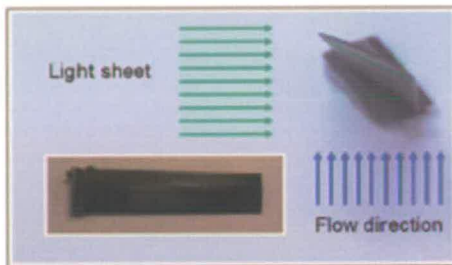


Figure 6. Schematic of the camera view and laser sheet orientation for a laboratory flare removal experiment. The inset (lower left) is an image of the gas turbine blade used.

it is feasible that the images reported in the latter study are dominated by particles at the high end of the diameter range.

4. Imaging of fluorescent tracers for PIV

To demonstrate the efficacy of the developed dye solutions for PIV, a laboratory experiment was performed to examine the flow against a turbine blade surface. The experiment was setup as shown schematically in figure 6 with the tip of the blade towards the camera, the laser sheet impinges on the lower surface of the blade and a flow is generated vertically upwards over the blade surface, which is representative of turbomachinery applications for PIV.

The tracers were evaluated using two single-cavity pulsed Nd:YAG lasers (Continuum Surelite II-10). The first set of measurements was performed using conventional 532 nm illumination by fitting doubling crystals to the laser cavities; the two laser beams were combined using a 532 beam splitter with two dichroic mirrors positioned on the beam path to remove any remaining 1064 nm energy.

Laser beams were formed into light sheets with a height of circa 40 mm at the focus. The exact alignment of the laser sheets was critical to ensure that the same volume was

illuminated by both the first and the second pulse. A JAI CV-A50 $\frac{1}{2}$ inch camera was placed directly into the sheet (protected by a suitable neutral density filter) to enable correct alignment of the two laser sheets.

A flow field was generated using three pressure-driven nebulizers (Med2000 Andy Flow); their seeding pressure was set to 0.5 bar with a regulator attached to a N_2 cylinder. The flow from the three nebulizers was collected in a flexible pipe and placed under the metal blade. The blade was tilted such that its entire lower surface was directly visible to the PIV camera and was illuminated by the laser sheet.

An Imager camera (LaVision Flowmaster 3, cooled but not intensified) was used with a Nikon 105 mm lens at F# 5.6. Images were recorded, corrected and processed using Davis version 7.2 from LaVision. Mie scattered light was recorded by the camera on double-framed images with a pulse separation of 70 μ s between laser pulses; a laser energy of 6 mJ per pulse was used for illumination of the flow.

Under this configuration, flare was generated on the surface of the blade as shown in the white saturated areas of figure 7. The laser light directly Mie scattered from the blade surface is many orders of magnitude more intense than that scattered by the 1 μ m tracers causing the greyscale range of the detector to be exceeded. Under saturation at particular pixels, charge is leaked out to the neighbouring area thereby generating a region of unusable pixels on the detector where the particle images cannot be observed and hence flow measurements are impossible.

The double framed images were processed using the adaptive multigrid cross-correlation algorithm in Davis; lens aberrations were accounted for using the de-warping tool available in Davis using images taken of a white light illuminated target. A window size of 128 \times 128 pixels was used for the first pass which was then decreased to 64 \times 64 pixels with 25% overlap for the second pass; these parameters were selected to provide a clear visualization of the low velocity vectors below the blade. The resulting vector field is shown in figure 8 which has the seeding image as background.

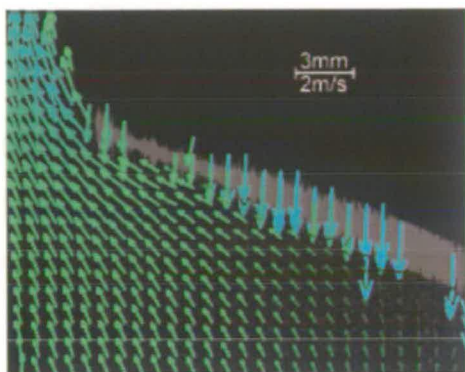


Figure 8. Velocity vectors of tracers with 532 nm illumination.

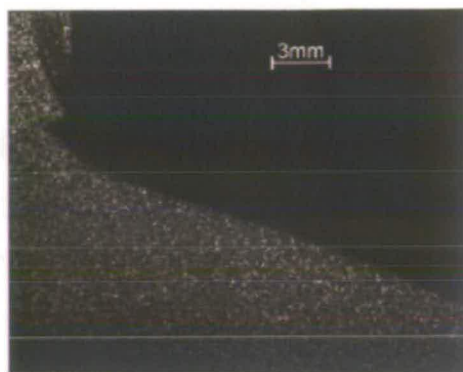


Figure 9. Imaging fluorescence of tracers with 355 nm illumination.

The resulting vector map shows that flare generated on the blade surface prevented seed imaging and velocity measurements within the region with saturated pixels, hence data reporting the interaction of the flow with the surface cannot be obtained. Similarly, light reflected from the surface also produced randomly located spurious vectors.

To achieve flare removal the Nd:YAG laser was frequency tripled to 355 nm by adding tripling crystals to both laser cavities. It was found that standard high reflectivity dielectric mirrors did not remove all of the second harmonic from the 355 nm pulse. This problem was overcome using equilateral fused silica prisms on both beams to separate the harmonics by refraction. The two beams were combined using a 355 nm half wave plate and a polarization mixer. Light sheets were formed and their correct alignment was obtained following a similar procedure as that for the 532 nm setup using the JAI CV-A50 $\frac{1}{2}$ inch camera. Bis-MSB tracers were used at a concentration of 10^{-2} M in *o*-xylene; the imaging lens blocked 355 nm Mie scattered radiation hence no additional filtering was required.

Measurements on the blade were repeated using 30 mJ UV illumination, acquiring double-framed images with a pulse separation of 70 μ s. In this case no flare was produced as shown in figure 9. The lower surface of the blade upon which the laser sheet is incident is visible. Blue fluorescence from the Bis-MSB doped tracers generated high contrast particles within the images. Such images could be obtained for several minutes before agglomeration of the tracers on the blade surface produced a detectable fluorescence.

After image correction, velocity vectors were calculated with the same cross-correlation parameters used for conventional 532 nm illumination. The vector map obtained is shown in figure 10. The inset figure demonstrates the ability to measure up to the blade surface. Vectors are obtained within 75 μ m of the surface corresponding to one interrogation window size at 4×4 pixels when the field of view is ~ 20 nm.

The removal of the image 'flare' has enabled velocity vectors to be obtained right up to the surface of the metal blade. It can also be seen that the continuity of the velocity field is

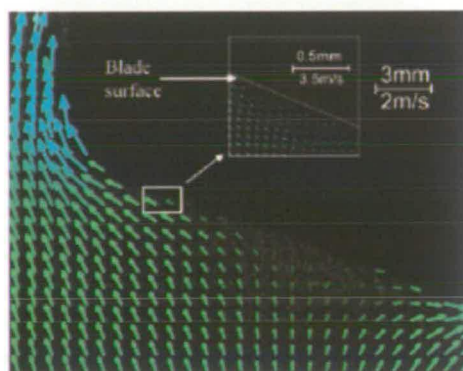


Figure 10. Velocity vectors of tracers with 355 nm illumination.

considerably improved. With Mie imaging, the presence of flare results in the loss of the vectors from all interrogation regions containing some saturated pixels (see figure 8) which increases the size of the region where the velocity information is lost. In contrast, with fluorescence imaging the velocity data show excellent continuity along the blade surface and around its left-hand edge.

5. Conclusion

A laboratory method, employing stabilized micro-emulsions, has been devised for assessing and optimizing the fluorescence properties of dye-doped droplets for use in particle imaging. Using this method, quantitative fluorescence spectroscopy can be performed on micron-sized droplets at the high dye concentrations required for successful PIV measurements in gas-phase flows. Micron-sized droplets of Bis-MSB in *o*-xylene show intense fluorescence at 450 nm, when excited at 355 nm, and are highly suitable for particle imaging using a frequency-tripled Nd:YAG laser. Concentrations up to 10^{-2} M

have been achieved, producing a higher fluorescence intensity than that previously obtained using Bis-MSB in olive oil [33]. The fluorescence properties of Bis-MSB are such that double pulsed PIV experiments can be successfully conducted with standard solid-state lasers and silicon-based CCD cameras.

The optimized tracers are not only significantly smaller ($< 1 \mu\text{m}$ mean diameter) than those developed previously [35] but can be imaged with a relatively low laser pulse energy of 30 mJ at 355 nm over a vertical field of view up to 40 mm.

The effectiveness of these fluorescent tracers for flare removal in PIV experiments has been demonstrated, enabling measurements to be made in close proximity to reflective or scattering surfaces. This fluorescent PIV technique is expected to find applications in boundary layer studies and flow structure interactions in turbomachinery, automotive and chemical process industries.

Acknowledgments

The authors would like to acknowledge funding from EPSRC under grant references GR/S69108 and GR/S69115. DA is grateful for support through a Roberto Rocca fellowship.

References

- [1] Adrian R J 1991 Particle-imaging techniques for experimental fluid-mechanics *Ann. Rev. Fluid Mech.* **23** 261–304
- [2] Prasad A K 2000 Particle image velocimetry *Curr. Sci.* **79** 51–60
- [3] Liu B, Yu X, Liu H, Jiang H, Yuan H and Xu Y 2006 Application of SPIV in turbomachinery *Exp. Fluids* **40** 621–42
- [4] Wemert M P 2000 Application of DPIV to study both steady state and transient turbomachinery flows *Opt. Laser Technol.* **32** 497–525
- [5] Yu X J and Liu B J 2007 Stereoscopic PIV measurement of unsteady flows in an axial compressor stage *Exp. Therm. Fluid Sci.* **31** 1049–60
- [6] Aleiferis P G, Hardalupas Y, Taylor A M, Ishii K and Urata Y 2005 Cyclic variations of fuel-droplet distribution during the early intake stroke of a lean-burn stratified-charge spark-ignition engine *Exp. Fluids* **39** 789–98
- [7] Kumar A, Gogate P R and Pandit A B 2007 Mapping of acoustic streaming in sonochemical reactors *Ind. Eng. Chem. Res.* **46** 4368–73
- [8] Rodriguez E, Castillejos A H and Acosta F A 2007 Experimental and numerical investigation of fluid flow and mixing in pachuca tanks *Metal. Mater. Trans. B* **38** 641–56
- [9] Arnot A, Schneider G, Neitzke K P, Agocs J, Sammler B, Shroder A and Kompenhans J 2003 Multi-window PIV for high-lift measurements, instrumentation in aerospace simulation facilities *ICIASF '03* pp 44–53
- [10] Konrath R, Klein C, Schröder A and Kompenhans Jr 2008 Combined application of pressure sensitive paint and particle image velocimetry to the flow above a delta wing *Exp. Fluids* **44** 357–66
- [11] Dantec Ltd 1998 Linking PIV and LIF to measure two-phase water-bubble flows *Dantec Newsletter* **5**
- [12] Walther J, Schaller J K, Wirth R and Tropea C 2000 Characterization of cavitating flow fields in transparent diesel injection nozzles using fluorescent particle image velocimetry (FPIV) *Liquid Atomization and Spray Systems* ed C Tropea and K Heukelbach (Darmstadt, Germany: Bremen) p 18
- [13] Meinhart C D, Wereley S T and Santiago J G 1999 PIV measurements of a microchannel flow *Exp. Fluids* **27** 414–9
- [14] Santiago J G, Wereley S T, Meinhart C D, Beebe D J and Adrian R J 1998 A particle image velocimetry system for microfluidics *Exp. Fluids* **25** 316–9
- [15] Melling A 1997 Tracer particles and seeding for particle image velocimetry *Meas. Sci. Technol.* **8** 1406–16
- [16] Gharib M, Herman M A, Yavrouian A H and Sarchia V 1985 Flow velocity measurement by image processing of optically activated tracers *AIAA 23rd Aerospace Sciences Meeting Paper No. 85-0172* p 6
- [17] Towers D P, Towers C E, Buckberry C H and Reeves M 1999 A colour PIV system employing fluorescent particles for two-phase flow measurements *Meas. Sci. Technol.* **10** 824–30
- [18] Boedec T and Simoons S 2001 Instantaneous and simultaneous planar velocity field measurements of two phases for turbulent mixing of high pressure sprays *Exp. Fluids* **31** 506–18
- [19] Rottenkolber G, Gindele J, Raposo J, Dullenkopf K, Hentschel W, Wittig S, Spicher U and Merzkirch W 2002 Spray analysis of a gasoline direct injector by means of two-phase PIV *Exp. Fluids* **32** 710–21
- [20] Lee J and Nishida K 2003 Simultaneous flow field measurement of D.L gasoline spray and entrained ambient air by LIF-PIV technique *Combustion and Flow Diagnostics* (Detroit, MI: Society of Automotive Engineers) pp 83–98
- [21] Driscoll K D, Sick V and Gray C 2003 Simultaneous air/fuel-phase PIV measurements in a dense fuel spray *Exp. Fluids* **35** 112–5
- [22] Jermy M C and Greenhalgh D A 2000 Planar dropletizing by elastic and fluorescence scattering in sprays too dense for phase Doppler measurement *Appl. Phys. B: Lasers Opt.* **71** 703–10
- [23] Huang J, Zhang H and Jin G 2008 Environment-friendly nontoxic degradable scintillation solution *CN Patent No. 101149350*, application No. 200610062711
- [24] Dikshith T S S and Diwan P V 2003 *Industrial Guide to Chemical and Drug Safety* (Hoboken, NJ: Wiley-Interscience)
- [25] Kyriakidis N B and Skarkalis P 2000 Fluorescence spectra measurement of olive oil and other vegetable oils *J. AOAC Int.* **83** 1435–9
- [26] Lakowicz R J 1999 *Principles of Fluorescence Spectroscopy* (New York: Kluwer/Plenum)
- [27] Reynolds G A and Drexhage K H 1975 New coumarin dyes with rigidized structure for flashlamp-pumped dye lasers *Opt. Commun.* **13** 222–5
- [28] Schimitschek E J, Trias J A, Hammond P R, Henry R A and Atkins R L 1976 New laser dyes with blue-green emission *Opt. Commun.* **16** 313–6
- [29] Nad S and Pal H 2001 Unusual photophysical properties of coumarin-151 *J. Phys. Chem. A* **105** 1097–106
- [30] Pal H, Nad S and Kumbhakar M 2003 Photophysical properties of coumarin-120: unusual behavior in nonpolar solvents *J. Chem. Phys.* **119** 443–52
- [31] Sujatha J and Mishra A K 1996 Bis-MSB, a laser dye as a polarization probe for microheterogeneous media *J. Photochem. Photobiol. A* **101** 245–50

- [32] Bush T E and Scott G W 1981 Fluorescence of Distyrylbenzenes *J. Phys. Chem.* **85** 144–6
- [33] Chennaoui M, McGhee E J, Towers C E, Jones A C and Towers D P 2006 Flare removal in gas phase PIV: Optimization of fluorescent tracers *13th Int. Symp. on Appl. Laser Techniques to Fluid Mechanics (Lisbon, Portugal, 26–29 June)*
- [34] Valeur B 2002 *Molecular Fluorescence: Principles and Applications* (Weinheim: Wiley-VCH)
- [35] Kosiwczuk W, Cessou A, Trinite M and Lecordier B 2005 Simultaneous velocity field measurements in two-phase flows for turbulent mixing of sprays by means of two-phase PIV *Exp. Fluids* **39** 895–908
- [36] Binks B P and Lumsdon S O 1999 Stability of oil-in-water emulsions stabilised by silica particles *Phys. Chem. Chem. Phys.* **1** 3007–16
- [37] Binks B P and Whitby C P 2004 Silica particle-stabilized emulsions of silicone oil and water: Aspects of emulsification *Langmuir* **20** 1130–7
- [38] Binks B P and Whitby C P 2005 Nanoparticle silica-stabilised oil-in-water emulsions: improving emulsion stability *Colloids Surf. A* **253** 105–15
- [39] Damaschke N, Nobach H, Norn T I, Semidetnov N and Tropea C 2005 Multi-dimensional particle sizing techniques *Exp. Fluids* **39** 336–50
- [40] Glover A R, Skippon S M and Boyle R D 1995 Interferometric laser imaging for droplet sizing: A method for droplet-size measurement in sparse spray systems *Appl. Opt.* **34** 8409–21
- [41] Semidetnov N and Tropea C 2004 Conversion relationships for multidimensional particle sizing techniques *Meas. Sci. Technol.* **15** 112–8

Optically efficient fluorescent tracers for multi-constituent PIV

D. A. Angarita-Jaimes · M. P. Ormsby ·
M. Chennaoui · N. C. Angarita-Jaimes ·
C. E. Towers · A. C. Jones · D. P. Towers

Received: 15 November 2007 / Revised: 22 July 2008 / Accepted: 20 August 2008 / Published online: 10 September 2008
© Springer-Verlag 2008

Abstract This paper was motivated by the need for improved instrumentation to study mixing processes in multi-constituent and multi-phase fluid systems. The development of a single colour camera PIV system that can image micron size spectrally distinct fluorescent droplets in a multi-constituent gas phase flow is reported. Concentrations of fluorescent dyes in solution have been optimised to achieve sufficient fluorescence visibility. The adopted philosophy is to exploit the inherent co-registration offered by a 3-chip colour CCD camera with the images recorded in the three colour planes enabling flow constituent/phase to be determined as well as pulse order. The results show that the spectral discrimination process is robust and in a well mixed gas-phase flow the average error between the flow velocities in the two constituents is <4%. The use of UV excitation (on suitably excitable dyes) has the added benefit of spectrally separating the excitation wavelength from the imaging bandwidth to allow 'flare removal'.

1 Introduction

PIV has become a powerful tool for measuring fluid velocity owing to its non-intrusive nature (Adrian 1991). In pulsed PIV a laser beam is focussed into a light sheet which

illuminates tracer particles in the flow. Light from the particles or tracers is then elastically scattered and imaged onto a CCD camera or photographic film either within the same frame or onto separate frames. After correlation analysis a 2D vector map of the fluid flow is produced (Westerweel 1997). One of the challenging application areas for PIV is in the quantification of multi-phase and multi-constituent flows (Hassan 1998). The application of conventional PIV techniques to such flows generates images from the tracers in both constituents or phases and hence velocity vectors across the overall image field. However, such an approach does not allow quantification of the flow fields in each component of the flow and hence further parameters such as relative velocity and mixing cannot be quantified.

A number of two-phase flows occur where one phase is naturally present as bubbles or solid particles—the dispersed phase. The size of the bubbles or solid particles is typically large (~100 µm) compared with the seed particles (~20 µm) in the continuous liquid phase. Therefore, the flow phases have been discerned based on particle image size (Jakobsen et al. 1996), or brightness (Kiger and Pan 2000). These techniques require a particle size ratio of ~5 for reliable processing (Kiger and Pan 2000). In the case of sprays injected into the gas phase the particle size range of the droplets may extend from the sub-micron to tens of microns and therefore overlaps the micron sized particles typically added to the gas phase (Melling 1997). Typical examples are fuel sprays for combustion in automotive and gas turbine engines, agricultural sprays and metered dose inhalers. Furthermore, there are multi-constituent gas phase flows where mixing is important and in such cases both components will need similarly sized seed particles to achieve adequate flow following. Hence flow constituent discrimination by particle size or brightness is

D. A. Angarita-Jaimes · M. P. Ormsby ·
N. C. Angarita-Jaimes · C. E. Towers · D. P. Towers (✉)
School of Mechanical Engineering, University of Leeds,
Leeds LS2 9JT, UK
e-mail: d.p.towers@leeds.ac.uk

M. Chennaoui · A. C. Jones
School of Chemistry, University of Edinburgh, West Main Road,
Edinburgh EH9 3JJ, UK

not feasible. In these cases optically active tracers, normally producing a fluorescent or phosphorescent emission over a range of wavelengths different from that of the illuminating laser beam, provide a means of identifying the origin of a particular tracer particle.

Optically active tracers were first used in full field instrumentation in 1985 to determine flow direction from phosphorescent image tails (Gharib et al. 1985). Fluorescent tracers are being developed for flare elimination in boundary layer measurements, and imaging of $\sim 2 \mu\text{m}$ fluorescent tracers over millimetre fields of view has been reported (Walther et al. 2000). Fluorescent tracers of $\sim 20 \mu\text{m}$ diameter have been used in liquid flows to remove flare close to large dispersed particles (Hassan 1998; Dantec 1998).

In multi-phase and multi-constituent flows in the gas phase fluorescent tracers are also the mechanism of choice to differentiate the seeding in one phase from that in another. Two groups have addressed the problem with regard to gasoline direct injection (GDI) sprays using 532 nm laser light sheets with conventional tracers in one phase and fluorescent tracers in the other (Rottenkolber et al. 2002, Boedec and Simoens 2001). The emission spectrum of the fluorescent dopant was selected to be separate from the excitation and hence combinations of filters were used on a pair of monochrome CCD cameras, positioned 180° opposite each other such that each camera only produced images of one type of tracer. Whilst multi-phase velocity vectors were produced, the data suffered from either poor validation rates (Boedec and Simoens 2001) or required the phases to have differing velocities (Rottenkolber et al. 2002) implying that the optical discrimination of the fluorescent tracers from the conventional tracers was not completely successful. Previous work in multi-constituent flows used rhodamine-doped droplets and conventional tracers illuminated with a first pulse at 532 nm and a second from a pulsed dye laser at $\sim 640 \text{ nm}$ (Towers et al. 1999). Images were obtained on two monochrome cameras with filters, such that one camera only imaged the second pulse and fluorescence emission, with the other recording Mie scattering from the first pulse. By performing logical operations between the images, based on the presence or absence of co-located fluorescence at the same pixel location as the green Mie scatter, it was possible to obtain separate fields for the first pulse tracers for each constituent of the flow. However, the efficiency of the dyes was insufficient to allow fluorescent droplets of $<5 \mu\text{m}$ to be imaged when using 532 nm as both fluorescence pump, requiring high energy $>100 \text{ mJ}$, and for Mie imaging, which only requires low energy 1–3 mJ. This led to the use of an inefficient optical system requiring dense filters that generated image distortions. All the gas phase multi-constituent and multi-phase flow work

reported depends on image processing algorithms to separate the flow constituent information from the two cameras. Therefore, sub-pixel registration is important to increase the reliability of processing, but is experimentally difficult, owing to the different distortions introduced by the filters used on each camera. Furthermore, constituent discrimination errors are introduced when particle images from the two constituents overlap. The measurement of 3-component velocities (via stereoscopic arrangements) in a two constituent/phase flow using such multi-camera setups for each view has not been attempted owing to the experimental complexity of the system.

Considering that no reliable data has been obtained on two-phase flows with the available techniques, we present a strategy for multi-constituent flow measurement in the gas phase, using an all solid state laser, a single 3-chip colour camera and the development of two fluorescent dopants with widely different emission spectra. For each constituent of the flow, a fluorescent dye was chosen to emit light at a particular wavelength in order to discriminate between the types of tracer particle and hence flow constituent or phase. The adopted philosophy is to exploit the inherent co-registration offered by a 3-chip colour CCD camera with the images recorded in the three colour planes, enabling flow constituent/phase to be determined as well as pulse order with the possibility of obtaining three-components of velocity by adding a second 3-chip colour camera in a stereoscopic arrangement. The use of UV excitation, from a frequency tripled Nd:YAG laser, has the added benefit of spectrally separating the excitation wavelength from the imaging bandwidth and hence filters in particular colour channels are not required. Experimental data is presented to confirm the performance of the approach. Using a single type of fluorescent tracer, a conventional single-phase PIV experiment can be performed where the laser light, or 'flare', scattered by the surfaces in an engineering rig, can be removed by appropriate filtering thereby allowing measurements in close proximity to the surface (Chennaoui et al. 2006).

2 Fluorescent tracer selection and imaging system

The desired properties of the fluorescent dyes in these applications are strong absorption at 355 nm (frequency tripled Nd:YAG), high quantum efficiency, sufficient spectral separation between excitation and emission wavelengths and a fluorescence emission spectrum in the high sensitivity range of silicon based CCD cameras. For use with colour cameras in the multi-constituent PIV experiments described here, it is also desirable for the fluorescence emission bandwidth to be contained within one of the primary colour bands corresponding to a

detection channel of the colour CCD, and for there to be sufficient chromatic separation between the illumination and the fluorescence and between the fluorescence and any wavelengths used for Mie scattering. It was found that dyes developed originally for dye lasers tend to offer higher solubility (to maximise fluorescent yield) in a range of solvents that are suitable for atomisation as gas phase seeding. Previously, Bis-MSB dye, which emits in the blue, 400–470 nm, when excited at 355 nm (McGhee et al. 2005), was employed at concentrations up to 5×10^{-3} molar (M). Here, an increased dye concentration has been achieved, improving the fluorescence intensity, by using xylene as a solvent. Dye concentrations up to 1×10^{-2} M have been achieved and are sufficiently stable for routine laboratory use. The other flow constituent may be seeded with conventional tracer particles and illuminated with 532 nm laser light to give Mie scattered images only, whereas combined 355- and 532-excitation of the Bis-MSB doped tracers will generate both fluorescence (blue) and Mie (green) images, thereby differentiating between the tracers. It is assumed that either the imaging lens will block any Mie scattered 355 nm radiation or that a long-pass filter with a cut-off wavelength at approximately 400 nm is used. With this strategy, the tracers may be discriminated using a first pulse of 355 and 532 nm radiation, with pulse energies of typically 50 and 2 mJ, respectively. The red image channel of a colour detector remains unused and hence an Nd:YAG pumped dye laser can generate a second pulse, giving Mie-scattered images from both types of tracer in the 620–660 nm region.

Red fluorescent tracer particles have also been investigated, based on DCM dye dissolved in DMSO. Similar concentrations up to 1×10^{-2} M have been achieved. DCM has absorption bands conveniently located at both 355 and 532 nm giving a wide range of applications. For single phase/constituent flows, the DCM tracers may be used with a filtered monochrome camera and a standard twin-cavity Nd:YAG laser with both outputs at 532 nm in order to remove flare from the images. The filter is selected to block the 532 nm excitation whilst transmitting the fluorescence. In multi-constituent flows, DCM tracers can be used in one flow constituent whilst the Bis-MSB tracers are used in the other. Simultaneous excitation of both dyes can be achieved using 355 nm excitation from one Nd:YAG cavity, giving chromatically separate images in the blue and red channels of a colour camera, thereby achieving flow constituent discrimination. A low energy, 1–2 mJ, second pulse at 532 nm will generate Mie scatter from both types of tracer in the green channel. Hence the two vector fields can be obtained. This approach has the advantage that only solid state lasers are required.

This work has utilised a 3-chip colour CCD Hitachi HV-F22F digital camera which internally separated the imaged



Fig. 1 Image of the tracer droplets doped with Bis-MSB (left) and DCM (right), excited by a 355 nm laser light sheet

light into bandwidths of red, green and blue that are directed to the appropriate CCD chip. This allowed three co-aligned images to be recorded simultaneously. An image of the experimental flow, where both the Bis-MSB and DCM doped tracer droplets are illuminated using a sheet of laser light at 355 nm, is shown in Fig. 1. Qualitatively it can be seen that the emissions from the Bis-MSB and DCM droplets are obtained in the blue and red channels of the CCD, respectively. If the fluorescence emission is ideally matched to the CCD response, completely separate images of the two types of tracer are obtained in the blue and red image layers. A second pulse at 532 nm will produce Mie scatter images of both tracers within the green layer. Cross-correlation between the red and green layer should produce vectors for one constituent and between the blue and green layer the vectors for the other constituent. The extra green Mie images of the opposite flow constituent generate randomly located correlations and hence there is higher background noise in the correlation plane, but the velocity vectors can still be obtained reliably providing there are two or more tracers in each interrogation area.

3 Experimental setup and drop sizing

The dyes were evaluated using two single-cavity pulsed Nd:YAG lasers (Continuum Surelite II-10) which were fitted with frequency doubling and tripling crystals, giving a first pulse of 532 nm light and a second of 355 nm. It was found that standard high reflectivity dielectric mirrors did not remove all of the second harmonic from the 355 nm pulse; this caused initial problems of crosstalk in the

information between the colour channels. The problem was overcome by using a dispersive fused silica 15 mm equilateral prism to separate the harmonics by refraction. The experimental system is shown schematically in Fig. 2. The laser beams were formed into light sheets to illuminate the flows using a combination of a negative spherical and positive cylindrical lens. In order to align the sheet foci of both wavelengths it was necessary to expand each beam at different distances relative to the cylindrical lens. Expanding plano-concave ($f = -200$ mm) lenses were positioned in each beam and mounted on micro-blocks, giving 3-axes of linear adjustment, to aid the alignment. The beams then met at a 532-nm dichroic mirror, which was clear backed, allowing the 355-nm beam to pass through unhindered. The co-aligned expanding beams were directed through a fused silica plano-convex cylindrical lens ($f = 300$ mm) to produce a laser sheet of height circa 30 mm at the focus. The exact alignment of the two light sheets was critical; a JAI CV-A50 1/2 inch camera, protected by a neutral density (ND) filter, was placed directly in the sheet. This allowed measurements of the beam profile, thickness and allowed sheet positioning; a representative image is shown in Fig. 3 including the horizontal intensity profile. In this image, both laser pulses are visible, the thicker sheet shown is the green pulse, inside which is the 355 nm sheet. The intensity of the laser sheets was significantly reduced to obtain this data and by different amounts (to prevent permanent damage to the camera). Allowing for the difference in camera sensitivity at the two wavelengths used it is expected that the laser sheets are more similar in thickness whilst the use of the alignment camera ensured that the centre of each sheet were precisely co-aligned.

Xylene and DMSO were used as solvents for the fluorescent tracers and solutions were drawn through separate pressure-driven medical nebulisers (Med2000 Andy Flow) into the sheet. A regulator attached to a N_2 cylinder allowed the pressure and hence seed density to be varied. The atomised droplets were removed from the laboratory environment using an extraction system. Images were recorded onto a Hitachi HV-F22F 3-chip colour camera

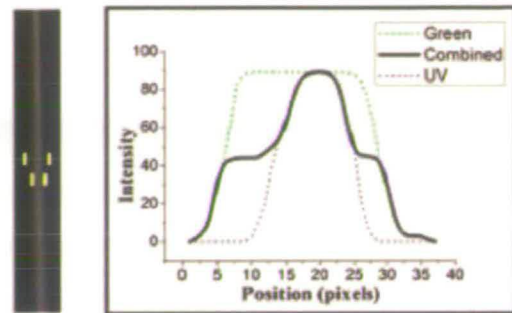
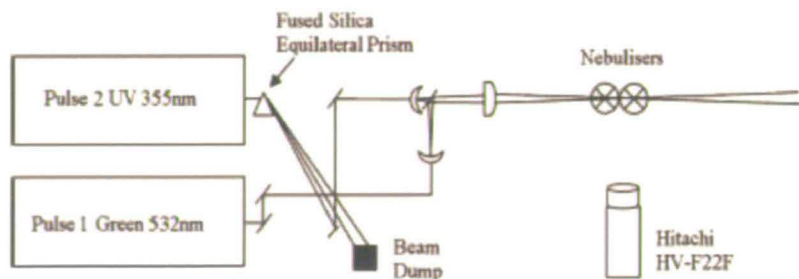


Fig. 3 Laser light sheet imaged on JAI CV-A50 and UV, green and combined horizontal intensity profile. Marks show edges of 532 nm (outer) and 355 nm (inner) laser sheets

and focused by a Nikon 105 mm lens at F#11. Brightness and sharpness on the camera were adjusted to reduce background noise level and due to a reduced sensitivity on the red channel (maximum of ~ 0.6 compared to green channel due to the presence of an IR blocking filter) the red gain was increased with all the other options left unchanged. The camera was used with a resolution of $1,280 \times 960$ pixels and the pixels are $4.65 \mu\text{m}$ square. The same settings were used for all the data presented in this paper. The lens aperture was set slightly more closed than in most PIV experiments (F#11) to give sharply focussed images in all 3 colour channels, i.e. to overcome any longitudinal chromatic aberration from the imaging optic and manufacturing tolerance on positioning of the CCD chips in the camera.

The fluorescence emission of micron sized droplets, typically used in gas phase PIV for adequate dynamic response, was analysed by exciting both types of tracers simultaneously with a 355 nm pulse. Initial examination of the images recorded showed that Bis-MSB (blue) tracers had sufficient signal-to-noise ratio whereas images from DCM (red) tracers did not. In order to ensure reliable vector processing, a wider drop-size distribution (larger mean drop size) was used for the red tracers by changing

Fig. 2 Experimental schematic



the nebulising conditions such that a higher fluorescence signal was obtained on the red channel.

The drop-size distribution for each type of tracer was determined using an interferometric method in which droplet size is calculated by measuring the angular frequency of interference fringes from defocused images. An Imager Intense camera (LaVision) was used with a Nikon Plan 20 0.4 ELWD microscope objective to obtain the required defocused imaging system (Damaschke et al. 2005). Conversion relationships between the number of interference fringes and the drop size (Semidetnov and Tropea 2004) are available and have been applied to the defocused imaging setup giving a value of approximately 1.5 fringes per micron. These conversion relationships are expected to be accurate within a few percent (Semidetnov and Tropea 2004).

Drop sizes were measured under experimental conditions (seeding pressure 0.35 bar) for a population of 1000 particles for each type of tracer. Mean droplet sizes of 1.04 μm for Bis-MSB (blue dye) and 2.25 μm for DCM (red dye) were obtained. The droplet size distribution for each solution is shown in Fig. 4.

The drop size distribution for the DCM (red) tracers spans from 1 to 5 μm but it needs to be established which part of the size distribution is recorded by the colour camera on the red channel. Small particles (<2 μm) will have a considerably lower fluorescence intensity than larger ones (2–4 μm), due to the power law dependence on particle diameter of the fluorescence signal (expected to be between a quadratic and cubic relationship). For this range of tracer sizes the particle image size is dominated by the diffraction limited performance of the imaging optic, hence the particle image diameter is approximately constant at 18 μm (approximately 4 pixels) for the magnification used. The particle images across the size range of all of the tracers therefore appear with an approximately uniform size and a Gaussian intensity profile of varying intensity for each colour channel. Furthermore, to remove crosstalk

between the colour channels (see Sect. 4), particles with low signal-to-noise ratio will be removed so the bigger droplets are the ones actually contributing to the cross-correlation process.

To quantify the fraction of the DCM-doped tracers with detectable fluorescence, two sets of images of the tracers were recorded separately on the red (fluorescence, 355 nm pulse) and green (Mie, 532 nm pulse) channels using the same seeding pressure of 0.35 bar. It is assumed that the 532 nm laser sheet energy is sufficient to make the entire distribution of tracers visible in the green layer of the colour camera. A Matlab code was developed to count the number of particles visible in an image. The ratio of number of red to number of green particles is an indicator of the part of the droplet size distribution being recorded, as only the bigger, more intense red particles will be captured. Based on a particle count evaluated over 30 green and red images an average of 73% of the particles present have sufficient fluorescence intensity to be imaged, indicating that approximately three quarters of the DCM droplet size distribution is recorded on the red channel under experimental conditions. Figure 5 shows the cumulative distribution of DCM drop size, highlighting the part of the distribution that is being recorded. Hence the mean drop size of the visible DCM doped tracers was evaluated to be 2.65 μm .

Both the Bis-MSB (blue) dye and the DCM (red) dye were used at a concentration of 10^{-2} M. No additional filtering was required to block the 355 nm Mie scattered light from reaching the CCD. To balance intensities between the Mie (first pulse) and fluorescence (second pulse) images neutral density filters were placed in the unexpanded green laser beam path to reduce its pulse energy to an appropriate level (this avoided beam profile variations found at reduced Q switch delay values). The 355 nm pulse energy was 95 mJ and only 1 mJ of 532 nm was required for Mie scattering into the green channel.

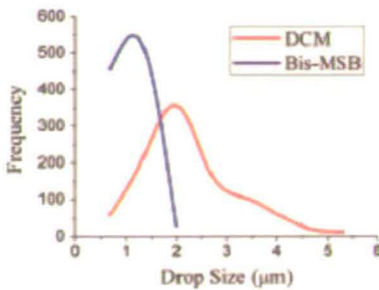


Fig. 4 Drop size distribution under experimental conditions

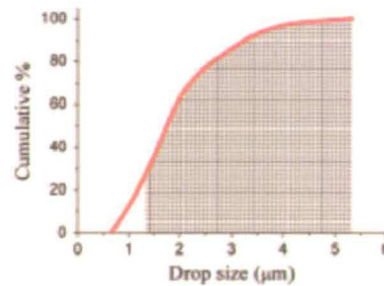


Fig. 5 Cumulative drop size distribution for DCM tracers highlighting the size range visible on the red channel of a Hitachi HV-F22F 3-chip colour camera

4 Data processing

A typical image obtained from the system is shown in Fig. 6. In this case the two seeding streams are largely spatially separated, with the Bis-MSB-doped (blue) tracers on the right and the DCM (red) tracers on the left. The image was illuminated using a pulse of 532 nm followed 50 μs later by a 355 nm pulse. Careful examination shows green to red particle pairs on the left hand side and green to blue image pairs on the right, with both flows going from the bottom to the top of the image. Figure 6 shows the original colour image (upper left) and the three separate colour channels shown in grey scales (image splitting was performed in Matlab).

In most colour CCD cameras the spectra of the red, green and blue channels are designed to overlap so that there are no colour-blind areas. However, this can also lead to crosstalk between colour channels, for example a ‘red’ fluorescent image produced a low signal in the blue and green channels. In this configuration the most damaging crosstalk is that between the red and blue images representing the separation of the images from the two flow constituents. The green channel still contains low level crosstalk from the other channels and the red and blue channels some low level crosstalk from the green Mie scattering. The potential for the DCM doped tracers to emit red fluorescence from the 532 nm pulse could also generate crosstalk but given the low pulse energy needed to produce

the Mie scattered images this is expected to be at a suitably low level.

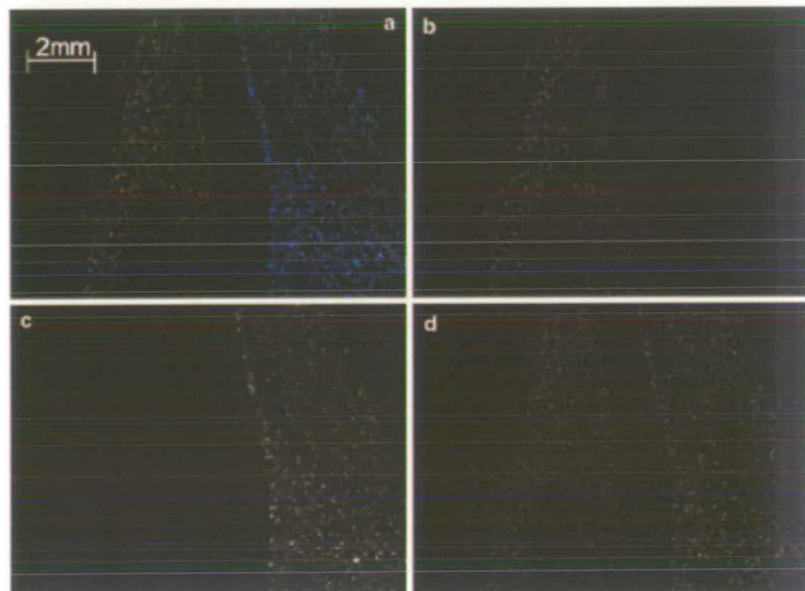
Crosstalk levels can be reduced using an approach initially applied in 3D surface contouring applications using colour imaging (Huang et al. 1999). This method was then adapted to obtain a quantitative evaluation of crosstalk between colour channels with 3-chip colour CCD cameras for 3D shape measurements (Zhang et al. 2006). Using this approach the coupling effects can be estimated for each channel respectively as the percentage of the intensity from a particular channel that is detected in the other two channels. For example, for an image in the red channel, C_{rg} and C_{rb} represent the intensities detected in the green and blue channels expressed as a percentage of the intensity on the red channel. A similar process is used for the other two channels to define the coupling matrix as proposed by Zhang et al. 2006:

$$\begin{bmatrix} C_{rr} & C_{rg} & C_{rb} \\ C_{gr} & C_{gg} & C_{gb} \\ C_{br} & C_{bg} & C_{bb} \end{bmatrix} \quad (1)$$

The first suffix for each term indicates the channel of the original image and the second suffix indicates the channel of the detected image. Elements along the diagonal are 1, i.e. $C_{rr} = C_{gg} = C_{bb} = 1$.

Images were taken separately of fluorescence emission from both types of tracers (red and blue) and Mie scattering (green) under experimental conditions. Each colour image

Fig. 6 RGB image (a) of spatially separate flow streams seeded with DCM doped tracers (left side of image) and Bis-MSB doped tracers (right side). Crosstalk compensated RGB component images are given in greyscale, red (b), blue (c) and green (d). Illumination by 532 and 355 nm light sheets with pulse separation 50 μs



was split into its RGB channels and a pixel-wise background subtraction performed on each channel. Greyscale intensity of particles in each image was measured on the three channels to obtain the crosstalk coefficients and the coupling matrix in Eq. 1:

$$\begin{bmatrix} 1 & 0.17 & 0.2 \\ 0.43 & 1 & 0.2 \\ 0.1 & 0.02 & 1 \end{bmatrix} \quad (2)$$

Equation 2 shows the coupling effects for the experimental setup used. There is a strong coupling effect between the green and the red channels and the green and the blue channels. By inverting the coupling matrix a set of corrected RGB intensities can be determined from a set of measured intensities pixel-wise across the image, thereby accounting for the crosstalk. The method was applied to a raw camera image and the results are shown in Fig. 6 where crosstalk between colour channels has been considerably reduced. Care was taken in capturing the PIV images from the flow field and in measuring the coupling effects to ensure that the intensities were maintained within the linear range of the camera.

DaVis version 7 from La Vision was used for data processing and cross-correlation analysis. A pre-processing stage was employed to perform a background subtraction of 15 grey scales to remove any residual low level crosstalk and also reduce background noise particularly on the blue channel.

Chromatic and lens distortions were accounted for in two stages. Firstly, images taken of a white-light-illuminated calibration plate were used to remove the distortions in each colour channel independently with the image de-warping tool in DaVis. Secondly, it is also necessary to estimate the distortions due to the combination of the offset between each of the three colour channels within the camera (since they are not exactly co-aligned) and chromatic lens distortions. For example, taking the green channel as the reference, there is a small offset from the green to the red and from the green to the blue images which produces false displacements on the vector maps.

A simple correction procedure was used in which images taken of a white-light-illuminated rough continuous surface were used to ensure that vectors would be obtained in every interrogation window across the whole field of view. Images were split into RGB channels using Matlab and pairs of images (red to green and blue to green) were cross-correlated in DaVis using the same calculation parameters as those later used for the vector calculation of the flow constituents.

The validity and repeatability of the correction procedure were assessed. Different surfaces were used under the same illumination conditions and the maximum difference in displacement in any interrogation region was found to be

20% with the overall offset pattern unchanged for different surfaces. Once a surface had been selected the repeatability was tested by using different light levels. The maximum difference of the average displacement was found to be 4% for different light levels. An average offset of 0.3 pixels was obtained between the red and green images and 0.75 pixels between the blue and green images. The displacements obtained in each interrogation window are then subtracted from the vector maps for the corresponding flow constituent to account for any false displacements.

5 Results and discussion

Following image distortion and crosstalk correction, the data were imported as double frames for green to red and green to blue. Background subtraction was performed and the adaptive multi-grid cross-correlation algorithm in DaVis employed to obtain the velocity vectors for each flow constituent. Finally, the vector fields corresponding to the chromatic distortion and CCD positioning offsets were removed. The resulting vector fields are shown colour coded for each flow constituent in Fig. 7 corresponding to the RGB image shown in Fig. 6. In this vector field it is clear that the crosstalk compensation has been successful and spatially separate regions corresponding to each tracer type have been obtained.

A second more interesting example is shown in Fig. 8, here the flow, generated using four nebulisers (two for each type of tracer) was brought together using a suitable pipe before being imaged. This produced a densely seeded image with abundant constituent mixing throughout. The measured region is sufficiently downstream for the two constituents to be considered as well mixed. The vector map is presented in Fig. 9 showing abundant clear regions of mixed flow where the blue vectors are thicker so that the interrogation regions with vectors from both types of tracers can be easily identified.

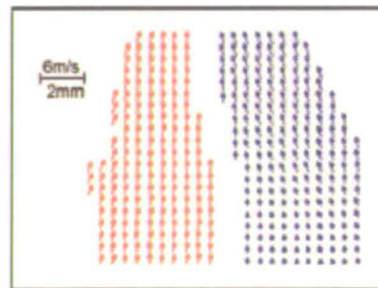


Fig. 7 PIV vectors found from cross-correlation of the data in Fig. 6. Red vectors from DCM-doped tracers, blue vectors Bis-MSB-doped tracers



Fig. 8 A second example of a multi-constituent flow. The RGB image shown was produced by illumination with 532 and 355 nm laser light sheets and a pulse separation of 50 μ s

The validity of the vector fields obtained was assessed using the post processing stage in DaVis in which a median filter and a ratio-threshold for the different peaks on the correlation plane were used to discard spurious vectors.

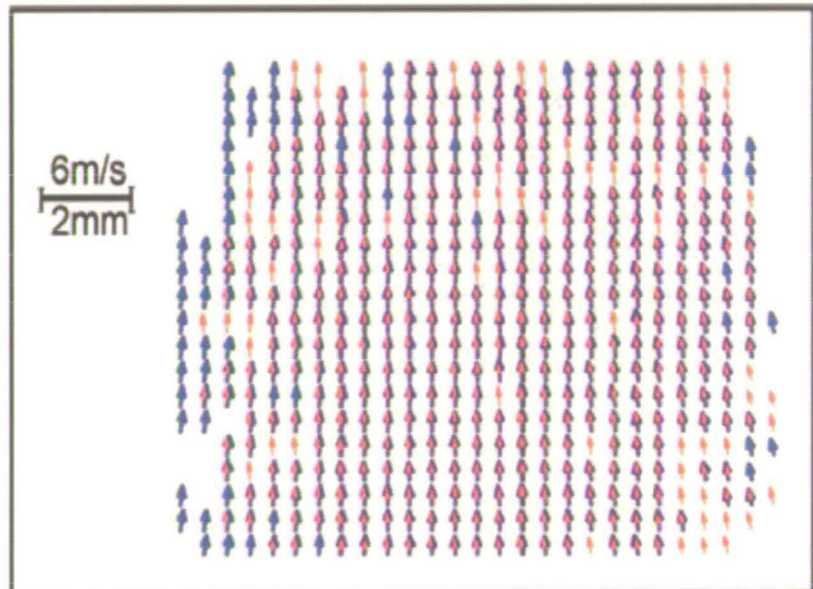
The vector fields in Fig. 9 were processed to generate velocity histograms to assess whether peak locking effects were evident in the data for either constituent. The histograms for both constituents and for both x and y velocity components showed no evidence of biasing towards integer values and hence it was concluded that peak locking effects

were not significant, i.e. the particle images in all 3 colour channels were well distributed over a number of pixels.

A quantitative comparison of the velocity vectors in each constituent has been generated by taking the resultant velocities (the magnitude of the two-component vector) from each interrogation region. By sorting the resultant velocities in ascending order for one constituent (DCM) and plotting the magnitude a continuous distribution is obtained, see Fig. 10 below. The 'position axis' refers to locations in Fig. 9 where vectors in both constituents were obtained and such that the magnitude of the velocity is increasing. The corresponding resultant velocity magnitude for the Bis-MSB tracers is plotted as points for the same positions as for the DCM tracers. It is clear that there is a good correspondence in the velocities measured at the same spatial position in the image. The average difference between the resultant velocity calculated between both types of tracers was found to be 0.25 pixels (0.046 m/s) equivalent to approximately 3.96% of the average displacement across the image.

As discussed above, larger droplets were required for DCM tracers (red) to ensure the data obtained were reliable. The limiting factors for the recording of red fluorescence are the reduced sensitivity on the red channel (compared to the blue and green channels) of the camera used and the aperture required (F# 11) for a sharp focus on the three colour planes. DCM tracers produced with a Laskin nozzle (monodisperse droplets, mean size 1 μ m) were tested separately with an Imager Intense camera (LaVision, a cooled

Fig. 9 PIV vectors found from cross-correlation of the data in Fig. 8. Red vectors from DCM-doped tracers, blue vectors Bis-MSB-doped tracers



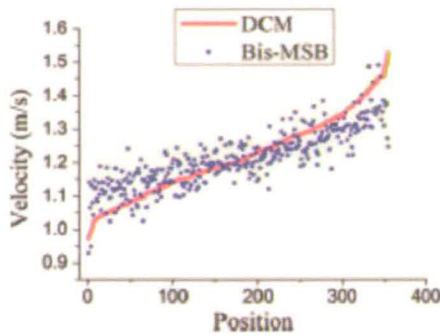


Fig. 10 Resultant velocity comparison for vector field in Fig. 9 with DCM-doped (red) and Bis-MSB-doped (blue) tracers

but not intensified camera) and focused with the same Nikon 105 mm lens. The particle images obtained were sufficiently bright to provide reliable PIV data. The fluorophores used here also have a strong potential for application in flare removal using either 355 or 532 nm illumination. The spectral separation between the excitation and the emission wavelengths provided could allow for PIV measurements in close proximity to surfaces.

6 Conclusions

Flow direction, displacements and associated velocity vectors have been measured successfully in a multi-constituent gas phase flow using a single 3-chip colour CCD camera and solid state lasers. Direct quantification of the fluid mixing velocities has been achieved and pertinent correction procedures have been implemented to reduce the effects of crosstalk and CCD offset.

The work has generated new highly efficient tracers for flare removal and tracer discrimination in multi-constituent and multi-phase flows. The use of xylene as a solvent for Bis-MSB has produced a greater fluorescence intensity than previously obtained as higher dye concentrations can be reached (*vis-à-vis* olive oil). The development of DCM-based, red-emitting, tracers that are excitable using either frequency doubled or frequency tripled pulses from an Nd:YAG laser, will enable a wide range of flare removal and multi-phase/constituent flow experiments to be performed with standard solid state lasers.

The use of a 3CCD camera for multi-constituent and multi-phase flows can also be extended to obtain three components of the velocity vector by adding a second colour camera in a stereoscopic imaging setup. This approach would be simpler to implement compared to the conventional method of multiple cameras for each stereo view with different optical filters.

Acknowledgments The authors would like to thank the Engineering and Physical Sciences Research Council (EPSRC) for funding under grant reference GR/S69108.

References

- Adrian RJ (1991) Particle imaging techniques for experimental fluid-mechanics. *Annu Rev Fluid Mech* 23:261–304
- Boedec T, Simoens S (2001) Instantaneous and simultaneous planar velocity field measurements of two phases for turbulent mixing of high pressure sprays. *Exp Fluids* 31:506–518
- Chemacui M, McGehee EJ, Towers CH, Jones AC, Towers DP (2006) Flare Removal in gas phase PIV: optimization of fluorescent tracers. In: 13th International symposium on applied laser techniques to fluid mechanics, Lisbon, Portugal, June 26–29
- Damaschke N, Nobach H, Norn T, Semidetnov N, Tropea C (2005) Multi-dimensional particle sizing techniques. *Experiments in Fluids* 39:336–350
- Dantec (1998) Linking PIV and LIF to measure two-phase water-bubble flows. *Dantec newsletter* 5 (1)
- Gharib M, Hernan MA, Yavrouian AH, Sarohia V (1985) Flow velocity measurement by imageprocessing of optically activated tracers. In: AIAA 23rd aerospace sciences meeting (Reno, Nevada, January), American Institute of Aeronautics and Astronautics Journal, Paper No. 85-0172
- Hawan YA (1998) Handbook of fluid dynamics. In: Johnson RW (ed) Multiphase flow measurements using particle image velocimetry, Chap. 36. CRC Press, West Palm Beach. ISBN-10: 0849325099
- Huang PS, Hu QY, Jin F, Chiang FP (1999) Color-encoded digital fringe projection technique for high-speed three-dimensional surface contouring. *Opt Eng* 38:1065–1071
- Jakobsen ML, Eason WJ, Greated C, Glas DH (1996) Particle image velocimetry: simultaneous two-phase flow measurements. *Meas Sci Technol* 7:1270–1280
- Kiger KT, Pan C (2000) PIV technique for simultaneous measurement of dilute two-phase flows. *ASME J Fluids Eng* 122:811–818
- McGehee EJ, Towers CH, Chemacui M, Jones AC, Towers DP (2005) Multi-constituent PIV using fluorescent particles and UV excitation. In: Sixth international symposium on particle image velocimetry, Pasadena, California, USA, September 21–23
- Melling A (1997) Tracer particles and seeding for particle image velocimetry. *Meas Sci Technol* 8:1406–1416
- Rottenkolber G, Gindele J, Raposo J, Dullenkopf K, Hentschel W, Wittig S, Spicher U, Merzkirch W (2002) Spray analysis of a gasoline direct injector by means of two-phase PIV. *Exp Fluids* 32:710–721
- Semidetnov N, Tropea C (2004) Conversion relationships for multidimensional particle sizing techniques. *Meas Sci Technol* 15:112–118
- Towers DP, Towers CH, Buckberry CH, Reeves M (1999) A colour PIV system employing fluorescent particles for two-phase flow measurements. *Meas Sci Technol* 10:824–830
- Walther J, Schaller JK, Wirth R, Tropea C (2000) Characterization of cavitating flow fields in transparent diesel injection nozzles using fluorescent particle image velocimetry (FPIV). In: ILASS Europe conference, paper I.8
- Westerweel J (1997) Fundamentals of digital particle image velocimetry. *Meas Sci Technol* 8:1379–1392
- Zhang Z, Towers CH, Towers DP (2006) Time efficient colour fringe projection system for 3D shape and color using optimum 3-frequency selection. *Opt Express* 14(4):6444–6455



pH sensing in living cells using fluorescent microspheres

Mark Bradley,^a Lois Alexander,^a Karen Duncan,^a Mourad Chennaoui,^b
Anita C. Jones^b and Rosario M. Sánchez-Martín^{a,*}

^aChemical Biology Section, School of Chemistry, University of Edinburgh, Joseph Black Building, West Mains Road, EH9 3JJ Edinburgh, United Kingdom

^bPhysical Chemistry Section, School of Chemistry, University of Edinburgh, Joseph Black Building, West Mains Road, EH9 3JJ Edinburgh, United Kingdom

Received 4 September 2007; revised 17 October 2007; accepted 22 October 2007

Available online 7 November 2007

Abstract—Intracellular pH in living cells is measured in real time at the single cell level using fluorescently covalently loaded microspheres as efficient carrier systems and stable sensors. The use of these sensors immobilized covalently onto polymeric particles allows analysis of intracellular pH flux over long period of time and eliminates the disadvantages such as dilution within the cell, elimination via leakage or compartmentalization.

© 2007 Elsevier Ltd. All rights reserved.

The pH of the cytosol affects a wide range of cellular processes and functions and, as a consequence, is regulated within a narrow range by a variety of transport proteins that transfer ions across the cellular membrane.^{1,2} Traditional methods to measure intracellular pH include the use of ³¹P NMR spectroscopy,³ microelectrodes⁴ and fluorescent probes,^{5,6} with recent approaches including the use of quantum dots (QDs)⁷ and indicators based on green fluorescent protein (GFP).⁸

Fluorescent indicators in particular are valuable tools for measuring changes in intracellular proton concentration, providing the necessary sensitivity required for optical pH measurements inside living cells. Typical fluorescent probes used for p*H*_i measurement are based on fluorescein and its many derivatives, which exhibit multiple pH-dependent equilibria.^{9,10} However, although fluorescein has been used to measure intracellular p*H*,¹¹ its use is restricted for two reasons. First because of its rapidity in leaking from cells and because it is very difficult to quantify intracellular pH (because the decrease in the cell fluorescence due to fluorescein leakage cannot be easily distinguished from that due to pH changes,¹² although

some fluorescein-derivatives such as BCECF and SNARF have been developed to overcome this problem).^{13,14} Second, because dyes of this type are typically loaded into the cell as their cell-permeable acetoxymethyl (AM) ester derivatives (the neutral molecule is able to pass across the membrane) and once inside the cell esterases cleave to reveal the acid groups; however, this method has disadvantages, such as compartmentalization and prolonged cellular leakage (as discussed above).¹⁵ Another common problem that is encountered with all potential sensors or cellular tags is dilution and cellular degradation, which results in little or no signal. Commonly used dextran conjugates offer a solution to these problems, but the drawback of this approach is their compartmentalization within endosomes, which requires the addition of chloroquine to facilitate release and subsequent pH sensing.⁷

To be used for p*H*_i measurements the fluorescent probe should be non-toxic, have a p*K*_a within the physiological range (generally between ~6.8 and 7.4) to allow detection of small pH changes typical in a cell, while having excitation and emission wavelengths suitable for detection by flow cytometry, fluorescence microscopy or other techniques relying on cell fluorescence analysis. Also the fluorescence should be stable overtime.¹⁶

Previously we have demonstrated that amino functionalised polystyrene microspheres can be used successfully for calcium sensing while avoiding dilution and cellular

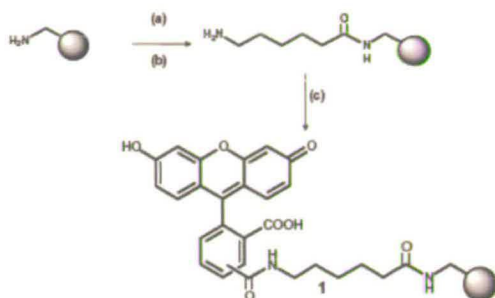
Keywords: Multifunctionalised microspheres; pH sensor; Fluorescent probes; Intracellular delivery; In situ sensing.

* Corresponding author. Tel.: +44 (0)131 651 3307; fax: +44 (0)131 650 6453.; e-mail: rosario.sanchez@ed.ac.uk

0960-894X/\$ - see front matter © 2007 Elsevier Ltd. All rights reserved.
doi:10.1016/j.bmcl.2007.10.075

degradation within the cells.¹⁷ In this paper, fluorescein-loaded microspheres are used for real-time pH sensing in living cells. Binding fluorescein covalently to microspheres eliminates leakage of the dye from cells and ensures a highly localised 'dye' that allows 'on-bead' analysis. Additionally, due to their micron size the labelled microspheres are easily visualised by microscopy.

The sensor-loaded microsphere **1** was prepared by coupling 5(6)-carboxyfluorescein onto 2 μm aminomethyl microspheres derivatized with an aminohexanoic acid spacer (Scheme 1).¹⁸ This synthesis was achieved follow-



Scheme 1. Preparation of fluorescein-labelled amino functionalised polystyrene microspheres **1**. Reagents and conditions: (a) *N*-Fmoc-aminohexanoic acid (5 equiv), HOBT (5 equiv), DIC (5 equiv), DMF, 12 h; (b) 20% piperidine in DMF; (c) 5(6)-carboxyfluorescein (5 equiv), HOBT (5 equiv), DIC (5 equiv), DMF, 12 h. HOBT = *N*-hydroxybenzotriazole; DIC = *N,N'*-diisopropylcarbodiimide, DMF = dimethylformamide.

ing Fmoc strategy for solid phase chemistry (see supporting information for experimental details).

Quantitative emission spectra were obtained using a custom-built system consisting of excitation and emission optical fibres mounted on a micro-capillary in which the sample was flown via a syringe pump. This setup allowed fluorescence measurement of a sample free from artefacts such as aggregation, scattering, photo-bleaching and sedimentation. In this manner spectrofluorimetric studies were carried out to evaluate how immobilization of the sensor affected its sensitivity to $[\text{H}^+]$ by examining the microspheres at different buffered pH values. All measurements of pH were made using the ratio of the fluorescence emitted at 525 and 610 nm. This ratio corrects for changes in cell volume and fluorochrome uptake.¹⁹ Importantly, the sensor had very similar fluorescence profile when bound to the microspheres as in solution (Fig. 1a) (for the 'in solution' details, see supporting information). Flow cytometry studies were also carried out to analyze the fluorescence properties as a function of pH and showed an identical profile (see Fig. 1b).

Several cell lines (B16F10, HEK-293T and L929) were treated in triplicate with 2 μm fluorescein-loaded microspheres **1** at a range of concentrations (0.1–0.8 mg/mL) over four different time periods (3, 6, 12 and 24 h) (for detailed protocol, see the supporting information). Following incubation, the excess microspheres were removed, and analysis by flow cytometry and fluorescence microscopy showed that cellular uptake of the microspheres was effective in all cases. The microspheres were delivered into the cells, with varying

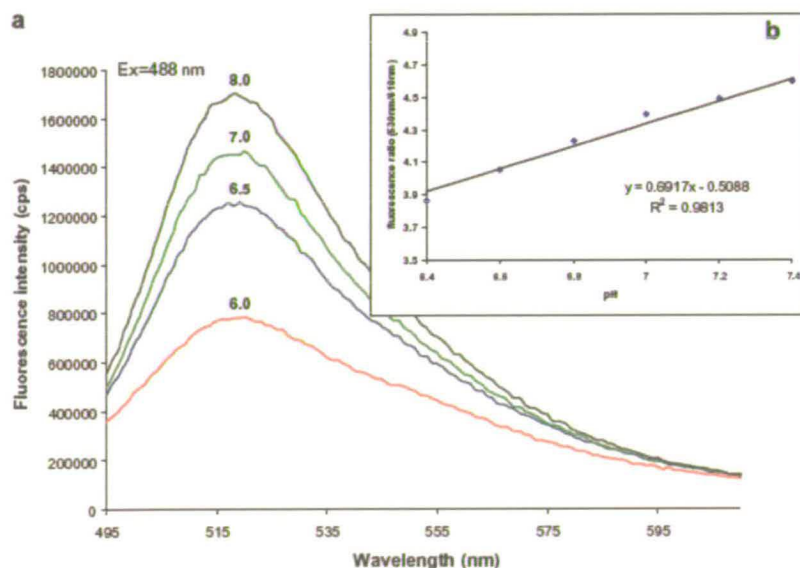


Figure 1. (a) Fluorescence emission spectra ($\lambda_{\text{ex}} = 488 \text{ nm}$) and (b) calibration curve of pH versus fluorescence intensity ratio (525 nm/610 nm) (obtained by flow cytometry analysis) for fluorescein-loaded microspheres **1** as a function of pH.²⁰

degrees of success depending on the cell type investigated. Figure 2a shows the results of HEK-293T cells (as a representative example) after incubation with 2 μm fluorescein-loaded microspheres (0.1 mg mL^{-1}) for 24 h. Figure 2b shows the confocal image obtained when B16F10 cells were incubated with 2 μm fluorescein-loaded microspheres (0.1 mg mL^{-1}) for 6 h. Cells containing the beads (ca. 30%) were isolated by fluorescence-activated cell sorting and were shown by confocal microscopy after 72 h of incubation at 37 °C to be healthy with the sensor-microspheres inside the cells. The cell membrane was stained with a red fluorescent dye (PKH26, Sigma–Aldrich) which allows long-term in vitro analysis of live cells. Figure 2c shows the flow cytometric analysis of the rate of uptake of fluorescein-labelled microspheres (0.1 mg mL^{-1}) over a range of incubation times. A total of 10,000 events per sample were analyzed. FITC (530/30 nm) band pass filters were used for fluorescence analysis of the cell suspensions. Cellular uptake was found to be concentration and time dependent.

To analyze the stability of the microspheres some experiments were performed. The fluorescence intensity of the microspheres inside cells was analyzed at different time points. We found that fluorescence was stable after these

incubation times (see supporting information for details). This result shows that the microspheres are stable and they are not metabolized by the intracellular enzymes.

To determine if the microspheres internalized by the cells are in lysosomes, an acidic organelle-selective fluorescent probe was used (LysoTracker Red DND-99, Invitrogen). The cells were incubated with fluorescein-loaded microspheres and the red dye at 37 °C. This experiment shows that the microspheres lie outside of the lysosomes, since the green fluorescence is anticorrelated with the red fluorescence, which marks the periphery of the lysosomes (see supporting information for details). This observed behaviour of the particles not being in the lysosomes greatly increases the potential applicability of these materials for cytosolic analysis.

Microsphere-induced cytotoxicity was investigated by a MTT assay to evaluate the impact of uptake on cell viability.²¹ The fluorescein-loaded microspheres were found to be non-toxic at all of the concentrations tested (see supporting information for details).

To evaluate the microspheres as intracellular pH sensors, the beads were examined in triplicate by flow cytometry with cells plated at various values of pH. A total of 10,000 events per sample were analyzed. The green fluorescence was recorded using the 515–545 nm band pass filter and the red fluorescence with the 600–620 nm band pass filter.

A calibration curve (fluorescence ratio against pH) was constructed from labelled cells resuspended in a high concentration of potassium buffer of appropriate known pH by treatment with nigericin before flow cytometry analysis.¹⁹ (In the presence of nigericin, an antiporter of H^+ and K^+ , the intracellular $[\text{H}^+]$ becomes equilibrated to the extracellular $[\text{H}^+]$.) Figure 3 shows the response obtained for HeLa and HEK-293T cells loaded with 2.0 μm fluorescein-labelled microspheres, showing

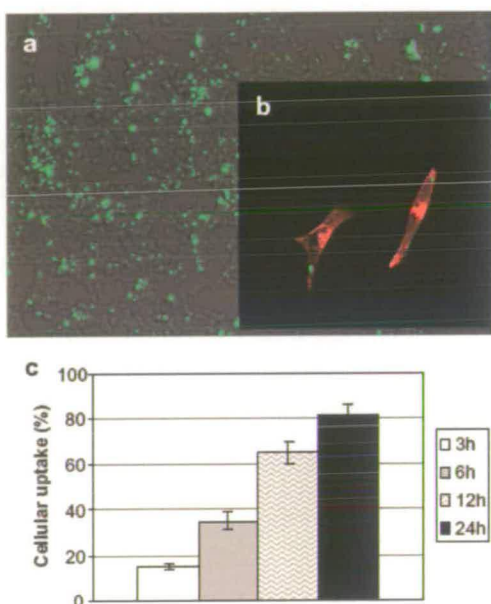


Figure 2. (a) Microscopy image for living HEK-293T cells after incubation at 37 °C for 24 h with 2 μm fluorescein microspheres. (superimposed image of bright phase and fluorescein filter images). (b) Confocal microscopy image of melanoma cells (B16F10) loaded with fluorescein microspheres 1 (green circles) after 6 h of incubation at 37 °C. (c) Flow cytometry results for cellular uptake of 2 μm fluorescently labelled microspheres into B16F10 cells overtime (0.1 mg/mL), at 37 °C with 5% CO_2 .

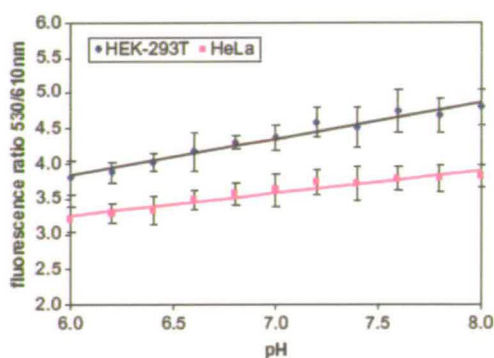


Figure 3. Fluorescence ratio of fluorescein-loaded microspheres 1 in two different living cell lines as a function of pH (obtained by flow cytometry analysis, performed in triplicate).²²

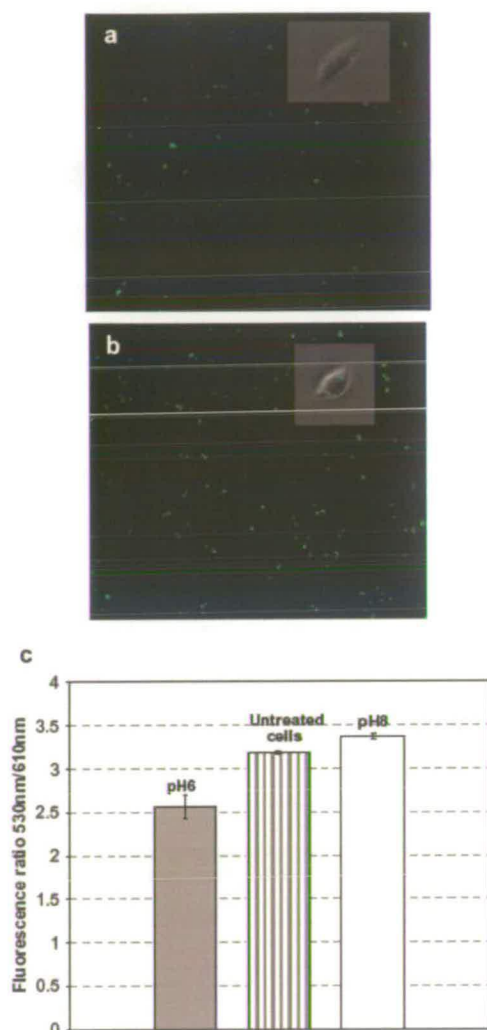


Figure 4. Fluorescence microscopy image of L929 living cells loaded with fluorescein microspheres 1 (green circles) after 12 h of incubation at 37 °C. (a and b) The green fluorescence images obtained for pH 6 and 8, respectively. (c) Quantitative analysis of fluorescence intensity ratio versus pH by microscopy.^{22,23}

how the fluorescence ratio increases as a function of intracellular pH (in equilibrium with extracellular pH) from 6.0 to 8.0. The differences in the fluorescent ratio between these two cell lines can be explained by the different capabilities of each cell line to take up microspheres.

Intracellular changes in the pH were also detected globally by microscopic examination of the fluorescein-labelled microspheres in cells. Fluorescence images of cells loaded with fluorescein microspheres were taken

at different pH values after treatment with nigericin. The images in Figure 4a and b, which are representative of all the cells that we observed, demonstrate qualitatively the pH sensitivity of these microspheres in cells. The fluorescence intensity increases when the pH increases from 6 to 8. The quantitative results in Figure 4c show that the fluorescence intensity increases by approximately 25% when pH is changed from 6 to 8. As expected, the value of the untreated cells was between pH 6 and 8.

Finally the fluorescein-loaded microspheres were compared with the traditional sensor fluorescein diacetate (FDA) by microscopy and flow cytometry. After 2 h of incubation, the fluorescence intensity for FDA decreased for the same pH value while there was no loss of fluorescence for the microspheres. These results show that the leakage problem was completely solved using the bead approach (see details in supporting information).

The use of fluorescein-loaded microspheres as intracellular pH sensors in living cells has been successfully proved using a number of different techniques such as spectrofluorometry, fluorescence microscopy and flow cytometry. Covalent binding of fluorescein to the microspheres dramatically improves the stability of the indicator overtime and eliminates leakage. At the same time it retains the properties of fluorescein for pH sensing. The fact that these polymeric particles are not toxic, in addition to their cytosolic localisation, makes them perfect candidates for intracellular pH sensing. These fluorescein-loaded microspheres provide a reliable way to perform long-term cell monitoring. These results encourage the possibility of use of this approach for other ions such as K⁺ or Na⁺ and for other applications such as monitoring of enzymatic activity or drug delivery.

Acknowledgements

This research was supported by the EPSRC. R.M.S.-M. thanks the Royal Society for a Dorothy Hodgkin Fellowship.

Supplementary data

Supplementary data associated with this article can be found, in the online version, at doi:10.1016/j.bmcl.2007.10.075.

References and notes

- Roos, A.; Boron, W. F. *Physiol. Rev.* 1981, 61, 296.
- Frelin, C.; Vigne, P.; Ladoux, A.; Lazdunski, M. *Eur. J. Biochem.* 1988, 174, 3.
- Kulichikhin, K. Y.; Aitio, O.; Chirkova, T. V.; Fagerstedt, K. V. *Physiol. Plant.* 2007, 129, 507.
- Sommer, S.; Jahn, A.; Funke, F.; Brenke, N. *Naturwissenschaften* 2000, 87, 283.

5. Koo, M. K.; Oh, C. H.; Holme, A. L.; Pervaiz, S. *Cytometry A* 2007, 71, 87.
6. Briggs, M. S.; Burns, D. D.; Cooper, M. E.; Gregory, S. J. *Chem. Commun.* 2000, 2323.
7. Liu, Y. S.; Sun, Y. P.; Vernier, P. T.; Liang, C. H.; Chong, S. Y. C.; Martin, A.; Gundersen, M. A. *J. Phys. Chem. C* 2007, 111, 2872.
8. Bizzarri, R.; Arcangeli, C.; Arosio, D.; Rici, F.; Faraci, P.; Cardarelli, F.; Beltram, F. *Biophys. J.* 2006, 90, 3300.
9. Diehl, H.; Horchak-Morris, N. *Talanta* 1987, 34, 739.
10. Klonis, N.; Sawyer, W. H. *J. Fluoresc.* 1996, 6, 147.
11. Khodorov, B.; Valkina, O.; Turovetsky, V. *FEBS Lett.* 1994, 341, 125.
12. Haworth, R. S.; Fliegel, L. *Mol. Cell. Biochem.* 1993, 124, 131.
13. Shimoda, L. A.; Luke, T.; Sylvester, J. T.; Shih, H. W.; Jain, A.; Swenson, E. R. *Am. J. Physiol.* 2007, 292, L1002.
14. Kang, M.; Walker, J. W. *Exp. Biol. Med.* 2006, 231, 865.
15. Tsien, R. Y. *Nature* 1981, 290, 527.
16. Tsien, R. Y. *Annu. Rev. Neurosci.* 1989, 12, 227.
17. Sanchez-Martin, R. M.; Cuttle, M.; Mittoo, S.; Bradley, M. *Angew. Chem. Int. Ed.* 2006, 45, 5472.
18. Sanchez-Martin, R. M.; Muzerelle, M.; Chitkul, N.; How, S. E.; Mittoo, S.; Bradley, M. *ChemBioChem* 2005, 6, 1341.
19. Franck, P.; Petitpain, N.; Cherlet, M.; Dardennes, M.; Maachi, F.; Schutz, B.; Poisson, L.; Nabet, P. *J. Biotechnol.* 1996, 46, 187.
20. A set of high $[K^+]$ buffers of varying $[H^+]$ were prepared by mixing appropriate proportions of KH_2PO_4 (135 mM) and K_2HPO_4 (110 mM) in 20 mM NaCl to give pH values in the range of 6.0–8.0.
21. Mosmann, T. *J. Immunol. Methods* 1983, 65, 55.
22. A set of high $[K^+]$ buffers of varying $[H^+]$ were prepared by mixing appropriate proportions of KH_2PO_4 (135 mM) and K_2HPO_4 (110 mM) in 20 mM NaCl to give pH values in the range of 6.0–8.0. Each cell sample was treated with nigericin (10 μ M) for 5 min before flow cytometry analysis. The samples were analyzed in a random order and each experiment was done in triplicate.
23. To perform quantitative analysis images of cells loaded with fluorescein microspheres were taken at two different positions in each well and the fluorescence intensity of every bead in the defined region measured (all experiments were done in duplicate with approximately 500 beads measured per image, giving a total of approximately 1000 fluorescent intensities per well and therefore, 2000 fluorescent intensities per pH value). These intensities were summed and averaged to give the values in Figure 4c.